UNIVERSIDADE da MADEIRA

CCM-Centro de Ciências Matemáticas

Primordial Black Holes and Cosmological Phase Transitions

Report of Progress of PhD Work
(Second year full time)

Laurindo Sobrinho, Pedro Augusto
Universidade da Madeira
Departamento de Matemática e Engenharias
9000-390 Funchal, Madeira
Portugal

CCM Nr. 19/08

CCM – Centro de **C**iências **M**atemáticas
Universidade da Madeira, P-9000 Funchal, Madeira
Tel. + 351 291 705181, Fax: +351-91-705189
e-mail: ccm@uma.pt
http://ccm.uma.pt

Primordial Black Holes and Cosmological Phase Transitions

Report of Progress of PhD Work
(Second year full time)

Laurindo Sobrinho, Pedro Augusto[1]
Departamento de Matemática e Engenharias, Universidade da Madeira

October 2008

Abstract

The Universe is a well developed structure on the scale of galaxies and smaller formations. This requires that at the beginning of the expansion of the Universe there should have existed fluctuations which lead to the formation of such structures. Inflation, a successful cosmological paradigm, allows us to consider the quantum origin of the fluctuations. Within this paradigm, we can explain not only all the inhomogeneities we see today but also the formation of Primordial Black Holes (PBHs). However, PBH formation requires the amplitude of the fluctuations to be above some threshold δ_c. During the cosmological phase transitions, δ_c experiences a reduction that favours PBH formation. We have considered this issue in the case of the Quantum Chromodynamics (QCD) and the Electroweak (EW) phase transitions. We have also given a similar treatment to the cosmological electron–positron annihilation epoch. Our results allow the determination of the fraction of the universe going into PBHs (β). We have obtained, considering a running–tilt power–law spectrum, results in the range $\beta \approx 0$ to $\beta \sim 10^{-4}$.

[1]PhD Supervisor

Contents

List of Figures

List of Tables

Acronyms

2dFGRS 2 degree Field Galaxy Redshift Survey

ACBAR Arcminute Cosmology Bolometer Array Receiver

AMSB Anomaly–Mediated Susy Breaking

CBI Cosmic Background Imager

CDM Cold Dark Matter

CMB Cosmic Microwave Background

EoS Equation of State

EW ElectroWeak

EWBG EW BaryoGenesis

FLRW Friedmann–Lemaître–Robertson–Walker metric

GMSB Gauge–Mediated Susy Breaking

GUT Grand Unification Theory

HDM Hot Dark Matter

HG Hadron Gas

Lambda CDM Lambda–Cold Dark Matter Model

LEP Large Electron Positron Collider

LGT Lattice Gauge Theory

LSP Lightest Supersymmetric Particle

LSS Large Scale Structure

LTE Local Thermodynamic Equilibrium

MSSM Minimal Supersymmetric extension of the Standard Model

mSUGRA minimal SUperGRAvity

PBH Primordial Black Hole

PDG Particle Data Group

QCD Quantum Chromodynamics

QGP Quark–Gluon Plasma

RHIC Relativistic Heavy Ion Collider

SDSS Sloan Digital Sky Survey

SLC Stanford Linear Collider

SMBH Supermassive Black Hole

SMPP Standard Model of Particle Physics

WIMP Weakly Interacting Massive Particle

WMAP Wilkinson Microwave Anisotropy Probe

Physical Constants and Parameters

speed of light in vacuum	c	$299792458 \text{ ms}^{-1}$
Planck constant	h	$6.62606896(33) \times 10^{-34}$ Js
gravitational constant	G	$6.67428(67) \times 10^{-11} \text{ m}^3\text{kg}^{-1}\text{s}^{-2}$
Boltzmann constant	k	$1.3806504(24) \times 10^{-23} \text{ JK}^{-1}$
Fermi coupling constant	G_F	$1.16637(1) \times 10^{-5} \text{ GeV}^{-2}$
electron charge	e	$1.602176487(40) \times 10^{-19}$ C
astronomical unit	AU	149597870660(20) m
parsec	pc	$3.0856775807(4) \times 10^{16} \text{ m} \approx 3.262$ ly
Planck mass	m_P	$2.17645(16) \times 10^{-8}$ kg
Planck length	l_P	$1.61624(12) \times 10^{-35}$ m
Planck time	t_P	$5.39121(40) \times 10^{-44}$ s
Solar mass	$M_\odot$	$1.98844(30) \times 10^{30}$ kg

Preface

Black Holes are objects predicted by the laws of Physics. So far, black holes (or black hole candidates) have been detected only by indirect means. On this PhD thesis we plan to investigate the possibility of direct detection of a black hole. We have started with primordial black holes (i.e., black holes formed in the early universe) because, as far as we know, those are the only ones that could have formed with substellar masses which makes them potential candidates for the *nearest detectable black hole*.

In this report we present the PhD work done during the second year (full time) mainly devoted to the determination of the fraction of the universe going into PBHs (β) during cosmological phase transitions. Sections 1 to 6 are devoted to a literature review although they have also some original work. In Section 1 we review the primordial Universe, in the context of the present work (e.g. number of degrees of freedom, scale factor, particle physics, inflation).

Section 2 is dedicated to the QCD phase transition with particular attention to the different models often used to describe it: Bag Model, Lattice Fit and Crossover. In Section 3 we discuss the EW phase transition and in Section 4 the cosmological electron–positron annihilation epoch.

In Section 5 we have considered the behaviour of primordial density fluctuations in the context of the mentioned cosmological phase transitions. In Section 6 we study the conditions for PBH formation and how this changes in the presence of a phase transition (δ_c decreases).

In Sections 7 to 11 we present our original results. In Section 7 we determine the variation of δ_c for the QCD phase transition in the case of a Bag Model, Lattice Fit or Crossover. In Section 8 we do the same for the EW phase transition in the case of a Crossover (SMPP) and in the case of a Bag Model (MSSM) while in Section 9 we do it for the electron–positron annihilation epoch.

In Section 10 we discuss the adopted power spectrum for the density fluctuations. In general, the requirement for abundant PBH formation demands fine–tunning. This is achieved, in our case, with two parameters giving the location and the amplitude of the peak on the spectral index.

Section 11 is devoted to the calculus of the fraction of the Universe going into PBHs during the considered cosmological phase transitions. We have explored the cases for which one gets the highest values for β (up to $\sim 10^{-4}$).

In Section 12 we present our future work plan. In the near future we want to determine the PBH distribution function in the universe and consequently determine the mean distance to the nearest one. In the not so near future we want to improve our results addressing other subjects such as the PBH merging and PBH relics. With the Large Hadron Collider (LHC) already in operation (since 10 September 2008), which might produce BHs, our work is very exciting indeed!

José Laurindo de Góis Nóbrega Sobrinho
Universidade da Madeira
October 2008

1 The Primordial Universe

The modern understanding of the early and present Universe hinges upon two standard models: the *Standard Model of Cosmology* and the *Standard Model of Particle Physics* (SMPP) (e.g. Boyanovsky et al., 2006). In this chapter we review a few topics, within the contexts of Cosmology and Particle Physics, which are important to our subsequent work.

1.1 Relativistic cosmology

According to observation we live in a flat, homogeneous and isotropic (on scales larger than 100 Mpc) expanding Universe (e.g. Jones & Lambourne, 2004). Thus, *Cosmology*, i.e. the study of the dynamical structure of the Universe as a whole, is based on the (e.g. d'Inverno, 1993)

Cosmological Principle– At each epoch, the Universe presents the same aspect from every point, except for local irregularities,

which is in essence, a generalization of the *Copernican Principle* that the Earth is not at the center of the Solar System. We are assuming that there is a *cosmic time* t with the Cosmological Principle valid for each spacelike hypersurface $t = const$. The statement that each hypersurface has no privileged points means that it is homogeneous. The principle also requires that each hypersurface has no privileged directions about any point, i.e., the spacelike hypersurfaces are isotropic and necessarily spherically symmetric about each point. The concepts of homogeneity and isotropy, however, do not apply to the Universe in detail (e.g. d'Inverno, 1993).

In 1923, H. Weyl addressed the problem of how a theory like *General Relativity* can be applied to a unique system like the Universe. He considered the assumption that there is a privileged class of observers in the Universe, namely, those associated with the smeared–out motion of the galaxies. We can work with this smeared–out motion because the relative velocities in each group of galaxies are, according to observation, small. Weyl introduced a fluid pervading space, which he called *the substractum*, in which the galaxies move like particles in a fluid. These ideas are contained on the (e.g. d'Inverno, 1993)

Weyl's Postulate – The particles of the substractum lie in space–time on a congruence of timelike geodesics diverging from a point in the finite or infinite past.

The postulate requires that the geodesics do not intersect except at a singular point in the past and possibly at a similar singular point in the future. There is, therefore, one and only one geodesic passing through each point of space–time, and consequently the matter at any point possesses a unique velocity. This means that the substractum may be taken to be a *perfect fluid*. Although galaxies do not follow this motion exactly, the deviations appear to be random and less than one–thousandth of the velocity of light (e.g. d'Inverno, 1993).

Relativistic Cosmology is based on three assumptions: (1) the Cosmological Principle, (2) Weyl's postulate and (3) General Relativity[2].

Weyl's postulate requires that the geodesics of the substractum are orthogonal to a family of spacelike hypersurfaces. We introduce coordinates (t, x^1, x^2, x^3) such that these spacelike hypersurfaces are given by constant t and such that the space coordinates (x^1, x^2, x^3) are constant along the geodesics. Such coordinates are called *comoving coordinates* (e.g. d'Inverno, 1993). Comoving observers are also called *fundamental observers*.

A flat, homogeneous and isotropic expanding Universe can be described by the *Friedmann–Lemaître–Robertson–Walker* (FLRW) metric (e.g. d'Inverno, 1993)

$$ds^2 = dt^2 - R^2(t)\left[\frac{dr^2}{1-\kappa r^2} + r^2\left(d\theta^2 + sin^2\theta d\phi^2\right)\right] \tag{1}$$

where $R(t)$ is the so called *scale factor* which describes the time dependence of the geometry (the distance between any pair of galaxies, separated by more than 100 Mpc, is proportional to $R(t)$) and κ is a constant which fixes the sign of the spatial curvature ($\kappa = 0$ for Euclidean space, $\kappa > 0$ for a closed elliptical space of finite volume and $\kappa < 0$ for an open hyperbolic space). Notice that, whatever the physics of the expansion, the space–time metric must be of the FLRW form, because of the isotropy and homogeneity (e.g. Longair, 1998).

Considering the FLRW metric (1), Weyl's postulate, General Relativity (with a *cosmological constant* term Λ) and a comoving coordinate system it turns out that the field equations lead to two independent equations sometimes called the *Friedmann–Lemaître equations* (e.g. Yao et al., 2006; Unsöld & Bascheck, 2002)

$$\left(\frac{\dot{R}}{R}\right)^2 = \frac{8\pi G\rho}{3} - \frac{\kappa}{R^2} + \frac{\Lambda}{3} \tag{2}$$

$$\frac{\ddot{R}}{R} = \frac{\Lambda}{3} - \frac{4\pi G}{3}(\rho + 3p) \tag{3}$$

where we have used relativistic units ($c = 1$) and a dot denotes differentiation with respect to cosmic time t. Equation (3) involves a second time derivative of R and so it can be regarded as an equation of motion, whereas equation (2), sometimes called *Friedmann equation*, only involves a first time derivative of R and so may be considered an integral of motion, i.e., an energy equation.

The addition of a cosmological constant term Λ is equivalent to assume that matter is not the only source of gravity and there is also an additional source of gravity in the form of a fluid with pressure p_Λ and energy density ρ_Λ

[2]For an introductory text on the Theory of General Relativity see (e.g. Schutz, 1985; d'Inverno, 1993).

(e.g Lyth, 1993). The Λ term was introduced by Einstein with the purpose of constructing a static cosmological model for the Universe. However, with the discovery of the expansion of the Universe (Slipher, 1917) the model became obsolete. More recently, a $\Lambda > 0$ term was introduced again in order to account for the remarkable discovery that the expansion of the Universe is, in fact, accelerating rather than retarding (Section 1.5).

Energy conservation leads to a third equation, which can also be derived from equations (2) and (3), and is just a consequence of the *First Law of Thermodynamics* (e.g. Yao et al., 2006)

$$\dot{\rho} = -3\frac{\dot{R}}{R}(\rho + p). \tag{4}$$

We need also an *equation of state* (EoS) relating the pressure p to the energy density ρ at a given epoch. This relation is, in general, non–trivial. However, in Cosmology, where one deals with dilute gases, the EoS can be written in a simple linear form (e.g. Carr, 2003; Ryden, 2003)

$$p = w\rho \tag{5}$$

where the dimensionless quantity w is the so–called *adiabatic index*. Normally w is a constant such that $0 \leq w \leq 1$. If $w = 0$ we are in the case of a pressureless matter–dominated universe and, if $w = 1$ we have a stiff EoS which may be the case if the universe is dominated by a *scalar field*[3] (e.g. Harada & Carr, 2005).

In the case of cosmological perturbations the radiation fluid behaves as a perfect (i.e. dissipationless) fluid, entropy (s) in a comoving volume is conserved and, one has a reversible process. The isentropic[4] sound speed can be written as (e.g. Schmid et al., 1999)

$$c_s^2 = \left(\frac{\partial p}{\partial \rho}\right)_s = w. \tag{6}$$

In the early hot and dense primordial Universe it is appropriate to assume an EoS corresponding to a gas composed of radiation and relativistic massive particles with $w = 1/3$ (e.g. Carr, 2003)

$$p = \frac{\rho}{3} \tag{7}$$

which means that, in the case of a radiation–dominated universe, the sound speed is given by

$$c_s = \frac{1}{\sqrt{3}}. \tag{8}$$

[3] A scalar field is a field that associates a scalar value to every point in space. On the other hand, a vector field associates a vector to every point in space. In quantum field theory, a scalar field is associated with spin 0 particles (scalar bosons) and a vector field is associated with spin 1 particles (vector bosons).

[4] A thermodynamic process that occurs at a constant entropy (s) is sayd to be isentropic. If it is a reversible process then it is identical to an adiabatic process, i.e., a thermodynamic process in which there is no energy added or subtracted from the system.

However, during inflation (Section 1.3) or in a universe dominated by a cosmological constant, w becomes negative and may not even be constant (e.g. Yao et al., 2006). If $w < 0$ the sound speed is imaginary (cf. equation 6). In this case we have perturbations with negative pressure that will not propagate as stable sound waves, but will have amplitudes that grow or decay with time (e.g. Ryden, 2003). The case $w < -1/3$ is of special interest because it provides a positive acceleration to the universe. Current measurements give $w = -0.967 \pm 0.073$ (Spergel et al., 2007) which means that the expansion of the universe is accelerating by the present time. We will thus consider, for simplicity, $w = -1$.

Inserting equation (5) into equation (4) we have

$$\dot{\rho} = -3(1+w)\rho\frac{\dot{R}}{R}. \tag{9}$$

Putting $w = -1$ in equation (9) one gets $\dot{\rho} = 0$ which means that in a universe dominated by a cosmological constant the energy density remains constant (or almost constant, if one considers $w \approx -1$ and $w \neq -1$). Integration of equation (9) yields

$$\rho(t) \propto R(t)^{-3(1+w)}. \tag{10}$$

Another important thermodynamic relation is the *Second Law of Thermodynamics*, which connects pressure and energy density. It can be written, in the case of a fluid without chemical potential, as (e.g. Schmid et al., 1999; Schwarz, 2003)

$$\rho = T\frac{dp}{dT} - p. \tag{11}$$

The entropy density for such a fluid is given by the Maxwell relation for the free energy (e.g. Schmid et al., 1999; Schwarz, 2003)

$$s = \frac{dp}{dT}. \tag{12}$$

From homegeneity we have that the free energy density reads (e.g. Schmid et al., 1999; Schwarz, 2003)

$$f(T) = -p(T) \tag{13}$$

which contains the full thermodynamic information. The sound speed (equation 6) can be written, from equations (11) and (12), also in the form (e.g. Schmid et al., 1999)

$$c_s^2 = \left(\frac{d\ln s}{d\ln T}\right)^{-1}. \tag{14}$$

During a first–order phase transition, for a fluid with negligible chemical potential, the entropy is conserved and, hence, $c_s^2 = 0$ during the transition (e.g.

Section 2.3). The conservation of entropy leads to the useful relation (e.g. Schmid et al., 1999)

$$\frac{dT}{d\ln R} = -\frac{3s}{ds/dT}. \tag{15}$$

In the following we consider the solutions of equation (2) when a single component dominates the energy density. Taking into account that, according to observation, we live in a flat Universe, we consider $\kappa = 0$. Note that even if $\kappa \neq 0$ at early times (when the scale factor is smaller) we can neglect the term κ/R^2 in equation (2) as long as $w > -1/3$ (e.g. Yao et al., 2006).

Inserting equation (10) into equation (2), with $\kappa = 0$ and $\Lambda = 0$, one obtains (e.g. Yao et al., 2006)

$$R(t) \propto t^{\frac{2}{3(1+w)}}. \tag{16}$$

For a radiation–dominated Universe ($w = 1/3$), equation (16) becomes

$$R(t) \propto t^{1/2}. \tag{17}$$

The radiation and matter densities in the Universe decrease as the expansion dilutes the number of atoms and photons. Radiation is also diminished due to the *cosmological redshift*, so its density falls faster than that of matter. When the age of the Universe was $\sim 10^6$ years it became matter–dominated. Now it is appropriate to assume an EoS corresponding to a pressureless gas ($w = 0$). For this matter–dominated Universe, equation (16) becomes

$$R(t) \propto t^{2/3}. \tag{18}$$

This might also be the case if the Universe experienced a dust–like phase during a phase transition on the radiation–dominated epoch (e.g. Carr et. al., 1994).

If the Universe is dominated by a positive cosmological constant Λ then we will have an EoS with $w < 0$. We will consider, for simplicity and observational consistency, $w = -1$. In this case the integration of equation (2) with $\kappa = 0$ and $\Lambda > 0$ leads to (e.g. Yao et al., 2006)

$$R(t) \propto \exp\left(\sqrt{\frac{\Lambda}{3}}ct\right) \tag{19}$$

which corresponds to an exponential expansion of the Universe.

Assuming that light propagates in Relativistic Cosmology in the same way as it does in General Relativity we will consider now how an observer O receives light from a receding galaxy. Without loss of generality we will take O to be at the origin of coordinates $r = 0$. Inserting the conditions for a radial null geodesic into the line element (1) we have (e.g. d'Inverno, 1993)

$$\frac{dt}{R(t)} = \pm\frac{dr}{(1-kr)^{1/2}} \tag{20}$$

where the + sign corresponds to a receding light ray and the − sign to an aproaching light ray. Consider a light ray emanating from a galaxy P with world line $r = r_1$, at coordinate t_1, and received by O at coordinate time t_0. Using equation (20) we have (e.g. d'Inverno, 1993)

$$\int_{t_1}^{t_0} \frac{dt}{R(t)} = -\int_{r_1}^{0} \frac{dr}{(1-kr)^{1/2}}. \tag{21}$$

Next, consider a second light ray emanating from P at time t_1+dt_1 and received at O at time $t_0 + dt_0$. Thus, we have

$$\int_{t_1+dt_1}^{t_0+dt_0} \frac{dt}{R(t)} = -\int_{r_1}^{0} \frac{dr}{(1-kr)^{1/2}}. \tag{22}$$

Comparing equations (21) and (22) it turns out that

$$\int_{t_1+dt_1}^{t_0+dt_0} \frac{dt}{R(t)} = \int_{t_1}^{t_0} \frac{dt}{R(t)}. \tag{23}$$

Assuming that $R(t)$ does not vary greatly over the intervals dt_1 and dt_0 we can take it outside the integral, yielding (e.g. d'Inverno, 1993)

$$\frac{dt_0}{R(t_0)} = \frac{dt_1}{R(t_1)}. \tag{24}$$

All fundamental particles of the substractum have world lines on which the spatial coordinates are constant and, hence, the metric reduces to $ds^2 = dt^2$. Here t measures the *proper time* along the substractum world lines. The intervals dt_1 and dt_0 are, respectively, the proper time intervals between the rays as measured at the source and observer. In an expanding Universe we have that $t_0 > t_1$ and so $R(t_0) > R(t_1)$ which means that the observer O will experience a *redshift* z given by (e.g. d'Inverno, 1993)

$$1 + z = \frac{\nu_0}{\nu_1} = \frac{R(t_0)}{R(t_1)} = \frac{dt_0}{dt_1} \tag{25}$$

where ν_1 and ν_0 are the frequencies measured by the emitter and the receiver, respectively. In a contracting Universe O will detect instead a *blue shift*.

The *Hubble parameter* H is defined as (e.g. d'Inverno, 1993)

$$H(t) = \frac{\dot{R}(t)}{R(t)} \tag{26}$$

and the *Hubble time* is defined as (e.g. Boyanovsky et al., 2006)

$$t_H(t) = \frac{1}{H(t)} = \frac{R(t)}{\dot{R}(t)}. \tag{27}$$

Multiplying t_H by the speed of light c one obtains the so called *Hubble radius* R_H (e.g. Boyanovsky et al., 2006)

$$R_H(t) = \frac{c}{H(t)} = c\frac{R(t)}{\dot{R}(t)} \tag{28}$$

which corresponds to the size of the *Observable Universe* at a given epoch. The mass contained inside a region with size R_H is called the *horizon mass* and it is given by

$$M_H(t) = \frac{4}{3}\pi R_H(t)^3 \rho(t). \tag{29}$$

Here we consider for $M_H(t)$ the approximation given by (e.g. Carr, 2005)

$$M_H(t) \approx \frac{c^3 t}{G} \approx 10^{15}\left(\frac{t}{10^{-23}\ \mathrm{s}}\right)\mathrm{g} \tag{30}$$

where c is the speed of light in the vacuum and G is the Gravitational constant. This expression is useful in the context of the study of PBHs. It is natural to assume that the mass of a PBH, when it forms, is of the order of M_H at that epoch (e.g. Carr, 2005). When $t \approx 10^{-23}$ s we have $M_H \approx 10^{15}$ g. These values represent, respectively, the time of formation and the initial mass of the PBHs that are presumed to be explodind by the present time (e.g. Sobrinho, 2003).

There are, however, some problems with the stantard Big Bang theory. In order to identify such problems let us start by dividing equation (2) by H^2

$$1 = \frac{8\pi G}{3H^2}\rho - \frac{\kappa}{R^2H^2} + \frac{c^2\Lambda}{3H^2}. \tag{31}$$

Consider the case $\Lambda = 0$. If $\kappa < 0$ the Universe will expand forever and if $k > 0$ the expansion will eventually give way to contraction. Between the two possibilities we have the critical case $\kappa = 0$. In this case one obtains from equation (31) the following expression for the density

$$\rho_c = \frac{3H^2}{8\pi G} \tag{32}$$

which is called the *critical density*. The *matter density parameter* is defined as (e.g. Unsöld & Bascheck, 2002)

$$\Omega_m = \frac{\rho}{\rho_c} \tag{33}$$

where ρ is the matter density of the Universe. We will introduce here also the quantities (e.g. Covi, 2003)

$$\Omega_\kappa = -\frac{\kappa}{H^2R^2} \tag{34}$$

$$\Omega_\Lambda = \frac{\rho_\Lambda}{\rho_c} = \frac{c^2\Lambda}{3H^2}. \tag{35}$$

With this definitions we can rewrite equation (31) in the simple form (e.g. Covi, 2003)

$$1 = \Omega = \Omega_m + \Omega_\kappa + \Omega_\Lambda. \tag{36}$$

In the standard Big Bang theory we have always $\ddot{R} < 0$ (cf. equation (3) with $\Lambda = 0$) which implies that the term R^2H^2 in equation (31) will always decrease. This indicates that Ω tends to shift away from unity with the expansion of the Universe. However, present observations suggest that $\Omega \sim 1$, i.e., Ω should have been very close to unity in the past. This turns out to be an extreme fine tuning of initial conditions. Unless initial conditions are chosen very accurately, the Universe soon collapses, or expands quickly before any structure formation. This is known as the *flatness problem* (e.g. Tsujikawa, 2003).

The *Cosmic Microwave Background* (CMB) radiation was released when the Universe was ~ 380000 years old (Section 1.7). At that epoch the Universe had cooled enough so that the opaque plasma neutralized into a transparent gas, allowing photons to, finally, travel freely. These CMB photons have been travelling mostly on straight lines since then, so they provide an image of what the Universe looked like at that epoch. Observation shows that the CMB is nearly homogeneous and isotropic (with anisotropies ant the 10^{-5} level, Section 1.7) which, therefore, implies that the observed Universe had become uniform in temperature by that time. In standard FLRW cosmology, a simple calculation shows that the uniformity could be established that quickly only if signals could propagate at 100 times the speed of light, a proposition clearly contradicting the known laws of Physics. This is known as the *horizon problem* (e.g. Guth, 2000).

From the view point of Particle Physics, *symmetry breaking*[5] leads to the production of many unwanted relics such as *monopoles*, *cosmic strings*, and *topological defects*. If these particles existed in the early stage of the Universe then their massive relics should be the dominant materials in the Universe (they would outweigh everything else in the Universe by a factor of about 10^{12}), which contradicts observations. This problem is generally called the *monopole problem* (e.g. Tsujikawa, 2003; Guth, 2000).

1.2 The Universe Timeline

The Big Bang theory is based on the observed Hubble's law redshift of distant galaxies that when taken together with the Cosmological Principle indicate that

[5]The basic idea underlying unified theories of the weak, strong, and electromagnetic interactions is that, prior to symmetry breaking, all vector mesons (which mediate these interactions) are massless, and there are no fundamental differences among the interactions. As a result of the symmetry breaking, however, some of the vector bosons acquire mass, and their corresponding interactions become short–range, thereby destroying the symmetry between the various interactions. For example, prior to the appearance of the constant scalar Higgs field H, the Glashow–Weinberg–Salam model was symmetrical, and EW interactions were mediated by massless vector bosons. With the Higgs field, some of the vector bosons (W^-, Z^0 and W^+) acquire masses of ~ 100 GeV, and the corresponding interactions become short–range (weak interactions), whereas the electromagnetic field boson (i.e., the photon) remains massless (e.g. Linde, 2005).

space is expanding according to the Friedmann–Lemaître model of General Relativity (Slipher, 1917; Hubble, 1929). Extrapolated into the past, these observations show that the Universe has expanded from a state in which all its matter and energy had immense temperatures and densities.

In fact, in the very early Universe the temperatures and densities were so high that the photons and the great variety of relativistic particles were in thermodynamic equilibrium. When the mean thermal energy $kT \gg mc^2$, conservation of energy implies that every elementary particle of rest mass m can be converted into every other particle. Creation and annihilation of particle–antiparticle pairs and the interactions with other particles thus keep any particular type of particle of mass m in equilibrium (and in large numbers) above the energy mc^2. As the average energy in the Universe decreased due to its expansion to a value less than the equivalent mass mc^2, particles of mass m which had decayed or been annihilated could no longer be replaced. This point is known as the *threshold* for that particular particle. Cosmic evolution is thus characterized by a sequencial 'dying off' of the various types of particles, beginning with the most massive. The temperature T or the average thermal energy kT in the radiation cosmos, can be written as a function of time as (e.g. Unsöld & Bascheck, 2002)

$$t[s] \simeq \frac{1.5}{(T[10^{10}\ K])^2} \simeq \frac{1}{(kT[MeV])^2}, \tag{37}$$

as long as $t \leq 2 \times 10^6$ years and leaving out of consideration the details of each types of relativistic particle.

Before one Planck time ($t_P \sim 10^{-43}$ s) all the four fundamental forces were unified into a single force. This phase of the Universe is called the *Planck Era*. During this era the theory of General Relativity, which treats space–time as a continuum, would have to be replaced by a still lacking *Quantum Theory of Gravity*. Only at the end of this era, i.e., when the Universe was $\sim 10^{-43}$ s old, gravity separated from the other three forces (e.g. Unsöld & Bascheck, 2002).

The period 10^{-43} s $< t <$ 10^{-35} s is is called the *Grand Unification Era*. During this era the electromagnetic, strong and weak interactions are unified in a single force mediated by an hypothetical boson X, with mass (energy) of order 10^{14} GeV, which converts leptons into quarks and vice versa. At this stage the Universe consists of a plasma composed of quarks, gluons, leptons, photons, bosons X as well as their respective antiparticles. They are all present in equal abundances and are continuoslly being interconverted due to mutual collisions (e.g. Unsöld & Bascheck, 2002).

When the temperature of the Universe goes below 10^{14} GeV it turns out that the decaying X bosons are no longer replaced by new X bosons. As a result, we have the *strong–electroweak phase transition*, i.e., the separation of the strong and EW interactions (e.g. Unsöld & Bascheck, 2002).

In order to explain problems such as 'flatness', 'horizon' and 'monopole', the present paradigm makes use of an inflationary stage of expansion in the very early Universe (Section 1.3). During inflation the scale factor $R(t)$ growns exponentially from an initial value R_i, corresponding to the instant $t_i \sim 10^{-35}$ s when the EW and strong forces separate (e.g. Narlikar & Padmanabhan, 1991). The inflationary stage is followed by a radiation–dominated era after a short period of reheating during which the energy stored in the field that drives inflation decays into quanta of many other fields, which, through scattering processes, reach a state of local thermodynamic equilibrium (e.g. Boyanovsky et al., 2006).

The period which goes from the end of this reheating process up to $t \sim 10^{-6}$ s is known as the *Quark Era*. During this era the Universe consists of a plasma composed of quarks, leptons, photons, gluons and their antiparticles. Particle–antiparticle pairs are constantly being created and annihilated. Conversion between quarks and leptons are not possible because X bosons no longer exist.

When the temperature of the Universe decays to ~ 180 GeV it is no longer possible to create top quarks (or anti–top quarks). Top and anti–top quarks annihilate each other and cease to exist in nature. It is also during the quark era that the tauon, and the bottom and charm quarks thresholds occur (Table 1). When the Universe temperature reaches ~ 100 GeV (corresponding to the mass of the $W^{\pm}$ and Z^0 bosons) another remarkable effect takes place: the weak force decouples from the electromagnetic force in a process called the *EW phase transition* (Section 3). It is only now that the four fundamental interactions are separarated (e.g. Unsöld & Bascheck, 2002), as we see them today.

When the temperature of the Universe goes from 2 GeV to 1 GeV almost all the baryons cease to be produced. This applies to the baryons Ω, Ξ, Σ and Λ. Among the decaying products we have neutrons (mean–life ~ 600 s (e.g. Jones & Lambourne, 2004) which is a very long time if compared with the age of the Universe at this stage) and protons. These were the first stable neutrons and protons ever produced in the Universe.

As the temperature falls through ~ 170 MeV the *Quark–Hadron phase transition* occurs (Section 2), i.e., quarks and gluons bind into stable hadrons (neutrons and protons). This marks the beginning of the *Hadron Era*. During the hadron era the kaons, pions and muons thresholds take place (Table 1).

When the Universe is 10^{-4} s old, and the last pions have just decayed, the *Lepton Era* begins. The Universe is now composed, according to the SMPP (Section 1.8), of photons, protons, neutrons, electrons, positrons, neutrinos and antineutrinos. Protons and neutrons turn into each other through reactions like: $e^- + p \longleftrightarrow \nu_e + n$, $e^+ + n \longleftrightarrow \bar{\nu}_e + p$, $n \longleftrightarrow p + e^- + \bar{\nu}_e$ (e.g. Lyth, 1993; Jones & Lambourne, 2004). When the Universe is ≈ 1 s old neutrinos decouple, i.e., the Universe becomes transparent to neutrinos. Finally, when the Universe is ≈ 3 s old, the electron threshold occurs marking the end of the Lepton Era.

About 200 s after the singularity, the Universe has cooled to $\sim 10^9$ K, allowing the synthesis of nuclei from protons and neutrons in a process called *Primordial Nucleosynthesis*. The first fusion reaction that could occur was that between a proton and a neutron to form a nucleus of deuterium (deuteron): $p + n \leftrightarrows {}^2_1\mathrm{H} + \gamma$. A deuteron can be broken apart by an incident γ–ray photon with energy ≥ 2.23 MeV. However at this stage ($t \sim 200$ s) the average photon energy in the universe decreased below that limit and hence, deuterium, once formed, would no longer be destroyed (e.g. Jones & Lambourne, 2004).

As soon as there was a significant abundance of deuterium, other nuclear

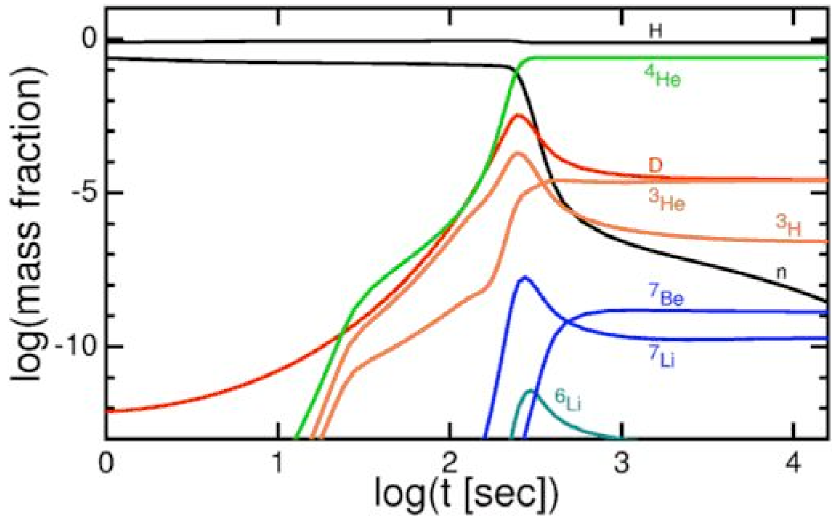

Figure 1: The time evolution of the abundances of the light elements produced during Primordial Nucleosynthesis. It is also shown the decrease of the neutron abundance (adapted from Burles et al., 1999).

reaction could then proceed with the formation of ${}^3_1$H (tritium), ${}^3_2$He, ${}^4_2$He, ${}^6_3$Li, ${}^7_3$Li and, ${}^7_4$Be. The reason why Primordial Nucleosynthesis did not progress to produce elements with higher mass numbers is due to two factors: i) the temperature of the universe which is by this time lower than required and, ii) there are no stable nuclides with mass number $A = 5$ or $A = 8$. When the Universe become $\sim$ 1000 s old the formation of nuclides effectively ceased leaving a Universe with primary matter content of hydrogen (mainly protons, i.e., ${}^1_1$H) and helium (mainly ${}^4_2$He), with trace amounts of beryllium and lithium (e.g. Jones & Lambourne, 2004, Figure 1).

The radiation and matter densities in the Universe decrease as the expansion dilutes the number of atoms and photons. Radiation also decreases due to the cosmological redshift (see equation 25), so its density falls faster than that of matter. Looking back in time, there was an instant, which corresponds to an age of the Universe of $\sim 10^4$ years (redshift $z \approx 3200$, e.g. Bennett et al., 2003; Hinshaw et al., 2008), when matter and radiation densities were just equal (cf. Table 1, Figure 2). Before that time the Universe was radiation–dominated.

At an age of $\sim 10^5$ years the universe had expanded and cooled enough ($T \sim 4000$ K), allowing nuclei and electrons to combine in order to form neutral atoms. This process, which is known as *recombination*[6], can be numerically defined as the instant in time when the number density of ions is equal to the number density of neutral atoms (e.g. Ryden, 2003).

[6]Some authors suggest that we should use the term *combination* instead because this is the very first time in the history of the universe when electrons and ions combined to form neutral atoms (e.g. Ryden, 2003).

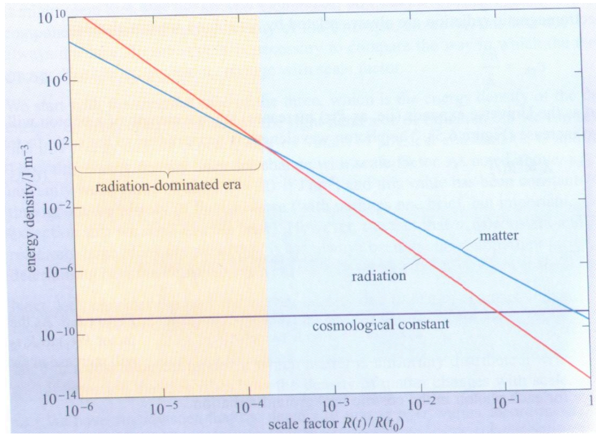

Figure 2: The energy densities of matter and radiation as a function of the scale factor $R(t)$. At a time when $R(t)/R(t_0) \approx 10^{-4}$ the energy densities of matter and radiation were equal ($R(t_0)$ represents the present day value of the scale factor). It is also represented the energy density due to the cosmological constant, which does not vary with redshift, and is exceeded by the energy densities in matter and radiation at early times (e.g. Jones & Lambourne, 2004).

When the universe was $\sim$ 380000 years old ($z \approx 1090$, e.g. Bennett et al., 2003; Hinshaw et al., 2008) and the temperature had dropped to $\sim$ 3000 K, the number density of free electrons was so low that the universe essentially became transparent and photons could travel unhindered from this time on. This is known as the *photon decoupling* epoch. The photons released during this epoch become the CMB (Section 1.7). Surrounding every observer in the universe there is a *last scattering surface* from which the CMB photons have been streaming freely (e.g. Ryden, 2003) becoming redshifted due to the expansion of the universe (Section 1.7).

The period between photon decoupling ($z \approx 1090$) and the formation of the first luminous objects ($z \sim 11$) is referred to as the *Cosmic Dark Ages*. That is because, during that period, there were no sources of radiation in the Universe, with the exception of the hyperfine 21–cm line of neutral hydrogen (e.g. Hirata & Sigurdson, 2007).

Reionization is the second of two major phase changes of hydrogen gas in the Universe (the first was recombination). Reionization occurred once objects started to form in the early Universe, which was energetic enough to ionize neutral hydrogen. As these objects formed and radiated energy, the Universe went from being neutral back to being an ionized plasma, at redshift $z \sim 11$ according to WMAP (Wilkinson Microwave Anisotropy Probe) results (Hinshaw et al., 2008).

When the universe was $\approx 2.8 \times 10^{17}$ s old (≈ 0.7 times the present age) it become dark energy–dominated (see Figure 2). The true nature of this dark energy, which is responsible for the observed non–linear acceleration of the universe, remains unknown (Section 1.8).

In Table 1 we present a timeline of the Universe according to the inflationary Big Bang model.

1.3 Inflation

In order to explain problems such as 'flatness', 'horizon' and 'monopole' the present paradigm makes use of an inflationary stage of expansion in the very early Universe. During inflation the scale factor $R(t)$ behaves like (e.g. Narlikar & Padmanabhan, 1991)

$$R(t) = R(t_i) \exp\left(H(t - t_i)\right). \tag{38}$$

The scale factor grows exponentially from an initial value $R_i = R(t_i)$, corresponding to the instant $t_i \sim 10^{-35}$ s when the EW and strong forces separate (e.g. Narlikar & Padmanabhan, 1991, cf. Table 1) to a value $R_e = R(t_e)$ according to (e.g. d'Inverno, 1993)

$$\frac{R_e}{R_i} = e^{N(t_e)} \tag{39}$$

where (e.g. Tsujikawa, 2003)

$$N(t_e) = \ln \frac{R_e}{R_i} = \int_{t_i}^{t_f} H dt \approx H t_e \tag{40}$$

gives the number of *e–folds* that elapsed during inflation. For example, the value $N = 70$ means that during inflation the scale factor have grown up by a factor of e^{70} ($\approx 10^{30}$). Although the exact value of $N(t_e)$ is unknown, in order to solve the mentioned problems, the inflationary stage must last a time interval such that $50 < N(t_e) < 70$ (e.g. Narlikar & Padmanabhan, 1991; Boyanovsky et al., 2006).

During inflation the scale factor $R(t)$ has a positive acceleration $\ddot{R}(t) > 0$ which means that the R^2H^2 term in equation (31) increases during inflation. As a result Ω rapidly approaches unity (see equation 36). After the inflationary period, the evolution of the Universe is followed by the conventional Big Bang phase (Section 1.2) and, despite this, Ω stays of order unity even in the present epoch, solving the flatness problem (e.g. Tsujikawa, 2003).

Inflation gives rise to a remarkable phenomenon: physical wavelengths grow faster than the size of the Hubble radius (see equation 28). This means that the region where the causality works is stretched on scales much larger than the Hubble radius, i.e., once a physical wavelength becomes larger than the Hubble radius, it is causally disconnected from physical processes. This solves the horizon problem (e.g. Boyanovsky et al., 2006). Notice that Inflationary cosmology suggests that, even though the observed Universe is incredibly large, it is only an infinitesimal fraction of the entire Universe (e.g. Guth, 2000).

Table 1: The Universe timeline according to the inflationary Big Bang model (data was taken mainly from Unsöld & Bascheck (2002) and Jones & Lambourne (2004).

Era	t(s)	T(K)	T(GeV)	Comments
Planck	–	–	–	Quantum Gravity
GUT	10^{-43}	10^{32}	10^{19}	Gravity separates
Quark	10^{-35}	10^{27}	10^{14}	Strong–electroweak phase transition Inflation begins
	$\sim 10^{-33}$	10^{27}	10^{14}	Inflation ends
	3×10^{-11}		172.5	t quark threshold
	$2.3 - 3.2 \times 10^{-10}$	10^{15}	100	EW phase transition
	10^{-8}		4.2	b quark threshold
	10^{-7}		1.78	Lepton τ threshold
			1.25	c quark threshold
			$1.6 - 1.2$	Hyperons threshold
	1.2×10^{-5}		0.50	Kaons threshold
Hadron	$0.63 - 1.1 \times 10^{-4}$	10^{13}	0.17	Formation of neutrons and protons
	1.6×10^{-4}		0.14	Pions threshold
	2.8×10^{-4}		0.106	Muons threshold
Lepton	3.5×10^{-4}	10^{12}		s quark threshold and last pions decay
	1	10^{10}		Decoupling of ν_e
	2			Neutron production stops
Photon	3	7.3×10^{9}	5×10^{-4}	Electron threshold
	200	10^{9}		Nucleosynthesis of ${}^2H$ stable
	10^{3}			Nucleosynthesis stops
Matter	2.5×10^{12}			Radiation–Matter equality
	9.0×10^{12}	4000		Recombination
	1.2×10^{13}	3000		Photon decoupling
	1.1×10^{16}	30		Reionization
Λ	2.8×10^{17}	≈ 4		Matter–Dark energy equality
	4.3×10^{17}	2.725		Present

Inflation is, perhaps, the simplest known mechanism to eliminate monopoles from the visible Universe, even though they are still in the spectrum of possible particles. The monopoles are eliminated simply by arranging the parameters so that inflation takes place after (or during) monopole production, so the monopole density is diluted to a completely negligible level (e.g. Guth, 2000).

The inflationary era is followed by the radiation–dominated and matter–dominated stages where the acceleration of the scale factor becomes negative. With a negative acceleration of the scale factor, the Hubble radius grows faster than the scale factor, and wavelengths that were outside, can now re–enter the Hubble radius. This is the main concept behind the inflationary paradigm for the generation of temperature fluctuations as well as for providing the seeds for *Large Scale Structure* (LSS) formation (e.g. Boyanovsky et al., 2006).

The basic ingredient for structure formation is the presence of initial density fluctuations, that can, in a later time, act as seeds for the gravitational collapse. Once a small overdensity appears, gravity causes it to grow and finally collapse into a bounded system. As a result we have an inhomogeneous Universe on small scales (e.g. Covi, 2003).

The density fluctuations cannot grow while the pressure of the plasma counteracts the gravitational force and, therefore, during the radiation era the system is still in the linear regime and only oscillations in the plasma (the so called *acoustic peaks*) take place. Later, when matter dominates, the pressure drops to zero and the fluctuations can grow: structures start to form and, consequently, the complicated non–linear regime begins (e.g. Covi, 2003).

Inflation gives a possible solution to the crucial problem of where the primordial fluctuations leading to the observed LSS come from. In fact, they have their origin in the ubiquitous vacuum fluctuations. The seed of the LSS has been observed in the form of tiny fluctuations imprinted on the CMB at the time of decoupling (e.g. Bringmann et al., 2002).

There are various inflationary scenarios (e.g. slow roll inflation, old inflation, new inflation, chaotic inflation, hybrid inflation, viscous inflation, tepid inflation, natural inflation, supernatural inflation, extranatural inflation, eternal inflation, extended inflation) differing essentially only in the choice of the potential $V(\phi)$ where ϕ represents the *inflaton*, i.e., the scalar field responsible for inflation (e.g. Boyanovsky et al., 2006). Each inflationary model makes precise predictions about the spectrum of its primordial fluctuations and this is how these models can be constrained by observations (e.g. Bringmann et al., 2002).

These different kinds of models can be roughly divided into three types (e.g. Tsujikawa, 2003): Type I: *large field* model, in which the initial value of the inflaton is large and rolls down to the potential minimum at smaller ϕ. Chaotic inflation is one of the representative models of this class (see Figure 3); Type II: *small field* model, in which the inflaton field is small initially and slowly evolves toward the potential minimum at larger ϕ. New inflation and natural inflation are the examples of this type (see Figure 4); Type III: *hybrid (double) inflation* model, in which inflation typically ends by the phase transition triggered by the presence of a second scalar field or by the second phase of inflation after the phase transition (see Figure 5).

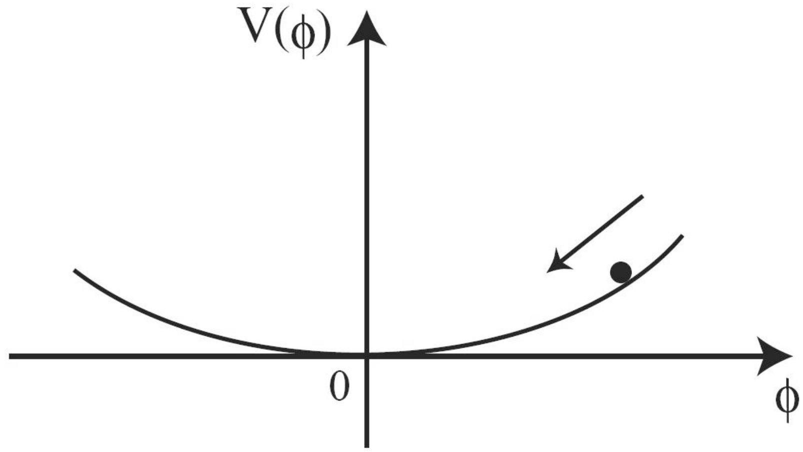

Figure 3: The schematic illustration of the potential of the chaotic inflation model. This belongs to the class of the *large field* model (Tsujikawa, 2003; Guth, 2000).

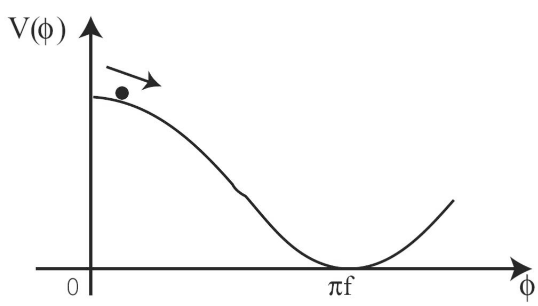

Figure 4: The schematic illustration of the potential of the natural inflation model which belongs to the class of the *small field* model. Here f represents the width of the inflaton potential (tipically $f \sim m_P \sim 10^{19}$ GeV). When $\phi = \pi f$ the potential vanishes (Tsujikawa, 2003).

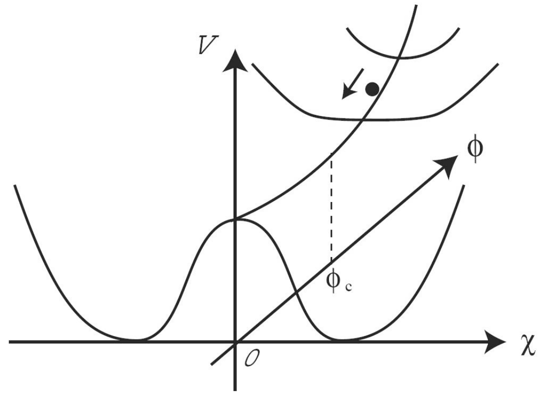

Figure 5: The schematic illustration of the potential of the hybrid (double) inflation model. This model is characterized by multiple scalar fields. In this example we have two scalar fields: ϕ and χ. For large ϕ we have a situation similar to the other models with a single field. However, when ϕ reaches the critical value ϕ_c a different behaviour takes place. In particular, the energy density during inflation can be much lower than normal while still giving suitably large density perturbations, and secondly the field ϕ can be rolling extremely slowly which is of benefit to particle physics model building (Liddle, 1999; Tsujikawa, 2003).

The inflaton ϕ is an homogeneous scalar field, whose potential energy $V(\phi)$ leads to the exponential expansion of the Universe. The number of e–folds that elapsed during inflation (equation 40) can be written also as a function of ϕ (e.g. Boyanovsky et al., 2006)

$$N(\phi(t)) = -\frac{1}{m_{pl}^2}\int_{\phi(t)}^{\phi_e}\frac{V(\phi)}{V'(\phi)}d\phi. \tag{41}$$

The energy density and the pressure density of the inflaton can be described, respectively, as (e.g. Liddle & Lyth, 1993)

$$\rho = \frac{1}{2}\dot{\phi}^2 + V(\phi) \tag{42}$$

$$p = \frac{1}{2}\dot{\phi}^2 - V(\phi). \tag{43}$$

Substituting equations (42) and (43) for equations (2) and (4) we get (e.g. Liddle & Lyth, 1993)[7]

$$H^2 = \frac{8\pi G}{3}\left(\frac{1}{2}\dot{\phi}^2 + V(\phi)\right) = \frac{8\pi}{3m_{pl}^2}\left(\frac{1}{2}\dot{\phi}^2 + V(\phi)\right) \tag{44}$$

[7]We have written equation (44) also in terms of the Planck mass $m_{pl} = (\hbar c/G)^{1/2}$ with $\hbar = c = 1$.

$$\ddot{\phi} + 3H\dot{\phi} + V'(\phi) = 0 \tag{45}$$

where we have considered $\kappa = 0$ and $\Lambda = 0$ in equation (44). Here, the prime denotes the derivative of the potential with respect to the inflaton field.

Amongst the wide variety of inflationary scenarios, slow roll inflation provides a simple and generic description of inflation consistent with the WMAP data (e.g. Boyanovsky et al., 2006). The basic premise of slow roll inflation is that the potential is fairly flat during the inflationary stage. This flatness not only leads to a slowly varying inflaton and Hubble parameter, hence ensuring a sufficient number of e–folds, but also provides an explanation for the gaussianity of the fluctuations as well as for the almost scale invariance of their power spectrum. Departures from scale invariance and gaussianity are determined by the departures from flatness of the potential, namely by derivatives of the potential with respect to the inflaton field (e.g. Boyanovsky et al., 2006). The slow roll approximation corresponds to (e.g. Carr, 2005)

$$\xi \ll 1, \quad |\eta| \ll 1 \tag{46}$$

where ξ and η are the so called *slow–roll parameters* which are determined by the derivatives of the inflaton potential in the following manner (e.g. Carr, 2005)

$$\xi = \frac{m_{pl}^2}{16\pi}\left(\frac{V'}{V}\right)^2 \tag{47}$$

$$\eta = \frac{m_{pl}^2}{8\pi}\frac{V''}{V}. \tag{48}$$

The inflationary era ends when ξ and $|\eta|$ grow to order unity (e.g. Tsujikawa, 2003). At that time the scalar field starts to roll faster and finally to oscillate around the minimum and finally it decays producing radiation and reheating the Universe (e.g. Covi, 2003). If the conditions (46) are valid then equations (44) and (45) are approximately given by (e.g. Boyanovsky et al., 2006)

$$H^2 = \frac{8\pi}{3m_{pl}^2}V(\phi) \tag{49}$$

$$3H\dot{\phi} + V'(\phi) = 0. \tag{50}$$

Inflation is now an established part of Cosmology with several important aspects, such as the superhorizon origin of density perturbations, having been spectacularly validated by WMAP (e.g. Boyanovsky et al., 2006). The gaussian and nearly scale invariant spectrum of primordial fluctuations generically predict by most inflationary models fits with high precision the data provided by WMAP (e.g. Spergel et al., 2007).

1.4 Cosmological phase transitions

The inflationary stage is followed by a radiation–dominated era after a short period of reheating during which the energy stored in the inflaton field decays into quanta of many other fields, which, through scattering processes, reach a state of local thermodynamic equilibrium. This period is followed by deccelerated expansion and cooling, with the Universe successively visiting the different energy scales at which particle and nuclear physics predict symmetry breaking phase transitions. Those phase transitions are broadly characterized as either second or first–order (e.g. Boyanovsky et al., 2006).

If a thermodynamic quantity changes discontinuously (for example as a function of temperature) we have a *first–order phase transition*. This happens because, at the point at which the transition occurs, there are two separate thermodynamic states in equilibrium. Any thermodynamic quantity that undergoes such a discontinuous change at the phase transition is referred to as an *order parameter*. Whether or not a first–order phase transition occurs often depends on other parameters that enter the theory. It is possible that, while another parameter is varied, the change in the order parameter of the phase transition decreases until they, together with all other thermodynamic quantities, become continuous at the transition point. In this case we refer to a *second order phase transition* at the point at which the transition becomes continuous (i.e., it shows a thermodynamic behaviour without discontinuities or singularities in the free energy or any of its derivatives), and a continuous *crossover* at the other points for which all physical quantities undergo no changes (e.g. Trodden, 1999). However, if the crossover is relatively sharp the situation may not be too different from a phase transition (e.g. Boyanovsky et al., 2006).

Phase transitions are the most important phenomena in particle cosmology since, without them, the history of the Universe would simply be one of gradual cooling. In the absence of phase transitions, the only departure from thermal equilibrium is provided by the expansion of the Universe (e.g. Trodden, 1999).

The SMPP (Section 1.8) predicts two phase transitions. The first one, at temperatures of ~ 100 GeV, is the *Electroweak phase transition* (Section 3) which was responsible for the spontaneous breaking of the EW symmetry, which gives the masses to the elementary particles. This transition is also related to the EW baryon–number violating processes, which had a major influence on the observed baryon–asymmetry of the Universe (e.g. Aoki et al., 2006b).

The second transition occurs at $T \approx 170$ MeV. It is related to the spontaneous breaking of the chiral symmetry of the *Quantum Chromodynamics* (QCD) when quarks and gluons become confined in hadrons (Section 2). At high temperatures asymptotic freedom of QCD predicts the existence of a deconfined phase (according to lattice QCD simulations), the *Quark–Gluon Plasma* (QGP). At low temperatures quarks and gluons are confined in a *Hadron Gas* (HG) (e.g. Schmid et al., 1999).

The QCD phase transition was pointed out, for a long time, as a prime candidate for a first–order phase transition (e.g. Jedamzik & Niemeyer, 1999). Recent results (e.g. Aoki et al., 2006b) provide strong evidence that the QCD transition is a simple Crossover instead. Here we will consider the two possibilities (see Section 2).

1.5 The Lambda–Cold Dark Matter Model

In the last few years there has been a wealth of observational evidence from CMB, LSS and high redshift supernovae Ia data that leads to the remarkable conclusions that: i) the spatial geometry of the Universe is flat ($\kappa = 0$), ii) the Universe is accelerating today, and iii) most of the matter is in the form of dark matter. The current understanding of cosmology is based on the so called *Lambda–Cold Dark Matter Model* (ΛCDM) in which the total energy density of the Universe has as main ingredients: 5% of baryonic matter, 25% of dark matter and 70% of dark energy (e.g. Boyanovsky et al., 2006).

Baryonic matter

Ordinary matter is mainly composed of protons and neutrons (which are baryons) and electrons (which are leptons). Since the baryons vastly outweigth the electrons, in the context of Cosmology, ordinary matter is called *baryonic matter* (e.g. Lyth, 1993). The luminous matter in the Universe accounts for only $\Omega_b \approx 0.042$ (Spergel et al., 2007) which means that there exists a great amount of *baryonic dark matter* in the Universe. This discrepancy is refered as the *missing matter problem* (e.g. d'Inverno, 1993).

Within a galaxy, baryons are expected to concentrate more in the central luminous part than in the dark halo. The reason is that baryons (electrons included) can emit radiation whereas non–baryonic dark matter interacts too weakly to do so (or it would not be dark). Baryons lose more energy, allowing them to settle more deeply into the galaxy centre. Baryons within galaxies could be in the form of non–emitting gas, failed stars or planets, ($\sim 0.01 - 0.1 M_{\odot}$), and dead stars (old white dwarfs, non–emitting neutron stars and black holes). In the intergalactic space, baryons can only be in the form of non–emitting gas because, as far as we know, bound objects form only within galaxies (e.g. Lyth, 1993) or within galaxy clusters.

Non–Baryonic Dark Matter

If $\Omega_m \approx 0.24$ as measured by WMAP (Spergel et al., 2007) then, besides baryonic matter (luminous and dark), there might exist a huge amount of *non–baryonic dark matter* (e.g. Lyth, 1993).

We can estimate the total amount of matter in a bound system, such as a galaxy or galaxy cluster, through its gravitational field, which can be deduced from the velocities of its components. One finds that each galaxy is surrounded by a dark halo accounting for most of its mass (e.g. Lyth, 1993).

Soon after the need for dark matter came to be widely accepted in the early 1980s, it became clear that the hypothesis fails completely if the dark matter consists of massive neutrinos, because their thermal motion wipes out small scale structure. Given the failure of this *Hot Dark Matter* (HDM) model, attention turned to the other extreme, of matter which has, by definition, negligible random motion. In its standard form, the *Cold Dark Matter* (CDM) model assumes that the Universe has a flat spatial geometry, a critical matter density (see equation 32) and a spectrum which is precisely scale invariant (e.g. Liddle & Lyth, 1993).

As implied by its name, the CDM is assumed to be cold, which, for most purposes, means non–relativistic. By definition, dark matter does not interact significantly with more conventional forms of matter by any means other than gravity, and, in particular, is beneficial for structure formation in that it is not subject to pressure forces from interaction with radiation which prevent baryonic density inhomogeneities on scales smaller than superclusters from collapsing before radiation decouples from matter. Structure can, thus, start to form earlier within dark matter, providing initial gravitational wells to kick–start structure formation within baryonic matter after decoupling (e.g. Liddle & Lyth, 1993).

The current best candidate for CDM are the so–called *weakly interacting massive particles* (WIMPs) that might have been produced in the very early Universe (e.g. Bertone et al., 2005).

Dark energy

Independent measurements of Type Ia supernovae have revealed that the expansion of the Universe is undergoing a non–linear acceleration rather than following strictly Hubble's law. To explain this acceleration, general relativity requires that much of the Universe consist of an energy component with large negative pressure. Its true nature remains unknown, although the present observations indicate that this *dark energy* can be described by a cosmological constant Λ (e.g. Boyanovsky et al., 2006).

The model assumes a nearly scale–invariant spectrum of primordial perturbations and a Universe without spatial curvature ($k = 0 \Rightarrow \Omega_\kappa = 0$). It also assumes that it has no observable topology, so that the Universe is much larger than the observable particle horizon. Those are predictions of cosmic inflation (Section 1.3).

The ΛCDM model has six parameters: the Hubble constant H_0, the baryon density Ω_b, the total matter density Ω_m (which includes baryons plus dark matter), the optical depth to reionization τ (which determines the redshift of reionization), the amplitude of the primordial fluctuations A_s and the slope for the scalar perturbation spectrum n_s (which measures how fluctuations change with scale; $n_s = 1$ corresponds to a scale–invariant spectrum). The values of these six free parameters as obtained from the WMAP data (Spergel et al., 2007) are presented in Table 2. The Hubble constant h is given in normalized units of 100 $\mathrm{kms^{-1}Mpc^{-1}}$ and the densities Ω_m and Ω_b are given as functions of h. Thus, the present value of the Hubble parameter H_0 is, according to the most recent WMAP observations

$$H_0 = 73.4\,\mathrm{kms^{-1}\,Mpc^{-1}} \approx 2.38 \times 10^{-18}\ \mathrm{s^{-1}} \tag{51}$$

and

$$\Omega_m \approx 0.24 \tag{52}$$

Table 2: The best fit values for the ΛCDM model free parameters according to the WMAP data (Spergel et al., 2007).

Parameter	Value	Description
h	$0.734^{+0.028}_{-0.038}$	Normalized Hubble constant
$100\Omega_b h^2$	$2.233^{+0.072}_{-0.091}$	Baryon density
$\Omega_m h^2$	$0.1268^{+0.0072}_{-0.0095}$	Total matter density
τ	$0.088^{+0.043}_{-0.054}$	Optical depth to reionization
A_s	$0.801^{+0.043}_{-0.054}$	Scalar fluctuation amplitude at $k = 0.002$ Mpc^{-1}
n_s	$0.951^{+0.015}_{-0.019}$	Scalar spectral index at $k = 0.002$ Mpc^{-1}

$$\Omega_b \approx 0.042. \tag{53}$$

Notice that the dark energy density Ω_Λ (cf. equation 35) is not a free parameter because, since the ΛCDM model assumes a flat Universe ($\Omega = 1$), we have, according to equation (36)

$$\Omega_\Lambda = 1 - \Omega_m \approx 0.76. \tag{54}$$

Other derived parameters are the age of the Universe t_0 (Section 1.6) and the critical density ρ_0 (cf. equation 32). Inserting the value of H_0 into equation (32) one obtains

$$\rho_c = \rho_0 \approx 1.013 \times 10^{-26} \text{ kgm}^{-3}. \tag{55}$$

The cosmological constant, which is also a derived parameter, is given by (see equations 32 and 35)

$$\Lambda = \frac{8\pi G}{c^2}\rho_\Lambda = \frac{8\pi G}{c^2}\Omega_\Lambda \rho_c = \frac{3H_0^2\Omega_\Lambda}{c^2}. \tag{56}$$

Inserting the obtained values for H_0 (equation 51) and Ω_Λ (equation 54) into equation (56) one obtains[8]

$$\Lambda \approx 1.44 \times 10^{-52} \text{ m}^{-2}. \tag{57}$$

[8]When one calculates the theoretical value of Λ one ends up with a value about 120 orders of magnitude larger than the experimentally measured one. This has been called the worst mismatch between theory and experiment in the whole of science (e.g. Weinberg, 2000).

The expansion of the Universe is sometimes described by means of a *deceleration parameter* q which is defined as (e.g. d'Inverno, 1993)

$$q(t) = -\frac{R\ddot{R}}{\dot{R}^2} = -\frac{\ddot{R}}{RH^2} \tag{58}$$

where $q > 0$ means that the expansion is slowing down and $q < 0$ means that the expansion is accelerating. Making use of equation (3) this becomes

$$q = \frac{4\pi G\rho}{3H^2}(1 + 3w) - \frac{\Lambda}{3H^2} \tag{59}$$

which shows that there is an intimate connection between the deceleration parameter q, the Hubble parameter H, the mean density of the Universe ρ and the Cosmological constant Λ. Taking into account equations (32), (33) and (35) we may write equation (59) in the form

$$q = \frac{1 + 3w}{2}\Omega_m - \Omega_\Lambda. \tag{60}$$

Notice that there would be an effective deceleration of the expansion of the Universe ($q > 0$) only if $\Omega_m > \Omega_\Lambda$. However it is usual to retain the historical deceleration parameter designation even when $q < 0$ which happens to be the case. In fact, considering $w = -1$, $\Omega_\Lambda = 0.76$, and $\Omega_m = 0.24$ we have, from equation (60), $q_0 = -1$.

1.6 The scale factor

The metric (1) leaves room for choice of a normalization. One common choice is to make the scale factor equal to unity at the present time (e.g. Liddle & Lyth, 1993)

$$R_0 = R(t_0) = 1. \tag{61}$$

This is convenient because, at any time, the scale factor will be related to the redshift z simply by (cf. equation 25)

$$R(t) = \frac{1}{1 + z(t)}. \tag{62}$$

We can now determine the Hubble parameter (equation 26) for the different epochs of the Universe. During the radiation–dominated epochs we have, according to expression (17), that

$$H(t) = \frac{1}{2t} \tag{63}$$

and during the dust–like phases or mater–dominated epochs we have, according to expression (18), that

$$H(t) = \frac{2}{3t}. \tag{64}$$

When the Universe becomes dominated by dark energy ($\Lambda > 0$) the Hubble parameter becomes constant in time (cf. expression 19)

$$H(t) = c\sqrt{\frac{\Lambda}{3}}. \tag{65}$$

Since inflation only lasts a few e–folds (see Section 1.3), the Hubble parameter can be taken as a constant during this period (e.g. Huang, 2007; Narlikar & Padmanabhan, 1991). From equation (40) we have

$$H(t) = \frac{N(t_e)}{t_e}. \tag{66}$$

Considering the normalisation (61) we can determine the proportionality constant in expression (19), yielding, for the scale factor of a Universe dominated by a positive cosmological constant, the result[9]

$$R(t) = \exp\left(c\sqrt{\tfrac{\Lambda}{3}}(t - t_0)\right), \quad t_{SN} \leq t \leq t_0 \tag{67}$$

where t_0 is the present time (i.e. the age of the Universe) and t_{SN} is the age of the universe at matter–Λ equality (corresponding to the instant when the expansion starts to accelerate). The dark energy domination is preceded by a matter–dominated stage which started when photons decoupled from matter. During matter domination the scale factor behaves according to expression (18). Considering that $R(t)$ is a continuous function of time we will write, for the matter–dominated stage

$$R(t) = \exp\left(c\sqrt{\tfrac{\Lambda}{3}}(t_{SN} - t_0)\right)\left(\tfrac{t}{t_{SN}}\right)^{2/3}, \quad t_{eq} \leq t \leq t_{SN} \tag{68}$$

where t_{eq} is the age of the Universe at radiation–matter equality. Before that time, the Universe was radiation–dominated up to the end of inflation at some instant $t = t_e$. During radiation domination the scale factor behaves according to expression (17). During the period ($t_e \leq t \leq t_{eq}$) the Universe experienced two phase transitions during which it might have been, for brief instants, dust–like (Section 2). When one goes backwards in time the first phase transition is the QCD. Considering that t_+ corresponds to the age of the Universe at the end of the QCD we write

$$R(t) = \exp\left(c\sqrt{\tfrac{\Lambda}{3}}(t_{SN} - t_0)\right)\left(\tfrac{t_{eq}}{t_{SN}}\right)^{2/3}\left(\tfrac{t}{t_{eq}}\right)^{1/2}, \quad t_+ \leq t \leq t_{eq} \tag{69}$$

[9] To our best knowledge, this sequence of formulae (equations 67–77) has never been deducted in the literature, although common-knowledge.

We consider that during the QCD epoch ($t_- \leq t \leq t_+$) the scale factor is given by

$$R(t) = \exp\left(c\sqrt{\frac{\Lambda}{3}}(t_{SN} - t_0)\right)\left(\frac{t_{eq}}{t_{SN}}\right)^{2/3}\left(\frac{t_+}{t_{eq}}\right)^{1/2} \times \\ \times \left(\frac{t}{t_+}\right)^{n_{qcd}}, t_- \leq t \leq t_+ \tag{70}$$

where $n_{qcd} = 2/3$ if the Universe experiences a dust–like phase during the QCD and $n_{qcd} = 1/2$ if the Universe continues to be radiation–dominated during that epoch. Between the end of the EW transition ($t = t_{EW+}$) and the beginning of the QCD phase transition ($t = t_-$) the Universe is radiation–dominated. Thus, we write

$$R(t) = \exp\left(c\sqrt{\frac{\Lambda}{3}}(t_{SN} - t_0)\right)\left(\frac{t_{eq}}{t_{SN}}\right)^{2/3}\left(\frac{t_+}{t_{eq}}\right)^{1/2}\left(\frac{t_-}{t_+}\right)^{n_{qcd}} \times \\ \times \left(\frac{t}{t_-}\right)^{1/2}, t_{EW+} \leq t \leq t_- \tag{71}$$

During the EW transition ($t_{EW-} \leq t \leq t_{EW+}$) we consider that the scale factor is given by

$$R(t) = \exp\left(c\sqrt{\frac{\Lambda}{3}}(t_{SN} - t_0)\right)\left(\frac{t_{eq}}{t_{SN}}\right)^{2/3}\left(\frac{t_+}{t_{eq}}\right)^{1/2}\left(\frac{t_-}{t_+}\right)^{n_{qcd}} \times \\ \times \left(\frac{t_{EW+}}{t_-}\right)^{1/2}\left(\frac{t}{t_{EW+}}\right)^{n_{ew}}, t_{EW-} \leq t \leq t_{EW+} \tag{72}$$

where $n_{ew} = 2/3$ if the Universe experiences a dust–like phase during that epoch and $n_{ew} = 1/2$ if the Universe continues to be radiation–dominated. Between the end of inflation ($t = t_e$) and the beginning of the EW phase transition ($t = t_{EW-}$) the Universe is radiation–dominated. We write

$$R(t) = \exp\left(c\sqrt{\frac{\Lambda}{3}}(t_{SN} - t_0)\right)\left(\frac{t_{eq}}{t_{SN}}\right)^{2/3}\left(\frac{t_+}{t_{eq}}\right)^{1/2}\left(\frac{t_-}{t_+}\right)^{n_{qcd}} \times \\ \times \left(\frac{t_{EW+}}{t_-}\right)^{1/2}\left(\frac{t_{EW-}}{t_{EW+}}\right)^{n_{ew}}\left(\frac{t}{t_{EW-}}\right)^{1/2}, t_e \leq t \leq t_{EW-} \tag{73}$$

During inflation the scale factor behaves according to expression (38). Thus, at the end of the inflationary period the scale factor can be written as

$$R(t_e) = R(t_i)\exp\left(H_i(t_e - t_i)\right). \tag{74}$$

On the other hand we have, from equation (73)

$$R(t_e) = \exp\left(c\sqrt{\frac{\Lambda}{3}}(t_{SN}-t_0)\right)\left(\frac{t_{eq}}{t_{SN}}\right)^{2/3}\left(\frac{t_+}{t_{eq}}\right)^{1/2}\left(\frac{t_-}{t_+}\right)^{n_{qcd}}\times$$
$$\times\left(\frac{t_{EW+}}{t_-}\right)^{1/2}\left(\frac{t_{EW-}}{t_{EW+}}\right)^{n_{ew}}\left(\frac{t_e}{t_{EW-}}\right)^{1/2}. \tag{75}$$

Combining equations (74) and (75) one finds an expression for $R(t_i)$. Inserting this expression into equation (38) one obtains, for the scale factor during inflation, the result

$$R(t) = \exp\left(c\sqrt{\frac{\Lambda}{3}}(t_{SN}-t_0)\right)\left(\frac{t_{eq}}{t_{SN}}\right)^{2/3}\left(\frac{t_+}{t_{eq}}\right)^{1/2}\left(\frac{t_-}{t_+}\right)^{n_{qcd}}\times$$
$$\times\left(\frac{t_{EW+}}{t_-}\right)^{1/2}\left(\frac{t_{EW-}}{t_{EW+}}\right)^{n_{ew}}\left(\frac{t_e}{t_{EW-}}\right)^{1/2}\times \tag{76}$$
$$\times\frac{\exp\left(H_i\left(t-t_i\right)\right)}{\exp\left(H_i\left(t_e-t_i\right)\right)}, t_i \le t \le t_e$$

where H_i corresponds to the value of the Huble parameter during inflation that we assume constant (cf. equation 66). Finally, considering that before inflation the Universe is radiation–dominated, we write

$$R(t) = \exp\left(c\sqrt{\frac{\Lambda}{3}}(t_{SN}-t_0)\right)\left(\frac{t_{eq}}{t_{SN}}\right)^{2/3}\left(\frac{t_+}{t_{eq}}\right)^{1/2}\left(\frac{t_-}{t_+}\right)^{n_{qcd}}\times$$
$$\times\left(\frac{t_{EW+}}{t_-}\right)^{1/2}\left(\frac{t_{EW-}}{t_{EW+}}\right)^{n_{ew}}\left(\frac{t_e}{t_{EW-}}\right)^{1/2}\times \tag{77}$$
$$\times\exp\left(-H_i\left(t_e-t_i\right)\right)\left(\frac{t}{t_i}\right)^{1/2}, t_p \le t \le t_i$$

where t_p represents the Planck time.

The scale factor R, the background temperature T and the redshift z at a given epoch are related according to the expression (e.g. Unsöld & Bascheck, 2002)

$$\frac{T(t)}{T_0} = \frac{R_0}{R(t)} = 1+z \tag{78}$$

where T_0 represents the present day background temperature ($T_0 \approx 2.725$).

The value of t_0, i.e., the age of the Universe, can be obtained with the help of expression (e.g. Yao et al., 2006)

$$H_0 t_0 = \int_0^\infty \frac{dz}{(1+z)H(z)}. \tag{79}$$

In the case of a flat Universe ($\Omega_m + \Omega_\Lambda = 1$) expression (79) can be written as (e.g. Yao et al., 2006)

$$H_0 t_0 = \frac{2}{3\sqrt{\Omega_\Lambda}} \ln \frac{1+\sqrt{\Omega_\Lambda}}{\sqrt{1-\Omega_\Lambda}}, \quad \Omega_m < 1. \tag{80}$$

Inserting H_0 (see equation 51) into equation (80) with $\Omega_\Lambda = 0.76$ we obtain, for the age of the Universe

$$t_0 \approx 4.3 \times 10^{17} \text{ s}. \tag{81}$$

Considering that during the cosmological constant domination the Hubble parameter stays constant (cf. equation 65) we have that $H(t_{SN}) = H_0$. Thus, inserting H_0 into equation (64) we obtain

$$t_{SN} \approx 2.8 \times 10^{17} \text{ s}. \tag{82}$$

Notice that if $\Lambda = 0$ this would correspond to t_0. This means that, in the absence of dark energy, the Universe would be younger by a factor of ≈ 1.5 (e.g. Jones & Lambourne, 2004).

The value of t_{eq} can be obtained with the help of equations (62) and (68) considering that $z \approx 3200$ at radiation–matter equality (e.g. Hinshaw et al., 2008)

$$t_{eq} \approx 2.5 \times 10^{12} \text{ s}. \tag{83}$$

Proceding the same way, one obtains, for the age of the universe at photon decoupling ($z \approx 1090$)

$$t_{dec} \approx 1.2 \times 10^{13} \text{ s}. \tag{84}$$

Taking $t_i = 10^{-35}$ s we have, from equations (63) and (66), that

$$t_e \sim 10^{-33} \text{ s} \tag{85}$$

valid for both $N(t_e) = 50$ and $N(t_e) = 70$.

The calculus of numerical values to t_-, t_+, t_{EW-} and t_{EW+} will be discused in Sections 2.4 and 3.2. For the moment, we present on Table 3 all these instants of time as well as the corresponding values for the scale factor. Notice that some of these values may be slightly different, depending on the values one chooses for n_{qcd}, n_{ew} and t_-.

In Figure 6 we show $R(t)$ during the QCD transition. Notice that the reduction on the scale factor during a dust–like QCD transition is not very significative. In fact the term t_-/t_+ is ~ 1 and, thus, it can be neglected in equations

(71) to (77). Notice, however, that this will not be the case if one is working locally (i.e., near t_- and t_+). In Section 2.4, for example, we want to determine numerical values for t_- and t_+. In that case, it does not make sence to consider $t_-/t_+ = 1$. The same idea is valid for the term t_{EW-}/t_{EW+}. According to this, we can replace equations (69) to (73) by the single equation

$$R(t) = \exp\left(c\sqrt{\tfrac{\Lambda}{3}}(t_{SN} - t_0)\right)\left(\tfrac{t_{eq}}{t_{SN}}\right)^{2/3}\left(\tfrac{t}{t_{eq}}\right)^{1/2}, \quad t_e \le t \le t_{eq} \tag{86}$$

Equations (67) and (68) remain unchanged. Equation (76) becomes

$$R(t) = \exp\left(c\sqrt{\frac{\Lambda}{3}}(t_{SN} - t_0)\right)\left(\frac{t_{eq}}{t_{SN}}\right)^{2/3}\left(\frac{t_e}{t_{eq}}\right)^{1/2} \frac{\exp\left(H_i\left(t - t_i\right)\right)}{\exp\left(H_i\left(t_e - t_i\right)\right)}, t_i \le t \le t_e \tag{87}$$

and equation (77) becomes

$$R(t) = \exp\left(c\sqrt{\tfrac{\Lambda}{3}}(t_{SN} - t_0)\right)\left(\tfrac{t_{eq}}{t_{SN}}\right)^{2/3}\left(\tfrac{t_e}{t_{eq}}\right)^{1/2} \exp\left(-H_i\left(t_e - t_i\right)\right)\left(\tfrac{t}{t_i}\right)^{1/2}, t_p \le t \le t_i \tag{88}$$

In Figure 7 we show $R(t)$ for the entire Universe timeline (i.e., from the Planck time t_p up to the present time t_0).

1.7 The Cosmic Microwave Background temperature

The existence of the Cosmic Microwave Background (CMB) radiation was first predicted by Gamow et al. (1948) but it was only in 1964 that it was observed (serendipitously) by the first time (Penzias & Wilson, 1965).

In 1989, NASA launched the *Cosmic Background Explorer* satellite (COBE), and the initial findings, released in 1990, were consistent with the Big Bang's predictions regarding the CMB. COBE found a residual temperature of 2.726 K and determined that the CMB was isotropic to about one part in 10^5 (Boggess et al., 1992). During the 1990s, CMB anisotropies were further investigated by a large number of ground–based experiments and the Universe was shown to be almost geometrically flat, by measuring the typical angular size of the anisotropies.

The CMB brings us information about the state of the Universe at the photon decoupling epoch ($z \approx 1090$) when the photons that reach us now had their last scattering (Section 1.2). The spectrum of the CMB at the present epoch is well described by a blackbody function with (e.g. Boyanovsky et al., 2006)

$$T_0 = 2.725 \pm 0.001\mathrm{K} \tag{89}$$

Table 3: The Scale Factor (equations 67–77) for different instants of time during the evolution of the Universe: t_p (Planck time), t_i (beginning of inflation), t_e (end of inflation), t_{EW-} (beginning of the EW transition – Section 3.2), t_{EW+} (end of the EW transition – Section 3.2), t_- (beginning of the QCD transition – Section 2.4), t_+ (end of the QCD transition – Section 2.4), t_{eq} (last scattering surface), t_{SN} (the instant when the Universe starts to accelerate) and t_0 (present time). Notice that we have indicated two values for t_-. The first one corresponds to the Bag Model results and the second one to the Lattice Fit results (cf. Section 2.4).

	t(s)	$R(t)$	
t_p	$\sim 10^{-43}$	$\sim 10^{-60}$	
t_i	$\sim 10^{-35}$	$\sim 10^{-56}$	
t_e	$\sim 10^{-33}$	$\sim 10^{-27}$	
t_{EW-}	2.30×10^{-10}	2.9×10^{-15}	
t_{EW+}	3.15×10^{-10}	3.5×10^{-15}	
t_-	6.25×10^{-5}	1.4×10^{-12}	(QCD Bag)
t_-	9.35×10^{-5}	1.9×10^{-12}	(QCD Lattice)
t_+	1.08×10^{-4}	2.1×10^{-12}	
t_{eq}	2.5×10^{12}	3.2×10^{-4}	
t_{SN}	2.8×10^{17}	0.73	
t_0	4.3×10^{17}	1	

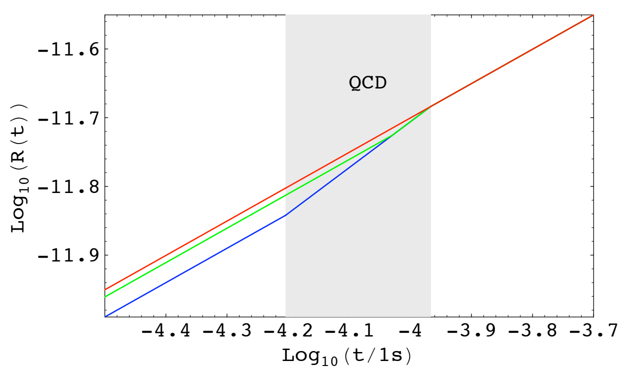

Figure 6: The scale factor during the QCD transition as a function of time. The gray region corresponds to the dust–like epoch, according to the Bag Model (Sections 2.3.1 and 2.4). The curves correspond, from top to bottom, to the: crossover case ($n_{qcd} = 1/2$), Lattice Fit ($n_{qcd} = 2/3$ and $t_- = 9.35 \times 10^{-5}$ s) and Bag Model ($n_{qcd} = 2/3$ and $t_- = 6.25 \times 10^{-5}$ s).

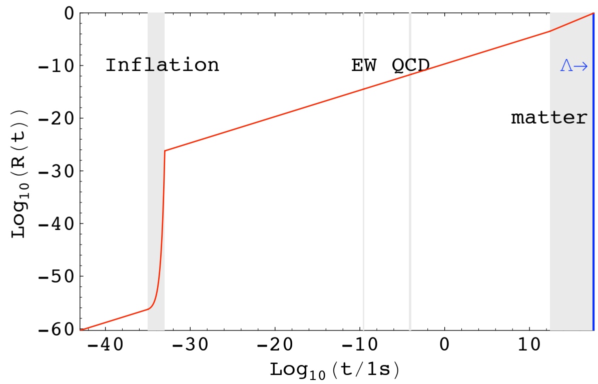

Figure 7: The scale factor as a function of time. The gray regions corresppond to the inflationary period, the EW and QCD transitions and the matter–dominated era. In blue (right side) we have the dark energy dominated era. The other regions (in white) correspond to radiation–dominated periods.

Another observable quantity inherent in the CMB is the variation in temperature (or intensity) from one part of the microwave sky to another. Since the first detection of these anisotropies by the COBE satellite in 1992, there has been intense activity to map the sky at increasing levels of sensitivity and angular resolution. Observations have shown us that the CMB contains anisotropies at the 10^{-5} level (e.g. Yao et al., 2006)

$$\frac{\Delta T}{T} \sim 10^{-5} \tag{90}$$

over a wide range of angular scales. Density fluctuations over the plasma in thermal equilibrium gave rise to temperature fluctuations (denser regions were hotter). Hence, the temperature anisotropies in the CMB bring us direct evidence of the density contrast at recombination. This small temperature anisotropy, whose existence is predicted by cosmological models, provides the clue to the origin of structure and is an important confirmation of theories of the early Universe (e.g. Boyanovsky et al., 2006).

These anisotropies are usually expressed by using a spherical harmonic expansion of the CMB sky (e.g. Yao et al., 2006)

$$T(\theta,\phi) = \sum_{l,m} a_{lm} Y_{lm}(\theta,\phi) \tag{91}$$

where $Y_{lm}(\theta,\phi)$ is the so–called spherical harmonic function of degree l and order m[10].

[10] $Y_{lm}(\theta,\phi)$ represents the angular part of the solution of Laplace's equation ($\nabla^2 f(r,\theta,\phi) = 0$). The degree l and order m are integers such that $l \geq 0$ and $|m| \leq l$. The coefficients a_{lm} are constants. The expansion is exact as long as l goes to infinity.

Theoretical models generally predict that the a_{lm} modes are Gaussian random fields. Tests show that this is an extremely good simplifying approximation, with only some relatively weak indications of non–Gaussianity or statistical anisotropy at large scales. With the assumption of Gaussian statistics, and if there is no preferred axis, then it is the variance of the temperature field which carries the cosmological information, rather than the values of the individual a_{lm} coefficients. In other words, the power spectrum in l fully characterizes the anisotropies (e.g. Yao et al., 2006).

On small sections of the sky where its curvature can be neglected, the spherical harmonic analysis becomes ordinary Fourier analysis in two dimensions and l becomes the Fourier wavenumber. Since the angular wavelength $\theta = 2\pi/l$, larger multipole moments correspond to smaller angular scales, with $l \sim 10^2$ representing degree scale separations. In this limit the power spectrum is usually displayed as (e.g. Hu & Dodelson, 2002)

$$\left(\frac{\Delta T}{T}\right)^2 = \frac{l(l+1)}{2\pi} C_l \tag{92}$$

where (e.g. Yao et al., 2006)

$$C_l \equiv \langle |a_{lm}|^2 \rangle. \tag{93}$$

The CMB mean temperature of 2.725 K (cf. equation 89) can be regarded as the *monopole* component (a_{00}) of CMB maps. Since all mapping experiments involve difference measurements, they are insensitive to this average level. Monopole measurements can only be made with absolute temperature devices, such as the *Far–InfraRed Absolute Spectrophotometer* (FIRAS) instrument on the COBE satellite. Such measurements of the spectrum are consistent with a blackbody distribution over more than three decades in frequency (e.g. Yao et al., 2006).

The largest anisotropy is in the $l = 1$ *dipole* first spherical harmonic, with amplitude 3.346 ± 0.017 mK. The dipole is interpreted to be the result of the Doppler shift caused by the solar system motion relative to the nearly isotropic blackbody field, as confirmed by measurements of the radial velocities of local galaxies (e.g. Yao et al., 2006).

Excess variance in CMB maps at higher *multipoles* ($l \geq 2$) is interpreted as being the result of perturbations in the density of the early Universe, manifesting themselves at the epoch of the last scattering of the CMB photons. In the hot Big Bang picture, this happens at a redshift $z \simeq 1090$, with little dependence on the details of the model (e.g. Yao et al., 2006).

In Figure 8 we show the theoretical CMB anisotropy power spectrum (according to the standard ΛCDM model). Notice that the physics underlying the C_l's can be separated into four main regions: the *ISW Rise* ($l \gtrsim 2$), the *Sachs–Wolfe plateau* ($l \lesssim 100$), the *acoustic peaks* ($100 \lesssim l \lesssim 1000$) and the *damping tail* ($l \gtrsim 1000$).

The horizon scale at photon decoupling corresponds to $l \approx 100$. Anisotropies at larger scales ($l < 100$) have not evolved significantly, and hence directly reflect

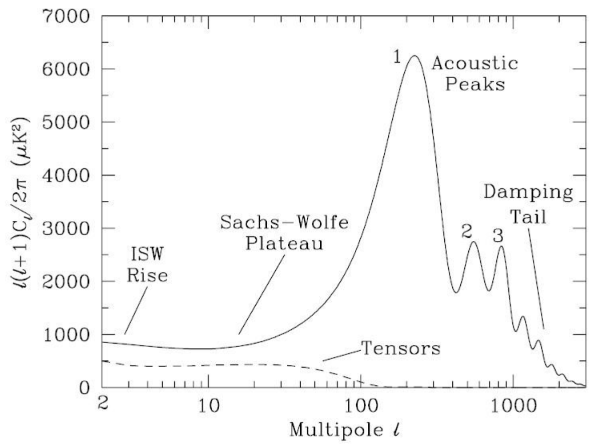

Figure 8: The theoretical CMB anisotropy power spectrum, using a standard ΛCDM model. The horizontal axis is logarithmic. Four regions, each covering roughly a decade in l, are labeled as: the ISW Rise; Sachs–Wolfe Plateau; Acoustic Peaks (numbers indicate the first, the second and, the third acoustic peak); and Damping Tail. Also shown is the shape of the tensor (gravity wave) contribution, with an arbitrary normalization (adapted from Yao et al., 2006).

the initial conditions. The combination of gravitational redshift and intrinsic temperature fluctuations leads to

$$\frac{\delta T}{T} \simeq \frac{1}{3}\frac{\delta\phi}{c^2} \tag{94}$$

where $\delta\phi$ is the perturbation to the gravitational potential. This is usually referred to as the *Sachs–Wolfe effect*. Assuming, in addition, a nearly scale–invariant spectrum of density perturbations, then $l(l+1)C_l$ is almost constant at large scales ($l < 100$) forming the so–called Sachs–Wolfe Plateau. The dominance of dark energy at low redshift, corresponding to $l \gtrsim 2$, leads to a rise above the Sachs–Wolfe Plateau. This is referred to as the *integrated Sachs-Wolfe effect* or ISW Rise (e.g. Yao et al., 2006).

Before the Universe became neutral the proton-electron plasma was tightly coupled to the photons, and these components behaved as a single photon–baryon fluid. Perturbations in the gravitational potential, dominated by the dark matter component, were steadily evolving. After recombination and photon decoupling, the phases of the oscillations were frozen–in, and projected on the sky as a harmonic series of acoustic peaks. The main peak (peak 1 at $l \approx 150$ in Figure 8) is the mode that went through 1/4 of a period, reaching maximal compression. The angular position of the peaks is a sensitive probe of the spatial curvature of the Universe (e.g. Yao et al., 2006). WMAP has provided perhaps the most striking validation of inflation as a mechanism for generating superhorizon fluctuations, through the measurement of the first acoustic peak in the temperature–polarization angular power spectrum at $l \sim 150$ (Spergel et al., 2007).

The recombination process is not instantaneous, giving a thickness to the last scattering surface. This leads to a damping of the anisotropies at the highest multipoles ($l > 1000$), corresponding to scales smaller than that subtended by this thickness. This effect leads to a cut off on the anisotropies for $l \gtrsim 2000$. Also, gravitational lensing, caused by structures at low redshift ($z \ll 1000$), would have the effect of partially flatten the peaks, generating a power-law tail. The WMAP data can reach the multipole $l \simeq 900$, up to the third acoustic peak (see Figure 8). In order to extend to higher multipoles (including the Damping Tail region), the WMAP team included in their analysis the data of other two CMB ground–based experiments: the *Arcminute Cosmology Bolometer Array Receiver* (ACBAR) and the *Cosmic Background Imager* (CBI) (e.g. Covi, 2003).

Information on the density contrast can also be obtained from the distribution of galaxies in our Universe. The main assumption, in this case, is that the visible matter follows the distribution of the invisible Dark Matter. Recent surveys include the *2 degree Field Galaxy Redshift Survey* (2dFGRS) which released data on 221 414 galaxies with measured redshift (e.g. Colless et al., 2003; Cole et al., 2005). An even larger survey is the *Sloan Digital Sky Survey* (SDSS). Its 6^{th} release of data (Adelman–McCarthy et al., 2008) already contains a total of 790 860 galaxies. From the distribution of the galaxies in the sky one can obtain the *two point correlation function* and the density contrast power spectrum (e.g. Covi, 2003).

Other ways to measure the density contrast rely on using photons of distant objects as a probe of the intervening matter or gas densities. *Lyman α forest* data measure the absorption lines in the spectra of distant quasars caused by intergalactic hydrogen and estimate the cosmic gas distribution out to large distances (e.g. Covi, 2003). On Figure 9 we show, as an example, the Lyman α forest of quasar RD $J030117 + 002025$.

1.8 The Standard Model of Particle Physics

The combination of the QCD theory and the EW is known as the *Standard Model of Particle Physics* (SMPP). The SMPP contains a finite number of parameters, which are unrelated, at least within the context of the theory itself. The SMPP is based on only two basic components: the fundamental quantum particles and the concept of interactions between them. A more complete theory of fundamental physics should explain the relationships among these parameters. The ultimate goal would be to determine the values of the parameters from pure mathematics, once the correct theory is discovered (e.g. Scott, 2006).

The current SMPP, experimentally tested with remarkable precision, describes the theory of strong, weak and electromagnetic interactions as a gauge theory[11]. The particle content is (see Figure 10): three families of *quarks*, three

[11] In Physics, gauge theories are a class of physical theories based on the idea that symmetry transformations can be performed locally as well as globally. Many powerful theories in Physics (e.g. EW theory, Electrodynamics, QCD) are described by Lagrangians which are

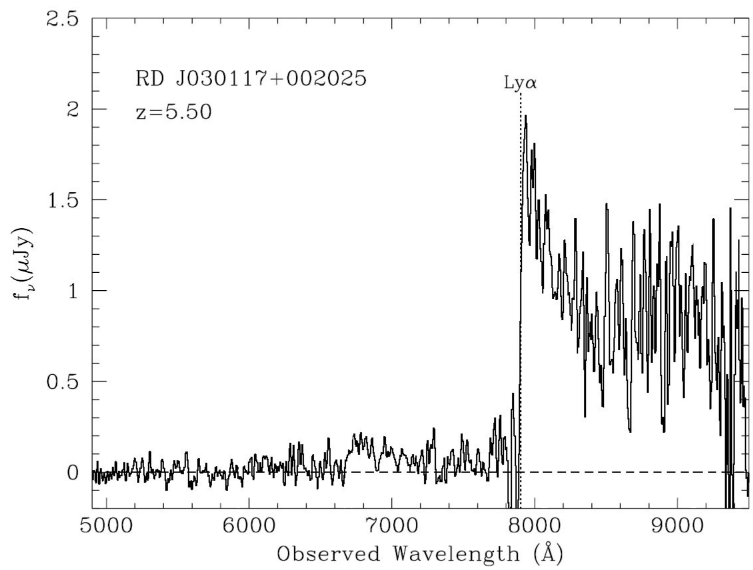

Figure 9: The spectrum of quasar RD $J030117 + 002025$ with redshift $z = 5.50$. The Lyman α emission line has been shifted from the ultraviolet ($1210\AA$) to the infrared ($7860\AA$) and the same happened to the absorption caused by hydrogen clouds between us and the quasar, each at its own redshift (covering $\sim 5000 - 8000\AA$ in this plot): the Lyα forest (adapted from Stern et al., 2000).

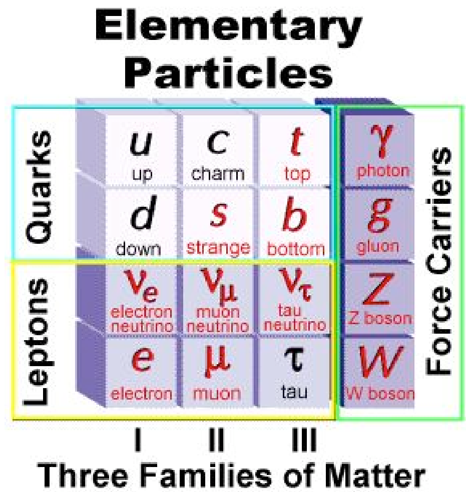

Figure 10: The particle content of the SMPP (http://www-sldnt.slac.stanford.edu) as regards fundamental fermions and bosons. Since there are eight different types of gluons (g), two W bosons and the (still hypothetical) Higgs boson (H) – not shown – there are a total of 25 particles.

families of *leptons*, and 13 gauge bosons (i.e., particles that act as carriers of the fundamental interactions): eight massless *gluons*, Z^0, $W^{\pm}$; the massless *photon*; the (yet to be discovered) scalar *Higgs* (e.g. Boyanovsky et al., 2006). These particles interact in only three ways: the electromagnetic interaction, the weak interaction and the strong interaction. Note that gravity is left outside the SMPP because we do not yet have a theory of quantum gravity.

The classification of fundamental particles is performed taking into account certain properties such as the rest mass, the electric charge and the spin. The spin must be an integer or an half–integer and is normally expressed in units of $\hbar$. Quantum particles with integer spin are called *bosons* and quantum particles with half–integer spin are called *fermions*. Fermions obey the *Exclusion Principle* (identical fermions cannot be at the same state at the same time) but bosons do not obey the Exclusion Principle.

A particle which does not react to the strong interaction is called a *lepton* (see Table 4, Figure 10). In the SMPP six of the 12 fermions are leptons: three electric charged particles (electron – e^-, muon – μ^-, tau – τ^-) and their associated neutrinos (ν_e, ν_μ, ν_τ). The remaining six fermions are quarks – particles which react to the strong interaction (see Table 5, Figure 10). Quarks

invariant under certain symmetry transformation groups. When they are invariant under a transformation identically performed at every space–time point they are said to have a global symmetry. Gauge theory extends this idea by requiring that the Lagrangians must possess local symmetries which enable symmetry transformations in a particular region of space–time without affecting what happens in another region. This requirement is a generalized version of the *Equivalence Principle* of general relativity.

Table 4: The three lepton families of the SMPP. For each particle it is indicated the respective electric charge e, spin s and mass m (according to the Particle Data Group (PDG) results – http://pdg.lbl.gov/2007/listings/contents_listings.html, Yao et al., 2006). For each charged lepton there is an anti–lepton with symmetric charge and the same mass and spin (e.g, the anti–particle of the electron is the positron, e^+, which is a particle with electric charge +1, spin 1/2 and mass 0.511 MeV. At the present it is not known if neutrinos are their own anti–particles (that would depend on the nature of the physics that gives them masses).

Family	Lepton	Symbol	e	s	m(MeV)
1	electron	e^-	-1	1/2	0.511
	electron neutrino	ν_e	0	1/2	$< 2 \times 10^{-6}$
2	muon	μ^-	-1	1/2	105.658
	muon neutrino	ν_μ	0	1/2	< 0.19
3	tau	τ^-	-1	1/2	1776
	tau neutrino	ν_τ	0	1/2	< 18.2

come in six flavours (up – u, down – d, strange – s, charm – c, top – t, bottom – b) and carry, besides a fractional electric charge, a *colour charge*. This colour charge comes in three types: red, green and blue. This means that there are 18 different quarks (6 flavours $\times$ 3 colours).

The pairings (e, μ_e) and (u, d) form a family of fundamental particles (Figure 10). Most of the matter we see around us ultimately consists of this family of four particles. It seems that most matter in the Universe requires representatives from only this family of fundamental particles. Yet, for some reason, this family is reproduced twice over (cf. Figure 10).

Bosons act as carrier particles of the fundamental forces (see Table 6). The photon, γ, is the carrier of the electromagnetic interaction. It acts on any particle that possesses electric charge. There are two carrier particles of the weak interaction: the W boson and the Z boson. The W boson is electrically charged and so, there are W^+ and W^- bosons (antiparticles of each other). The Z boson is electrically neutral (Z^0). The weak interaction acts on all particles including neutrinos (the only interaction felt by neutrinos).

The boson responsible for the strong interaction is the *gluon* (g) which couples to the colour charge. The gluon possesses himself a colour charge, i.e. gluons are themselves subject to the strong force. They exchange gluons with other gluons which allows the possibility of *glueballs* (bound states of 'pure glue') and

Table 5: The three quark families of the SMPP. For each particle it is indicated the respective electric charge e, spin s and mass m (according to the PDG results – http://pdg.lbl.gov/2007/listings/contents_listings.html, Yao et al., 2006). For each quark there is an anti–quark with symmetric charge and the same mass and spin (e.g., the up antiquark, $\bar{u}$, is a particle with electric charge $-2/3$, spin 1/2 and mass 1.5 to 3 MeV).

Family	Quark	Symbol	e	s	m(MeV)
1	up	u	2/3	1/2	1.5 to 3
	down	d	$-1/3$	1/2	3 to 7
2	strange	s	$-1/3$	1/2	95 (±25)
	charm	c	2/3	1/2	1250 (±90)
3	bottom	b	$-1/3$	1/2	4200 (±70)
	top	t	2/3	1/2	172500 (±2700)

Table 6: Fundamental Bosons within the SMPP. For each boson it is shown the respective electric charge e, spin s and mass m (according to the PDG results – http://pdg.lbl.gov/2007/listings/contents_listings.html, Yao et al., 2006).

Interaction	Boson	Symbol	q	s	m(MeV)
electromagnetic	photon	γ	0	1	0
weak	W	W^-	-1	1	80403
	Z	Z^0	0	1	91188
	W	W^+	$+1$	1	80403
strong	gluon	g	0	1	0

hybrid mesons (bound states of a gluon, quark and antiquark).

There are six types of gluons that can change the colour charge of a quark (but not its flavour): red–antigreen, red–antiblue, green–antired, green–antiblue, blue–antired, and blue–antigreen. For example, if a red quark interacts with a red–antigreen quark then it will become a green quark. In addition, there are two different gluons that couple to the color charge on a quark wihtout changing the quark color. These gluons can be regarded as mixtures of blue–antiblue, red–antired, and green–antigreen.

A distinct feature of the EW interactions is that the $W^{\pm}$ and Z^0 bosons that mediate them are massive which means that it is not possible to describe weak interactions in terms of a gauge field theory. However, although the theory has a symmetry, it is not necessary that the ground state of the theory has the same symmetry, that is, the symmetry may be spontaneously broken. This is a suffcient requirement for producing masses for gauge bosons. In the SMPP, this is accomplished by introducing a scalar field, called the *Higgs* scalar, into the theory (e.g. Gynther, 2006).

Associated with this field there is a spin zero boson and charge zero – the *Higgs boson*, H (with a mass yet to be determined – it is still a purely hypothetical particle – the only one of the SMPP). As a quark or lepton moves trough space, it interacts with the Higgs field; the field becomes distorted in the vicinity of the particle. It is this distortion that causes the particle to have mass.

Most of our present experimental knowledge about the SMPP Higgs boson comes from the study of e^+e^- collisions performed at *Large Electron Positron Collider* (LEP) and the *Stanford Linear Collider* SLC between 1988 and 2000. No direct evidence for the existence of the SMPP Higgs has been produced. This allows us to set a lower limit on the Higgs mass of 114.4 GeV, mainly based of the non–observation of Higgs bosons in association with a Z^0, followed by the eventual decay of the Higgs into a heavy fermion–antifermion pair (e.g. Ellis et al., 2007).

Hadrons are composite particles made up of quarks (as far as we know there are no free quarks in nature at the present stage of the Universe). Hadrons with integer spin are called *mesons* (bosonic hadrons) and those with half–integer spin are called *baryons* (fermionic hadrons).

Every meson consists of a quark–antiquark pair. This means that we have five quark flavours $\times$ five anti–quark flavours = 25 different possible combinations[12]. However, the observed number of different mesons is, by far, much larger than this one. That is because, for each quark–antiquark combination, there are, in general, many excited states. For example, the π^+ meson corresponds to the lower energy state (fundamental state) of the $u\bar{d}$ combination ($m \approx 139.57$ MeV). Examples of excited states for the π^+ meson (just to name a few) comprehend the ρ^+ ($m \approx 775.4$ MeV), the $a_0(1450)$ ($m \approx 1474$ MeV), and the $\pi_2(1650)$ ($m \approx 1672.4$ MeV).

[12]The top quark is left outside because the probability of formation for top mesons is, according to theory, negligibly small (e.g. Fabiano, 1997). Besides that, there are no reports on the detection of top mesons (e.g. Yao et al., 2006).

Some of the quark–antiquark combinations are observed only in superpositions. That is, for example, the case of the neutral pion (π^0) which is a superposition of the combinations $u\bar{u}$ and $d\bar{d}$. The superposition occurs because the two combinations share the same set of quantum numbers.

The combination $d\bar{s}$ is called neutral Kaon (K^0). Although K^0 and its antiparticle $\bar{K}^0$ are usually produced via the strong force, they decay weakly. Thus, once created, the two are better thought of as composites of two weak eigenstates which have vastly different lifetimes: the long–lived (5.116×10^{-8} s) neutral kaon called *K–Long* and the short–lived (8.953×10^{-11} s) neutral kaon called *K–Short*. On table 7 we show the fundamental mesons as well as their most common excited states.

Table 7: The fundamental mesons and their most common excited states. For each meson and antimeson it is indicated the symbol, the quark content, the electric charge e, the spin s, the mean lifetime t and, whenever possible, the two most probable decaying reactions with corresponding probabilities (for more data on these and other mesons consult the PDG – http://pdg.lbl.gov/2007/listings/contents_listings.html, Yao et al., 2006).

Name	Meson symbol	Antimeson symbol	quark content		e	s	m(MeV)	$t(s)$	Most probable decaying reaction		Second most probable decaying reaction	
pion	π^+	π^-	$u\bar{d}$	$\bar{u}d$	±1	0	139.57	2.6×10^{-8}	$\pi^\pm\to\mu^\pm+\nu_\mu$	99.99%		
neutral pion	π^0	(self)	$\left(u\bar{u}-d\bar{d}\right)/\sqrt{2}$	–	0	0	134.98	8.4×10^{-17}	$\pi^0\to\gamma+\gamma$	98.80%		
charged kaon	K^+	K^-	$u\bar{s}$	$\bar{u}s$	±1	0	493.68	1.24×10^{-8}	$K^\pm\to\mu^\pm+\nu_\mu$	63.4%	$K^\pm\to\pi^\pm+\pi^0$	21%
neutral kaon	K^0	$\bar{K}^0$	$d\bar{s}$	$\bar{d}s$	0	0	497.648	–	–	–	–	
K–Short	K_S^0	(self)	$\left(d\bar{s}-s\bar{d}\right)/\sqrt{2}$	–	0	0	497.648	8.953×10^{-11}	$K_S^0\to\pi^++\pi^-$	69.2%	$K_S^0\to\pi^0+\pi^0$	30.7%
K–Long	K_L^0	(self)	$\left(d\bar{s}+s\bar{d}\right)/\sqrt{2}$	–	0	0	497.648	5.116×10^{-8}	$K_L^0\to\pi^\pm+e^\mp+\nu_e$	40.6%	$K_L^0\to\pi^\pm+\mu^\mp+\nu_\mu$	27%
charged rho	ρ^+	ρ^-	$u\bar{d}$	$\bar{u}d$	±1	1	775.4	–	$\rho^\pm\to\pi^\pm+\pi_0$	$\approx100\%$		
neutral rho	ρ^0	(self)	$\left(u\bar{u}-d\bar{d}\right)/\sqrt{2}$	–	0	1	775.49	–	$\rho^0\to\pi^++\pi^-+\gamma$	–	$\rho^0\to\pi^0+\gamma$	–
omega	ω	(self)	$\left(u\bar{u}+d\bar{d}\right)/\sqrt{2}$	–	0	1	782.65	–	$\omega\to\pi^++\pi^-+\pi^0$	89.1%	$\omega\to\pi^0+\gamma$	8.9%
phi	φ	(self)	$s\bar{s}$	–	0	1	1019.46	–	$\varphi\to K^++K^-$	49.3%	$\varphi\to K_S^0+K_L^0$	34.0%
eta	η	(self)	$\left(u\bar{u}+d\bar{d}-2s\bar{s}\right)/\sqrt{6}$	–	0	0	547.51	–	$\eta\to\gamma+\gamma$	39.4%	$\eta\to\pi^0+\pi^0+\pi^0$	32.5%
eta prime	η'	(self)	$\left(u\bar{u}+d\bar{d}+s\bar{s}\right)/\sqrt{6}$	–	0	0	957.78	–	$\eta'\to\pi^++\pi^++\eta$	44.5%	$\eta'\to\rho^0+\gamma+(\pi^++\pi^-+\gamma)$	29.4%
charged D	D^+	D^-	$c\bar{d}$	$\bar{c}d$	±1	0	1869.62	1.04×10^{-12}	$D^\pm\to K^0+...+\bar{K}^0+...$	61%	$D^\pm\to K^\pm+...$	27%
neutral D	D^0	$\bar{D}^0$	$c\bar{u}$	$\bar{c}u$	0	0	1864.84	4.1×10^{-13}				
strange D	D_s^+	D_s^-	$c\bar{s}$	$\bar{c}s$	±1	0	1968.2	5.0×10^{-13}	$D_s^\pm\to K^0+...+\bar{K}^0+...$	39%	$D_s^\pm\to K^\pm+...$	13%
J/Psi	J/ψ	(self)	$c\bar{c}$	–	0	1	396.92	–	$J/\psi\to hadrons$	88%	$J/\psi\to e^++e^-$	6%
charged B	B^+	B^-	$u\bar{b}$	$\bar{u}b$	±1	0	5297.0	1.638×10^{-12}	$B^\pm\to l^\pm+\nu_l+...$	10.9%		
neutral B	B^0	$\bar{B}^0$	$d\bar{b}$	$\bar{d}b$	0	0	5279.5	1.530×10^{-12}	$B^0\to l^++\nu_l+...$	10.4%		
strange B	B_s^0	$\bar{B}_s^0$	$s\bar{b}$	$\bar{s}b$	0	0	5367.5	1.466×10^{-12}	$B_s^0\to D_s^-+...$	94%		
charmed B	B_c^+	B_c^-	$c\bar{b}$	$\bar{c}b$	±1	0	6286	4.6×10^{-11}	$B_c^\pm\to J/\psi+l^\pm+\nu_l$	–	$B_c^\pm\to J/\psi+\pi^\pm$	–
Upsilon	Υ	(self)	$b\bar{b}$	–	0	1	9460.3	–	$\Upsilon\to\tau^++\tau^-$	2.6%	$\Upsilon\to\mu^++\mu^-$	2.5%

A baryon consists of a triplet of quarks. This means that we have 35 different possible combinations[13]. The most common baryons in the present universe are *nucleons*, i.e., protons and neutrons. The proton consists of two up quarks and one down quark (uud) and the neutron consists of one up quark and two down quarks (udd).

Hyperons are baryons containing at least a strange quark, but no charm or bottom quarks (e.g. Σ^-, Σ^0, Σ^+, Ξ^-, Ξ^0, Λ^0, Ω^-). Charmed baryons are baryons containing at least a charm quark, but no bottom quarks (e.g. Ξ_c^+, Ξ_c^0, Ξ_{cc}^+, Δ_c^+, Ω_c^0). Bottom baryons are baryons containing at least a bottom quark (e.g. Ξ_b^-, Ξ_b^0, Δ_b^0).

Some of the 35 triplets have never been observed (e.g. ubb, sbb). However, the number of known baryons is much larger than the number of different quark triplets. That is due to the existence of many excited states for each configuration. For example, in the case of the proton (uud) there are at least 25 known excited states (e.g. $N(2190)^+$ with mass $\approx$ 2190 MeV, $N(1710)^+$ with mass $\approx$ 1710 MeV, Δ^+ with mass $\approx$ 1232 MeV)[14]. On table 8 we show the most stable known baryons.

Antibaryons are triplets made of antiquarks. For each baryon there is an antibaryon, which is an antiparticle with the same mass and opposite electric charge, obtained by replacing each quark by the corresponding antiquark[15]. For example, the antiparticle of the proton (uud), is the antiproton ($\bar{u}\bar{u}\bar{d}$), an antibaryon with $m \approx 938.272$ MeV and $e = -1$.

---

[13]The 35 different quark triplets are: uuu, uud, uus, uuc, uub, udd, uds, udc, udb, uss, usc, usb, ucc, ucb, ubb, ddd, dds, ddc, ddb, dss, dsc, dsb, dcc, dcb, dbb, sss, ssc, ssb, scc, scb, sbb, ccc, ccb, cbb and bbb. The top quark was left outside because the probability of formation of a *top baryon* is negligibly small.

[14]For a complete list of currently known baryons (including excited states) see http://pdg.lbl.gov/2007/tables/contents_tables.html.

[15]Baryons are matter (they are made of quarks) and antibaryons are antimatter (they are made of antiquarks). The same idea does not apply to mesons and antimesons. That is because a meson (or antimeson) consists of a quark–antiquark pair.

Table 8: The most stable known baryons. For each baryon it is shown the symbol, the quark content, the electric charge e, the spin s, the mass m, the mean lifetime t, the most probable decaying reaction(s) and probabilities. In the case of charmed and bottom baryons it is not known, in general, the most probable decaying reaction. In these cases we have selected one or two examples (if available) of possible decaying reactions (according to the PDG results – http://pdg.lbl.gov/2007/listings/contents_listings.html, Yao et al., 2006).

Name	Symbol	quarks	e	s	m(MeV)	$t(s)$	Most probable decaying reaction		Second most probable decaying reaction	
proton	p	uud	+1	1/2	938.272	$> 10^{29}$ years				
neutron	n	udd	0	1/2	939.565	885.7	$n \to p + e^- + \bar{\nu}_e$	100%		
sigma	Σ^-	dds	−1	1/2	1197.45	1.48×10^{-10}	$\Sigma^- \to \pi^- + n$	99.8%		
	Σ^0	uds	0	1/2	1192.64	7.4×10^{-20}	$\Sigma^0 \to \Lambda^0 + \gamma$	100%		
	Σ^+	uus	+1	1/2	1189.37	8.0×10^{-11}	$\Sigma^+ \to \pi^+ + n$	52%	$\Sigma^+ \to \pi^0 + p$	48%
xi	Ξ^-	dss	−1	1/2	1321.7	1.64×10^{-10}	$\Xi^- \to \Lambda^0 + \pi^-$	99.9%		
	Ξ^0	uss	0	1/2	1314.9	2.9×10^{-10}	$\Xi^0 \to \Lambda^0 + \pi^0$	99.5%		
charmed xi	Ξ_c^+	usc	+1	1/2	2467.9	4.42×10^{-13}	$\Xi_c^+ \to \Lambda^0 + \bar{K}^0 + \pi^+$	—	$\Xi_c^+ \to p + K^- + \pi^+$	—
	Ξ_c^0	dsc	0	1/2	2471.0	1.12×10^{-13}	$\Xi_c^0 \to p + K^- + K^- + \pi^+$	—	$\Xi_c^0 \to \Lambda^0 + \bar{K}^0 + \pi^+ + \pi^-$	—
double charmed xi	Ξ_{cc}^+	dcc	+1	1/2	3518.9	$< 3.3 \times 10^{-14}$	$\Xi_{cc}^+ \to p + D^+ + \pi^+$	—	$\Xi_{cc}^+ \to \Lambda_c^+ + K^- + \pi^+$	—
bottom xi	Ξ_b^0	usb	0	1/2	—	1.42×10^{-12}	—	—		
	Ξ_b^-	dsb	−1	1/2	—	1.42×10^{-12}	$\Xi_b^- \to J/\psi + \Xi^-$	—		
lambda	Λ^0	uds	0	1/2	1115.68	2.63×10^{-10}	$\Lambda^0 \to p + \pi^-$	63.9%	$\Lambda^0 \to n + \pi^0$	35.8%
charmed lambda	Λ_c^+	udc	+1	1/2	2286.46	2.0×10^{-13}	$\Lambda_c^+ \to p + K^- + \pi^+$	5%	$\Lambda_c^+ \to p + \bar{K}^0 + \pi^0$	3.3%
bottom lambda	Λ_b^0	udb	0	1/2	5620.2	1.41×10^{-12}	$\Lambda_b^0 \to \Lambda_c^+ + l^- + \bar{\nu}_l + \pi^+ + \pi^-$ (here l represents any lepton)	5.6%	$\Lambda_b^0 \to \Lambda_c^+ + l^- + \bar{\nu}_l$	5.0%
omega	Ω^-	sss	−1	3/2	1672.5	8.2×10^{-11}	$\Omega^- \to \Lambda^0 + \pi^+$	67.8%	$\Omega^- \to \Xi^0 + \pi^-$	23.6%
charmed omega	Ω_c^0	ssc	0	1/2	2697.5	6.92×10^{-14}	$\Omega_c^0 \to \Xi^0 + K^- + \pi^+$	—	$\Omega_c^0 \to \Omega^- + \pi^+$	—

1.9 The Minimal Supersymmetric extension of the SMPP

Supersymmetry (SUSY) is a generalization of the space–time symmetries of quantum field theory that transforms fermions into bosons and vice versa. SUSY also provides a framework for the unification of particle physics and gravity, which is governed by the Planck energy scale (10^{19} GeV) where the gravitational interactions become comparable in magnitude to the gauge interactions (e.g. Yao et al., 2006).

The *Minimal Supersymmetric extension of the Standard Model* (MSSM) consists of taking the fields of the two–Higgs–doublet extension of the SMPP[16]

$$H_u = \left(H_u^+,\, H_u^0\right) \quad \text{and} \quad H_d = \left(H_d^0,\, H_d^-\right)$$

and adding the corresponding supersymmetric partners (e.g. Yao et al., 2006). The supersymmetric partners of the gauge and Higgs bosons are fermions, whose names are obtained by appending *ino* at the end of the corresponding SMPP particle name (e.g. Yao et al., 2006). In Table 9 we show a list of the SMPP particles and the respective MSSM *sparticles*.

The enlarged Higgs sector of the MSSM, which constitutes the minimal structure needed to guarantee the cancellation of anomalies from the introduction of the higgsino superpartners (e.g. Yao et al., 2006), corresponds to eight degrees of freedom (Section 1.10). When the EW symmetry is broken, three of them are the *would–be Nambu–Goldstone bosons* (G^0, $G^\pm$), which become the longitudinal components of the Z^0 and $W^\pm$ massive vector bosons[17]. The remaining five Higgs scalar mass eigenstates consist of three neutral scalars h^0, H^0, and A^0; and a charge $+1$ scalar H^+, and its conjugate charge -1 scalar H^-. The masses of A^0, H^0 and $H^\pm$ can in priciple be arbitrarly large. On the other hand the mass of h^0 is upper bounded around ~ 150 GeV (e.g. Martin, 2006).

The supersymmetric partners of the EW gauge bosons (γ, Z^0 and $W^\pm$) are called *gauginos* and the supersymmetric partners of the Higgs boson are called *higgsinos* (e.g. Yao et al., 2006). Note, however, that before EW symmetry breaking the γ and Z^0 fields are decomposed into a B (superpartner: *Bino* $\tilde{B}$) and W^0 (superpartner: $\tilde{W}^0$) fields. After the EW symmetry breaking, the W^0 and the B fields mix to produce the physical Z^0 and γ fields, while the corresponding *s–fields*[18] mix to produce the zino $\tilde{Z}^0$ and the massless photino $\tilde{\gamma}$ (e.g. Aitchison, 2005).

The higgsinos and EW gauginos mix with each other because of the effects of EW symmetry breaking. The neutral higgsinos ($\tilde{H}_u^0$, $\tilde{H}_d^0$) and the neutral gauginos ($\tilde{B}$, $\tilde{W}^0$) combine to form four mass eigenstates called *neutralinos*. The charged higgsinos ($\tilde{H}_u^+$, $\tilde{H}_d^-$) and winos ($\tilde{W}^+$, $\tilde{W}^-$) mix to form two mass

[16] A general property of any (renormalizable) supersymmetric extension of the SMPP is the presence of, at least, two Higgs doublets, which leads to an *extended Higgs sector* (e.g. Ellis et al., 2007).

[17] A vector boson is a boson with spin 1. A vector boson, A, can be decomposed into a transverse component ($A_\perp$) and a longitudinal component ($A_\parallel$; parallel to the direction of motion) such that the transversality condition ($\nabla . A_\perp = 0$) and the irrotational condition of the longitudinal component ($\nabla \times A_\parallel = 0$) are satisfied.

[18] Super–fields.

Table 9: The SMPP particles and their supersymmetric partners (sparticles) according to the MSSM. Note, however, that before EW symmetry breaking the γ (superpartner photino) and Z^0 (superpartner zino) fields are decomposed into a B (superpartner: *Bino* $\tilde{B}$) and W^0 (superpartner: *Wino* $\tilde{W}^0$) fields.

Particle	Symbol	Spin	Sparticle	Symbol	Spin
electron	e	1/2	selectron	$\tilde{e}$	0
muon	μ	1/2	smuon	$\tilde{\mu}$	0
tau	τ	1/2	stau	$\tilde{\tau}$	0
electron neutrino	ν_e	1/2	selectron sneutrino	$\tilde{\nu_e}$	0
muon neutrino	ν_μ	1/2	smuon sneutrino	$\tilde{\nu_\mu}$	0
tau neutrino	ν_τ	1/2	stau sneutrino	$\tilde{\nu_\tau}$	0
top	t	1/2	stop	$\tilde{t}$	0
bottom	b	1/2	sbottom	$\tilde{b}$	0
charm	c	1/2	scharm	$\tilde{c}$	0
strange	s	1/2	sstrange	$\tilde{s}$	0
up	u	1/2	sup	$\tilde{u}$	0
down	d	1/2	sdown	$\tilde{d}$	0
photon	γ	1	photino	$\tilde{\gamma}$	1/2
W	$W^\pm$	1	Wino	$\tilde{W}^0$	1/2
Z	Z^0	1	Zino	$\tilde{Z}$	1/2
gluon	g	1	gluino	$\tilde{g}$	1/2
Higgs	H	0	Higgsino	$\tilde{H}$	1/2

eigenstates with charge ± 1 called *charginos*. We will denote the neutralino and chargino mass eigenstates by $\tilde{N}_i$ $(i = 1, 2, 3, 4)$ and $\tilde{C}_i^{\pm}$ $(i = 1, 2)$ [19]. By convention, these are labeled in ascending order, so that $m_{\tilde{N}_1} < m_{\tilde{N}_2} < m_{\tilde{N}_3} < m_{\tilde{N}_4}$ and $m_{\tilde{C}_1} < m_{\tilde{C}_2}$. The lightest neutralino, $\tilde{N}_1$, is usually assumed to be the *lightest supersymmetric particle* (LSP), unless there is a lighter gravitino or unless *R–parity*[20] is not conserved, because it is the only MSSM particle that can make a good dark matter candidate (e.g. Martin, 2006).

There is a likely limit where EW symmetry breaking effects can be viewed as a small perturbation on the neutralino mass matrix. In that limit, the neutralino mass eigenstates are very nearly a *bino–like* $\tilde{N}_1 \approx \tilde{B}$, a *wino–like* $\tilde{N}_2 \approx \tilde{W}^0$ and *higgsino–like* $\tilde{N}_3, \tilde{N}_4 \approx (\tilde{H}_u^0 \pm \tilde{H}_d^0)/\sqrt{2}$ (e.g. Martin, 2006).

The *gluino* is the superpartner of the gluon. This colour octet fermion is unique among all of the MSSM sparticles because it cannot mix with any other particle in the MSSM. It is reasonable to suspect that the gluino is considerably heavier than the lighter neutralinos and charginos (e.g. Martin, 2006).

The supersymmetric partners of the quarks and leptons are spin–zero bosons: the *squarks*, charged *sleptons*, and *sneutrinos*. For a given fermion f, there are two supersymmetric partners, f_L and f_R which are scalar partners of the corresponding left and right handed fermion. However, in general, f_L and f_R are not mass–eigenstates, since there is $f_L - f_R$ mixing[21] (e.g. Yao et al., 2006).

In the MSSM there are 32 distinct masses corresponding to undiscovered particles, not including the gravitino[22]. Assuming that the mixing of first– and second–family squarks and sleptons is negligible, the mass eigenstates of the MSSM are listed in Table 10.

The *Snowmass Points and Slopes* (SPS) are a set of benchmark points and parameter lines in the MSSM parameter space corresponding to different scenarios in the search for SUSY at present and future experiments (see e.g. Allanach et al., 2002, for a list of SPS scenarios).

The currently most popular SUSY breaking mechanisms are *minimal supergravity* (mSUGRA), *gauge–mediated SUSY breaking* (GMSB) and *anomaly–mediated SUSY breaking* (AMSB) (e.g. Allanach et al., 2002).

Here we consider, as an example, SPS1 which is a typical mSUGRA scenario. This model features a near–decoupling limit for the Higgs sector, and a bino–

[19] An alternative notation is: $\tilde{\chi}_i^0$ $(i = 1, 2, 3, 4)$ for neutralinos and $\tilde{\chi}_i^{\pm}$ $(i = 1, 2)$ for charginos.

[20] The concept of R–parity was introduced into the MSSM (and other extensions of the SMPP) in order to account to the observed conservation of the baryon number and the lepton number. Particles have $R = +1$ and sparticles have $R = -1$ (e.g. Barbier et al., 2005).

[21] In principle, any scalars with the same electric charge, R–parity, and colour quantum numbers can mix with each other (e.g. Martin, 2006).

[22] If supersymmetry breaking occurs spontaneously, then a massless *Goldstone fermion* called the *goldstino* ($\tilde{G}$) must exist. The goldstino would then be the LSP and could play an important role in supersymmetric phenomenology. However, the goldstino is a physical degree of freedom only in models of spontaneously–broken global supersymmetry. If supersymmetry is a local symmetry, then the theory must incorporate gravity; the resulting theory is called *supergravity*. In models of spontaneously–broken supergravity, the goldstino is absorbed by the *gravitino* (the superpartner of the *graviton*). By this super–Higgs mechanism, the goldstino is removed from the physical spectrum and the gravitino acquires mass (e.g. Yao et al., 2006).

like $\tilde{N}_1$ LSP; nearly degenerate wino–like $\tilde{N}_2$, $\tilde{C}_1$; and higgsino–like $\tilde{N}_3$, $\tilde{N}_4$, $\tilde{C}_2$. The gluino is the heaviest superpartner. The squarks are all much heavier than the sleptons, and the lightest sfermion is an stau (e.g. Martin, 2006). The mass spectrum of supersymmetric particles and Higgs boson according to the SPS1a scenario is represented in Figure 11 and in Table 11. Note that in this scenario the masses of the second family coincide with the masses of the first family.

At the moment we only have lower limit masses for these particles (cf. Table 11) and a list of assumptions that we see as reasonable. For example, it is perhaps not unlikely that (e.g. Martin, 2006):

- The LSP is the lightest neutralino $\tilde{N}_1$.
- The gluino will be much heavier than the lighter neutralinos and charginos.
- The squarks of the first and second families are nearly degenerate and much heavier than the sleptons.
- The lighter stop $\tilde{t}_1$ and the lighter sbottom $\tilde{b}_1$ are probably the lightest squarks.
- The lightest charged slepton is probably a stau $\tilde{\tau}$.
- The left–handed charged sleptons are likely to be heavier than their right-handed counterparts.
- The lightest neutral Higgs boson h^0 is lighter than about 150 GeV, and may be much lighter than the other Higgs scalar mass eigenstates A^0, $H^{\pm}$, H^0.

Extensions of the MSSM can be introduced, where the Higgs sector is further enlarged and the Higgs masses are less constrained. As an example we have the so–called *Next–to–Minimal Supersymmetric Standard Model* (NMSSM), whose Higgs sector includes not only two Higgs doublets, but also an additional singlet. Such an extension may slightly decrease the level of fine–tuning required to reconcile the present stringent lower bounds on supersymmetric particles and Higgs boson masses with the measured value of the Fermi scale (e.g. Ellis et al., 2007).

1.10 Degrees of freedom

In the early Universe collision and decay processes are continuously creating and destroying particles. Considering thermal equilibrium (i.e., each process is taking place at the same rate as its inverse) then the number of particles of a given species i, per momentum state, is given by (e.g. Lyth, 1993)

$$f(p) = g_i(T)\left[e^{\frac{E-\mu}{T}} \pm 1\right]^{-1} \tag{95}$$

where $g_i(T)$ counts the effective number of relativistic *helicity degrees of freedom* of that particle species at a given photon temperature T; p is the momentum, E

Table 10: The MSSM particles in terms of gauge eigenstates and mass eigenstates. In the MSSM there are 32 distinct masses to be determined corresponding to 32 undiscovered particles.

Particles	Spin	Parity	Gauge Eigenstates	Mass Eigenstates
Higgs bosons	0	$+1$	$H_u^0\ H_d^0\ H_u^+\ H_d^-$	$h^0\ H^0\ A^0\ H^\pm$
squarks	0	-1	$\tilde{u}_L\ \tilde{u}_R\ \tilde{d}_L\ \tilde{d}_R$ $\tilde{s}_L\ \tilde{s}_R\ \tilde{c}_L\ \tilde{c}_R$ $\tilde{t}_L\ \tilde{t}_R\ \tilde{b}_L\ \tilde{b}_R$	(same) (same) $\tilde{t}_1\ \tilde{t}_2\ \tilde{b}_1\ \tilde{b}_2$
sleptons	0	-1	$\tilde{e}_L\ \tilde{e}_R\ \tilde{\nu}_e$ $\tilde{\mu}_L\ \tilde{\mu}_R\ \tilde{\nu}_\mu$ $\tilde{\tau}_L\ \tilde{\tau}_R\ \tilde{\nu}_\tau$	(same) (same) $\tilde{\tau}_1\ \tilde{\tau}_2\ \tilde{\nu}_\tau$
neutralinos	1/2	-1	$\tilde{B}^0\ \tilde{W}^0\ \tilde{H}_u^0\ \tilde{H}_d^0$	$\tilde{N}_1\ \tilde{N}_2\ \tilde{N}_3\ \tilde{N}_4$
charginos	1/2	-1	$\tilde{W}^\pm\ \tilde{H}_u^+\ \tilde{H}_d^-$	$\tilde{C}_1^\pm\ \tilde{C}_2^\pm$
gluino	1/2	-1	$\tilde{g}$	(same)

Table 11: Mass spectrum of the supersymmetric particles and the Higgs boson according to the SPS1a scenario (e.g. Aguilar–Saavedra et al., 2006; Allanach et al., 2002). It is also shown the experimental lower limit for the mass of each particle (in the case of the h^0 we have an upper limit instead). See Yao et al. (2006) for a detailed list of lower mass limits and more details on this subject.

Particle	Spin	Mass (GeV)	Experimental lower limit (GeV)
h^0	0	116.0	< 150
H^0	0	425.0	
A^0	0	424.9	
$H^{\pm}$	0	432.7	
$\tilde{N}_1$	1/2	97.7	46
$\tilde{N}_2$	1/2	183.9	62
$\tilde{N}_3$	1/2	400.5	100
$\tilde{N}_4$	1/2	413.9	116
$\tilde{C}_1^{\pm}$	1/2	183.7	94
$\tilde{C}_2^{\pm}$	1/2	415.4	94
$\tilde{e}_R$	0	125.3	73
$\tilde{e}_L$	0	189.9	107
$\tilde{\nu}_e$	0	172.5	94
$\tilde{\mu}_R$	0	125.3	94
$\tilde{\mu}_L$	0	189.9	94
$\tilde{\nu}_\mu$	0	172.5	94
$\tilde{\tau}_R$	0	107.9	82
$\tilde{\tau}_L$	0	194.9	82
$\tilde{\nu}_\tau$	0	170.5	94
$\tilde{u}_R$	0	547.2	250
$\tilde{u}_L$	0	564.7	250
$\tilde{d}_R$	0	546.9	250
$\tilde{d}_L$	0	570.1	250
$\tilde{s}_R$	0	547.2	250
$\tilde{s}_L$	0	564.7	250
$\tilde{c}_R$	0	546.9	250
$\tilde{c}_L$	0	570.1	250
$\tilde{t}_1$	0	366.5	92
$\tilde{t}_2$	0	585.5	92
$\tilde{b}_1$	0	506.3	89
$\tilde{b}_2$	0	545.7	89
$\tilde{g}$	1/2	607.1	241

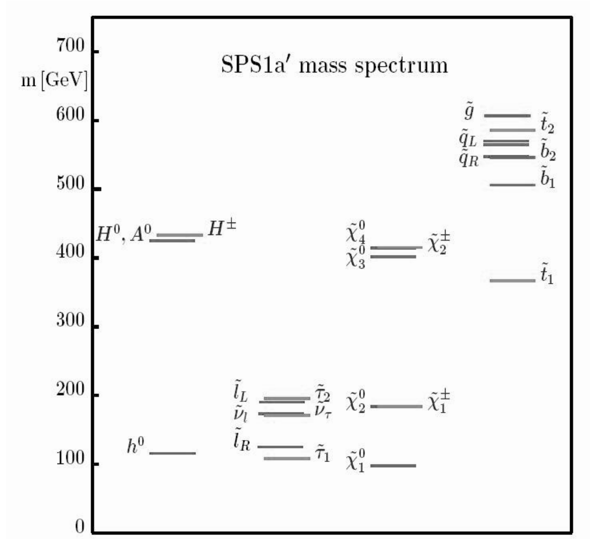

Figure 11: Mass spectrum of supersymmetric particles and the Higgs boson according to the SPS1a scenario (cf. Table 11 for mass values). Here ($\tilde{l}_L$,$\tilde{l}_R$, $\tilde{\nu}_l$) and ($\tilde{q}_L$, $\tilde{q}_R$) represent the first and the second families of sleptons and squarks respectively (e.g. Aguilar–Saavedra et al., 2006; Allanach et al., 2002).

is the energy ($E = \sqrt{p^2 + m^2}$) and the sign is + for fermions and − for bosons. The quantity $\mu = \mu(T)$ is the *chemical potential*[23] of the species. The chemical potential is conserved in every collision (e.g. Lyth, 1993).

In the early Universe all known particle species are freely created and destroyed. The only significant restriction is that each collision must respect conservation of the electric charge, baryon number and the three lepton numbers. Since the photon carries none of these charges it turns out that $\mu_\gamma = 0$ and equation (95) leads to the blackbody distribution (e.g. Lyth 1993). The same goes for any particle which is its own antiparticle. If the antiparticle is distinct,

[23] In the context of Particle Physics the chemical potential measures the tendency of particles to diffuse. Particles tend to diffuse from regions of high chemical potential to those of low chemical potential. In a system with many particle species each of them has its own chemical potential. The chemical potential of the i-th particle species is defined as

$$\mu_i = \left(\frac{\partial U}{\partial N_i}\right)_{s,V,N_{j\neq i}}$$

where U is the total internal energy of the system, s is the entropy, V is the volume and N_i is the number of particles of the i-th species. Being a function of internal energy, the chemical potential applies equally to both fermion and boson particles. That is, in theory, any fundamental particle can be assigned a value of chemical potential, depending upon how it changes the internal energy of the system into which it is introduced. QCD matter is a prime example of a system in which many such chemical potentials appear (e.g. Baierlein, 2001).

it turns out that particle and antiparticle have opposite values of μ. As a result, μ vanishes if the number density n of particles and the respective number density $\bar{n}$ of antiparticles are equal. Otherwise, μ is determined by the imbalance $n - \bar{n}$ (e.g. Lyth, 1993).

If the charges are all zero then all of the chemical potentials are zero and (95) turns out to be some sort of generalized blackbody distribution (e.g. Lyth, 1993)

$$f(p) = g_i(T)\left[e^{\frac{E}{T}} \pm 1\right]^{-1}. \tag{96}$$

The charge density of the Universe is zero to very high accuracy. If that was not the case then the expansion of the Universe would be governed by electrical repulsion instead of gravity. The net baryon number of the Universe is not zero but it is small in the sence that (e.g. Lyth, 1993)

$$\eta = \frac{n_B}{n_\gamma} \ll 1 \tag{97}$$

where n_B is the baryon density and n_γ the photon density.

Assuming that the same goes for the three lepton numbers (although we cannot measure them directly) it turns out that the generalized blackbody distribution is valid to great accuracy for all the relativistic species in equilibrium. Since there are $(2\pi)^{-3}d^3pd^3x$ states in a given volume of phase space, the particle number density n and the energy density ρ of particles of a particular species i are given by (e.g. Lyth, 1993)

$$n_i = \frac{g_i(T)}{(2\pi)^3}\int_0^\infty f(p)4\pi p^2 dp \tag{98}$$

$$\rho_i = \frac{g_i(T)}{(2\pi)^3}\int_0^\infty Ef(p)4\pi p^2 dp \tag{99}$$

If the mass m of the species in question is such that $T \gg m$ then one is on the relativistic regime and it is a good approximation to consider $E = p$. Taking this into account and inserting (96) into equations (98) and (99) we obtain, separately for fermions and bosons (e.g. Lyth, 1993)

$$\rho_{B,i} = \frac{\pi^2}{30}g_i(T)T^4 \tag{100}$$

$$\rho_{F,i} = \frac{7}{8}\frac{\pi^2}{30}g_i(T)T^4 \tag{101}$$

$$n_{B,i} = \frac{\zeta(3)}{\pi^2}g_i(T)T^3 \tag{102}$$

$$n_{F,i} = \frac{3}{4}\frac{\zeta(3)}{\pi^2}g_i(T)T^3 \tag{103}$$

where $\zeta(3) \approx 1.2021$. According to the generalized blackbody distribution each relativistic species contributes with $\sim T^4$ to ρ and $\sim T^3$ to n. When $T < m$

we are in the non–relativistic regime and we have ρ and n falling rapidly. The reason is that the energy available in a collision is now insufficient to create the species (e.g. Lyth, 1993).

As the temperature T falls below the mass m of a given species, particle–antiparticle pairs rapidly annihilate (according to the generalized blackbody distribution) and only one kind of particle of that species survives. The imbalance $n - \bar{n}$ becomes significant and μ no longer vanishes. However, even if the surviving particles do not decay, their contribution to ρ and n during the radiation–dominated era are negligible (e.g. Lyth, 1993).

If we are interested in the total energy density (i.e., in the energy density due to all the particle species for which $m \ll 3T$) then it may be useful to introduce the *effective number of helicity degrees of freedom* at a particular epoch (i.e., characterized by a given temperature T) defined as (e.g. Liddle & Lyth, 1993)

$$g(T) = \sum_{bosons} g_i(T) + \frac{7}{8} \sum_{fermions} g_i(T) \tag{104}$$

where the sum goes over all particle species with $m \ll 3T$. Notice that the fermionic degrees of freedom are suppressed by a factor of 7/8 with respect to bosonic degrees of freedom. This is due to the difference between Fermi–Dirac statistics and Bose–Einstein statistics (e.g. Hands, 2001).

We may write, with the help of equation (104), the total energy density for a radiation–dominated Universe as (e.g. Schwarz, 2003)

$$\rho = \frac{\pi^2}{30} g(T) T^4. \tag{105}$$

In particle physics *helicity* h is the projection of the angular momentum of the particle to the direction of motion. Because angular momentum with respect to an axis has discrete values, helicity is discrete too. For a relativistic particle ($m \ll 3T$) there are two possible helicity eigenstates usually referred to as *left–handed* and *right–handed* states[24] (e.g. Hands, 2001).

For each quark flavour we have to count two electric charges (quark + anti–quark), two helicity states and three colour states. This gives a total of $2 \times 2 \times 3 =$ 12 degrees of freedom per quark. In the case of gluons we have to consider that each one of the eight colour charges could have one of two helicity states. Thus, gluons contribute with $2 \times 8 = 16$ degrees of freedom.

Each neutral lepton (i.e. neutrino) contributes with two degrees of freedom corresponding to two possible helicity states. On the other hand each charged lepton contibutes with four degrees of freedom corresponding to two helicity states $\times$ two charges (lepton and anti–lepton). The photon contributes with two degrees of freedom corresponding to two possible helicity states.

The Higgs boson contributes with 4 degrees of freedom corresponding to the two possible helicity states of the *scalar doublet*. The $W^{\pm}$ and Z^0 bosons

[24]The antineutrinos observed so far all have right–handed helicity, while the neutrinos are left–handed.

Table 12: The number of degrees of freedom for each kind of particle within the SMPP: g_i is the contribution due to a single particle, N is the number of species of a particular particle and $g_N = Ng_i$ is the total contribution for $g(T)$ of each kind of particle.

Particle	g_i	N	g_N
quark	$12\frac{7}{8}$	6	63.0
charged lepton	$4\frac{7}{8}$	3	10.5
neutrino	$2\frac{7}{8}$	3	5.25
photon	2	1	2
gluon	2	8	16
EW bosons	2	3	6
Higgs	4	1	4

contribute with 6 degrees of freedom corresponding to three species times two possible helicity states. However at the EW transition (Section 3) the W and Z contribution becomes 9. This is due to the Higgs mechanism during which the W and Z bosons acquire mass and a third polarization degree of freedom (e.g. Ignatius, 1993).

The meson π contributes with 3 degrees of freedom (one for each kind of π meson: π^-, π^0 and π^+). We may have to consider also the contribution of kaons. This would be 4 degrees of freedom (e.g. Boyanovsky et al., 2006). On Table 12 we have listed the contribution of each SMPP fundamental particle to the total number of degrees of freedom.

As it was already mentioned it is a good approximation to treat all particles with $m \ll 3T$ as though they were massless. The contribution of all other particles can be neglected in the total energy density (e.g Schwarz, 2003). This is why we did not consider the contribution of composite particles such as protons and neutrons. For example, in the case of the proton we have $m_p \approx 900$ MeV. Considering that protons form at the QCD epoch when the temperature of the Universe was $T_c = 170$ MeV it turns out that in this case we do not have $m \ll 3T$ and thus, we can safelly neglect the contribution of the proton to the total number of degrees of freedom.

At very high temperatures ($T > m_t \sim 172.5$ GeV) all the particles of the SMPP contribute to the effective number of degrees of freedom $g(T)$ (cf. equation 104) giving (e.g. Ignatius, 1993)

$$\begin{aligned} g(T) &= g_\gamma + g_{W^\pm,Z^0} + g_g + g_H + \tfrac{7}{8}\,[\, g_{e,\mu,\tau} + g_\nu + g_q \,] = \\ &2 + 3\times 2 + 8\times 2 + 4 + \tfrac{7}{8}\,[3\times 4 + 3\times 2 + 6\times 12] = 106.75. \end{aligned} \tag{106}$$

As the expansion of the Universe goes on, the temperature decreases and it will equal, successively, the threshold of each particle leading to smaller values of $g(T)$. This evolution is represented on Table 13 where we have, in the first row, the case when all the particles are present and, on the final row, the present day case with only neutrinos and photons.

At temperatures above 1 MeV, electrons, photons and neutrinos have the same temperature. Below this temperature the three neutrino flavours are decoupled chemically and kinetically from the radiation plasma. This early decoupling from thermal evolution with the rest of the Universe is due to the fact that neutrinos interact with other particles only via weak interactions (e.g. Gynther, 2006). As a result, the entropy of the relativistic electrons is transferred to the photon entropy, but not to the neutrino entropy when electrons and positrons annihilate. This leads to an increase of the photon temperature relative to the neutrino temperature by (e.g Schwarz, 2003)

$$T_\nu = \left(\frac{4}{11}\right)^{1/3} T_\gamma. \tag{107}$$

As a result, below $T \sim 1$ MeV we have to consider the effective number of degrees of freedom of the energy density, g_ρ, and the number of degrees of freedom of the entropy density, g_s (e.g Schwarz, 2003). The present value of g_ρ is (e.g. Coleman & Ross, 2003)

$$g_\rho(T) = g_\gamma + 6\times\frac{7}{8}\left(\frac{4}{11}\right)^{4/3} \approx 3.363. \tag{108}$$

On the other hand we have $g_s(T) \approx 3.909$ at the present (e.g Schwarz, 2003).

At the temperature of the QCD transition ($T_c \approx 170$ MeV, see Section 2) the number of degrees of freedom changes very rapidly, since quarks and gluons are coloured. Before the QCD transition we have $g = 61.75$ (or $g = 51.25$ not including the strange quark) and after the transition we have $g = 17.25$ (cf. Table 13) which gives $\Delta g \approx 45$. At still higher temperatures, heavier particles are excited, but within the SMPP nothing so spectacular as the QCD transition happens. Within the SMPP the EW transition is only a tiny effect (e.g. Schwarz, 2003) with $\Delta g = 96.25 - 95.25 = 1$.

This situation is drastically changed if one considers the MSSM (see Section 1.9). On Table 14 we list the contribution that each particle and each sparticle species might give to $g(T)$. Note that the contributions from squarks, sleptons and gluinos is identical to that of, respectively, quarks, leptons and gluons (apart from the factor 7/8). The Higgs sector now is formed by two doublets

Table 13: The evolution of the number of degrees of freedom $g(T)$ in the Universe according to the SMPP (equation 104). As the expansion goes on, and the temperature T decreases, some particle species cease to exist (because T eventually gets below the particle threshold) lowering the value of $g(T)$.

Temperature	Leptons	Quarks	g_F	*Bosons*		g_B	$g(T)$
$T > m_t$	$\nu\ e^-\ \mu\ \tau$	$u\ d\ s\ c\ b\ t$	90	$\gamma\ g\ W\ H$		28	106.75
$m_H < T < m_t$	$\nu\ e^-\ \mu\ \tau$	$u\ d\ s\ c\ b$	78	$\gamma\ g\ W\ H$		28	96.25
$m_{W,Z} < T < m_H$	$\nu\ e^-\ \mu\ \tau$	$u\ d\ s\ c\ b$	78	$\gamma\ g\ W$		27	95.25
$m_b < T < m_{W,Z}$	$\nu\ e^-\ \mu\ \tau$	$u\ d\ s\ c\ b$	78	$\gamma\ g$		18	86.25
$m_\tau < T < m_b$	$\nu\ e^-\ \mu\ \tau$	$u\ d\ s\ c$	66	$\gamma\ g$		18	75.75
$m_c < T < m_\tau$	$\nu\ e^-\ \mu$	$u\ d\ s\ c$	62	$\gamma\ g$		18	72.25
$m_s < T < m_c$	$\nu\ e^-\ \mu$	$u\ d\ s$	50	$\gamma\ g$		18	61.75
$T_c < T < m_s$	$\nu\ e^-\ \mu$	$u\ d$	38	$\gamma\ g$		18	51.25
$m_\pi < T < T_c$	$\nu\ e^-\ \mu$		14	γ	π	5	17.25
$m_\mu < T < m_\pi$	$\nu\ e^-\ \mu$		14	γ		2	14.25
$m_e < T < m_\mu$	$\nu\ e^-$		10	γ		2	10.75
$T < m_e$	ν		6	γ		2	7.25

Table 14: The number of degrees of freedom for each kind of particle within the MSSM: g_i is the contribution due to a single particle, N is the number of species of a particular particle and $g_N = N g_i$ is the total contribution for $g(T)$ of each kind of particle.

Particle	g_i	N	g_N
quark	$12\frac{7}{8}$	6	63.0
charged lepton	$4\frac{7}{8}$	3	10.5
neutrino	$2\frac{7}{8}$	3	5.25
photon	2	1	2
gluon	2	8	16
EW bosons	2	3	6
Higgs	4	2	8
squark	12	6	72
charged slepton	4	3	12
sneutrino	2	3	6
neutralino	$2\frac{7}{8}$	4	7.0
chargino	$4\frac{7}{8}$	2	7.0
gluino	$2\frac{7}{8}$	8	14.0

which gives 2×4 degrees of freedom. Each neutralino contributes with two degrees of freedom corresponding to two possible helicity states and each chargino contributes with four degrees of freedom (two charges $\times$ two helicity states).

In order to account for these extra degrees of freedom we replace equation (104) by the more general

$$g(T) = \sum_{bosons} g_i(T) + \frac{7}{8} \sum_{fermions} g_i(T) + \\ + \sum_{sfermions} g_i(T) + \frac{7}{8} \sum_{bosinos} g_i(T). \tag{109}$$

At very high temperatures when all the particles contribute to the effective number of degrees of freedom we have, according to equation (109)

$$\begin{aligned} g(T) = {} & g_\gamma + g_{W^\pm, Z^0} + g_g + g_H + \frac{7}{8} [\, g_{e,\mu,\tau} + g_\nu + g_q \,] + \\ & + g_{\tilde{e},\tilde{\mu},\tilde{\tau}} + g_{\tilde{\nu}} + g_{\tilde{q}} + \frac{7}{8} [\, g_{\tilde{g}} + g_{\tilde{N}} + g_{\tilde{C}^\pm} \,] = \\ & = 2 + 3 \times 2 + 8 \times 2 + 8 + \frac{7}{8} [3 \times 4 + 3 \times 2 + 6 \times 12] + \\ & + 3 \times 4 + 3 \times 2 + 6 \times 12 + \frac{7}{8} [8 \times 2 + 4 \times 2 + 2 \times 4] = \\ & = \frac{443}{4} + 118 = \frac{915}{4} = 228.75. \end{aligned} \tag{110}$$

The SMPP has $g = 106.75$ when the temperature is larger than all particle masses (cf. equation 106) while the MSSM has $g = 228.75$ (which is more than twice 106.75). In Figure 12 we sketch the curve $g(T)$. Notice the drastic change on $g(T)$ during the QCD transition. During the EW transition the change on the value of $g(T)$ is significant only when considering the MSSM.

On Table 15 we show the evolution of $g(T)$ for the MSSM, starting with $g(T) = 228.75$, which corresponds to the case when all particles are present (cf. equation 110), down to $g(T) = 95.25$, when the temperature equals the threshold of the LSP. From that point on, the evolution of $g(T)$ proceeds within the SMPP, according to Table 13. As already mentioned, the Higgs sector of the MSSM contributes with eight real scalar degrees of freedom (cf. Section 1.9). Three of them get swallowed (during the EW transition) by the $W^\pm$ and Z^0 bosons. The other five are distributed by the mass eigenstates H^+, H^-, H^0, A^0 and h^0.

Table 15: The evolution of the number of degrees of freedom $g(T)$ in the Universe according to the MSSM (SPS1a scenario, see Section 1.9) starting with $g(T) =$ 228.75, which corresponds to the case when all particles are present. As the expansion goes on, and the temperature T decreases, some particle species cease to exist (because T eventually gets below the particle threshold) lowering the value of $g(T)$. At the bottom we have the case $g(T) = 95.25$ which corresponds to the threshold of the LSP. From that point on, the evolution of $g(T)$ proceeds within the SMPP (Table 13).

Temperature (GeV)	Particles	g_i	$g(T)$
> 607.1			228.75
607.1	$\tilde{g}$	$16\frac{7}{8}$	214.75
585.5	$\tilde{t}_2$	6	208.75
570.1	$\tilde{c}_L\ \tilde{d}_L$	12	196.75
564.7	$\tilde{u}_L\ \tilde{s}_L$	12	184.75
547.2	$\tilde{u}_L\ \tilde{s}_L$	12	172.75
546.9	$\tilde{c}_R\ \tilde{d}_R$	12	160.75
545.7	$\tilde{b}_2$	6	154.75
506.3	$\tilde{b}_1$	6	148.75
432.7	$H^{\pm}$	2	146.75
425.0	H^0	1	145.75
424.9	A^0	1	144.75
415.4	$\tilde{C}_2^{\pm}$	$4\frac{7}{8}$	141.25
413.9	$\tilde{N}_4$	$2\frac{7}{8}$	139.50
400.5	$\tilde{N}_3$	$2\frac{7}{8}$	137.75
366.5	$\tilde{t}_1$	6	131.75
194.9	$\tilde{\tau}_L$	2	129.75
189.9	$\tilde{e}_L\ \tilde{\mu}_L$	4	125.75
183.9	$\tilde{N}_2$	$2\frac{7}{8}$	124.00
183.7	$\tilde{C}_1^{\pm}$	$4\frac{7}{8}$	120.50
172.5	t	$12\frac{7}{8}$	110.00
172.5	$\tilde{\nu}_e\ \tilde{\nu}_\mu$	4	106.00
170.5	$\tilde{\nu}_\tau$	2	104.00
125.3	$\tilde{e}_R\ \tilde{\mu}_R$	4	100.00
107.9	$\tilde{\tau}_R$	2	98.00
116.0	h^0	1	97.00
97.7	$\tilde{N}_1$	$2\frac{7}{8}$	95.25

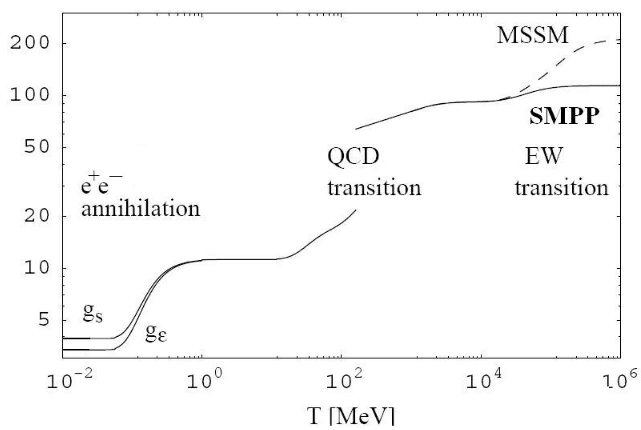

Figure 12: The effective number of degrees of freedom $g(T)$. The full line is the prediction of the SMPP, the dashed line shows the MSSM, according to the SPS1a scenario (see Section 1.9). Below $T \sim 1$ MeV we have to consider, separately, the effective number of degrees of freedom of the energy density here represented by g_ε, and the number of degrees of freedom of the entropy density, g_s (adapted from Schwarz, 2003).

2 The QCD phase transition

2.1 The QCD transition mechanism

When the age of the Universe was $\sim 10^{-5}$ s a spontaneous breaking of the *chiral symmetry*[25] of QCD occured. As a result, quarks and gluons became confined in hadrons.

In recent years most attention has focussed on the possibility of recreating the *Quark–Gluon Plasma* (QGP) in terrestrial laboratories in relativistic heavy–ion collisions. Extensive experimental work is currently being done with heavy ion collisions to study the QCD transition (most recently at the *Relativistic Heavy Ion Collider*, RHIC) (e.g. Aoki et al., 2006b).

At the QCD epoch the Universe can be treated as a radiation fluid made up of quarks, gluons, leptons and photons (e.g. Boyanovsky et al., 2006). Baryons are tightly coupled to the radiation fluid at the QCD scale. Their energy density is negligible with respect to that of the other relativistic particles and their *chemical potential* is negligible $\mu_B \approx 0$ (e.g. Schwarz, 2003).

Both for the cosmological transition and for RHIC, the net baryon densities are quite small, and so the baryonic chemical potential is much less than the typical hadron masses (≈ 45 MeV at RHIC and negligible in the early Universe). A calculation at $\mu = 0$ is directly applicable for the cosmological transition and most probably also determines the nature of the transition at the RHIC (e.g. Aoki et al., 2006a,b).

There is some apparent similarity in cosmology and heavy–ion collision physics. From present observations of remote objects in the Universe, we look into the past. Combining observational facts, like the distribution and the red-shift of galaxies, one can develop a picture of the early stages of the Universe. The situation in heavy–ion collision physics is very similar to this one. Observing the created hadrons at a very late stage, one tries to extrapolate back to the hottest and densest stages. Due to this similarity the process of heavy–ion collision is sometimes called the *Little Bang*. Notice, however, that we are dealing with different scales in both cases and that in the case of the Big Bang we are also dealing with an expanding Universe (e.g. Kämpfer, 2000).

In recent years, considerable efforts have been devoted to the determination of the phase diagram of QCD at finite temperature and density. In Figure 13 we have a schematic representation of the QCD phase transition for different choices of the quark masses $m_{u,d}$ and m_s when $\mu = 0$. In the limits of zero and infinite quark masses (lower left and upper right corners), order parameters corresponding to the breaking of a symmetry can be defined, and one finds, numerically, that a first–order transition takes place at a finite temperature T_c. On the other hand, one observes an analytic crossover at intermediate quark masses. Hence, each corner must be surrounded by a region of first–

[25] Chiral symmetry is a symmetry of QCD in the limit of vanishing quark masses. We know, however, that quark masses are finite (see Table 5). But compared with hadronic scales the masses of the two lightest quarks, up and down, are very small, so that chiral symmetry may be considered an approximate symmetry of the strong interactions (e.g. Koch, 1997).

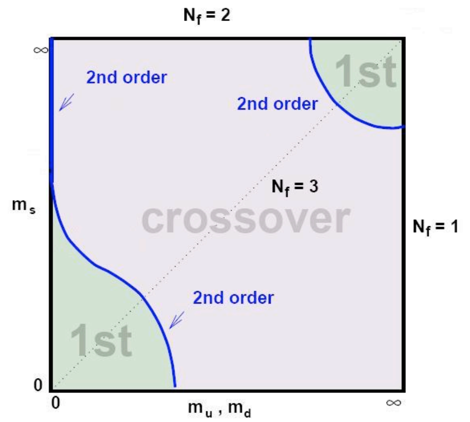

Figure 13: Schematic phase transition behaviour of $N_f = 2+1$ flavour QCD for different choices of quark masses ($m_{u,d}$ and m_s), at vanishing chemical potential ($\mu = 0$) (adapted from Laermann & Philipsen, 2003).

order transition, bounded by a second–order line as in Figure 13 (Forcrand & Philipsen, 2006).

The critical temperature T_c is one of the most fundamental quantities in QCD thermodynamics and is important in phenomenological studies of heavy–ion collisions. Recently, several groups have tried to determine T_c near the physical mass parameter in $2+1$ flavour QCD by simulations with improved *staggered quarks* (i.e. including fermionic fields in LGT). According to the results obtained, a tentative conclusion is that the critical temperature in the chiral limit is in the range 164 MeV $-$ 186 MeV. In order to improve the results further, simulations at lighter quark masses are necessary (Ejiri, 2007).

In Figure 14 we have a naive phase diagram of strongly interacting matter in the $T-n$ plane (n is the baryon density) where we consider $T_c = 170$ MeV.

Besides the radiation fluid, we might have as second fluid at the QCD epoch the CDM: kinetically coupled (made up of neutralinos) and kinetically decoupled (made up of *axions* and preexisting PBHs). Although CDM represents a major component of the present Universe this was not the case at the QCD scale. In fact, at that epoch we have (e.g. Schmid et al., 1999; Boyanovsky et al., 2006)

$$\rho^{CDM}(T_c) \sim 10^{-8} \rho^{RAD}(T_c) \tag{111}$$

which means that the gravity generated by CDM can be neglected (e.g. Boyanovsky et al., 2006).

In a first–order phase transition the QGP supercools until hadronic bubbles are formed at some temperature $T_{sc} \approx 0.95 T_c$ (e.g. Hwang, 2007). The crucial parameters for *supercooling* are the surface tension σ (i.e. the work that has to be done per unit area to change the phase interface at fixed volume) and the

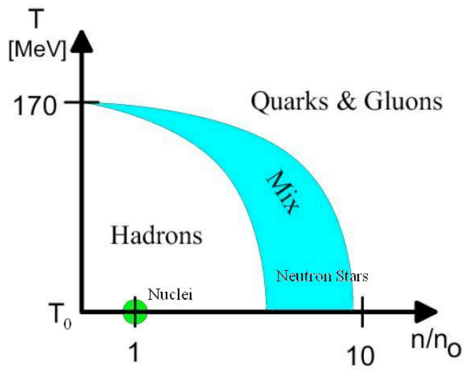

Figure 14: Naive phase diagram of strongly interacting matter in the $T-n$ plane. Here n is the baryon density, n_0 is the present value of n, $T_c = 170$ MeV, and $T_0 = 2.725$ K is the CMB temperature. At the present time the mixed phase occurs, in the universe, only at the level of atomic nuclei (green circle) or within compact objects such as neutron stars (adapted from Kämpfer, 2000).

latent heat (e.g. Schmid et al., 1997)

$$l = T_c \Delta s. \tag{112}$$

The value of latent heat which is avaliable only from *quenched lattice QCD* (gluons only, no quarks) is given by (e.g. Schmid et al., 1999)

$$l \approx 1.4 T_c^4. \tag{113}$$

The latent heat should be compared with the difference in entropy between an ideal *Hadron Gas* (HG) and an ideal QGP. This defines the ratio (e.g. Schmid et al., 1997)

$$R_l = \frac{l}{(T_c \Delta s)^{ideal}}. \tag{114}$$

A first–order phase transition is classified as strong if $R_l \approx 1$. The Bag Model (Section 2.3.1) gives $R_l = 1$ and from quenched lattice QCD we have, from equation (113), $R_l \approx 0.2$ (e.g. Schmid et al., 1999).

Without dirt (e.g. PBHs, axions) the bubbles *nucleate* due to thermal fluctuations in a process called *homogeneous nucleation* (e.g. Schmid et al., 1999). For homogeneous nucleation the period of supercolling is $\Delta t_{sc} \sim 10^{-3} t_H$, with t_H being the Hubble time (cf. equation 27) at the beginning of the transition. The typical bubble nucleation distance is $d_{nuc} \approx 1\text{cm} \approx 10^{-6} R_H$ with R_H being the Hubble radius (cf. equation 28) (e.g. Schmid et al., 1999).

The change in free energy of the system by creating a spherical bubble with radius R is (e.g. Schmid et al., 1999)

$$\Delta F = \frac{4\pi}{3}\left(p_{QGP} - p_{HG}\right) R^3 + 4\pi\sigma R^2. \tag{115}$$

Hadronic bubbles grow very fast, within $\Delta t_{nuc} \sim 10^{-6} t_H$ until the released heat has reheated the Universe to T_c and prohibits further bubble formation (e.g. Schmid et al., 1999). By that time, only a small fraction of the volume of the observable universe has gone through the transition (e.g. Boyanovsky et al., 2006). For the remaining 99% of the transition, both phases (QGP and HG) coexist at constant pressure (e.g. Schmid et al., 1999):

$$p_c = p_{QGP}(T_c) = p_{HG}(T_c). \tag{116}$$

Bubbles can grow only if they are created with radii greater than the critical bubble radius R_{crit}. Smaller bubbles disappear again due to the fact that the energy gained from the bulk of the bubble is more than compensated by the surface energy in the bubble wall. The value of R_{crit} is given by the maximum value of ΔF (e.g. Schmid et al., 1999)

$$R_{crit} = \frac{2\sigma}{p_{HG}(T) - p_{QGP}(T)}, \tag{117}$$

which diverges at $T = T_c$ meaning that bubble formation should stop after reheating. The probability of forming a critical bubble per unit volume and unit time can be written as (e.g. Schmid et al., 1999)

$$I \approx T_c^4 \exp\left(-\frac{A}{\eta^2}\right) \tag{118}$$

where

$$A = \frac{16\pi}{3}\frac{\sigma^3}{l^2 T_c} \tag{119}$$

and

$$\eta = 1 - \frac{T}{T_c}. \tag{120}$$

Using the results obtained from quenched lattice QCD we have $A = 3 \times 10^{-5}$ (e.g. Boyanovsky et al., 2006).

During the period of coexistence hadronic bubbles grow slowly (due to the expansion of the Universe only) causing a continuous growth of the volume fraction occupied by the hadron phase, at the expense of the quark–gluon phase. The latent heat released from the bubbles is distributed into the surrounding QGP (by a supersonic shock wave and by neutrino radiation) keeping the Universe at constant temperature T_c. This reheats the QGP to T_c and prohibits further bubble formation. Since the amplitude of the shock is very small, on scales smaller than the neutrino mean free path (which is $10^{-6} R_H$ at T_c), heat transport by neutrinos is the most efficient (e.g. Boyanovsky et al., 2006).

The transition is completed when all space is occupied by the hadron phase (e.g. Jedamzik, 1998; Schmid et al., 1999; Boyanovsky et al., 2006). A sketch of homogeneous bubble nucleation is shown in Figure 15. In Figure 16 it is

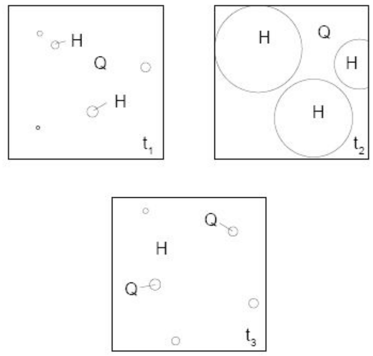

Figure 15: Sketch of a first–order QCD transition via homogeneous bubble nucleation: above the critical temperature the Universe is filled with a quark-gluon plasma (Q). After a small amount of supercooling the first hadronic bubbles (H) nucleate at t_1, with mean separation d_{nuc}. At $t_2 > t_1$ these bubbles have grown and have released enough latent heat to quench the formation of new bubbles. The supercooling, bubble nucleation, and quenching takes just 1% of the full transition time. In the remaining 99% of the transition time the bubbles grow following the adiabatic expansion of the Universe. At t_3 the transition is almost finished (Boyanovsky et al., 2006).

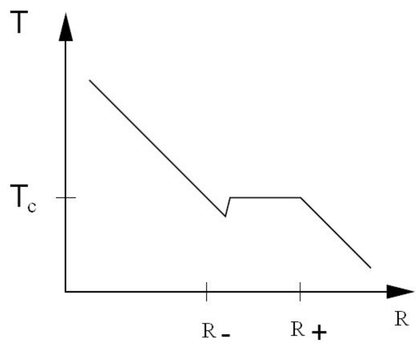

Figure 16: Qualitative behaviour of the temperature T as a function of the scale factor R during a first–order QCD transition with small supercooling. Above the critical temperature T_c the Universe cools down thanks to its expansion ($R < R_-$). After a tiny period of supercooling (in the figure the amount of supercooling and its duration are exaggerated) bubbles of the new phase nucleate. During the rest of the transition both phases coexist in pressure and temperature equilibrium ($R_- < R < R_+$). Therefore the temperature is constant. For $R > R_+$ the temperature decreases again due to the expansion of the Universe (adapted from Schwarz, 2003).

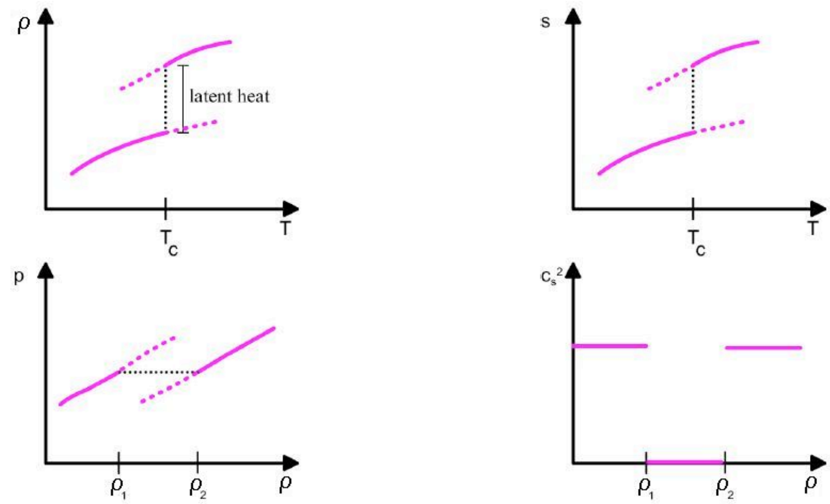

Figure 17: Schematic sketch of the thermodynamic state variables for a strong ($R_l \approx 1$) first–order phase transition. Upper row: Energy density ρ and entropy density s as a function of the temperature. Lower row: Pressure p and sound speed c_s as a function of the energy density (adapted from Kämpfer, 2000).

represented the qualitative behaviour of the temperature T as a function of the scale factor R during a first–order phase transition with small supercooling.

For a first–order transition at coexistence temperature T_c, the conditions of thermodynamic equilibrium are the equality of pressure p and temperature T between high–energy and low–energy density phases. This will be correct as long as we assume the Universe as a fluid with no chemical potential ($\mu = 0$), i.e., a fluid with no relevant conserved quantum number (e.g. Schmid et al., 1999). One may consider a region sufficiently large ($\gg R_H$) to include material in both phases such that the pressure response of matter to slow adiabatic expansion, compression, or collapse in that region is negligible. This may be expressed by defining an effective isentropic speed of sound c_s (see equation 14) for the matter in a state of phase mixture. The sound speed relates pressure gradients to density gradients. This relation is essential for the evolution of density fluctuations. In thermodynamic equilibrium (Jedamzik, 1997)

$$c_s^2 = \left(\frac{\partial p}{\partial \rho}\right)_s = 0 \tag{121}$$

holds exactly during the entire transition and suddenly rises back to $1/\sqrt{3}$ (cf. equation 8) at the end of the transition (e.g. Schwarz, 2003). In Figure 17 it is represented a sketch of the thermodynamic state variables for a strong ($R_l \approx 1$, see equation 114) first–order phase transition.

Whether a phase transition occurs in or out of *Local Thermodynamic Equi-*

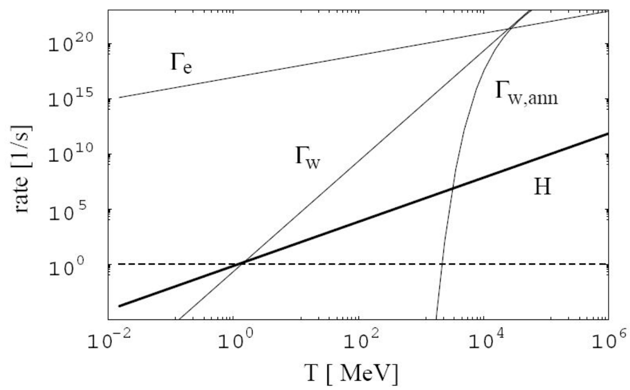

Figure 18: The Hubble rate H and the typical interaction rates of weak (Γ_w) and electric (Γ_e) processes that involve relativistic particles, as well as the typical rate of a weak annihilation rate $\Gamma_{w,ann}$ for a particle mass of 100 GeV. The dashed line indicates the rate $1/s$. At $t_H \sim 1$s, the weak interaction rate falls below the expansion rate (chemical and kinetic decoupling of neutrinos, kinetic decoupling of neutralinos); at temperatures of the order of 1-10 GeV neutralinos freeze–out. The electric interaction rate stays well above the Hubble rate up to the epoch of photon decoupling, which occurs well after the epochs we show here (Schwarz, 2003).

librium (LTE) depends on the comparison of two time scales: the cooling rate due to cosmological expansion (e.g. Boyanovsky et al., 2006)

$$\frac{1}{T(t)}\frac{dT(t)}{dt} = -\frac{1}{R(t)}\frac{dR(t)}{dt} = -H(t) \tag{122}$$

and the rate of equilibration Γ. LTE follows when $\Gamma > H(t)$, in which case the evolution is adiabatic in the sense that the thermodynamic functions depend slowly on time through the temperature (e.g. Boyanovsky et al., 2006, see Figure 18). Strong, electric, and weak interactions keep all relativistic particles in kinetic and chemical equilibrium down to temperatures of ~ 1 MeV. At that point neutrinos and neutrons decouple chemically and kinetically from the rest of the radiation fluid (e.g. Schwarz, 2003).

When the cosmological expansion is too fast (namely $H(t) \gg \Gamma$) LTE cannot happen, the temperature drops too fast for the system to have time to relax to LTE and the phase transition occurs via a *quench* from the high into the low temperature phase (e.g. Boyanovsky et al., 2006).

In the case of the QCD transition the isentropic condition applies after initial supercooling, bubble nucleation, and sudden reheating to T_c. During this part of the transition, which takes about 99% of the transition time, the fluid is extremely close to thermal equilibrium, because the time to reach equilibrium is very much shorter than a Hubble time, i.e. the fluid makes a reversible transformation (see Schmid et al., 1999, for more details).

The expansion of the Universe is very slow compared to the strong, electromagnetic and weak interactions around T_c. Thus, leptons, photons and the QGP/HG are in thermal and chemical equilibrium at cosmological time scales. All components have the same temperature locally, i.e., smeared over scales of $\sim 10^{-7} R_H$. At larger scales, strongly, weakly and electromagnetically interacting matter makes up a single perfect (i.e. dissipationless) radiation fluid (e.g. Schmid et al., 1999).

In the case of a Crossover, instead of a first–order phase transition, the sound speed decreases but does not vanish completely (e.g. Kämpfer, 2000). If the Crossover is smooth, then no out–of–equilibrium aspects are expected as the system will evolve in LTE (e.g. Boyanovsky et al., 2006).

If there is some cosmic dirt in the Universe such as PBHs, monopoles, strings, and other kinds of defects, then the typical nucleation distance may differ significantly from the scenario of homogeneous nucleation. That is because, in a first–order phase transition, the presence of impurities lowers the energy barrier and, thereby, the maximum amount of superccoling achieved during the transition (Christiansen & Madsen, 1996).

A sketch of inhomogeneous bubble nucleation is shown in Figure 19. The basic idea is that temperature inhomogeneities determine the location of bubble nucleation. In cold regions, bubbles nucleate first. However, if the mean distance between bubbles (Δ_{nuc}) is larger than the amplitude of the fluctuations δ_{rms}, then the temperature inhomogeneities are negligible and the phase transition proceeds via homogeneous nucleation (Boyanovsky et al., 2006).

2.2 Signatures of the QCD transition

A strong first–order QCD phase transition could lead to observable signatures today. That is because, during phase coexistence, the Universe is effectively unstable to gravitational collapse for all scales exceeding the mean distance between hadron or quark–hadron bubbles (e.g. Jedamzik, 1998).

There are two kinds of effects emerging from the cosmological QCD phase transition: the ones that affect scales $\lambda \leq d_{nuc}$ (e.g. formation of quark nuggets, generation of isothermal baryon fluctuations, generation of magnetic fields and gravitational waves) and the ones that affect scales $\lambda \leq R_H$ (e.g. formation of CDM clumps, modification of primordial gravitational waves, formation of PBHs).

As the first–order phase transition weakens, these effects become less pronounced. Recent results provide strong evidence that the QCD transition is a Crossover (cf. Section 2.3.3) and thus the above scenarios (and many others), which arise from a strong first–order phase transition, are ruled out (e.g. Aoki et al., 2006b). Bearing this in mind, we briefly describe some of the mentioned QCD signatures.

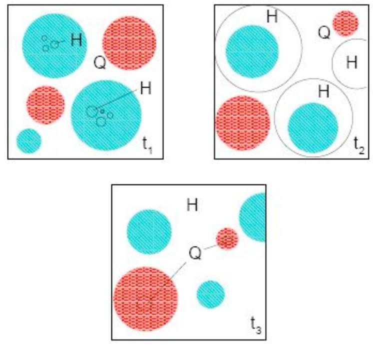

Figure 19: Sketch of a first–order QCD transition in the inhomogeneous Universe: at t_1 the coldest spots (dark gray) are cold enough to render the nucleation of hadronic bubbles (H) possible, while most of the Universe remains in the quark–gluon phase (Q). At $t_2 > t_1$ the bubbles from the cold spots have merged and have grown to bubbles as large as the fluctuation scale. Only the hot spots (light gray) are still in the QGP phase. At t_3 the transition is almost finished. The last QGP drops are found in the hottest spots of the Universe. The mean separation of these hot spots can be much larger than the homogeneous bubble nucleation separation (Ignatius & Schwarz, 2001).

Quark nuggets

Bodmer (1971) suggested the possibility that *strange quark matter* might be the ground state of *bulk matter*, instead of ^{56}Fe. The idea of strange quark matter is based on the observation that the Pauli Principle allows more quarks to be packed into a fixed volume in phase space if three instead of two flavours are available. Thus, the energy per baryon would be lower in strange quark matter than in nuclei. However, the strange quark is heavy compared with the up and down quarks, which counteracts the advantage from the Pauli Principle (e.g. Boyanovsky et al., 2006).

Witten (1984) pointed out that a separation of phases during the coexistence of the hadronic and the quark phase could gather a large number of baryons in *strange quark nuggets*. These quark nuggets could contribute to the dark matter existing today (e.g. Boyanovsky et al., 2006). However, it was realized that the quark nuggets would evaporate when the temperature is above 50 MeV (e.g. Boyanovsky et al., 2006). While cooling, the quark nuggets lose baryons unless they contain much more than 10^{44} baryons initially. The number of baryons inside an Hubble volume at the QCD epoch is $\sim 10^{50}$ which implies that d_{nuc} should have been of ~ 300 m in order to allow quark nugget formation. This is $\sim 10^4$ too large compared to the d_{nuc} suggested by recent lattice results (e.g. Schmid et al., 1999).

Isothermal baryon fluctuations

The large isothermal baryon fluctuations, induced during the separation of phases, could lead to inhomogeneous initial conditions for nucleosynthesis. The requirement is that d_{nuc} must be greater than the proton diffusion length which is ~ 3 m at the QCD epoch. This is more than 10^2 times larger than the d_{nuc} value based on lattice results (e.g. Boyanovsky et al., 2006; Schmid et al., 1999).

Gravitational waves

In principle, primordial gravitational waves (e.g. from cosmological inflation) present a clean probe of the dynamics of the early Universe, since they know only about the Hubble expansion (e.g. Boyanovsky et al., 2006). The dramatic drop in relativistic degrees of freedom during the QCD phase transition (see Section 1.10) induces a jump of 30% in the primordial spectrum of gravitational waves. Today this jump might be, in principle, observed at $\sim 10^{-8}$ Hz for pulsar timing (e.g. Boyanovsky et al., 2006).

In Figure 20 we show the energy density, per logarithmic frequency interval Ω_{gw}, for primordial gravitational waves from the QCD transition. The length scales that cross into the horizon after the transition (left hand side of Figure 20) are unaffected, whereas modes that cross the horizon before the transition are damped by an additional factor ≈ 0.7. The modification of the differential spectrum has been calculated for a first–order Bag Model and a Crossover QCD transition. In both cases the step extends over one decade in frequency. Notice that the detailed form of the jump is almost independent from the order of the transition (e.g. Boyanovsky et al., 2006). In Figure 20 it is also indicated the frequency range in which limits on Ω_{gw} have been reported from pulsar timing residuals. Unfortunately, todays technology does not enable us to detect primordial gravitational waves at frequencies around 10^{-7} Hz, because their expected amplitude is too small (e.g. Boyanovsky et al., 2006).

QCD balls

If *axions* existed and if the reheating scale after inflation is above the *Peccei-Quinn*[26] scale, collapsing axion domain walls could trap a large number of quarks. At some point the collapse would be stopped by the Fermi pressure of the quarks, which would then settle in a colour superconducting phase. This process takes place during the QCD transition, but does not require a first–order transition, contrary to the idea of strange quark nuggets (e.g. Schwarz, 2003).

2.3 QCD models

There are three main models often used in the study of the QCD transition: the *Bag Model*, the *Lattice Fit* and the *Crossover*. Although recent results provide

[26]In particle physics, the *Peccei–Quinn theory* is, perhaps, one of the most famous proposed solution to the *Strong CP problem* (the puzzling question: why QCD does not seem to break the CP–symmetry?), involving hypothetical particles called axions.

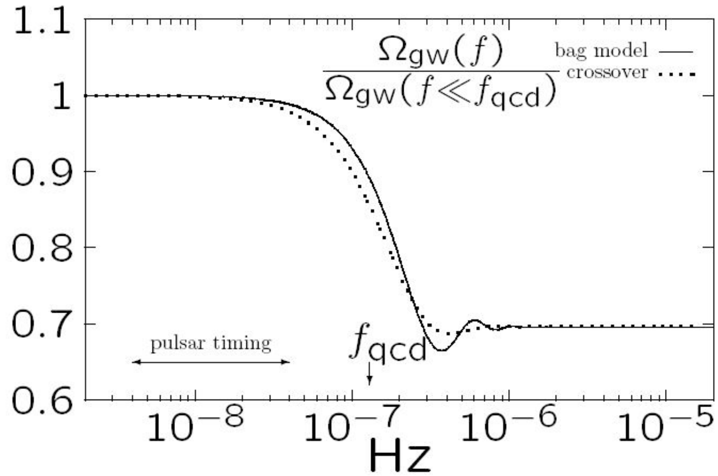

Figure 20: The modification of the energy density, per logarithmic frequency (f) interval, for primordial gravitational waves from the QCD transition (e.g. Boyanovsky et al., 2006), according to two models (Bag model and crossover). It is also indicated the frequency range in which limits on Ω_{gw} have been reported from pulsar timing residuals.

strong evidence that the QCD transition is just a smooth crossover (Aoki et al., 2006b) we will describe, in the following sections, all three models.

In the context of PBH production, we are particularly interested on the duration of the transition and on the behaviour of the sound speed for each case. In Figure 21 we show the typical curves for the sound speed during the QCD transition as a function of the scale factor R for the three models. We next detail the behaviour shown in Figure 21 for each model.

2.3.1 The Bag Model

If the transition from $T > T_c$ to $T < T_c$ is continuous but sharp, as evidenced by the lattice data (cf. Figures 23 and 24), the behaviour may not be too different from an actual transition which may be modelled by a simpler EoS which would allow an analytic treatment (e.g. Boyanovsky et al., 2006).

The MIT Bag Model provides a semiphenomenological description of an EoS that features a quark–hadron transition (e.g. Boyanovsky et al., 2006). It gives a simple parametrization for the pressure p, energy density ρ and entropy s at the QCD scale. The Bag Model represents the short distance–dynamics by an ideal gas of quarks and gluons and the long–distance confinement effects by a constant negative contribution to the pressure, the *bag constant* B (e.g. Schwarz, 2003; Schmid et al., 1999).

The simplest version of the model considers the thermodynamics in two

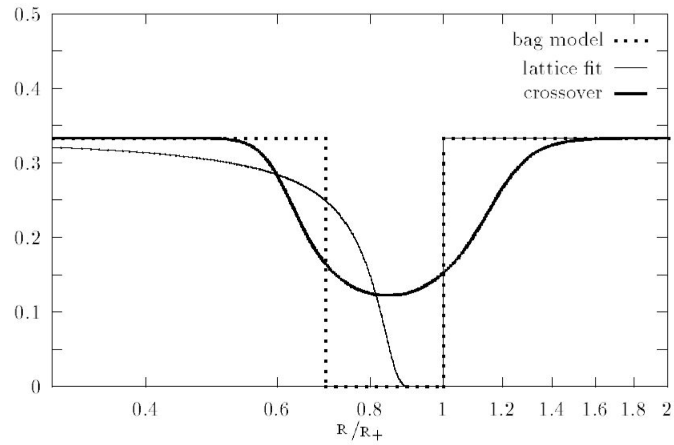

Figure 21: The behaviour of the sound speed (equation 14) during the QCD transition as a function of the scale factor R (adapted from Schwarz, 2003). During a first–order transition (Lattice Fit and Bag Model) the sound speed vanishes, suddenly rising, at the end of the transition ($R = R_+$), to the original value $1/\sqrt{3}$.

different regions: a high temperature region ($T > T_c$) where we have a gas of massless quarks and gluons (QGP) and a low temperature region ($T < T_c$) where we have a gas of free massless pions (HG). At $T = T_c$ quarks, gluons and pions coexist in equilibrium at constant pressure and temperature (e.g. Boyanovsky et al., 2006).

The pressure for the high temperature region, which corresponds to a QGP is given, for vanishing chemical potential ($\mu = 0$), by (e.g. Schmid et al., 1999)

$$p_{QGP}(T) = p_{QGP}^{ideal}(T) - B \tag{123}$$

where we have, considering that gluons and existing quarks are effectively massless at $T \approx T_c$, that (e.g. Schmid et al., 1999)

$$p_{QGP}^{ideal}(T) = \frac{\pi^2}{90} g_{QGP} T^4 \tag{124}$$

where g_{QGP} corresponds to the number of degrees of freedom of the QGP at the beginning of the transition (see Section 1.10). The low temperature region, which corresponds to an HG, can be modeled as a gas of massless pions with (e.g. Schmid et al., 1999)

$$p_{HG}(T) = \frac{\pi^2}{90} g_{HG} T^4 \tag{125}$$

where g_{HG} represents the number of degrees of freedom of the HG at the end of the transition (see Section 1.10).

Taking into account the pressure coexistence condition (cf. equation 116) we obtain, from equations (123) and (125), the following expression for the bag constant (e.g. Cardall & Fuller, 1998; Schmid et al., 1999)

$$B = \frac{\pi^2}{90}\left(g_{QGP} - g_{HG}\right) T_c^4. \tag{126}$$

The energy density ρ and entropy density s for the Bag Model follow from equations (11), (12) and (123). In the case of the energy density we have, for the QGP phase (e.g. Schmid et al., 1999)

$$\rho_{QGP}(T) = \rho_{QGP}^{ideal}(T) + B \tag{127}$$

with

$$\rho_{QGP}^{ideal}(T) = \frac{\pi^2}{30} g_{QGP} T^4 \tag{128}$$

and for the HG phase we get (e.g. Boyanovsky et al., 2006)

$$\rho_{HG}(T) = \frac{\pi^2}{30} g_{HG} T^4. \tag{129}$$

The evolution of the average energy density ρ as a function of time during a first–order QCD transition is given by (Jedamzik, 1997)

$$\rho(t) = \left(\frac{R(t_-)}{R(t)}\right)^3 \left(\rho_{QGP}(T_c) + \frac{1}{3}\rho_{HG}(T_c)\right) - \frac{1}{3}\rho_{HG}(T_c). \tag{130}$$

With the help of equations (126), (127), (128), and (129) this becomes

$$\rho(t) = \frac{1}{3}\frac{\pi^2}{30} T_c^4 \left[4 g_{QGP} \left(\frac{R(t_-)}{R(t)}\right)^3 - g_{HG}\right]. \tag{131}$$

In the case of the entropy density, we have, for the QGP (e.g. Schmid et al., 1999; Jedamzik, 1997)

$$s_{QGP}(T) = s_{QGP}^{ideal}(T) = \frac{2\pi^2}{45} g_{QGP} T^3 \tag{132}$$

and for the HG

$$s_{HG}(T) = s_{HG}^{ideal}(T) = \frac{2\pi^2}{45} g_{HG} T^3. \tag{133}$$

In this model, the entropy, jumps at the critical temperature T_c. This is due to the fact that on the coexistence line both, pressure and temperature, are constant. This jump in the entropy (which is depicted in Figure 22), means that the Bag Model leads to a first–order phase transition with a latent heat (equation 112, e.g. Boyanovsky et al., 2006; Schmid et al., 1999)

$$l = T_c \Delta s = \frac{2\pi^2}{45}(g_{QGP} - g_{HG}) T_c^4 = 4B. \tag{134}$$

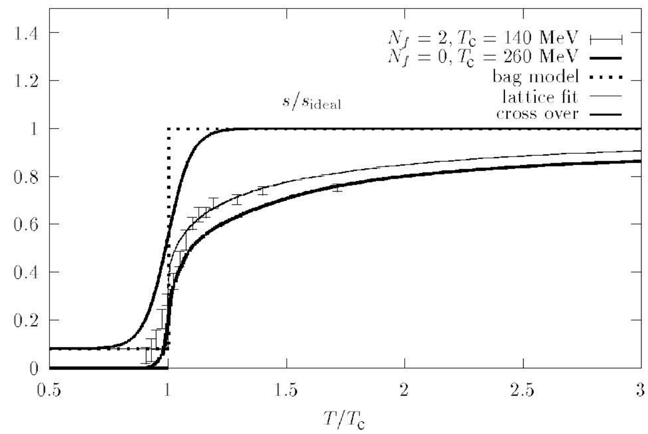

Figure 22: The entropy density of hot QCD relative to the entropy density of an ideal QGP for the Lattice Fit QCD data ($N_f = 0$ and $N_f = 2$ quark flavours), Bag Model, and for a smooth Crossover (adapted from Schmid et al., 1999).

It is useful to write a single expression for the entropy on the Bag Model as (Schwarz, 1998)

$$s(T) = \frac{2\pi^2}{45} g_{HG} T^3 \left[1 + \frac{\Delta g}{g_{HG}} \Theta(T - T_c) \right] \tag{135}$$

where $\Delta g = g_{QGP} - g_{HG}$ and the function Θ is defined as (Schwarz, 1998)

$$\Theta(T - T_c) = \begin{cases} 0 & \text{if } T < T_c \\ 1 & \text{if } T > T_c \end{cases} \tag{136}$$

The typical value for the bag constant is given by $B^{1/4} \sim 200$ MeV (e.g. Boyanovsky et al., 2006). Inserting $B^{1/4} = 200$ MeV into equation (134) one gets, considering two quark flavours ($g_{QGP} = 51.25$, cf. Section 1.10) and three massless pions ($g_{HG} = 17.25$, cf. Section 1.10), that $T_c \approx 145$ MeV, which is not too far from the lattice result $T_c \sim 170$ MeV (e.g. Boyanovsky et al., 2006, Section 2.3.2).

In the Bag Model the sound speed stays at $c_s^2 = 1/3$ before and after the transition and vanishes during the transition (e.g. Schwarz, 2003) as can be inferred from Figure 21.

2.3.2 Lattice Fit

Lattice Gauge Theory (LGT) is the study of *Gauge Theories* on a space–time that as been discretized onto a lattice. One hopes that performing simulations on larger and larger lattices, while making the lattice spacing, a, smaller and smaller, the behaviour of the continuum theory can be recovered. In the case of the QCD transition the critical temperature T_c is calculated in the chiral limit using $T = (N_t a)^{-1}$ where N_t represents the temporal lattice size (e.g. Ejiri, 2007).

The only known first principle method to study QCD non–perturbatively in a wide temperature range is LGT (e.g. Boyanovsky et al., 2006). Lattice QCD discretises the Lagrangian on a four–dimensional lattice and extrapolates the results to vanishing lattice spacing (e.g. Aoki et al., 2006a). There are some QCD results and model calculations to determine the order of the transition at $\mu = 0$ and $\mu \neq 0$ for different fermionic contents. Unfortunately, none of these approaches can give an unambiguous answer on the order of the transition for physical values of the quark masses. The only known systematic technique which could give a final answer is the Lattice Fit (e.g. Aoki et al., 2006b).

It has been established that lattice QCD without dynamical quarks exhibits a thermal first–order phase transition at a critical temperature of $T_c \approx 270$ MeV. For dynamical quarks, lattice QCD calculations provide a range of estimates for T_c. In the case of two–flavour QCD, $T_c \approx 175$ MeV, whereas for three–flavour QCD, $T_c \approx 155$ MeV, almost independently of the quark mass. For the most interesting case of two light quark flavours (up and down) and the more massive strange quark, a value of $T_c \approx 170$ MeV has been obtained recently. We will adopt a transition temperature $T_c = 170$ MeV, bearing in mind that the systematic uncertainty is probably of the order 10 MeV (e.g. Boyanovsky et al., 2006).

In recent years particular attention has been devoted on determining the order of the QCD phase transition and the correct value of T_c. For massless quarks, the theoretical expectation is a second order transition for two quark flavours and a first–order transition for three and more quark flavours. On the lattice, for two light quarks the results are inconclusive. The consensus that seems to be emerging is that for the physical masses of two light (up and down) and one heavier (strange) quark there is a sharp crossover between a high temperature gas of quark and gluon quasiparticles and a low temperature hadronic phase without any thermodynamic discontinuities. This is displayed in Figure 23 which summarizes results from LGT for the energy density and pressure (both divided by T^4 to compare to a free gas of massless quarks and gluons) as a function of T/T_c. Notice the sharp decrease in the energy density and pressure at $T = T_c$ (e.g. Boyanovsky et al., 2006).

A strong decrease on the sound speed, already above Tc, has been observed in lattice QCD with $c_s^2(T_c) \approx 0.1$. Figure 24 displays the sound speed for quenched QCD, clearly showing a dramatic decrease for $T < 2T_c$ and approaching $1/\sqrt{3}$ for $T \gg T_c$ in agreement with an ultrarelativistic gas of quarks and gluons (e.g. Boyanovsky et al., 2006).

The high temperature behaviour is not quite given by the Stephan–Boltzmann law (cf. Figure 23) suggesting that even at high temperatures the plasma is not described by free quarks and gluons up to temperatures $T \sim 4T_c \sim 700$ Mev (e.g. Boyanovsky et al., 2006).

We need a suitable analytic representation for the Lattice QCD data. Schmid

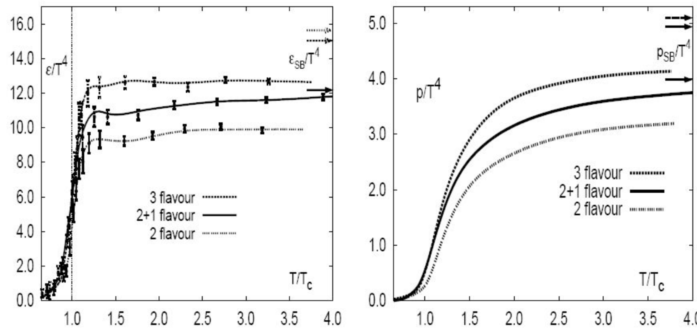

Figure 23: The energy density ε and pressure p (both divided by T^4 to compare to a free gas of massless quarks and gluons) as a function of T/T_c for the QCD transition in an LGT. The arrows mark the Stephan-Boltzmann result (Karsch et al., 2000; Ejiri, 2000).

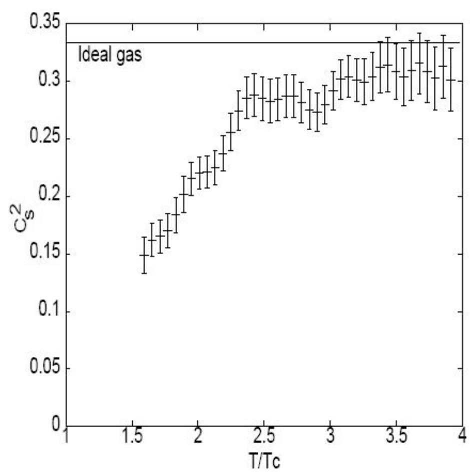

Figure 24: The square speed of sound c_s^2 as a function of T/T_c for the QCD transition in a LGT (Gupta, 2003).

et al. (1999) had considered to fit the entropy density with

$$s(T) = \frac{2\pi^2}{45}T^3 \left[g_{HG} + \Delta g \Theta(T - T_c) \left(R_L + (1 - R_L) \left(1 - \frac{T_c}{T} \right)^{\gamma} \right) \right] \quad (137)$$

which is valid for $T > T_c$. Here Θ and R_L are given by equations (136) and (114) respectively, $\Delta g = g_{QGP} - g_{HG}$ and a good fit is obtained for $0.3 < \gamma < 0.4$. We consider, for the rest of the text, $\gamma = 1/3$. In Figure 22 we show the curve of $s(T)$ (labeled 'lattice fit').

The other thermodynamic quantities (for $T > T_c$) can be derived from equation (137). Below T_c again is valid the equation for an ideal HG as in the case of the Bag Model (Schmid et al., 1999).

Inserting the entropy fit given by equation (137) into equation (14) we obtain (Schmid et al., 1999)

$$c_s^2 \propto \left(1 - \frac{T_c}{T} \right)^{1-\gamma} \quad (138)$$

valid for $T \geq T_c$. In order to recover $c_s^2 = 1/3$ when $T \gg T_c$ we consider

$$c_s^2 = \frac{1}{3} \left(1 - \frac{T_c}{T} \right)^{1-\gamma}. \quad (139)$$

For $T = T_c$ we have $c_s^2 = 0$ and for $T < T_c$ we get, once again, $c_s^2 = 1/3$. In Figure 25 we show expression (139), as well as the results obtained for quenched QCD (Figure 24), for $T \geq T_c$ with $T_c = 170$ MeV. The analytic approach given by equation (139) and the numerical results obtained from quenched QCD (Figure 24) both show a similar behaviour, in particular, when T gets below $\sim 2T_c$.

It is useful to have also an expression for c_s^2 as a function of time t. Inserting expression (78) into expression (139) we obtain

$$c_s^2(t) = \frac{1}{3} \left(1 - \frac{R(t)}{R(t_-)} \right)^{1-\gamma} \quad (140)$$

valid for $t \leq t_-$ where t_- corresponds to the beginning of the phase transition. Considering equation (86) or, alternatively, equation (71), we may write equation (140) in the form

$$c_s^2(t) = \frac{1}{3} \left[1 - \left(\frac{t}{t_-} \right)^{1/2} \right]^{1-\gamma}. \quad (141)$$

2.3.3 Crossover

Recent results provide strong evidence that the QCD transition is a Crossover, at least using staggered fermions, i.e., including fermionic fields in LGT (Aoki et al., 2006a,b).

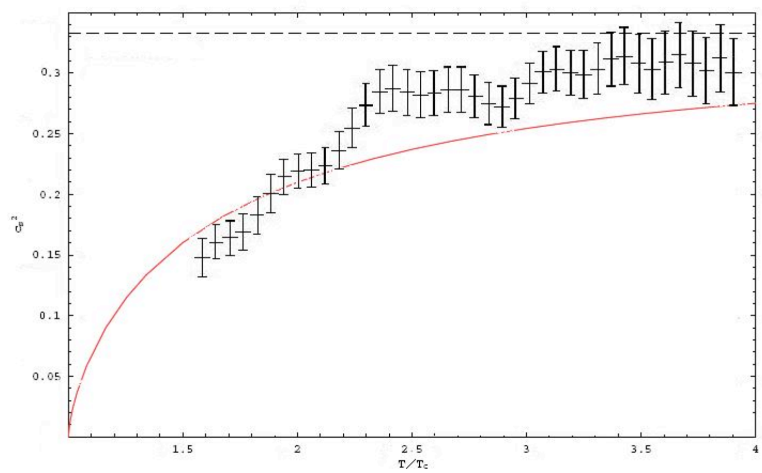

Figure 25: The behaviour of the sound speed c_s^2 as a function of T/T_c during the QCD transition according to the Lattice model (solid line – equation 139) and the numerical results obtained from quenched QCD. The dashed line represents the ideal gas case, i.e., $c_s^2 = 1/3$. When $T = T_c$ the sound speed vanishes.

The value of T_c for the QCD Crossover is not unique. Different observables lead to different numerical T_c values even in the continuum and thermodynamic limit. This is a well–known phenomenon on the water–vapour phase diagram. The peak of the renormalized *chiral susceptibility* predicts $T_c = 151$ MeV, whereas T_c based on the *strange quark number susceptibility* and *Polyakov loops* result in 175 MeV and 176 MeV, respectively (Aoki et al., 2006b). On Table 16 we summarize the results obtained by Aoki et al. (2006b) and Bernard et al. (2005), considering three quark flavours.

The entropy density for a Crossover can be written as (e.g. Schmid et al.,

Table 16: The critcal temperature T_c for the QCD Crossover for different observables.

T_c (MeV)	Reference	Observable
151	Aoki et al. (2006b)	Chiral susceptibility
169	Bernard et al. (2005)	Chiral susceptibility
175	Aoki et al. (2006b)	Strange quark number susceptibility
176	Aoki et al. (2006b)	Polyakov loops

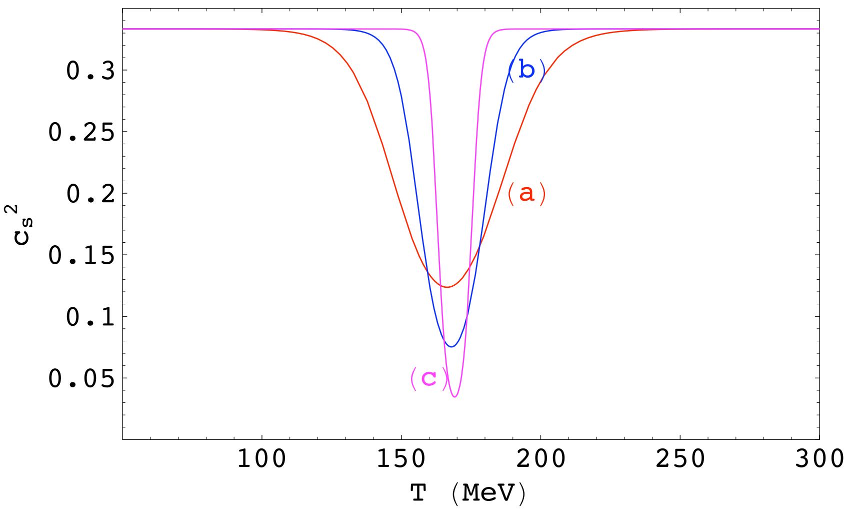

Figure 26: The sound speed $c_s^2(T)$ for the QCD Crossover with $T_c = 170$ MeV and different values for the parameter ΔT: (a) $\Delta T = 0.1T_c$, (b) $\Delta T = 0.05T_c$ and (c) $\Delta T = 0.02T_c$. Notice that the sound speed decreases around T_c but does not reach zero (with the exception of the limiting case $\Delta T \longrightarrow 0$ – see Figure 27).

1999; Schwarz, 1998)

$$s(T) = \frac{2\pi^2}{45} g_{HG} T^3 \left[1 + \frac{1}{2}\frac{\Delta g}{g_{HG}}\left(1 + \tanh\left(\frac{T - T_c}{\Delta T}\right)\right)\right] \qquad (142)$$

where $\Delta g = g_{QGP} - g_{HG}$ and the value of ΔT must be choosen in order to fit the modeled results. When $\Delta T \longrightarrow 0$ we recover the Bag Model, i.e., a first–order phase transition (Section 2.3.1). Both models coincide at temperatures far away from T_c (Schwarz, 1998). QCD Lattice data indicate that $0 \leq \Delta T < 0.1T_c$ (e.g. Schmid et al., 1999; Bernard et al., 1997).

The other thermodynamic quantities can be derived from equation (142). For example, inserting the entropy (142) into equation (14) we obtain, for the sound speed during a QCD Crossover, the following result

$$c_s^2(T) = \left[3 + \frac{\Delta g T \mathrm{sech}\left(\frac{T-T_c}{\Delta T}\right)^2}{\Delta T\left(g_{HG} + g_{QGP} + \Delta g \tanh\left(\frac{T-T_c}{\Delta T}\right)\right)}\right]^{-1} . \qquad (143)$$

In Figure 26 we show the curve for c_s^2 as a function of temperature with $T_c = 170$ MeV and with ΔT assuming different values. As it was already mentioned, when $\Delta T \longrightarrow 0$ we recover the Bag Model sound speed profile. Notice that, for a Crossover, the speed of sound decreases but does not reach zero. The minimum value for the sound speed is attained for $T \approx T_c$. Thus, considering $T = T_c$ in

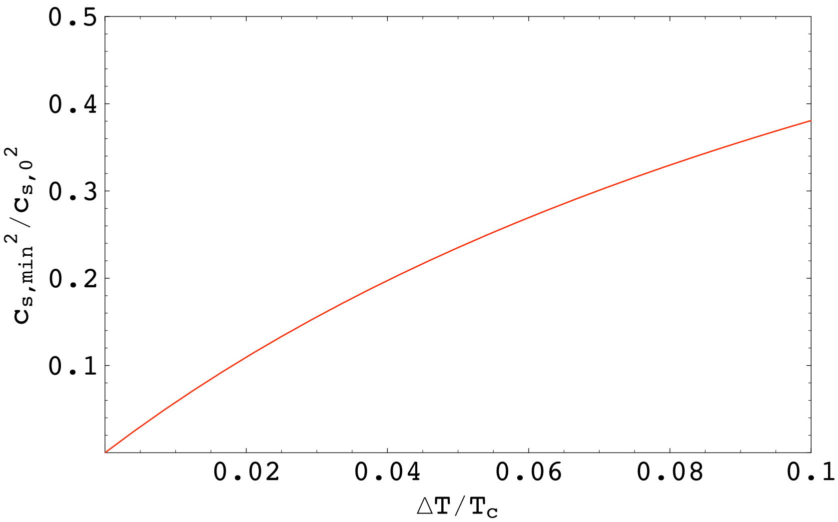

Figure 27: The minimum value attained by the sound speed $c^2_{s,min}$ as a function of the parameter ΔT for the QCD Crossover (see equation 144).

equation (143) we obtain the following expression giving an approximate value for the minimum sound speed during a QCD Crossover

$$c^2_{s,min} \approx \left[3 + \frac{g_{QGP} - g_{HG}}{\frac{\Delta T}{T_c}(g_{QGP} + g_{HG})} \right]^{-1} . \tag{144}$$

In Figure 27 we have the curve for $c^2_{s,min}$ as a function of the ΔT parameter when $T_c = 170$ MeV. Notice that when $\Delta T = 0$ we have $c^2_{s,min} = 0$ and when $\Delta T = 0.1 T_c$ we have $c^2_{s,min} \approx 0.38 c^2_{s,0} \approx 0.13$ ($c^2_{s,0} = 1/3$ is the sound speed for an ideal gas).

2.4 The duration of the QCD transition

If one wants to study how a given fluctuation behaves during the QCD phase transition then it is of crucial importance to know the duration of the transition. This means that, if we want to perform numerical integrations then we need to define a specific beginning $t = t_-$ and a specific end $t = t_+$ to the QCD transition. Here t_- and t_+ are the limits for the time interval during which the speed of sound vanishes. This is aplicable in the case of a first–order transition (Bag Model and Lattice Fit). In the case of a Crossover we will define an effective duration instead.

Taking into account that the temperature of the Universe during the QCD phase transition is T_c we can obtain, with the help of equation (78) a numerical

Table 17: The value of ΔR (cf. equation 148) as a function of the number of degrees of freedom for the Bag Model ($R_l = 1$) and for the Lattice Fit ($R_l = 0.2$). $\Delta g = g_{QGP} - g_{HG}$ with $g_{QGP} = 61.75$ (51.25) with (without) strange quarks and $g_{HG} = 21.25$ (17.25) with (without) kaons (cf. Section 1.10).

R_l	g_{HG}	g_{QGP}	Δg	ΔR
1	17.25	51.25	34	1.44
0.2	17.25	51.25	34	1.12
1	21.25	61.75	40.5	1.43
0.2	21.25	61.75	40.5	1.11

value for $R(t_+)$ (i.e. the value of the scale factor at the end of the transition)

$$R(t_+) = \frac{T_0}{T_c}. \tag{145}$$

On the other hand, equation (70) or equation (86), becomes, for $t = t_+$

$$R(t_+) = \exp\left(c\sqrt{\frac{\Lambda}{3}}(t_{SN} - t_0)\right)\left(\frac{t_{eq}}{t_{SN}}\right)^{2/3}\left(\frac{t_+}{t_{eq}}\right)^{1/2}. \tag{146}$$

Inserting equation (145) into equation (146) we obtain for the instant when the transition ends

$$t_+ = t_{SN}\left(\frac{t_{eq}}{t_{SN}}\right)^{-1/3}\exp\left(-2c\sqrt{\frac{\Lambda}{3}}(t_{SN} - t_0)\right)\left(\frac{T_0}{T_c}\right)^2. \tag{147}$$

The evolution of the scale factor during the QGP and HG coexistence in a first–order QCD transition, i.e., during the $c_s^2 = 0$ part, is determined by the entropy conservation (e.g. Schwarz, 2003; Schmid et al., 1997)

$$\Delta R = \frac{R(t_+)}{R(t_-)} = \left(\frac{s(t_-)}{s(t_+)}\right)^{1/3} = \left(1 + R_l\frac{\Delta g}{g_{HG}}\right)^{1/3} \tag{148}$$

where R_l is given by equation (114), $\Delta g = g_{QGP} - g_{HG}$, $g_{QGP} = 61.75$ (51.25) with (without) strange quarks and $g_{HG} = 21.25$ (17.25) with (without) kaons (cf. Section 1.10). Inserting these values into equation (148) it turns out that, in the case of a Bag Model ($R_l = 1$), the Universe expands by a factor of $\Delta R \approx 1.44$ until all QGP has been converted into the HG, whereas for a Lattice Fit ($R_l = 0.2$) the Universe expands by a factor of $\Delta R \approx 1.1$ (see e.g. Schwarz, 2003, and Table 17 for more details).

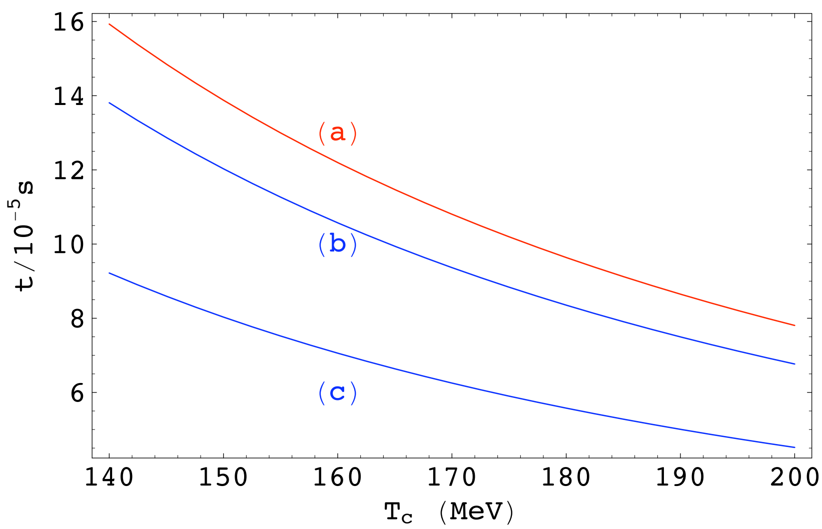

Figure 28: The beginning (t_-) and the end (t_+) of the QCD phase transition as a function of the transition temperature T_c: (a) t_+, valid for both the Bag Model and the Lattice Fit; (b) t_- for the Lattice Fit and (c) t_- for the Bag Model.

When $t = t_-$ equation (70) becomes

$$R(t_-) = \exp\left(c\sqrt{\frac{\Lambda}{3}}(t_{SN} - t_0)\right)\left(\frac{t_{eq}}{t_{SN}}\right)^{2/3}\left(\frac{t_+}{t_{eq}}\right)^{1/2}\left(\frac{t_-}{t_+}\right)^{2/3} \tag{149}$$

where we have considered $n_{qcd} = 2/3$. From equations (146) and (149) we obtain

$$t_- = \frac{t_+}{\sqrt{\Delta R^3}}. \tag{150}$$

For example, when $T_c = 170$ MeV we obtain, from equation (147), the value $t_+ \approx 1.08 \times 10^{-4}$ s which is valid (according to the assumptions made in the preceding paragraphs) for both the Bag Model and the Lattice Fit. Inserting this value into equation (150) one obtains $t_- \approx 6.25 \times 10^{-5}$ s in the case of the Bag Model and $t_- \approx 9.37 \times 10^{-5}$ s in the case of the Lattice Fit. In Figure 28 we present the curves for t_+ and t_- as functions of the critical temperature T_c.

For the Crossover case we consider that the sound speed minimum value is attained for $t \approx t_+$ (corresponding to $T \approx T_c$). During the QCD Crossover the Universe continues to be radiation–dominated with the scale factor given by equation (86). Inserting equation (86) into equation (78) we obtain an expression for the temperature T as a function of the time t valid for the QCD Crossover:

$$T(t) = T_0\left[\exp\left(c\sqrt{\frac{\Lambda}{3}}(t_{SN} - t_0)\right)\left(\frac{t_{eq}}{t_{SN}}\right)^{2/3}\left(\frac{t}{t_{eq}}\right)^{1/2}\right]^{-1}. \tag{151}$$

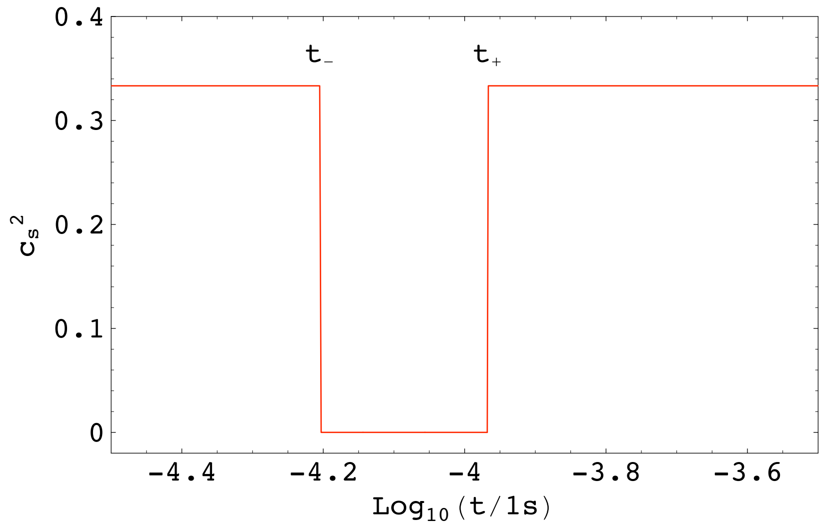

Figure 29: The sound speed $c_s^2(t)$ for the QCD phase transition according to the Bag Model with $T_c = 170$ MeV. During the coexistence phase, which occurs between the instants $t_- = 6.25 \times 10^{-5}$ s and $t_+ = 1.08 \times 10^{-4}$ s, the sound speed drops to zero.

On the Bag Model and Lattice Fit cases, the temperature remains constant ($T = T_c$) for a while. The same does not occur during a Crossover where the temperature continues to decrease with time. Inserting expression (151) into equation (143) we obtain, for the speed of sound during the QCD Crossover, the following expression

$$c_s^2(t) = \left[3 + \frac{\Delta g T(t) \mathrm{sech}\left(\frac{T(t)-T_c}{\Delta T}\right)^2}{\Delta T \left(g_{HG} + g_{QGP} + \Delta g \tanh\left(\frac{T(t)-T_c}{\Delta T}\right)\right)} \right]^{-1} . \tag{152}$$

We are now able to present the sound speed profile for the QCD phase transition for a given temperature T_c as a function of time. In Figure 29, 30 and 31 we show the curve $c_s^2(t)$ for, respectively, the Bag Model, the Lattice Fit and the Crossover for a QCD temperature of $T_c = 170$ MeV.

According to the Lattice Fit the sound speed decreases until it vanishes at some instant t_- (cf. Figure 30). It is useful to know not only the interval during which $c_s = 0$, but also, the interval during which c_s^2 makes its way down from 1/3 to zero.

Therefore, we define $T_1 > T_c$ as the temperature for which c_s^2 equals 95% of its 'background' value: $c_{s,0}^2 = 1/3$. This corresponds to some instant of time $t_1 < t_-$. From equation (139), with $T_c = 170$ MeV and $\gamma = 1/3$, one obtains $T_1 \approx 2296$ MeV $\approx 13.5 T_c$. Similarly, from equation (141), with $t_- = 9.37 \times 10^{-5}$ s and $\gamma = 1/3$ one obtains $t_1 \approx 5.1 \times 10^{-7}$ s.

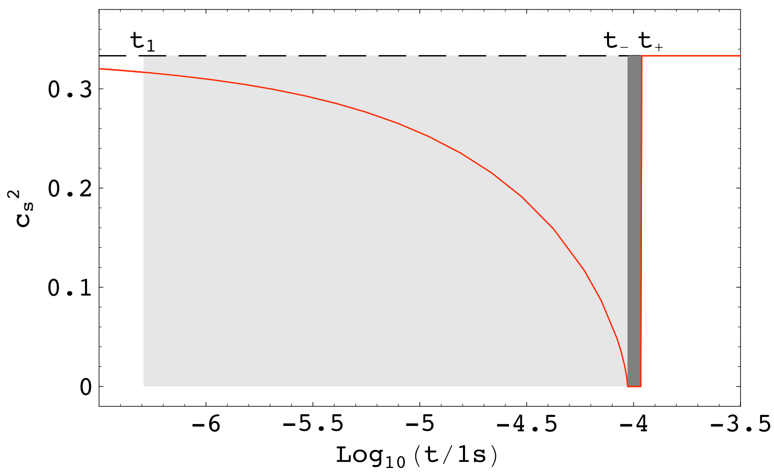

Figure 30: The sound speed $c_s^2(t)$ for the QCD phase transition according to the Lattice Fit with $T_c = 170$ MeV. During the coexistence phase, which occurs between the instants $t_- = 9.37 \times 10^{-5}$ s and $t_+ = 1.08 \times 10^{-4}$ s the sound speed drops to zero (dark gray zone). For $t_1 = 5.1 \times 10^{-7}$ s the sound speed equals 95% of its 'background' value. The dashed line represents the ideal gas case for which $c_s^2 = 1/3$.

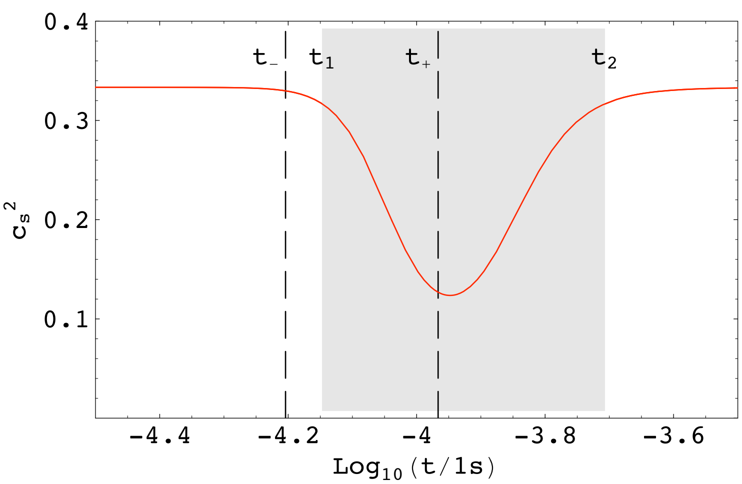

Figure 31: The sound speed $c_s^2(t)$ for the QCD phase transition in the case of a Crossover with a reference temperature $T_c = 170$ MeV and $\Delta T = 0.1T_c$. The dashed lines represent, for reference, the location of the first–order phase transition according to the Bag Model ($t_- = 6.25 \times 10^{-5}$ s, $t_+ = 1.08 \times 10^{-4}$ s). Between the instants $t_1 \approx 7.1 \times 10^{-5}$ s and $t_2 \approx 1.96 \times 10^{-4}$ s the sound speed stays below 95% of its 'background' value ($c_{s,0}^2 = 1/3$).

Table 18: The width of the QCD Crossover in terms of temperature as a function of the parameter ΔT (cf. equation 143) when $T_c = 170$ MeV. T_1 represents the temperature when the sound speed gets less than 95% of its 'background' value 1/3 and T_2 represents the temperature when the sound speed reaches, once again, 95% of 1/3 ($T_2 < T_c < T_1$). The width of the QCD Crossover is given by $T_1 - T_2$.

$\frac{\Delta T}{T_c}$	T_2 (MeV)	T_1 (MeV)	$T_1 - T_2$ (MeV)
0.01	163	176	13
0.02	158	180	22
0.03	153	185	32
0.04	149	189	40
0.05	144	192	48
0.06	140	196	56
0.07	137	199	62
0.08	133	203	70
0.09	130	206	76
0.10	126	209	83

For the QCD Crossover we define an effective duration as the interval for which the sound speed stays below 95% of its 'background' value $c_{s,0}^2 = 1/3$. We want to determine the temperatures T_1 and T_2 such that

$$c_s^2(T_1) = c_s^2(T_2) = 0.95c_{s,0}^2, \quad T_2 < T_c < T_1. \tag{153}$$

The duration or width of the QCD Crossover in terms of temperature is, then, given by $T_2 - T_1$. With the help of equation (143) we have obtained the values for T_1 and T_2 for different values of the parameter ΔT for the case $T_c = 170$ MeV. The results are those shown on Table 18 and Figure 32.

It is useful to have also the width of the QCD Crossover in terms of time. In that case, the transition width will be given by $t_2 - t_1$ with the instants t_1 and t_2 satisfying the condition

$$c_s^2(t_1) = c_s^2(t_2) = 0.95c_{s,0}^2 \quad , t_1 < t_c < t_2 \tag{154}$$

where $t_c = t_+$. With the help of equation (152) we obtained the values for t_1 and t_2 for different values of the parameter ΔT for the case $t_c = 1.08 \times 10^{-4}$ s corresponding to $T_c \approx 170$ MeV. The results are those shown on Table 19 and Figure 33. On Table 20 we present a sum up of the results for the duration of the QCD phase transition according to the different models.

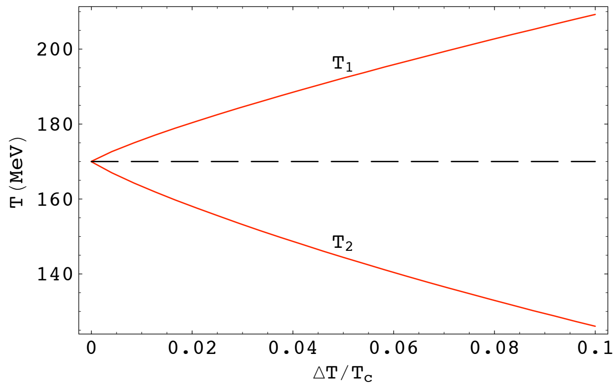

Figure 32: The width of the QCD Crossover in terms of temperature as a function of the parameter ΔT (cf. equation 143) when $T_c = 170$ MeV (dashed line). Here, T_1 represents the temperature when the sound speed gets less than 95% of its 'background' value (1/3) and T_2 represents the temperature when the sound speed reaches, once again, 95% of its 'background' value. Thus, the width of the QCD Crossover, for a given ΔT, is given by $T_1 - T_2$.

Table 19: The width of the QCD Crossover in terms of time as a function of the parameter ΔT (cf. equation 152) when $t_c = 1.08 \times 10^{-4}$ s corresponding to $T_c \approx 170$ MeV. The instant t_1 represents the time when the sound speed gets less than 95% of its 'background' value (1/3) and t_2 represents the instant when the sound speed reaches, once again, 95% of its 'background' value. The time width of the QCD Crossover is given by $t_2 - t_1$.

$\frac{\Delta T}{T_c}$	$t_1(\times 10^{-5}$ s)	$t_2(\times 10^{-5}$ s)	$t_2 - t_1(\times 10^{-5}$ s)
0.01	10.1	11.7	1.6
0.02	9.6	12.5	2.9
0.03	9.2	13.3	4.1
0.04	8.8	14.1	5.3
0.05	8.5	15.0	6.5
0.06	8.1	15.8	7.7
0.07	7.9	16.7	8.8
0.08	7.6	17.7	10.1
0.09	7.4	18.6	11.2
0.10	7.1	19.6	12.5

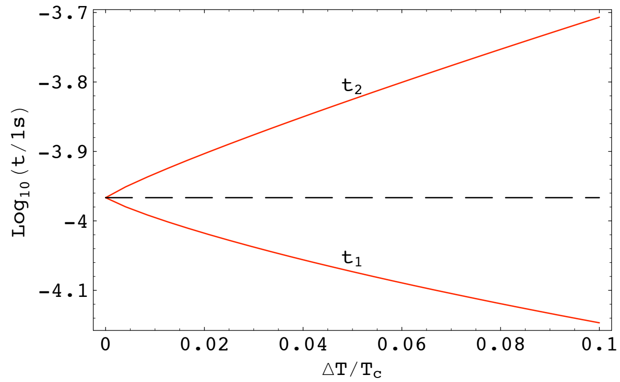

Figure 33: The width of the QCD Crossover in terms of time as a function of the parameter ΔT (cf. equation 152) when $t_c = 1.08 \times 10^{-4}$ s (dashed line) corresponding to $T_c \approx 170$ MeV. Here, t_1 represents the instant when the sound speed gets less than 95% of its 'background' value (1/3) and t_2 represents the instant when the sound speed reaches, once again, 95% of its 'background' value. Thus, the width of the QCD Crossover, for a given ΔT, is given by $t_2 - t_1$.

Table 20: The width of the QCD phase transition according to the Bag Model, Lattice Fit and Crossover when $T_c = 170$ MeV. The sound speed vanishes in the interval $t_- < t < t_+$ and is below 95% of its 'background' value $c_{s,0}^2 = 1/3$ in the interval $t_1 < t < t_2$. Here Δt represents the interval during which the sound speed value is less than 95% of 1/3.

Model	$t_1(\times 10^{-5}$ s)	$t_-(\times 10^{-5}$ s)	$t_+(\times 10^{-5}$ s)	$t_2(\times 10^{-5}$ s)	$\Delta t(\times 10^{-5}$ s)	$\frac{\Delta t}{\Delta t_{BAG}}$
Bag	–	6.25	10.8	–	4.6	1
Lattice	0.051	9.37	10.8	–	10.7	2.33
Crossover ($\Delta T = 0.01 T_c$)	10.1	–	–	11.7	1.6	0.35
Crossover ($\Delta T = 0.05 T_c$)	8.5	–	–	15.0	6.5	1.41
Crossover ($\Delta T = 0.1 T_c$)	7.1	–	–	19.6	12.5	2.72

3 The EW phase transition

The first phase transition predicted by the SMPP is the *EW phase transition* which occurs at a temperature $T_{EW} \sim 100$ GeV and at a time scale $t_{EW} \sim 10^{-10}$ s (e.g. Unsöld & Bascheck, 2002). At this temperature, which corresponds to an energy scale of the order of the masses of the Z^0 and $W^{\pm}$ vector bosons (cf. Table 6), the weak interactions become short ranged after a symmetry breaking phase transition. For $T < T_{EW}$ the Z^0 and $W^{\pm}$ vector bosons acquire masses through the Higgs mechanism while the photon remains massless, corresponding to the unbroken symmetry of the electromagnetic interactions (e.g. Boyanovsky et al., 2006).

The value of T_{EW} was estimated considering that the restoration of symmetry would happen when $T \sim G_F^{-1/2}$ where $G_F \approx 1.16637 \times 10^{-5}$ GeV^{-2} (e.g. Stuart, 1999) is the *Fermi coupling constant* (e.g. Gynther, 2006).

In the EW standard model (*Glashow–Salam–Weinberg model*) the Higgs field is responsible for the dynamical mass generation via spontaneous symmetry breaking. At sufficiently high temperatures, $T > T_{EW}$, the expectation value of the Higgs field is zero, i.e., the symmetry is restored and particles are massless. At $T < T_{EW}$ the symmetry breakes and particle masses become finite (e.g. Kämpfer, 2000). During this transition, according to the SMPP, all particles except the Higgs acquire their mass by the mechanism of spontaneous symmetry breaking (e.g. Schwarz, 2003).

Csikor et al. (1998) obtained, using a nonperturbative analysis, that the phase transition is of first–order for Higgs masses less than 66.5 ± 1.4 GeV while for larger Higgs masses only a rapid crossover is expected (see Figure 34). This value must be perturbatively transformed to the full Standard Model yielding 72.4 ± 1.7 GeV (Csikor et al., 1998). The exact determination of this critical Higgs–mass value, $m_{H,c}$, at which the first–order EW phase transition changes to a crossover is important given its implications for the standard model (e.g. Karsch et al., 1996).

The location of the endpoint of the first–order phase transition line is seen to move to smaller values of the Higgs mass as the chemical potentials μ are increased, indicating that the chemical potentials make the transition weaker. At the same time, the critical temperature is slightly increased. The value $m_{H,c} \approx 72$ GeV corresponds to the case $\mu = 0$. If, for example, $\mu \approx 30$ GeV then we have $m_{H,c} \approx 66$ GeV (e.g. Gynther, 2006).

Both the QCD and the EW theories contain a phase transition. The exact properties and critical temperatures of the transitions depend on the chemical potentials and the values of parameters of the theories. The EW phase diagram is considered in terms of the leptonic chemical μ_L potentials and the theory is parametrized by the Higgs mass, while the QCD phase diagram is considered in terms of the baryonic chemical potential μ_B and the theory is parametrized in terms of the strange quark mass. When the masses parameterizing the theories are small we have for both cases a first–order phase transition. However, as the chemical potentials are increased, the critical temperature of the EW phase transition increases, while the critical temperature of the QCD phase transition

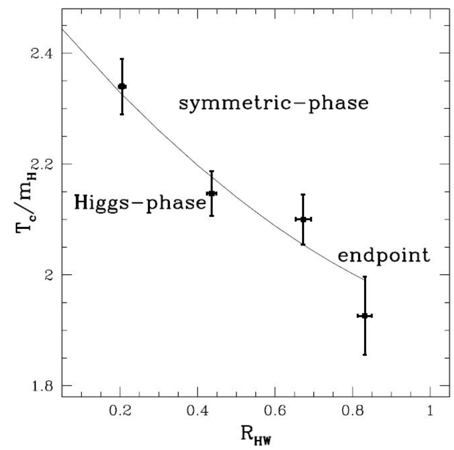

Figure 34: Phase diagram of the $SU(2)$–Higgs model in the $T_c/m_H - R_{HW}$ plane with $R_{HW} = m_H/m_W$. The continuous line, representing the phase–boundary, is a quadratic fit to the data points. Above the line we are in the symmetric phase and below we are in the symmetry broken phase. However, this line, as an endpoint at $R_{HW} \approx 0.82$ (Csikor et al., 1998).

decreases (see Figure 35). Thus, the responses of the systems on introducing the chemical potentials are opposite (e.g. Gynther, 2006).

Perhaps the main difference between the EW and the QCD transitions is that only during the latter was the Universe reheated back to the critical temperature (see Section 2.1). This is due to the much larger value of latent heat in the QCD transition (e.g. Ignatius, 1993).

The current mass limit for the Higgs is 114.3 GeV at 95% confidence level (see Yao et al., 2006) suggesting that the standard model does not feature a sharp EW phase transition (either first or second order) but it is rather a smooth Crossover (e.g. Boyanovsky et al., 2006). Since the change in relativistic degrees of freedom is tiny ($\Delta g = 1$, cf. Section 1.10) this is also a very boring event from the thermodynamical perspective (e.g. Schwarz, 2003). Since the Higgs sector of the theory carries only four of the total of 106.75 degrees of freedom (see Section 1.10), the contribution of the Higgs to the pressure is not easily visible (e.g. Gynther, 2006). Nevertheless, a first–order phase transition is still allowed in several extensions of the SMPP, including the MSSM (e.g. Kajantie et al., 1998, Section 1.9).

3.1 The critical temperature

In the minimal standard model, EW symmetry breaking is induced by the ground state of a single doublet scalar field. We can write the potential for the real scalar component of the doublet which acquires a vacuum expectation

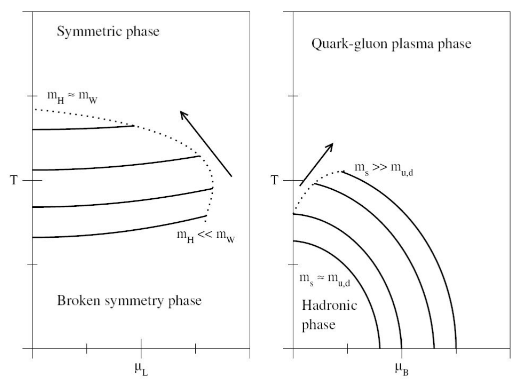

Figure 35: Schematic plots of the EW (left) and QCD (right) phase diagrams in terms of temperature and the relevant chemical potentials (μ_L and μ_B are, respectively, the leptonic and the baryonic chemical potentials). The solid lines correspond to the critical lines for a number of different Higgs/strange quark masses and the dotted lines indicate the location of the endpoint of the first–order phase transition line as the masses are varied. The arrows the order of magnitude in which masses increase along the dotted lines (Gynther, 2006).

value as (e.g. Anderson & Hall, 1992)

$$U(\phi) = \frac{\lambda_0}{4}\left(\phi^2 - \phi_0^2\right)^2 \tag{155}$$

where ϕ_0 is the expectation value of the Higgs field and λ_0 is related to the Higgs boson mass by (e.g. Anderson & Hall, 1992)

$$m_H^2 = 2\lambda_0\phi_0^2. \tag{156}$$

The EW phase transition takes place when the expectation value of the Higgs field passes from its high temperature value $\langle\phi\rangle = 0$ to its nonzero value in the low temperature broken phase (e.g. Mégevand, 2000).

To reliably analyze the dynamics of this field, we need to include the interactions of the Higgs field with virtual particles and with the heat bath (Anderson & Hall, 1992). The one–loop, zero temperature potential, $V(\phi)$ can be written as the sum of the classical potential and a one–loop correction (Anderson & Hall, 1992)

$$V(\phi) = U(\phi) + \bar{V}_1(\phi). \tag{157}$$

If we adopt the renormalization prescriptions (e.g. Anderson & Hall, 1992)

$$V''(\phi_0) = m_H^2 \tag{158}$$

$$V'(\phi_0) = 0 \tag{159}$$

for each degree of freedom to which the Higgs boson is coupled, the zero temperature one–loop correction to the effective potential is (see Anderson & Hall, 1992)

$$\bar{V}_1(\phi) = \pm\frac{1}{64\pi^2}\left[m^4(\phi)\ln\frac{m^2(\phi)}{m^2(\phi_0)} - \right.$$
$$\left. -\frac{3}{2}m^4(\phi) + 2m^2(\phi)m^2(\phi_0) - \frac{1}{2}m^4(\phi_0)\right] \tag{160}$$

where $\pm$ is for bosons (fermions) and $m(\phi)$ is the mass of the particle in the presence of the background field ϕ. In addition to these quantum corrections, we must also include the interaction between the Higgs field and the hot EW plasma. Taking the Higgs boson sufficiently light, the effective potential for the standard model can be reliably written as (e.g. Anderson & Hall, 1992)

$$V(\phi, T) = D(T^2 - T_0^2)\phi^2 - ET\phi^3 + \frac{\lambda_T}{4}\phi^4. \tag{161}$$

All the parameters in equation (161) depend on the particle content of the theory (e.g. Mégevand, 2000). Parameter D contains contributions from all the particles that acquire their masses through the Higgs mechanism and is given by (Anderson & Hall, 1992)

$$D = \frac{1}{8\phi_0^2}\left(2m_W^2 + m_Z^2 + 2m_t^2\right), \tag{162}$$

while the coefficient ot the term linear in temperature E, which has only boson contributions, is given by (Anderson & Hall, 1992)

$$E = \frac{1}{4\pi\phi_0^3}\left(2m_W^3 + m_Z^3\right). \tag{163}$$

In the SMPP we have $D \sim 10^{-1}$ and $E \sim 10^{-2}$ while in the MSSM, due to the larger particle zoo (see e.g. Table 11), D and E can be more than an order of magnitude larger than in the SMPP (e.g. Mégevand, 2000).

The temperature–dependent ϕ^4 coupling can be written as (e.g. Gynther, 2006)

$$\lambda_T = \lambda - \frac{3}{16\pi^2\phi_0^4}\left(2m_W^4\ln\frac{m_W^2}{c_BT^2} + m_Z^4\ln\frac{m_Z^2}{c_BT^2} - 4m_t^4\ln\frac{m_t^2}{c_FT^2}\right) \tag{164}$$

where the masses are evaluated at $\langle\phi\rangle = \phi_0$ and we have $c_B \simeq 5.41$ and $c_F \simeq 2.64$ (Anderson & Hall, 1992). Although the parameter λ_T is temperature–dependent, it is almost constant in the range of temperatures in which the phase transition can take place. However, this parameter is very sensitive to the Higgs mass (e.g. Mégevand, 2000).

The potential (161) is to be regarded as a phenomenological one, valid in the vicinity of T_c. The parameters T_0, D, E and λ_T are to be chosen so that the potential quantitatively correctly describes the phase transition (Ignatius, 1993).

The physical Higgs mass is related to λ by (Anderson & Hall, 1992)

$$m_H^2 = (2\lambda + 12B)\,\phi_0^2 \tag{165}$$

where

$$B = \frac{3}{64\pi^2\phi_0^4}\left(2m_W^4 + m_Z^4 - 4m_t^4\right). \tag{166}$$

The temperature T_0 is defined as the temperature where $V''(\phi = 0) = 0$, i.e., the lowest temperature where the symmetric vacuum can exist (e.g. Ignatius, 1993); it is given by (Anderson & Hall, 1992)

$$T_0^2 = \frac{1}{4D}\left(m_H^2 - 8B\phi_0^2\right) \equiv \chi^2(m_t, m_H)m_H^2. \tag{167}$$

Here all the masses are measured at zero temperature and $\phi_0 = 246$ GeV is the value of the scalar condensate at $T = 0$ (e.g. Gynther, 2006).

At high temperatures, i.e., temperatures well above T_0, the only minimum of the potential is achieved when the expectation value of the scalar field vanishes ($\langle\phi\rangle = 0$) and, thus, the symmetry is exact. As the early Universe cools down from this high temperature, a second local minimum of the potential first appears (as an inflection point) when the temperature reaches (Anderson & Hall, 1992)

$$T_* = \frac{T_0}{\sqrt{1 - \frac{9}{8}\frac{E^2}{\lambda_T D}}}. \tag{168}$$

The value of the field when $T = T_*$ is given by (Anderson & Hall, 1992)

$$\phi_* = \frac{3ET_*}{2\lambda_T}. \tag{169}$$

At lower temperatures, this point splits into a barrier ϕ_- and a local minimum ϕ_+ which subsequently evolves as (Anderson & Hall, 1992)

$$\phi_\pm = \frac{3ET}{2\lambda_T}\left(1 \pm \sqrt{1 - \frac{8}{9}\frac{\lambda_T D}{E^2}\left(1 - \frac{T_0^2}{T^2}\right)}\right). \tag{170}$$

The cubic term in $V(\phi, T)$ is responsible for the coexistence of two minima separated by a barrier, and subsequently, for the eventual first–order nature of the phase transition. Hence, the strength of the transition depends on the value of the parameter E (e.g. Mégevand, 2000).

The evolution of ϕ_- and ϕ_+ is shown in Figure 36. We define the temperature T_c to be the temperature at which the second minimum becomes degenerate with

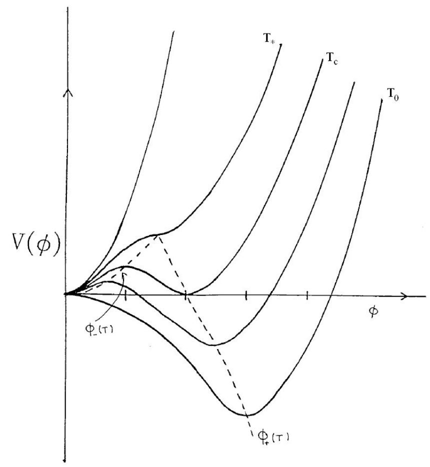

Figure 36: A schematic plot of the evolution of the scalar potential V for different values of temperature. Also represented is the evolution of ϕ_- and ϕ_+. Here T_0 represents the temperature for which $V''(\phi = 0) = 0$, i.e., the lowest temperature where the symmetric vacuum can exist (equation 167), T_* is the temperature for which a second local minimum of the potential first appears (equation 168) and T_c is the temperature at which that second minimum becomes degenerate with the origin (equation 171) (adapted from Anderson & Hall, 1992).

the origin: $V(\phi_+(T_c)) = 0$. Hence, if we divide equation (161) by ϕ^2, T_c occurs where the resulting quadratic equations have two real equal roots. This gives the relation[27] (Anderson & Hall, 1992)

$$T_c = \frac{T_0}{\sqrt{1 - \frac{E^2}{\lambda_{T_0} D}}}. \tag{171}$$

At this critical temperature T_c the two minima become degenerate, and below this temperature the stable minimum of V is at (e.g. Mégevand, 2000)

$$\phi_+ = \frac{3ET}{2\lambda_{T_0}} \left(1 + \sqrt{1 - \frac{8}{9} \frac{\lambda_{T_0} D}{E^2} \left(1 - \frac{T_0^2}{T^2} \right)} \right). \tag{172}$$

When the temperature reaches T_0 the barrier between minima disappears, and $\phi = 0$ becomes a maximum of the potential as it is clear from Figure 36 (e.g. Mégevand, 2000).

[27] Some authors (e.g. Gynther, 2006) prefer to indicate λ_{T_c} instead of λ_{T_0}. In fact, as we shall see, the difference between T_c and T_0 is very small and, hence, $\lambda_{T_c} \approx \lambda_{T_0}$. We prefer to indicate λ_{T_0} because we will determine the value of T_c with the help of the value of T_0.

The number $E^2/\lambda_{T_0} D$ is, in general, small, and the difference between T_c and T_0 is $\Delta T \lesssim 10^{-2} T_c$. However, things change rapidly as the temperature falls from T_c to T_0 (e.g. Mégevand, 2000).

The exact temperature of the transition T_t depends on the evolution of the bubbles after they are nucleated, which, in turn, depends on the viscosity of the plasma (e.g. Mégevand, 2000).

Considering the present known values for m_W, m_Z, m_t and m_H (see Section 1.8) we obtain $D \approx 0.179$, $B \approx -0.00523$, $E \approx 0.0101$, $\lambda \approx 0.1393$, $T_0 \approx$ 137.8 GeV, $\lambda_{T_0} \approx 0.1321$ and $T_c \approx 138.1$ GeV. The value obtained for T_c agrees with the value indicated in the literature which is $T_c \sim 100$ GeV. Thus, we consider

$$T_c = 100 \text{ GeV}. \tag{173}$$

In the case of the MSSM we have to consider two scalars ϕ_1 and ϕ_2 corresponding to the two complex Higgs doublets H_1 and H_2 (cf. Section 1.8). The potential can now be written in the standard form (e.g. Trodden, 1999)

$$\begin{aligned} V(\phi_1, \phi_2) = {} & \lambda_1(\phi_1^\dagger \phi_1 - v_1^2)^2 + \lambda_2(\phi_2^\dagger \phi_2 - v_2^2)^2 + \\ & + \lambda_3 \left[(\phi_1^\dagger \phi_1 - v_1^2) + (\phi_2^\dagger \phi_2 - v_2^2) \right]^2 + \\ & + \lambda_4 \left[(\phi_1^\dagger \phi_1)(\phi_2^\dagger \phi_2) - (\phi_1^\dagger \phi_2)(\phi_2^\dagger \phi_1) \right] \end{aligned} \tag{174}$$

where $v_1 \equiv \langle H_1^0 \rangle$ and $v_2 \equiv \langle H_2^0 \rangle$ are the respective vacuum expectation values of the two doublets, † represents the Hermitian conjugate, and the λ_i's are coupling constants. Notice that it is not restrictive to assume that the only non–vanishing vacuum expectation values are v_1 and v_2, which are both real and positive (e.g. Espinosa et al., 1993).

Even in the MSSM we may continue to apply for the free energy the SMPP–like form given by equation (161), as long as we are in the limit in which the pseudoscalar particle of the Higgs sector is heavy ($m_A \gg T_c$)(e.g. Mégevand, 2000). In that case the potential ϕ in equation (161) is given by (e.g. Moreno et al., 1997)

$$\phi = \sqrt{2} \left(\phi_1^0 \cos\beta + \phi_2^0 \sin\beta \right) \tag{175}$$

where (e.g. Espinosa et al., 1993)

$$\beta = \frac{v_2}{v_1} = \frac{\langle H_2^0 \rangle}{\langle H_1^0 \rangle}. \tag{176}$$

Although the one–loop approximation can be used to calculate the characteristics of the phase transition, it is not guaranteed to be a reliable method. For an improved analysis (making use of two–loop corrections to the effective potential) see e.g. Arnold & Espinosa (1993); Fodor & Hebecker (1994). Espinosa (1996) has pointed out that two–loop corrections to the finite temperature effective potential in the MSSM can have a dramatic effect on the strength of the EW phase transition by making the time interval $(t_{EW+} - t_{EW-})$ larger.

3.2 EW phase transition models

Lattice results have shown that the EW phase transition in the SMPP is an analytic crossover (e.g. Aoki et al., 2006b). A first–order phase transition is allowed only within the context of some extensions of the SMPP such as the MSSM (see Section 1.9). If one adopts the SPS1a scenario (cf. Figure 11) for the MSSM then we have $m_A \sim 400$ GeV (cf. Table 11) which means that, if one takes $T_c \sim 100$ GeV, equation (161) could be regarded as an acceptable approximation for the potential.

3.2.1 Crossover (SMPP)

We will adopt, for the EW Crossover, the results obtained for the QCD Crossover (Section 2.3.3). Thus, we write the entropy density as (cf. equation 142)

$$s(T) = \frac{2\pi^2}{45} g_{EW} T^3 \left[1 + \frac{1}{2}\frac{\Delta g}{g_{EW}}\left(1 + \tanh\left(\frac{T - T_c}{\Delta T}\right)\right)\right] \tag{177}$$

where $\Delta g = 96.25 - 95.25 = 1$ and $g_{EW} = 95.25$ is the number of degrees of freedom after the EW Crossover.

The other thermodynamic quantities can be derived from equation (177). For example, inserting the entropy (177) into equation (14) we obtain, for the sound speed during a EW Crossover, the following result (cf. equation 143)

$$c_s^2(T) = \left[3 + \frac{\Delta g T \operatorname{sech}\left(\frac{T-T_c}{\Delta T}\right)^2}{\Delta T\left(g_{EW} + g'_{EW} + \Delta g \tanh\left(\frac{T-T_c}{\Delta T}\right)\right)}\right]^{-1} \tag{178}$$

where $g'_{EW} = 96.25$ is the number of degrees of freedom existing before the EW Crossover.

The value of ΔT must be choosen in order to fit eventual results. The lowest value for δ_c during the EW Crossover is attained when $\Delta T \approx 0.013 T_c$ (see Section 8.1). In Figure 37 we show the curve for c_s^2 as a function of the temperature with $T_c = 100$ GeV and with ΔT assuming different values. Notice that when $\Delta T \longrightarrow 0$ the sound speed aproaches zero but only for an instant. For larger values of ΔT the sound speed decreases less. The minimum value for the sound speed is attained for $T \approx T_c$. Thus, considering $T = T_c$ in equation (178), we obtain the following expression giving an approximate value for the minimum sound speed during an EW Crossover

$$c_{s,min}^2 \approx \left[3 + \frac{g'_{EW} - g_{EW}}{\frac{\Delta T}{T_c}(g'_{EW} + g_{EW})}\right]^{-1}. \tag{179}$$

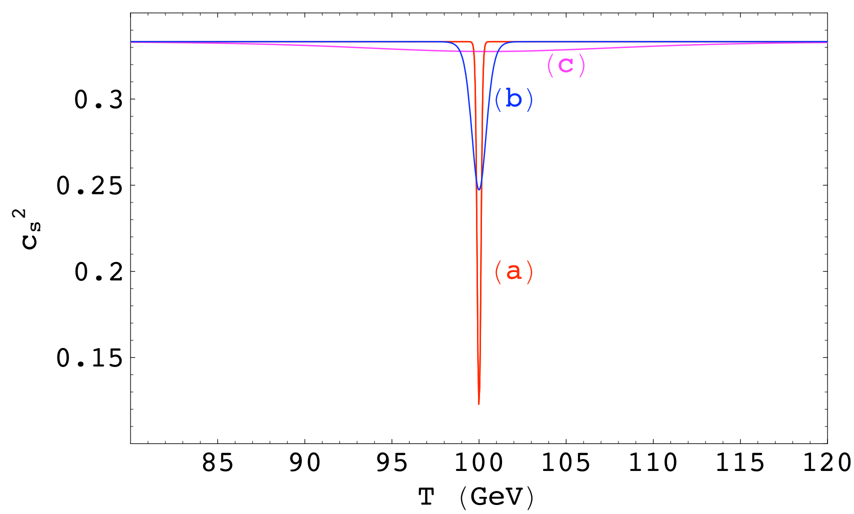

Figure 37: The sound speed $c_s^2(T)$ for the EW Crossover with $T_c = 100$ GeV and: (a) $\Delta T = 0.001T_c$; (b) $\Delta T = 0.005T_c$; (c) $\Delta T = 0.1T_c$. Notice that the sound speed decreases around T_c but does not reaches zero (with the exception of the limiting case $\Delta T \longrightarrow 0$).

In Figure 38 we show the curve for $c^2_{s,min}$ as a function of the ΔT parameter for the EW Crossover ($T_c = 100$ GeV) and, for comparison purposes, the corresponding curve for the QCD Crossover ($T_c = 170$ MeV). It is clear that during the EW Crossover the effects due to the reduction on the sound speed are less obvious than for the QCD case.

For the EW Crossover case, we consider that the sound speed minimum value is attained for $t \approx t_{EW+}$ (corresponding to $T \approx T_c$). During the EW Crossover the Universe continues to be radiation–dominated with the scale factor given by equation (86). Recalling equation (151) that gives the temperature as a function of time during the EW Crossover and inserting it into equation (178), we obtain, for the speed of sound during the EW Crossover, the following expression

$$c_s^2(t) = \left[3 + \frac{\Delta g T(t) \mathrm{sech}\left(\frac{T(t)-T_c}{\Delta T}\right)^2}{\Delta T\left(g_{EW} + g'_{EW} + \Delta g \tanh\left(\frac{T(t)-T_c}{\Delta T}\right)\right)}\right]^{-1} . \tag{180}$$

Taking into account that $T_c = 100$ GeV $\approx 7.7\times10^{14}$ K, we obtain, from equation (151), that $t_c \approx 3.12 \times 10^{-10}$ s. This corresponds to the instant of time when the sound speed reaches its minimum value. In Figure 39 we represent, again, the curves of Figure 37 but now as a function of time.

We consider the effective duration of the QCD Crossover the interval for which the sound speed stays below[28] 99% of its 'background' value $c^2_{s,0} = 1/3$.

[28] We do not consider 95%, as we did in the QCD case, because the reduction of the sound

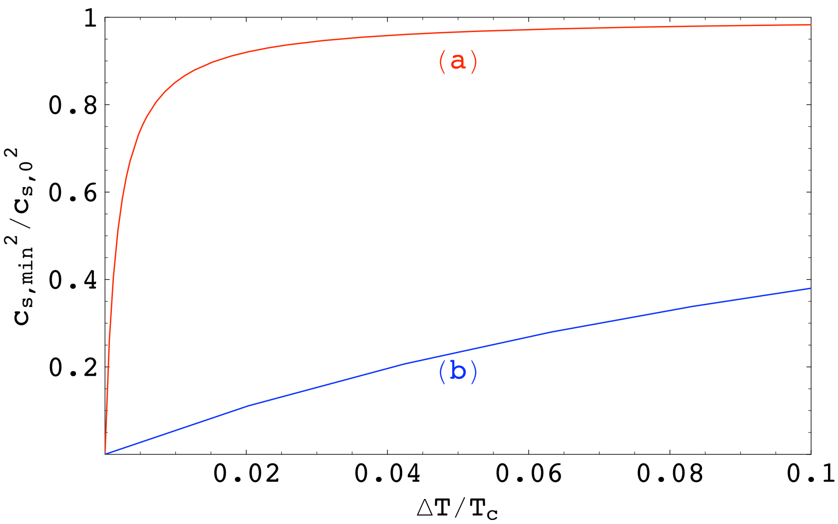

Figure 38: The minimum value attained by the sound speed, $c^2_{s,min}$, as a function of the parameter ΔT during: (a) the EW Crossover (see equation 179); (b) the QCD Crossover (see equation 144, Figure 27).

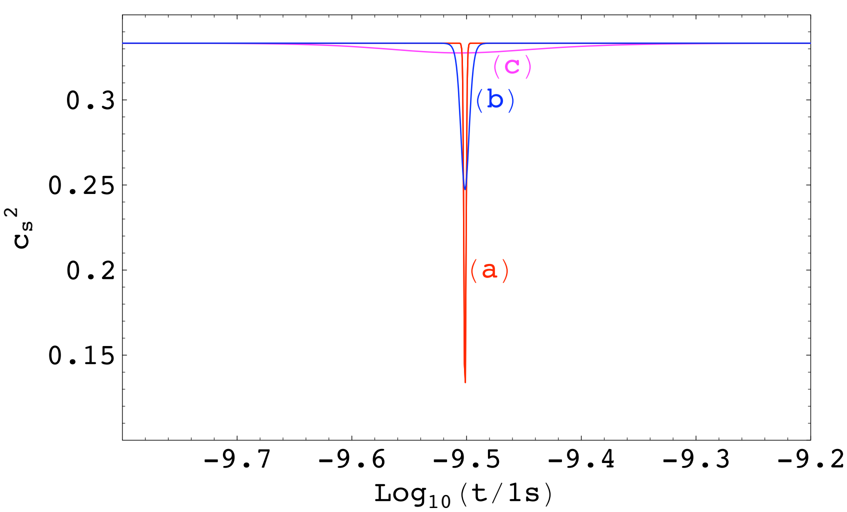

Figure 39: The sound speed $c_s^2(t)$ for the EW phase transition in the case of a Crossover with a reference temperature $T_c = 100$ GeV and: (a) $\Delta T = 0.001T_c$, (b) $\Delta T = 0.005T_c$, (c) $\Delta T = 0.1T_c$.

Table 21: The width of the EW Crossover in terms of temperature as a function of the parameter ΔT (cf. equation 178) when $T_c = 100$ GeV. T_1 represents the temperature when the sound speed gets below 99% of its 'background' value 1/3 and T_2 represents the temperature when the sound speed reaches, once again, 99% of 1/3 ($T_2 < T_c < T_1$). The width of the EW Crossover is given by $T_1 - T_2$.

$\frac{\Delta T}{T_c}$	T_2 (GeV)	T_1 (GeV)	$T_1 - T_2$ (GeV)
0.001	99.65	100.35	0.7
0.013	97.45	102.60	5.15
0.1	92.80	108.30	15.5

With the help of equations (178) and (180), we obtain the effective width of the EW Crossover for a few values of the parameter ΔT. The results are shown in Table 21 (in terms of temperature) and in Table 22 (in terms of time).

3.2.2 Bag Model (MSSM)

In this section we consider the EW phase transition as a first–order phase transition within the context of the MSSM. We adopt a Bag Model and whenever possible we adopt, for simplicity, the ideas and results presented for the QCD transition (Section 2.3.1).

During the EW phase transition the system can exist in two phases: a symmetric high temperature phase with pressure $P_h(T)$ (h for high) and a low temperature phase with broken symmetry and pressure $P_l(T)$ (l for low). At the transition temperature T_c we have $P_h(T_c) = P_l(T_c)$. In Figure 40 we show a qualitative representation of the EoS of the system. For $T_0 < T < T_c$ the system can exist in a metastable supercooled symmetric phase and for $T_c < T < T_+$ in a metastable superheated broken symmetry phase (Enqvist et al., 1992).

The EoS giving the pressure for the EW matter near $T = T_c$ can be written as (Enqvist et al., 1992)

$$P_l(T) = \frac{\pi^2}{90} g_l T^4 + B(T) \tag{181}$$

$$P_h(T) = \frac{\pi^2}{90} g_h T^4 \tag{182}$$

where g_h and g_l correspond to the number of degrees of freedom at the beginning and at the end of the transition respectively. The function $B(T)$, which plays

speed during the EW Crossover is much less significant than it was in the QCD case.

Table 22: The width of the EW Crossover in terms of time as a function of the parameter ΔT (cf. equation 180) when $T_c = 100$ GeV. t_1 represents the instant when the sound speed reaches less than 99% of its 'background' value (1/3) and t_2 represents the instant when the sound speed reaches, once again, 99% of 1/3 ($t_1 < t < t_2$). The width of the EW Crossover is given by $t_2 - t_1$.

$\frac{\Delta T}{T_c}$	$t_2(\times 10^{-10}$ s)	$t_1(\times 10^{-10}$ s)	$t_2 - t_1(\times 10^{-11}$ s)
0.001	3.14	3.10	0.44
0.013	3.29	2.97	3.22
0.1	3.63	2.66	9.64

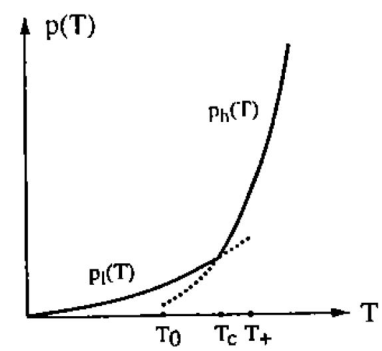

Figure 40: The EoS with a first–order phase transition and with two metastable branches (Enqvist et al., 1992) – see text for more details.

the role of the QCD's Bag constant (see Section 2.3.1), is derived from the potential V. However we use a simpler version, based on the approximation (Enqvist et al., 1992)

$$B(T) \approx l\left(1 - \frac{T}{T_c}\right) \approx \frac{l}{2}\left(1 - \frac{T^2}{T_c^2}\right). \tag{183}$$

If one wants to study how a given fluctuation behaves during the EW phase transition, then it is of crucial importance to know the duration of the transition. This means that we need to define a specific beginning $t = t_{EW-}$ as well as a specific end $t = t_{EW+}$ to the EW transition. Here t_{EW-} and t_{EW+} are the limits for the time interval during which the sound speed vanishes. Although the temperature of the Universe is not constant during the EW phase transition, is stays all the time near the critical value T_c. Thus, the value of $R(t_{EW+})$ (i.e. the value of the scale factor at the end of the transition) is given, approximately, by (see equation 78)

$$R(t_{EW+}) \approx \frac{T_0}{T_c}. \tag{184}$$

On the other hand, for $t = t_{EW+}$ equation (86) becomes

$$R(t_{EW+}) = \exp\left(c\sqrt{\frac{\Lambda}{3}}(t_{SN} - t_0)\right)\left(\frac{t_{eq}}{t_{SN}}\right)^{2/3}\left(\frac{t_{EW+}}{t_{eq}}\right)^{1/2}. \tag{185}$$

Inserting equation (184) into equation (185) we obtain, for the instant when the transition ends

$$t_{EW+} = t_{SN}\left(\frac{t_{eq}}{t_{SN}}\right)^{-1/3}\exp\left(-2c\sqrt{\frac{\Lambda}{3}}(t_{SN} - t_0)\right)\left(\frac{T_0}{T_c}\right)^2. \tag{186}$$

The evolution of the scale factor while the high and low temperature phases coexist in a first–order EW phase transition, i.e., during the $c_s^2 = 0$ part, may be determined by the entropy conservation as long as we assume that the transition evolves close to equilibrium (e.g. Jedamzik & Niemeyer, 1999). Thus, we here adopt equation (148) from the QCD case, writing it in the form

$$\Delta R = \frac{R(t_{EW+})}{R(t_{EW-})} = \left(\frac{s(t_{EW-})}{s(t_{EW+})}\right)^{1/3} = \left(1 + \frac{\Delta g}{g_l}\right)^{1/3}. \tag{187}$$

When $t = t_{EW-}$ equation (72) becomes

$$R(t_{EW-}) = \exp\left(c\sqrt{\frac{\Lambda}{3}}(t_{SN} - t_0)\right)\left(\frac{t_{eq}}{t_{SN}}\right)^{2/3}\left(\frac{t_{EW+}}{t_{eq}}\right)^{1/2}\left(\frac{t_{EW-}}{t_{EW+}}\right)^{2/3} \tag{188}$$

where we consider $n_{ew} = 2/3$ and $n_{qcd} = 1/2$. From equations (185) and (188) we obtain

$$t_{EW-} = \frac{t_{EW+}}{\sqrt{\Delta R^3}}. \tag{189}$$

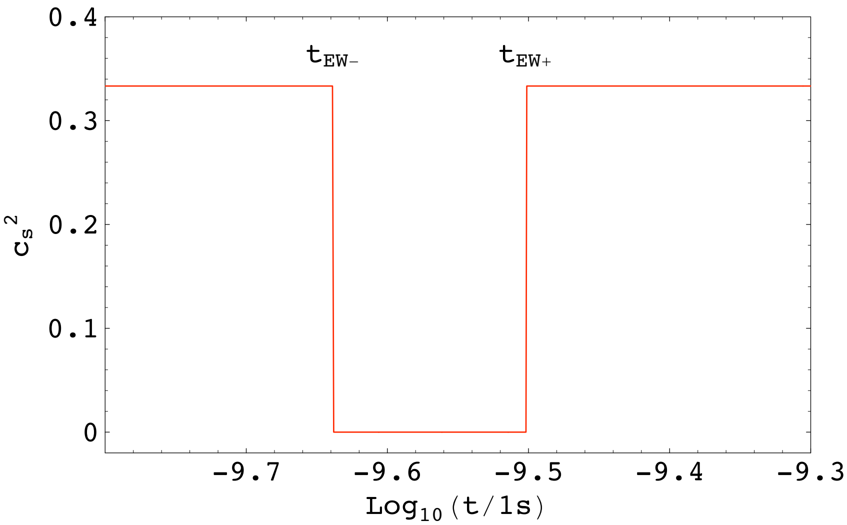

Figure 41: The sound speed $c_s^2(t)$ for the EW phase transition according to the Bag Model with $T_c = 100$ GeV. During the coexistence phase, which occurs between the instants $t_{EW-} = 2.3 \times 10^{-10}$ s (see text for more details) and $t_{EW+} = 3.15 \times 10^{-10}$ s, the sound speed drops to zero.

Considering $T_c = 100$ GeV we obtain, with the help of equation (186), the value $t_{EW+} = 3.15 \times 10^{-10}$ s. In order to determine the value of t_{EW-} one must determine first the value of ΔR. This is a problem, because we need to know the value of $\Delta g = g_h - g_l$ (see equation 187). We consider, for g_l (i.e., the number of degrees of freedom at the end of the transition), in accordance with the SMPP, the value $g_l = 95.25$. However, we do not have any clue for the real value of g_h. In the context of the MSSM it may be as large as 228.75 when all particles and superpartners are present (cf. Table 15) and, in the context of the SMPP it is $g_h = 96.25$. Within this range of values ΔR varies between ≈ 1.0035 and ≈ 1.3392. Inserting this values into equation (189) with $t_{EW+} = 3.15 \times 10^{-10}$ s it turns out that t_{EW-} should be between 2.03×10^{-10} s and 3.13×10^{-10} s.

We consider here $t_{EW-} = 2.3 \times 10^{-10}$ s, corresponding to $\Delta g \approx 80$. In Figure 41 we show the sound speed profile for the EW transition, according to these results. It must be noted, however, that the value of t_{EW-} was introduced only with the purpose of giving an example. At this stage, we do not have any observational evidence supporting this or any other value. In fact, we do not have any concludent results on the existence of extensions of the SMPP beyond the EW cosmological phase transition.

3.3 The baryogenesis problem

There is a large body of observational evidence that suggests that there is more matter than antimatter in the Universe up to scales of the order of the Hubble radius. The value of this asymmetry is quantified by the ratio (e.g. Boyanovsky et al., 2006)

$$\eta = \frac{n_b - n_{\bar{b}}}{n_\gamma} \tag{190}$$

where n_b, $n_{\bar{b}}$ and n_γ are, respectively, the baryon, antibaryon and photon densities. This is the only free input parameter that enters in nucleosynthesis calculations of the primordial abundance of light elements. The agreement between the WMAP results and the most recent analysis of the primordial deuterium abundance yields (e.g. Boyanovsky et al., 2006)

$$\eta = (6.1 \pm 0.3) \times 10^{-10}. \tag{191}$$

The origin of this baryon asymmetry is one of the deep mysteries in particle physics and cosmology. One might hope that the baryon asymmetry can be generated at the EW phase transition, if the transition is of strong first–order. If the EW phase transition is second order or a continuous crossover, the associated departure from equilibrium is insufficient to lead to a relevant baryon number production. This means that for *EW baryogenesis* (EWBG) to succeed, we either need the EW phase transition to be strongly first–order or other methods of destroying thermal equilibrium; for example, topological defects should be present at the phase transition (e.g. Trodden, 1999).

The current mass limit for the Higgs is 114.3 GeV at 95% confidence level (e.g. Yao et al., 2006) suggesting that the SMPP does not feature a sharp EW phase transition (either first or second order) but just a smooth Crossover (Section 3.2.1). This means that baryogenesis cannot be explained in the SMPP. One has to explore beyond the SMPP scenarios. The most natural choice is the MSSM (Section 1.9) where a strong first–order phase transition is allowed (e.g. Csikor, 1999).

An alternative scenario for baryogenesis proposes that a primordial asymmetry between leptons and antileptons or *leptogenesis* is responsible for generating the baryon asymmetry. The leptogenesis proposal depends on the details of the origin of neutrino masses and remains a subject of ongoing study (e.g. Boyanovsky et al., 2006).

Rangarajan et al. (2002) suggest another alternative scenario for baryogenesis. The baryon asymmetry is created at temperatures much below the EW phase transition temperature during the evaporation of PBHs. When a PBH is evaporating it heats up the plasma around it to a temperature much higher than the ambient temperature, for a short time. This can also happen due to the decay of massive particles. For appropriate PBH masses (or, particle masses) the temperature of the hot region rises above the EW phase transition temperature T_{EW} and the EW symmetry is restored locally. Due to the transfer of energy out of this region, the hot region will cool and the temperature will fall below T_{EW}. Thus, in these hot regions the EW phase transition occurs again and baryon asymmetry is there generated.

Brandenberger et al. (1999, 1998) had proposed that baryogenesis may be realized at the QCD phase transition. The scenario is based on the existence of *domain walls* separating the metastable vacua of low energy QCD from the stable vacuum. The walls acquire a negative fractional baryon charge, leaving behind a compensating positive baryon charge in the bulk. In this sense, this is a charge separation rather than a charge generation mechanism. They claim that it is possible, without fine tuning of parameters, to obtain a reasonable value of the baryon to entropy ratio in the bulk.

Another proposed scenario is that of $GUT Baryogenesis$ in which the baryon asymmetry is generated during the GUT epoch at scales of order 10^{16} GeV (e.g. Riotto & Trodden, 1999).

4 The electron–positron annihilation

During a first–order cosmological phase transition the Universe experiences a drastic reduction on the sound speed. In fact the speed of sound vanishes for a while (see e.g. QCD phase transition, Section 2). Less dramatic reductions may also occur during higher–order phase transitions or particle annihilation periods in the early Universe (e.g. Jedamzik & Niemeyer, 1999; Kämpfer, 2000).

This is the case, for example, of the electron–positron (e^+e^-) annihilation process which becomes predominant as soon as the radiation temperature drops below the mass of the electron (~ 1 MeV). A reduction in the sound speed value of order $10-20\%$ for a few Hubble times does occur during the cosmic e^+e^- annihilation. There is the possibility of an enhancement in PBH formation on the e^+e^- annihilation horizon mass scale of approximately, $M \sim 10^5 M_\odot$ (Jedamzik, 1997).

The neutrino degrees of freedom are not affected at all by this process. As a result, we have the disappearance of four fermionic degrees of freedom, i.e., the ones corresponding to electrons and positrons (e.g. Zimdahl & Pavón, 2001). Thus, we have (cf. Table 13) $\Delta g = 10.75 - 7.25 = 3.5$.

Below temperatures of ~ 1 MeV the three neutrino flavours are decoupled chemically and kinetically from the plasma and the entropy of the relativistic electrons is transfered to the photon entropy, but not to the neutrino entropy when electrons and positrons annihilate. This leads to an increase of the photon temperature relative to the neutrino temperature by (e.g. Schwarz, 2003)

$$\frac{T_\nu}{T_\gamma} = \left(\frac{4}{11}\right)^{1/3}. \tag{192}$$

There are other annihilation processes that could lead to an equivalent reduction on the speed of sound (e.g. muon annihilation). In this work we concentrate on the electron–positron annihilation process and on its eventual consequences in the context of PBH production.

We adopt for the profile of the sound speed during the e^+e^- annihilation process, for simplicity, an expression similar to (143) or (178). Thus, we consider

$$c_s^2(T) = \left[3 + \frac{\Delta g T \mathrm{sech}\left(\frac{T-T_c}{\Delta T}\right)^2}{\Delta T\left(g_{ep} + g'_{ep} + \Delta g \tanh\left(\frac{T-T_c}{\Delta T}\right)\right)}\right]^{-1} \tag{193}$$

where $g'_{ep} = 10.75$ and $g_{ep} = 7.25$. We also consider a critical temperature $T_c = 1$ MeV. The parameter ΔT must be determined in order to achieve results: reductions of order $10-20\%$ on the sound speed must take place.

The minimum value for the sound speed is attained for $T \approx T_c$. Considering $T = T_c$ in equation (193) we obtain the following expression giving an approximate value for the minimum speed of sound during the e^+e^- annihilation process:

$$c_{s,min}^2 \approx \left[3 + \frac{g'_{ep} - g_{ep}}{\frac{\Delta T}{T_c}(g'_{ep} + g_{ep})}\right]^{-1}. \tag{194}$$

Table 23: The reduction of the speed of sound during the electron–positron annihilation and the corresponding values for the parameter ΔT ($T_c = 1$ MeV).

c_s reduction	$\frac{\Delta T}{T_c}$
20%	0.115
15%	0.169
10%	0.276
5%	0.600

Assuming different reductions, in the range 5%–20%, on the value of the speed of sound we have obtained, from equation (194), the corresponding values for the parameter ΔT (see Table 23).

In Figure 42 we show the curve for the sound speed as a function of the temperature with $T_c = 1$ MeV and with ΔT assuming the values corresponding to a reduction of 10% and 20% on the sound speed value (Table 23). For the temperature as a function of time during the electron–positron annihilation we recover here equation (151). Inserting expression (151) into equation (193) we obtain, for the sound speed during the electron–positron annihilation, the following:

$$c_s^2(t) = \left[3 + \frac{\Delta g T(t) \mathrm{sech} \left(\frac{T(t)-T_c}{\Delta T} \right)^2}{\Delta T \left(g_{ep} + g'_{ep} + \Delta g \tanh \left(\frac{T(t)-T_c}{\Delta T} \right) \right)} \right]^{-1}, \tag{195}$$

with $T_c = 1$ MeV. Taking into account that 1 MeV $\approx 7.7 \times 10^9$ K we obtain from equation (151) $t_c \approx 3.15$ s. This corresponds to the instant of time for which the speed of sound reaches its minimum value. In Figure 43 we represent, again, the curves of Figure 42 but now as a function of time.

We have considered as a reasonable effective duration for the e^+e^- annihilation process the interval for which the sound speed stays below 99% of its 'background' value $c_{s,0}^2 = 1/3$. With the help of equations (193) and (195) we have obtained this effective width for the values of the parameter ΔT that we have already considered on Table 23. The obtained results are shown on Table 24 (in terms of temperature) and on Table 25 (in terms of time).

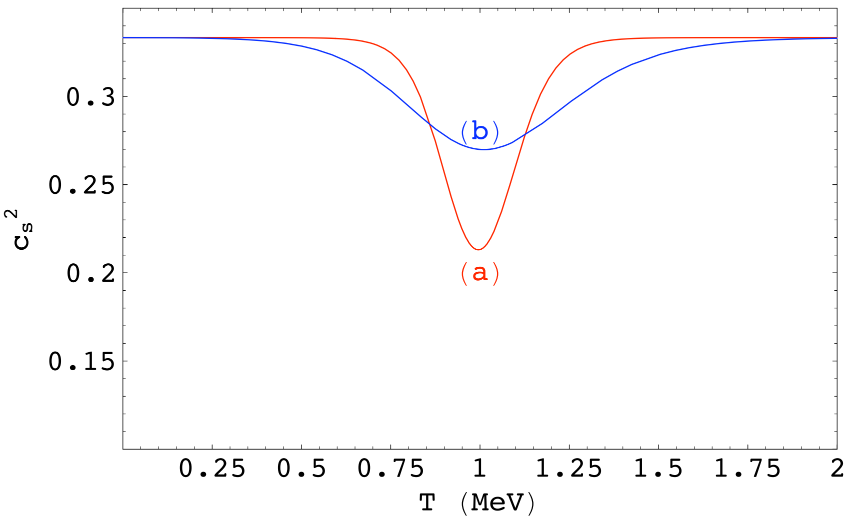

Figure 42: The sound speed $c_s^2(T)$ during the electron–positron annihilation with $T_c = 1$ MeV and: (a) $\Delta T = 0.115T_c$ (reduction of 20%), (b) $\Delta T = 0.276T_c$ (reduction of 10%).

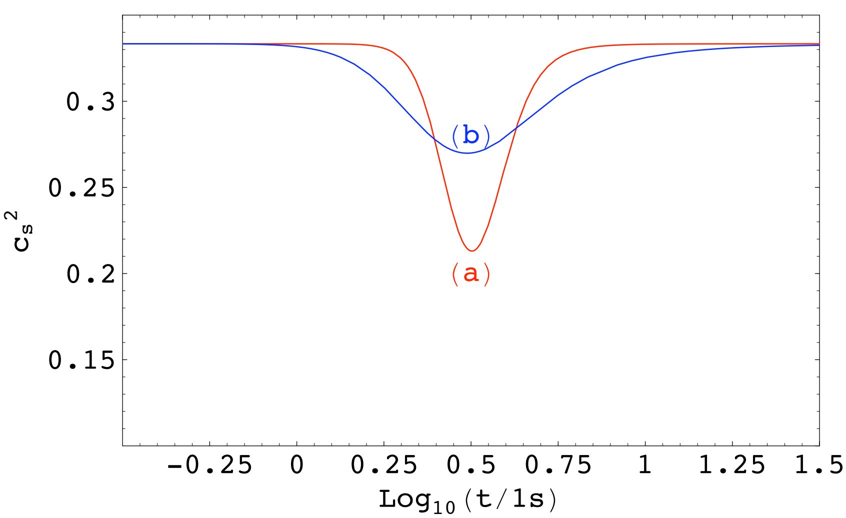

Figure 43: The sound speed $c_s^2(t)$ during the electron–positron annihilation with $T_c = 1$ MeV and: (a) $\Delta T = 0.115T_c$ (reduction of 20%), (b) $\Delta T = 0.276T_c$ (reduction of 10%).

Table 24: The width of the cosmological electron–positron annihilation in terms of temperature as a function of the parameter ΔT (cf. equation 193) when $T_c = 1$ MeV. T_1 represents the temperature when the sound speed gets less than 99% of its 'background' value 1/3 and T_2 represents the temperature when the sound speed reaches, once again, 99% of 1/3 ($T_2 < T_c < T_1$). The effective width of the process is given by $T_1 - T_2$.

$\frac{\Delta T}{T_c}$	T_2 (MeV)	T_1 (MeV)	$T_1 - T_2$ (MeV)
0.115	0.65	1.35	0.70
0.169	0.60	1.45	0.85
0.276	0.45	1.70	1.25
0.600	0.25	2.35	2.10

Table 25: The width of the cosmological electron–positron annihilation in terms of time as a function of the parameter ΔT (cf. equation 195) when $T_c = 1$ MeV. t_1 represents the instant when the sound speed gets less than 99% of its 'background' value 1/3 and t_2 represents the instant when the sound speed reaches, once again, 99% of 1/3 ($t_1 < t < t_2$). The effective width of the process is given by $t_2 - t_1$.

$\frac{\Delta T}{T_c}$	t_2(s)	t_1(s)	$t_2 - t_1$(s)
0.115	7.39	1.71	5.61
0.169	8.67	1.49	7.18
0.276	15.42	1.08	14.3
0.600	50.0	0.57	49.4

5 Fluctuations

It was already realized many years ago that a spectrum of primordial fluctuations can lead to the formation of PBHs (e.g. Carr & Hawking, 1974; Carr, 1975; Novikov et al., 1979). What was initially considered was a spectrum of classical fluctuations instead of a spectrum of quantum fluctuations. We have now in cosmology a paradigm based on the existence of Inflation (Section 1.3) which allows us to consider the quantum origin of the fluctuations (Polarski, 2001). During inflation fluctuations of quantum origin, of the *inflaton* (i.e. the scalar field driving inflation) are produced. These fluctuations are then stretched to scales much larger than the Hubble radius R_H (equation 28) at the time when they were produced.

Once a physical wavelength becomes larger than the Hubble radius, it is causally disconnected from physical processes. The inflationary era is followed by a radiation–dominated and matter stages where the acceleration of the scale factor becomes negative (see Sections 1.1 and 1.2). With a negative acceleration of the scale factor, the Hubble radius grows faster than the scale factor, and wavelengths that were outside, can re–enter the Hubble radius. This is the main concept behind the inflationary paradigm for the generation of temperature fluctuations as well as for providing the seeds for LSS formation (e.g. Boyanovsky et al., 2006). In fact, with this mechanism we can explain all the inhomogeneities we see today even on the largest cosmological scales as well as the production of PBHs (Polarski, 2001).

WMAP has provided perhaps the most striking validation of inflation as a mechanism for generating superhorizon fluctuations, through the measurement of an anticorrelation peak in the temperature–polarization angular power spectrum at $l \sim 150$ corresponding to superhorizon scales (e.g. Boyanovsky et al., 2006, Section 1.7).

5.1 The quantum–to–classical transition

Although there is a great diversity of inflationary models (Section 1.3), they generically predict a gaussian and nearly scale invariant spectrum of primordial fluctuations which is an excellent fit to the highly precise wealth of data provided by the WMAP (e.g. Boyanovsky et al., 2006).

The inhomogeneities that we observe today do not display any property typical of their quantum origin. On the large cosmological scales probed by the observations, the fluctuations appear to us as random classical quantities. This means that there was, at some time in the past, a *quantum–to–classical* transition (Polarski, 2001).

Each field mode can be split into two linearly independent solutions: the *growing mode* and the *decaying mode*. At reentrance inside the Hubble radius, during the radiation–dominated or the matter–dominated stage, the decaying mode is usually vanishingly small, and can, therefore, be safely neglected. As a result, the field mode behaves like a stochastic classical quantity (for more details see Polarski (2001) and Polarski & Starobinsky (1996)).

The classical behaviour of the inflationary fluctuations is very accurate for the description of the CMB temperature anisotropy and LSS formation. In the context of PBH formation this is not always the case. The smallest PBHs can be produced as soon as the fluctuations reenter the Hubble radius right after inflation. However, at this stage the decaying mode still had no time to disappear completely and, as a consequence, one cannot speak about classical fluctuations (Polarski, 2001).

The degree to which the effective quantum–to–classical transition will occur is given by the ratio (Polarski, 2001)

$$D_k = \frac{\phi_{k,gr}}{\phi_{k,dec}} \tag{196}$$

of the growing mode (gr) to the decaying mode (dec) of the peculiar gravitational potential $\phi(k)$. Very large values of D_k will correspond to an effective quantum–to–classical transition. Equation (196) can be written as a function of the PBH mass (Polarski, 2001)

$$D(M) = 4AGH_k^2 \frac{M}{M_p^2} \tag{197}$$

where A is the growth factor of $\phi(k)$ between the inflationary stage and the radiation–dominated stage, H_k is the Hubble parameter at Hubble radius crossing during the inflationary stage and M_p is the Planck mass. The ratio $D(M)$ will grow with increasing PBH masses M, due essentially to the last term in expression (197). Clearly, there is a range of scales where D will not be large and the quantum nature of the fluctuations is important (Polarski, 2001).

PBHs with masses less than $M_* \approx 10^{15}$ g will have either completely evaporated or, in any case, be in the latest stage of their evaporation. Expression (197) evaluated at this natural cut–off for PBH masses gives $D(M_*) \simeq 10^{28}$ which means that one can safely use the effective classicality of the fluctuations for PBHs with initial masses $M \geq M_*$, i.e., all the non–evaporated PBHs. Hence, for all PBHs produced after approximately 10^{-23} s (cf. equation 30), the quantum–to–classical transition is already extremely effective. This means that quantum interference for these PBHs is essentially suppressed and one can really work to tremendously high accuracy with classical probability distributions (Polarski, 2001). During the rest of the text we consider only classical fluctuations.

5.2 Density fluctuations

The simplest way to describe a classical fluctuation is in terms of an overdensity or density contrast (e.g. Carr, 1975)

$$\delta(m) = \frac{\Delta m}{m} \tag{198}$$

where m is the average mass of the perturbed region and Δm is the excess of mass associated with the perturbation. If we want to treat the evolution of the spectrum of fluctuations we must consider instead $\delta(\vec{r})$; which can be defined as (e.g. Musco et al., 2005)

$$\delta(\vec{r}) = \frac{\rho(\vec{r},t) - \overline{\rho}}{\overline{\rho}} \tag{199}$$

where $\rho(\vec{r},t)$ represents the density evolution inside a region of radius r and $\overline{\rho}$ represents the average cosmological density. It may be useful to write this last expression in the form

$$\rho = \overline{\rho}(1+\delta). \tag{200}$$

Each perturbation $\delta(\vec{r})$ can be written as a Fourier series defined in a comoving box much bigger than the observable Universe (e.g. Liddle & Lyth, 1993)

$$\delta(\vec{r}) = \sum_k \delta_k e^{i\vec{k}.\vec{r}} \tag{201}$$

where k represents the wavenumber. Each physical scale $\lambda(t)$ is defined by some wavenumber k and evolves with time according to (Blais et al., 2003; Bringmann et al., 2002)

$$\lambda(t) = 2\pi\frac{R(t)}{k} \tag{202}$$

where $R(t)$ is the scale factor (Section 1.6). The name 'scale' is appropriate because features with size r are dominated by wavenumbers of order $k \sim r^{-1}$ (e.g. Liddle & Lyth, 1993). For a given physical scale, the horizon crossing time t_k is conventionally defined by (e.g. Blais et al., 2003; Bringmann et al., 2002)

$$ck = R(t_k)H(t_k) \tag{203}$$

where H is the *Hubble parameter* (Section 1.1). This corresponds to the time when that scale reenters the Hubble radius which will inevitably happen after inflation for scales that are larger than the Hubble radius at the end of inflation (e.g. Blais et al., 2003; Bringmann et al., 2002).

If there is a perturbation associated with the scale entering the horizon at time t_k and if that perturbation is large enough, then it will begin to collapse into a PBH at a later time $t_c > t_k$. We refer to this instant t_c as the *turnaround point*.

For a perturbation of a fixed size, its collapse cannot begin before it goes through the cosmological horizon. The size of a PBH when it forms, therefore, is related to the horizon size, or, equivalently, to the horizon mass M_H (equation 30) when the collapsing perturbation enters the horizon.

Next we determine the relation between the size of the overdense region at turnaround $S_c(t_c)$ and the scale factor at horizon crossing $R_k(t_k)$. In the unperturbed region we consider the FLRW metric (Section 1.1). The evolution of the scale factor, for a FLRW universe can be written in the form (Carr, 1975)

$$\left(\frac{dR}{dt}\right)^2 = \frac{8\pi G}{3}\overline{\rho}(t)R(t)^2 \tag{204}$$

where $\overline{\rho}$ represents the average cosmological density. Note that this is just one of the Friedmann–Lemaître equations (Section 1.1, equation 2) where we have considered $k = 0$ (flat universe) and we have neglected the cosmological constant term (which is a reasonable choice at early epochs).

In the perturbed region we consider the metric (Carr, 1975)

$$ds^2 = d\tau^2 - S^2(\tau)\left[\frac{dr^2}{1-\Delta\epsilon r^2} + r^2\left(d\theta^2 + sin^2\theta d\phi^2\right)\right] \tag{205}$$

where $\Delta\epsilon$ is the perturbed total energy per unit mass and the time τ is proper time as measured by comoving observers. Here $S(\tau)$ plays the role of a scale factor for the perturbed region. The evolution of $S(\tau)$ can be written in the form (Carr, 1975)

$$\left(\frac{dS}{d\tau}\right)^2 = \frac{8\pi G}{3}\rho(\tau)S(\tau)^2 - \Delta\epsilon \tag{206}$$

where $\rho(\tau)$ represents the density in the perturbed region.

Considering that initially the overdense region is comoving with the unperturbed background we consider $\tau_k = t_k$ (here the subscript k denotes a quantity evaluated when the fluctuation crosses the horizon), $S_k = R_k$ and $(dS/d\tau)_k = (dR/dt)_k$. With these choices we obtain for $\Delta\epsilon$ the expression

$$\Delta\epsilon = \frac{8\pi G}{3}R_k^2\left(\rho_k - \overline{\rho}_k\right) \tag{207}$$

Inserting this into equation (206) and taking into account that $\rho_k = \overline{\rho}_k(1+\delta_k)$ (cf. equation 200) we obtain

$$\left(\frac{dS}{d\tau}\right)^2 = \frac{8\pi G}{3}\left(\rho(\tau)S(\tau)^2 - \rho_k R_k^2\frac{\delta_k}{1+\delta_k}\right). \tag{208}$$

The density $\rho(\tau)$ can be written as (cf. Section 1.1, equation 10)

$$\rho(\tau) = K_s S(\tau)^{-3(1+w)} \tag{209}$$

where K_s is a constant. In the case of $\rho_k(t_k)$ we have

$$\rho_k = K_k R_k^{-3(1+w_k)} \tag{210}$$

where K_k is a constant and w_k is the adiabatic index when the fluctuation crosses the horizon. Inserting expressions (209) and (210) into equation (208) we obtain

$$\left(\frac{dS}{d\tau}\right)^2 = \frac{8\pi G}{3}\frac{K_s}{1+\delta_k}\left(\frac{1+\delta_k}{S(\tau)^{1+3w}} - \frac{K_k}{K_s}\frac{\delta_k}{R_k^{1+3w_k}}\right). \tag{211}$$

The turnaround point is reached when the perturbed region stops expanding, i.e., when $dS/d\tau = 0$. Thus, the evaluation of equation (211) at the turnaround point gives

$$S_c^{1+3w_c} = \frac{K_s}{K_k}R_k^{1+3w_k}\left(\frac{1+\delta_k}{\delta_k}\right) \tag{212}$$

where the subscript c denotes a quantity evaluated at the turnaround point.

5.3 Fluctuations during the QCD phase transition

5.3.1 Bag Model

Let us consider how a fluctuation evolves in the presence of a QCD phase transition according to the Bag Model. Here we follow very closely the model proposed by Cardall & Fuller (1998). Let ρ_1 and ρ_2 ($\rho_2 < \rho_1$) represent the energy densities at the start and at the end of the phase transition, respectively. Here we are assuming, for simplicity, that we have for $\rho > \rho_1$ a pure quark–gluon radiation plasma ($w = 1/3$), for $\rho < \rho_2$ a pure hadron radiation plasma ($w = 1/3$) and for $\rho_2 < \rho < \rho_1$ a mixed phase that can be treated as dust ($w = 0$).

Fluctuation dynamics in the presence of a phase transition should be independent of the temperature, energy density, and horizon mass at which the transition occurs. It is dependent, however, on the strength of the transition, as well as on the exact time t_k at which the fluctuation crosses the horizon; in particular, if shortly before onset, during, or shortly after completion of the transition (Jedamzik & Niemeyer, 1999). In order to characterize the horizon crossing time and the turnaround point in terms of density we introduce here the quantities, x and y, defined as

$$x = \frac{\overline{\rho}_k}{\rho_1} \tag{213}$$

$$y = \frac{\rho_1}{\rho_2}. \tag{214}$$

When $x = 1$ ($\overline{\rho}_k = \rho_1$) we are at the beginning of the phase transition and when $x = y^{-1}$ ($\overline{\rho}_k = \rho_2$) we are at the end of the phase transition. A given fluctuation has $x > 1$ if it crosses the horizon before the beginning of the phase transition, $y^{-1} < x < 1$ if it crosses the horizon during the phase transition and $x < y^{-1}$ if it crosses the horizon after the completion of the phase transition. For each situation we must consider also the possible locations of the turnaround point. As a result, we have six different classes of density fluctuations as shown in Table 26.

It is very useful to use x as a function of time. We can obtain this with the help of equation (131). We start with the expressions for ρ_1 and ρ_2

$$\rho_1 = \rho(t_-) = \frac{1}{3}\frac{\pi^2}{30}T_c^4\left(4g_{QGP} - g_{HG}\right), \tag{215}$$

$$\rho_2 = \rho(t_+) = \frac{1}{3}\frac{\pi^2}{30}T_c^4\left[4g_{QGP}\left(\frac{t_-}{t_+}\right)^2 - g_{HG}\right], \tag{216}$$

where we have used, in the case of ρ_2, equation (70) for $R(t_+)$ and equation (71) for $R(t_-)$. We can now write, with the help of equations (131) and (215):

$$x(t) = \frac{\rho(t)}{\rho_1} = \frac{4g_{QGP}\left(\frac{R(t_-)}{R(t)}\right)^3 - g_{HG}}{4g_{QGP} - g_{HG}} \tag{217}$$

Table 26: Classification of overdense regions according to the state of matter at the horizon crossing time and at the turnaround point for the QCD phase transition (Cardall & Fuller, 1998).

Class	Horizon Crossing phase	Turnaround phase
A	quark–gluon	quark–gluon
B	quark–gluon	mixed
C	quark–gluon	hadron
D	mixed	mixed
E	mixed	hadron
F	hadron	hadron

where $R(t_-)$ is given by equation (71) and $R(t)$ is given by: i) equation (69) if $x \leq y^{-1}$; ii) equation (70) if $y^{-1} < x < 1$; iii) equation (71) if $x \geq 1$. The value of y, which defines the end of the transition, can now be determined evaluating $x(t_+)$. It turns out that for the Bag Model case (cf. Section 2.3.1), with $g_{QGP} = 61.75$ and $g_{HG} = 21.25$, one obtains

$$y^{-1} = x(t_+) = \frac{4g_{QGP}\left(\frac{t_-}{t_+}\right)^2 - g_{HG}}{4g_{QGP} - g_{HG}} \approx 0.272. \tag{218}$$

In Figure 44 we show the curve $x(t)$. Notice that, equation (217) is to be used only during the first–order QCD transition: more precisely, in the neighborhood of the transition. For example, if one considers $x \ll y^{-1}$ then x will eventually become negative which does not make sense.

It will also be useful to know the expression which gives the turnaround point for each class of fluctuations. For classes A and F, which evolve completely during a radiation–dominated phase ($w = w_k = w_c = 1/3$), we obtain, taking into account that $S_k = R_k$, that $K_s/K_k = 1$. In this case we have, from equation (212) the result

$$S_{c,A} = S_{c,F} = R_k\left(\frac{1+\delta_k}{\delta_k}\right)^{1/2}. \tag{219}$$

For class D, which evolves completely during the dust phase ($w = w_k = w_c = 0$) we have, according to equation (212)

$$S_{c,D} = R_k\frac{1+\delta_k}{\delta_k}. \tag{220}$$

For classes B, C and E the value of the adiabatic index w varies during the fluctuation. For example, in the case of class B we have $w_k = 1/3$ and $w_c = 0$.

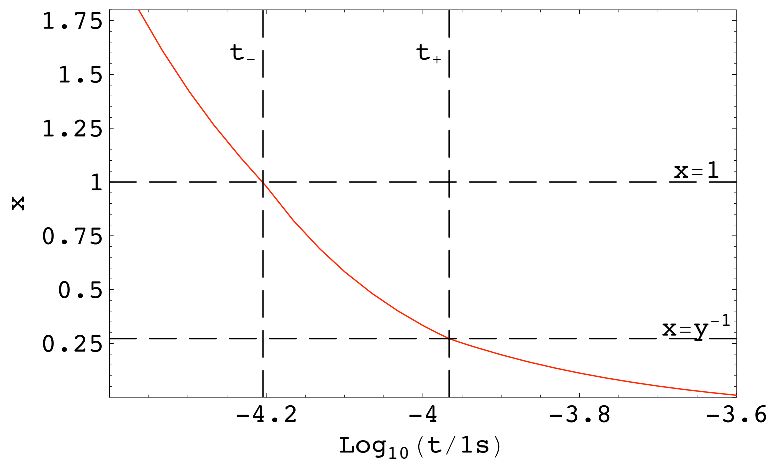

Figure 44: The function $x(t)$ for the QCD Bag Model (equation 217).

The change on the value of w occurs when $t = t_-$, or equivalently, when $x = 1$ (i.e., at the beginning of the transition). Considering that $\rho(\tau)$ is a continuous function, we write

$$K_k S_1^{-3(1+w_k)} = K_s S_1^{-3(1+w_c)} \tag{221}$$

where S_1 represents the size of the overdense region at the beginning of the transition. This leads to

$$\frac{K_s}{K_k} = \frac{S_1^{3w_c}}{S_1^{3w_k}} = \frac{1}{S_1} \tag{222}$$

In the case of class E we have $w_k = 0$ and $w_c = 1/3$. Now the change of w occurs when $t = t_+$ or, equivalently, when $x = y^{-1}$ (i.e., at the end of the transition). The continuity of the density, ρ, now leads to

$$\frac{K_s}{K_k} = \frac{S_2^{3w_c}}{S_2^{3w_k}} = S_2 \tag{223}$$

where S_2 represents the size of the overdense region at the end of the transition. Finally, in the case of fluctuations of class C, we have $w_k = w_c = 1/3$ with an intermediate period during which $w = w' = 0$. Applying the continuity condition for ρ successively at $t = t_+$ and $t = t_-$ we obtain, in the case of class C

$$\frac{K_s}{K_k} = \frac{S_2^{3w_c}}{S_1^{3w_k}} \frac{S_1^{3w'}}{S_2^{3w'}} = \frac{S_2}{S_1}. \tag{224}$$

The expression for S_1, which is valid and useful for fluctuations of classes B and C, can be obtained considering that ρ_1 is reached from radiation domination (i.e. $\rho \sim S^{-4}$ and $\rho \sim R_k^{-4}$). From energy conservation we have the condition $\rho_1 S_1^4 = \rho_k R_k^4$ which can be combined with equation (200) in order to obtain

$$S_1 = x^{1/4}(1+\delta_k)^{1/4} R_k. \tag{225}$$

The expression for S_2, useful for fluctuations of class C, can be obtained considering that ρ_2 is reached from the radiation phase (i.e. $\rho \sim S^{-4}$ and $\rho \sim R_k^{-4}$). From energy conservation we have the condition $\rho_2 S_2^4 = \rho_k R_k^4$ which can be combined with equation (200) in order to obtain

$$S_{2_C} = (xy)^{1/4}(1+\delta_k)^{1/4} R_k. \tag{226}$$

On the other hand, the expression for S_2 suitable for fluctuations of classes E and F, can be obtained considering that ρ_2 is reached from the dust–like phase (i.e. $\rho \sim S^{-3}$ and $\rho \sim R_k^{-3}$). From energy conservation we have the condition $\rho_2 S_2^3 = \rho_k R_k^3$ which can be combined with equation (200) in order to obtain

$$S_{2_E} = (xy)^{1/3}(1+\delta_k)^{1/3} R_k. \tag{227}$$

We are now ready to determine expressions for the turnaround points of classes B, C and E. From equation (212), with the constant K_s/K_k given by equation: (222)–class B, (224)–class C, and (223)–class E; and with S_1 given by equation (225) and S_2 given by equation (226) in the case of fluctuations of class C and by equation (227) in the case of fluctuations of class E, we obtain

$$S_{c,B} = R_k x^{-1/4} \frac{(1+\delta_k)^{3/4}}{\delta_k}, \tag{228}$$

$$S_{c,C} = R_k y^{1/6} \left(\frac{1+\delta_k}{\delta_k}\right)^{1/2}, \text{ and} \tag{229}$$

$$S_{c,E} = R_k (xy)^{1/6} \frac{(1+\delta_k)^{2/3}}{\delta_k^{1/2}}. \tag{230}$$

The separation between classes (A,B,C) and classes (D,E) is given by the condition $\rho_1 = \rho_k$. With the help of equation (200) this becomes

$$\delta_k = x^{-1} - 1. \tag{231}$$

On the other hand the separation between classes (D,E) and class (F) is given by the condition $\rho_2 = \rho_k$. With the help of equation (200) this becomes

$$\delta_k = (xy)^{-1} - 1. \tag{232}$$

The separation between classes A and B can be obtained noting that what distinguishes these classes is the location of the turnaround point. Thus, considering $S_{c,A}$ (equation 219) equal to $S_{c,B}$ (equation 228), we obtain

$$x = \frac{1+\delta_k}{\delta_k^2}. \tag{233}$$

The same idea can be applied in order to determine the separation between classes B and C. Thus, considering $S_{c,B} = S_{c,C}$ we obtain

$$x^{-3/2}y^{-1} = \frac{\delta^3}{(1+\delta)^{3/2}}. \tag{234}$$

Finally, the separation between classes D and E can be determined considering $S_{c,D} = S_{c,E}$ which yields

$$xy = \frac{(1+\delta_k)^2}{\delta_k^3}. \tag{235}$$

Solving the equation $S_{c,C} = S_{c,D}$ we obtain

$$y = \left(\frac{1+\delta_k}{\delta_k}\right)^3 \tag{236}$$

which means that classes C and D have only a single point in common on the (δ,x) plane. Putting $y^{-1} = 0.272$ (cf. equation 218) it turns out that $\delta \approx 1.86$. This result means that class D fluctuations do not exist for $\delta < 1.8$ and that class C fluctuations do not exist for $\delta > 1.8$.

In Figure 45 we represent the regions in the (δ,x) plane corresponding to the classes of perturbations listed in Table 26. Notice that we must distinguish between the average cosmological background and the state of matter on a particular overdense region. For example, when $x = 10^{-0.6} \approx 0.25$ the average cosmological background is already in the hadron phase ($0.25 < y^{-1}$) but an overdense region with, for example, $\delta = 0.9$ continues to be in the mixed phase. This is because overdense regions do not expand with the rest of the background Universe and, so, the state of matter on those regions evolve slower. That is why the border between classes E and F (for example) is a function of δ (i.e. depends on the amplitude of the fluctuation) instead of being just a simple horizontal line.

5.3.2 Lattice Fit

Let us now consider how a fluctuation evolves during a first–order QCD phase transition according to the Lattice Fit (Section 2.3.2). We adopt a model similar to the one considered for the Bag Model (Section 5.3.1). One difference is that, in the case of the Lattice Fit, the mixed phase period is shorter. Another difference is that before the mixed phase (i.e. during the last instants of the quark–gluon phase) the reduction on the sound speed value is not abrupt (see e.g. Figure 30).

In order to characterize the horizon crossing time and the turnaround point we make use, once again, of x and y as defined by equations (213) and (214). We consider also the six different classes of fluctuations shown on Table 26. Equation (217), which gives x as a function of time, continues to be valid here

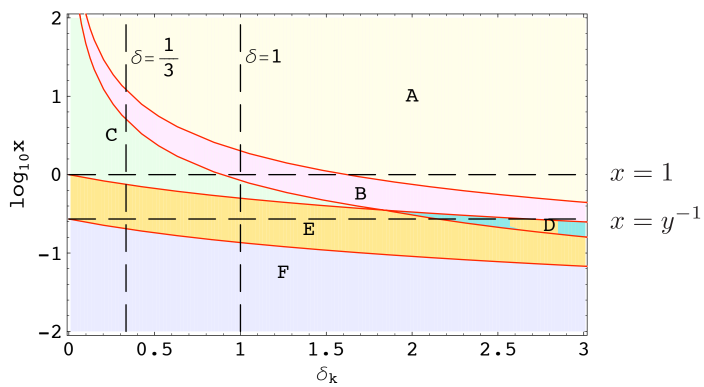

Figure 45: Regions in the (δ,x) plane corresponding to the classes of perturbations listed in Table 26 for the QCD Bag Model case. The variable x identifies the epoch when a perturbation enters the horizon: $x > 1$ ($x < 1$) corresponds to overdense regions that enter the horizon before (after) the average cosmological density begins the transition from the QGP to the HG. The quantity δ_k is the overdensity $\Delta\rho/\bar{\rho}$ of the perturbation at horizon crossing. A PBH will form if $1/3 \leq \delta_k < 1$. (adapted from Cardall & Fuller, 1998).

(as long as we do not move too far away from the transition epoch). The end of the transition is now given by

$$y^{-1} = x(t_+) = \frac{4g_{QGP}\left(\frac{t_-}{t_+}\right)^2 - g_{HG}}{4g_{QGP} - g_{HG}} \approx 0.729 \tag{237}$$

which differs from the Bag Model value (cf. equation 218) because in the case of the Lattice Fit we have a different value for t_- (cf. Table 20).

Equations (219) to (230), which gives the turnaround point for each class of fluctuation, and the values of S_1 and S_2 are still valid here as long as we use the correct value for y (cf. equation 237). The same goes for equations (231) and (232), which give the separations between classes C, E, and F. However, the separations between classes A, B, and C, in the case of the Lattice Fit, are not given by equations (233) and (234). We have to derive a new set of equations in order to account for the influence of the period $t_k < t < t_-$ (see Section 7.3).

In Figure 46 we show the regions in the (δ,x) plane corresponding to the classes of fluctuations listed on Table 26 for the Lattice Fit case. We have considered that the sound speed stays equal to $1/\sqrt{3}$ outside the interval $t_- < t < t_+$ and vanishes inside (c.f. Bag Model – Figure 45). Note that by inserting $y^{-1} = 0.729$ into equation (236) we conclude that fluctuations of class D cannot exist, in the context of the Lattice Fit, for $\delta < 9.0$ and that fluctuations of class C cannot exist above $\delta \approx 9.0$.

As we mentioned above (cases A, B, and C) Figure 46 does not exactly say the truth. We show it only for comparison purposes.

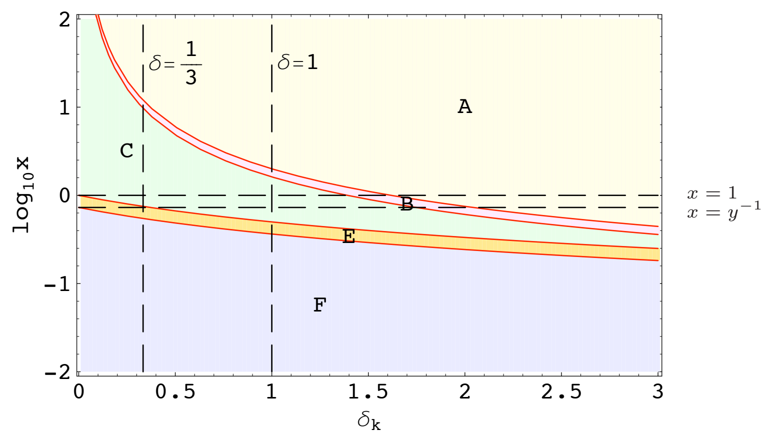

Figure 46: Regions in the $(\delta,\ \log_{10} x)$ plane corresponding to the classes of perturbations listed in Table 26 for the QCD Lattice Fit case (cf. Bag Model in Figure 45) – correct, except for A, B, and C (Section 7.3 gives the correct graph). Here we are considering that the sound speed vanishes in the interval $t_- < t < t_+$ and is equal to $1/\sqrt{3}$ outside this interval. Fluctuations of class D (not represented) cannot exist for $\delta_k < 9.0$. On the other hand fluctuations of class C cannot exist above $\delta_k \approx 9.0$ (see text for more details).

5.3.3 Crossover

We now consider the evolution of a fluctuation during the QCD Crossover. In this case there is no dust–like stage between the QGP plasma phase and the HG phase but rather a smooth change from one phase to the other. We assume that during the Crossover the Universe continues to be radiation–dominated[29]. Taking $w_k = w_c = 1/3$, equation (212), relating the size of the perturbed region at the horizon crossing time with the respective size at the turnaround point, can be written as[30]

$$S_c = R_k \left(\frac{1+\delta_k}{\delta_k} \right)^{1/2} . \tag{238}$$

We use this result for the entire Crossover. Here it does not make sense to consider different classes of fluctuations as we did for the Bag Model and the Lattice Fit (cf. Table 26). Expressions for S_c and R_k are obtained from the scale factor $R(t)$. In the case of a QCD Crossover, the scale factor $R(t)$ is given

[29]Although the adiabatic index decreases a bit during the transition, we assume $w = 1/3$ as a good approximation. During a first–order transition, the decrease on the value of w is more pronounced and although it does not reach zero (pure dust–like phase) we assume $w = 0$ (see e.g. Schmid et al., 1999).

[30]Here, we consider $K_s/K_k = 1$. If one uses the correct values for w_k and w_c then, we would have K_s/K_k, very close, but not necessarily equal to unity.

by equation (86). Thus, we have

$$R_k = R(t_k) = \exp\left(c\sqrt{\frac{\Lambda}{3}}(t_{SN} - t_0)\right)\left(\frac{t_{eq}}{t_{SN}}\right)^{2/3}\left(\frac{t_k}{t_{eq}}\right)^{1/2} \tag{239}$$

and

$$S_c = R(t_c) = \exp\left(c\sqrt{\frac{\Lambda}{3}}(t_{SN} - t_0)\right)\left(\frac{t_{eq}}{t_{SN}}\right)^{2/3}\left(\frac{t_c}{t_{eq}}\right)^{1/2}. \tag{240}$$

Inserting expressions (239) and (240) into equation (238) we obtain a relation between the horizon crossing time t_k and the turnaround time t_c as

$$t_c = t_k \frac{1+\delta_k}{\delta_k}. \tag{241}$$

5.4 Fluctuations during the EW phase transition

5.4.1 Crossover (SMPP)

We now describe the evolution of a fluctuation during the EW Crossover in the same way that we did for the QCD Crossover case (cf. Section 5.3.3). Thus, R_k and S_c are given, once again, by expressions (239) and (240). In addition, the relation between the turnaround instant t_c and the horizon crossing time t_k is given by expression (241).

5.4.2 Bag Model (MSSM)

Let us consider how a fluctuation evolves in the presence of a first–order EW phase transition according to the Bag Model. Here we continue to follow the model proposed by Cardall & Fuller (1998) for the QCD first–order phase transition (see Section 5.3.1). Considering the possible locations of t_k and t_c, we define six different classes of density fluctuations (Table 27).

It is very useful to have x as a function of time. We get this by adapting equation (217) derived for the QCD case. Thus, we have

$$x(t) = \frac{4g'_{EW}\left(\frac{R(t_{EW-})}{R(t)}\right)^3 - g_{EW}}{4g'_{EW} - g_{EW}} \tag{242}$$

which is valid only in the neighborhood of the EW transition. Here $R(t_{EW-})$ is given by equation (73) and $R(t)$ is given by: i) equation (71) if $x \le y^{-1}$; ii) equation (72) if $y^{-1} < x < 1$; iii) equation (73) if $x \ge 1$.

The value of y, which defines the end of the EW transition, can now be determined evaluating $x(t_{EW+})$. If one assumes $\Delta g \approx 80$ and $g_{EW} = 95.25$ (see Section 3.2.2), then one obtains

$$y^{-1} = x(t_{EW+}) = \frac{4g'_{EW}\left(\frac{t_{EW-}}{t_{EW+}}\right)^2 - g_{EW}}{4g'_{EW} - g_{EW}} \approx 0.460. \tag{243}$$

Table 27: Classification of overdense regions according to the state of matter at the horizon crossing and at turnaround for the EW first–order phase transition.

Class	Horizon Crossing phase	Turnaround phase
A	high	high
B	high	mixed
C	high	low
D	mixed	mixed
E	mixed	low
F	low	low

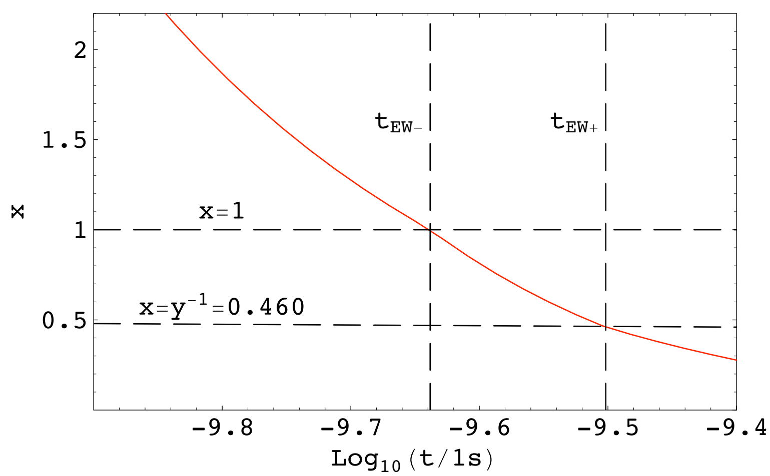

Figure 47: The function $x(t)$ for the EW Bag Model–like phase transition (equation 242).

In Figure 47 we show the curve $x(t)$. Equations (219) to (236), derived for the QCD transition, are quite general and, hence, we simply adopt them here without making any changes.

Inserting $y^{-1} = 0.460$ into equation (236) it turns out that $\delta \approx 3.4$. This result means that class D fluctuations do not exist for $\delta < 3.7$ and that class C fluctuations do not exist for $\delta > 3.7$.

5.5 Fluctuations during the e^+e^- annihilation

We now describe the evolution of a fluctuation during the cosmological electron–positron annihilation process in the same way that we did for the QCD Crossover case (cf. Section 5.3.3). Thus, R_k and S_c are, once again, given by expressions (239) and (240). In addition, the relation between the turnaround instant t_c and the horizon crossing time t_k will be given by expression (241).

6 PBH formation

6.1 The condition for PBH formation

The collapse of an overdense region, forming a BH, is possible only if the *root mean square* of the primordial fluctuations, averaged over a Hubble volume, is larger than a threshold δ_{min}. There is also an upper bound δ_{max} corresponding to the case for which a separate Universe will form. Thus a PBH will form when the density contrast δ, averaged over a volume of the linear size of the Hubble radius, satisfies (Carr, 1975)

$$\delta_{min} \leq \delta \leq \delta_{max}. \tag{244}$$

The lower and upper bounds of δ can be determined following analytic arguments. Consider, for simplicity, a spherically–symmetric region with radius R and density $\rho = \rho_c + \delta\rho$ embedded in a flat Universe with the critical density ρ_c. Within spherical symmetry the inner region is not affected by matter in the surrounding part of the Universe. The expansion of this region will come to an halt, at some stage, followed by a collapse. In order to reach a complete collapse, the potential energy, V, at the time of maximal expansion (e.g. Kiefer, 2003)

$$V \sim \frac{GM^2}{R} \sim G\rho^2 R^5 \tag{245}$$

has to exceed the inner energy, U, given by (e.g. Kiefer, 2003)

$$U \sim pR^3 \tag{246}$$

where p is the pressure. In the radiation–dominated era (which is the era of interest for PBH formation) an overdense region will collapse to a BH provided that the size of the region, when it stops expanding, is bigger than the *Jeans Length*[31] R_J (e.g. Kiefer, 2003)

$$R \geq R_J = \sqrt{\frac{1}{3G\rho}}. \tag{247}$$

In order to prevent the formation of a separate Universe we must ensure, also, that the radius of the collapsing region, R, is smaller than the curvature radius of the overdense region at the moment of collapse (e.g. Kiefer, 2003)

$$R < \frac{1}{\sqrt{G\rho}}. \tag{248}$$

One then has the condition

$$1 > R \geq \sqrt{\frac{1}{3}}, \tag{249}$$

[31] The Jeans Length is the critical radius of a region where thermal energy, which causes the region to expand, is counteracted by gravity; this causes the region to collapse.

which is evaluated at the time of collapse, for the formation of the PBH. In particular, when the fluctuation enters the horizon in a radiation–dominated Universe, one gets (e.g. Carr, 1975; Kiefer, 2003)

$$\delta_{min} \equiv \frac{1}{3} \leq \delta < 1 \equiv \delta_{max}, \tag{250}$$

where the lower bound comes from condition (247) and the upper bound comes from condition (248). The extreme δ_{max} corresponds to the situation for which a separate Universe forms and δ_{min} corresponds to the threshold of PBH formation. If $\delta < \delta_{min}$ the fluctuation dissipates and there is no PBH formation (see Section 2.4.3 of Sobrinho & Augusto, 2007).

The correct value of δ_{min} has been a matter of discussion (see Table 3 of Sobrinho & Augusto, 2007). We have already seen that the value $\delta_{min} = 1/3$ is suggested by analytic arguments. However, numerical simulations considering critical phenomena in the PBH formation (see Section 2.4.1 of Sobrinho & Augusto, 2007) reveal a higher value, $\delta_{min} \approx 0.7$, which is almost twice the old value. Another study using *peaks theory* (Green et al., 2004) leads to $\delta_{min} \approx 0.3 - 0.5$, which is in good agreement with the analytic approach ($\delta_{min} = 1/3$). Taking into account that the threshold δ_{min} arises from critical behaviour, we will refer to δ_{min} in the rest of the text as δ_c.

The value of the threshold δ_c is constant, with some exceptions, throughout the radiation–dominated Universe. Exceptions are phase transitions (Sections 2 and 3) and annihilation processes (Section 4). During these epochs the speed of sound vanishes or, at least, diminishes and, as a result, δ_c becomes smaller (Sections 7, 8 and 9). This is very important because a smaller δ_c will favour PBH production (Section 11). The condition for PBH formation is written as

$$\delta_c \leq \delta < 1. \tag{251}$$

For radiation domination ($w = 1/3$), the size of the overdense region at turn-around (i.e. at the moment when the kinetic energy of the expansion is zero), its Schwarzschild radius, the Jeans length, and the cosmological horizon size are all of the same order of magnitude. On the contrary, for dust domination ($w = 0$), the Jeans length is much smaller than the horizon size. For an overdense region that experiences a radiation phase for much of its evolution and a dust–like phase for the rest we define an *effective Jeans length* (e.g. Cardall & Fuller, 1998)

$$R_{J,eff} = \sqrt{\frac{1}{3G\rho_c}\,(1-f)} \tag{252}$$

where f denotes the fraction of the overdense region spent in the dust–like phase of the transition.

6.2 The mechanism of PBH formation

The ultimate fate of an initially super–horizon density fluctuation, upon horizon crossing, is mainly determined by a competition between dispersing pressure forces and the fluctuations self–gravity. For a radiation–dominated Universe there is an approximate equality between the Jeans mass, M_J, and the horizon mass, M_H. For a fluctuation exceding a critical threshold δ_c at horizon crossing, gravity dominates and a PBH forms. On the other hand, a fluctuation with $\delta < \delta_c$ is dispersed by pressure forces (e.g. Jedamzik & Niemeyer, 1999).

The pressure response of a radiation fluid is given by equation (14). Any decrease of the pressure response of the radiation fluid may yield a reduction of the threshold δ_c. Such a behaviour is expected to occur during cosmological first–order phase transitions (e.g. Jedamzik & Niemeyer, 1999).

A reduction of the PBH formation threshold for fluctuations which enter the cosmological horizon during first–order phase transitions may have cosmological implications, even if only modest. The slightest reduction of δ_c may result in the formation of PBHs with masses of the order of the horizon mass during the first–order phase transition, yielding a highly peaked PBH mass function (e.g. Jedamzik & Niemeyer, 1999).

Jedamzik & Niemeyer (1999) studied the evolution of density fluctuations upon horizon crossing during a cosmological first–order phase transition. In Figure 48 we show, as an example, the evolution of the radial energy density profile of a fluctuation, with overdensity $\delta = 0.535$, from the initial horizon crossing time t_0 to $20.1t_0$. The fluctuations self–gravity exceeds pressure forces such that the fluctuation separates from the Hubble flow and recollapses to high–energy densities at the center until an event horizon forms ($t \approx 5t_0$). The resulting young PBH rapidly increases its mass up to $M_{PBH} \approx 0.06M_H(t_0)$ ($t \approx 5.5t_0$). Subsequent accretion of material on the young PBH continues until the immense pressure gradients close to the event horizon launch an outgoing pressure wave which significantly dilutes the PBH environment. Accretion thereafter is negligible. As a result we have, in this example, the formation of a PBH with initial mass $M_{PBH} \approx 0.34M_H(t_0)$.

The existence of a phase transition facilitates the PBH formation process as is evident from Figure 49. Figure 49 is a zoom into the core of the fluctuation shown in Figure 48. For comparison, this figure also shows the evolution of a fluctuation with the same initial conditions, but entering the cosmological horizon during an ordinary radiation–dominated epoch, by the dotted line. The strong pressure gradients experienced by the fluctuation entering the horizon during an epoch with EoS $p = \rho/3$ prevent, in this case, the formation of a PBH (Jedamzik & Niemeyer, 1999).

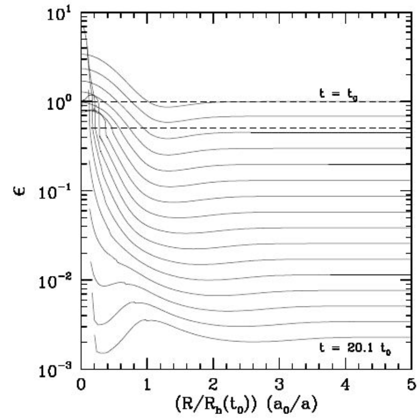

Figure 48: Energy density, ϵ, as a function of scaled circumferential radius, $R_{sc} = (R/R_k(t_0))(a_0/a)$, for a fluctuation with initial density contrast $\delta = 0.535$ at horizon crossing. The initial horizon at t_0 is located at $R_{sc} = 1$. From top to bottom, solid lines show the fluctuation at 1., 1.22, 1.49, 1.82, 2.23, 2.72, 3.32, 4.06, 4.95, 6.05, 7.39, 9.03, 11.0, 13.5, 16.4, and 20.1 times the initial time t_0. The two horizontal dotted lines indicate the regime of energy densities in which fluid elements exist within mixed phases. The formation of a PBH with $M_{pbh} \approx 0.34 M_H(t_0)$ results (Jedamzik & Niemeyer, 1999).

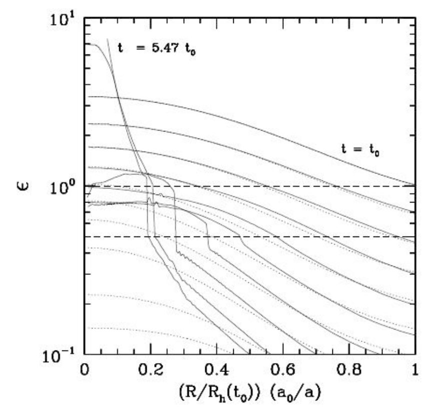

Figure 49: A zoom into the upper left region of Figure 48. From top to bottom, solid lines show the fluctuation at 1.0, 1.22, 1.49, 1.82, 2.22, 2.72, 3.32, 4.06, 4.95, and 5.47 times the initial time t_0. The horizontal dashed lines indicate the energy densities at onset and completion of the phase transition. The dotted lines show, for comparison, the evolution of a fluctuation with the same initial fluctuation parameters, but entering the cosmological horizon during an epoch with EoS $p = \rho/3$ (Jedamzik & Niemeyer, 1999).

7 The threshold δ_c during the QCD epoch

7.1 Bag Model

During a first–order QCD phase transition we replace the lower limit in the condition (251) by (e.g. Cardall & Fuller, 1998)

$$\delta_c \to \delta_c(1-f) \tag{253}$$

where f denotes the fraction of the overdense region spent in the dust–like phase. Therefore, the larger the fraction of time a fluctuation spends in the mixed phase regime, the smaller the required amplitude of the perturbation (at horizon crossing) for collapse into a BH (e.g. Cardall & Fuller, 1998). Next, we present the expressions for f for each class of fluctuations of interest to us (cf. Table 26, e.g. Cardall & Fuller, 1998)

$$f_A = 0 \tag{254}$$

$$f_B = \frac{S_{c,B}^3 - S_1^3}{S_{c,B}^3} = 1 - \frac{x^{3/2}\delta_k^3}{(1+\delta_k)^{3/2}} \tag{255}$$

$$f_C = \frac{S_{2_C}^3 - S_1^3}{S_{c,C}^3} = \frac{x^{3/4}\delta_k^{3/2}}{y^{1/2}(1+\delta_k)^{3/4}}(y-1) \tag{256}$$

$$f_E = \frac{S_{2_{EF}}^3 - S_1^3}{S_{c,E}^3} = \frac{(xy)^{1/2}\delta_k^{3/2}}{1+\delta_k}(1-y^{-1}) \tag{257}$$

$$f_F = \frac{S_{2_{EF}}^3 - S_1^3}{S_{c,F}^3} = \frac{(xy)^{3/4}\delta_k^{3/2}}{(1+\delta_k)^{3/4}}(1-y^{-1}) \tag{258}$$

where the quantities S_1, S_{2_C}, $S_{2_{EF}}$, $S_{c,B}$, $S_{c,C}$, $S_{c,E}$, and $S_{c,F}$ are given by equations (225), (226), (227), (228), (229), (230), and (219), respectively.

In the next section we study PBH formation during the QCD phase transition, from fluctuations of classes A, B, C, E and F, according to the Bag Model. We divide the study into Before, During, and After. At the end of the section we compile the results. The study will mostly be done for $\delta_c = 1/3$ but we will also consider the effect of larger values of δ_c (up to 0.7).

7.1.1 Before the mixed phase

When $x \geq 1$ we are dealing with fluctuations of classes A, B or C (cf. Figure 45). For a given x we can determine, with the help of equations (233) and (234), the range of amplitudes which correspond to each class.

For example, for the case $x = 2$, we have from equation (233), that[32] $\delta = 1$, and from equation (234) that $\delta \approx 0.58$. This means that when $x = 2$ the

[32]In order to simplify the writing we represent the density constrast at the horizon crossing time t_k by δ (instead of δ_k).

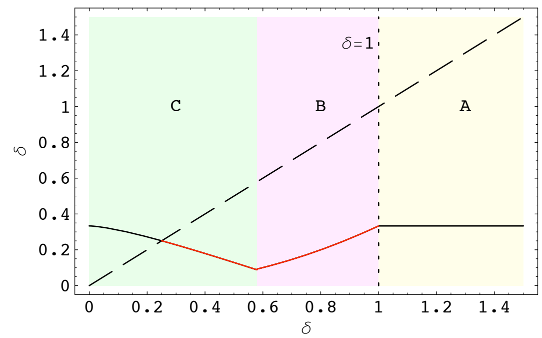

Figure 50: PBH formation during the QCD transition according to the Bag Model for the case $x = 2$ and $\delta_c = 1/3$. The solid curve corresponds to the function $(1 - f)\delta_c$ and the dashed curve to the identity δ. The pink region corresponds to fluctuations of class B (see text). To the left of this region we have fluctuations of class C (green) and to the right fluctuations of class A (yellow). The borders between the different classes are given by $\delta_{AB} = 1$ and $\delta_{BC} \approx 0.58$. Collapse to a BH occurs for values of δ for which the dashed line is above the solid curve (while $\delta < 1$). The intersection point at $\delta \approx 0.25$ marks a new threshold δ_{c1} for PBH formation (adapted from Cardall & Fuller, 1998).

overdensity will be of class C if $0 < \delta < 0.58$, of class B if $0.58 < \delta < 1$ and of class A if $\delta > 1$.

In order to identify the values of δ for which collapse to a BH occurs (when $x = 2$ and $\delta_c = 1/3$), we plot in Figure 50 both $(1-f)\delta_c$ and δ itself as functions of δ. Notice that one should use the function f appropriate to each class (i.e. f_A – equation 254; f_B – equation 255; f_C – equation 256). We can, then, have PBHs formed from fluctuations of classes B and C only, since fluctuations of class A would lead to the formation of a separate Universe (since for them we always have $\delta > 1$)–Section 6.1.

Fluctuations of class C with $\delta < 0.25$ dissipate before forming a PBH. This point $\delta_{c1} \approx 0.25$ marks a new and lower threshold for PBH formation during the QCD phase transition when $x = 2$.

In Figure 51 we plot the cases: (a) $x = 15$, (b) $x = 30$, and (c) $x = 90$ with $\delta_c = 1/3$ for all the three cases. In the case $x = 15$ there are two regions for which PBH formation is allowed: i) a region for $\delta \geq 1/3$, which corresponds to PBH formation from fluctuations of class A during the radiation–dominated Universe; ii) a region between $\delta_{c1} \approx 0.15$ and $\delta_{c2} \approx 0.27$ corresponding to the formation of PBHs from fluctuations of classes B and C. The gap between $\delta = 0.27$ and $\delta = 1/3$ corresponds to: i) fluctuations of class A which dissipate because they have $\delta < 1/3$; ii) fluctuations of class B which dissipate because they do not spend enough time on the dust–like phase, allowing collapse to begin.

The case $x = 30$ is similar to the case $x = 15$. Notice, however, that now the

Table 28: The value of x corresponding to the intersections points $\delta_{c2} = \delta_c$ and $\delta_{c1} = \delta_{c2}$ as a function of δ_c, for the QCD phase transition according to the Bag Model.

δ_c	$\delta_{c2} = \delta_c$	$\delta_{c1} = \delta_{c2}$
1/3	12.0	54.8
0.4	8.8	38.7
0.5	6.0	25.4
0.6	4.5	18.0
0.7	3.5	13.4

region $[\delta_{c1}, \delta_{c2}]$ is much smaller. In the case $x = 90$ the fluctuations of classes B and C do not lead any longer to the formation of PBHs.

Figure 52 indicates the region in the (x, δ) plane for which collapse to a BH occurs ($x > 1$ and $\delta_c = 1/3$). Without the phase transition, this would be a straight horizontal line at $\delta = 1/3$. The intersection points $\delta_{c1} = \delta_{c2}$ ($x \approx 54.8$) and $\delta_{c2} = \delta_c = 1/3$ ($x \approx 12.0$) turn out to be very important for the calculation of β (see Section 11).

In Figure 53 we consider, again, the cases $x = 2$, $x = 30$ and $x = 90$ but now with δ_c assuming several values between 1/3 and 0.7. The new window for PBH formation, i.e., the region between δ_{c1} and δ_c or δ_{c2}, is larger for smaller values of δ_c.

Figure 54 shows the region in the (x, δ) plane for which collapse to a BH occurs with $x > 1$ for $\delta_c = 1/3$ and for $\delta = 0.7$. Without the phase transition, these would be two straight horizontal lines at $\delta = 1/3$ and $\delta = 0.7$. The intersection points $\delta_{c1} = \delta_{c2}$ ($x \approx 54.8$ when $\delta_c = 1/3$; $x \approx 13.6$ when $\delta_c = 0.7$) and $\delta_{c2} = \delta_c$ ($x \approx 12.0$ when $\delta_c = 1/3$; $x \approx 3.5$ when $\delta_c = 0.7$) are relevant for the calculus of β (see Section 11). For more examples see Table 28 where we show the results for other values of δ_c between the limits 1/3 and 0.7.

We interpolated the values presented in Table 28 in order to obtain the relation $x(\delta_c)$ for the special cases $\delta_{c1} = \delta_{c2}$ and $\delta_{c2} = \delta_c$. We obtained the cubic polynomials

$$x_{\delta_{c1}=\delta_{c2}}(\delta_c) \approx -843.192\delta_c^3 + 1620.83\delta_c^2 - 1083.54\delta_c + 266.998 \tag{259}$$

$$x_{\delta_{c2}=\delta_c}(\delta_c) \approx -164.72\delta_c^3 + 317.654\delta_c^2 - 214.03\delta_c + 54.1305 \tag{260}$$

which are represented in Figure 55. In Table 29 we have a compilation of the values of δ_{AB}, δ_{BC}, δ_{c1} and δ_{c2} for different values of x and δ_c.

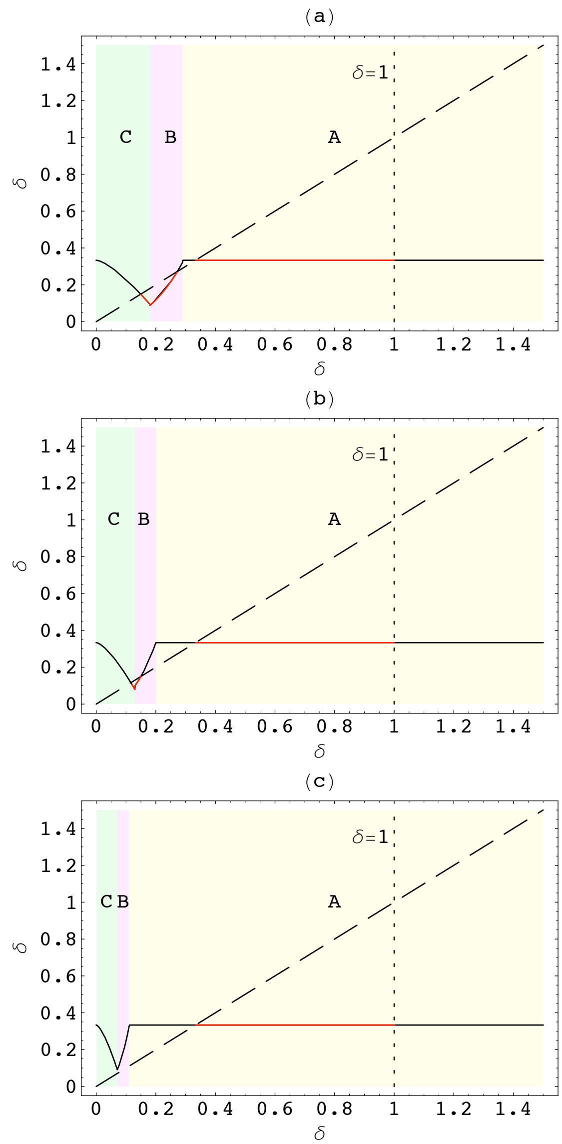

Figure 51: PBH formation during the QCD transition according to the Bag Model for the cases: (a) $x = 15$, (b) $x = 30$, and (c) $x = 90$; with $\delta_c = 1/3$. The solid curve corresponds to the function $(1 - f)\delta_c$ and the dashed curve corresponds to the identity δ. The borders between the different classes are given by: (a) $\delta_{AB} \approx 0.29$, $\delta_{BC} \approx 0.18$; (b) $\delta_{AB} \approx 0.20$, $\delta_{BC} \approx 0.13$; and (c) $\delta_{AB} \approx 0.11$, $\delta_{BC} \approx 0.07$. Collapse to a BH occurs for values of δ for which the dashed line is above the solid curve (while $\delta < 1$). In the case $x = 15$ we have three intersections points: $\delta_{c1} \approx 0.15$, $\delta_{c2} \approx 0.27$ and $\delta_c = 1/3$. This means that we now have two regions for PBH formation: $0.15 \leq \delta \leq 0.27$ and $1/3 \leq \delta < 1$. In the case $x = 30$ we have $\delta_{c1} \approx 0.12$ and $\delta_{c2} \approx 0.15$ (see text and Figure 50 for more details, adapted from Cardall & Fuller, 1998).

Table 29: The values of δ_{AB}, δ_{BC}, δ_{c_1} and δ_{c_2} (where applicable) for different values of x (with $x > 1$) and δ_c for the QCD phase transition according to the Bag Model (see Figures 50, 51 and 53).

x	δ_c	δ_{AB}	δ_{BC}	δ_{c_1}	δ_{c_2}
2	1/3	1	0.58	0.25	–
15		0.29	0.18	0.15	0.27
30		0.20	0.13	0.12	0.15
90		0.11	0.07	–	–
2	0.4	1	0.58	0.28	–
15		0.29	0.18	0.16	0.24
30		0.20	0.13	0.12	0.14
90		0.11	0.07	–	–
2	0.5	1	0.58	0.33	–
15		0.29	0.18	0.17	0.21
30		0.20	0.13	–	–
90		0.11	0.07	–	–
2	0.6	1	0.58	0.36	–
15		0.29	0.18	0.18	0.19
30		0.20	0.13	–	–
90		0.11	0.07	–	–
2	0.7	1	0.58	0.39	–
15		0.29	0.18	–	–
30		0.20	0.13	–	–
90		0.11	0.07	–	–

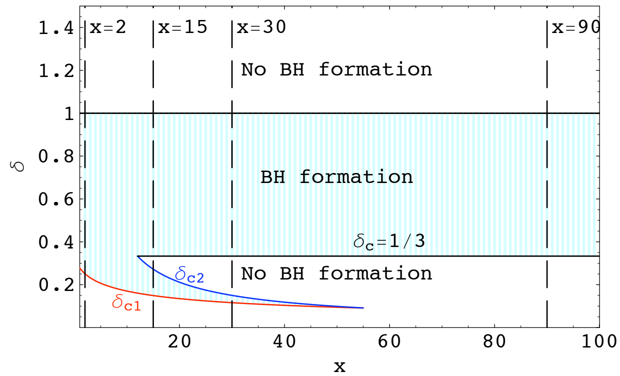

Figure 52: The curve in the (x, δ) plane indicating which parameter values lead to collapse to a BH, according to the QCD Bag Model, in the case $x > 1$ and $\delta_c = 1/3$. We show the values of x corresponding to the cases presented in Figures 50 and 51. The intersection point $\delta_{c1} = \delta_{c2}$ corresponds to $x \approx 54.8$ and the intersection point $\delta_{c2} = \delta_c = 1/3$ corresponds to $x \approx 12.0$. (adapted from Cardall & Fuller, 1998).

7.1.2 During the mixed phase

When $y^{-1} < x < 1$ we are dealing with fluctuations of classes B, C or E (cf. Figure 45). Notice that fluctuations of class A could reach also the range $y^{-1} < x < 1$ but only if they have $\delta > 1$ which leads to the formation of a separate Universe. For a given x we can determine, with the help of equations (231) and (234), the range of amplitudes which correspond to each class.

For example, for the case $x = 0.927$, we have, from equation (231), that $\delta \approx 0.079$ and from equation (234) that $\delta \approx 0.94$. This means that when $x = 0.927$ the overdensity will be of class E if $\delta < 0.079$, of class C if $0.079 < \delta < 0.94$ and of class B if $\delta > 0.94$. The division between class B and A occurs according to equation (233) when $\delta \approx 1.7$.

In Figure 56 we plot both $(1 - f)\delta_c$ and δ itself as functions of δ for the cases: (a) $x = 0.927$, (b) $x = 0.6$, and (c) $x = 0.308$ with $\delta_c = 1/3$ for all the three cases. The appropriate function f was used to each class (i.e. f_B – equation 255; f_C – equation 256; f_E – equation 257). In the case $x = 0.927$ PBHs are formed from fluctuations of classes B and C. Fluctuations of class C with $\delta < 0.28$ dissipate without forming a PBH. This point $\delta_{c1} \approx 0.28$ marks the new threshold for PBH formation during the QCD phase transition when $x = 0.927$.

In the case $x = 0.6$ PBHs can form from fluctuations of class C or class E, but no longer from fluctuations of class B. The new threshold for PBH formation is $\delta_{c1} \approx 0.29$. Finally, in the case $x = 0.308$ PBHs can only form from fluctuations of class E (the separation between classes E and C occurs for $\delta_{CE} \approx 2.24$). The new threshold for PBH formation is $\delta_{c1} \approx 0.30$.

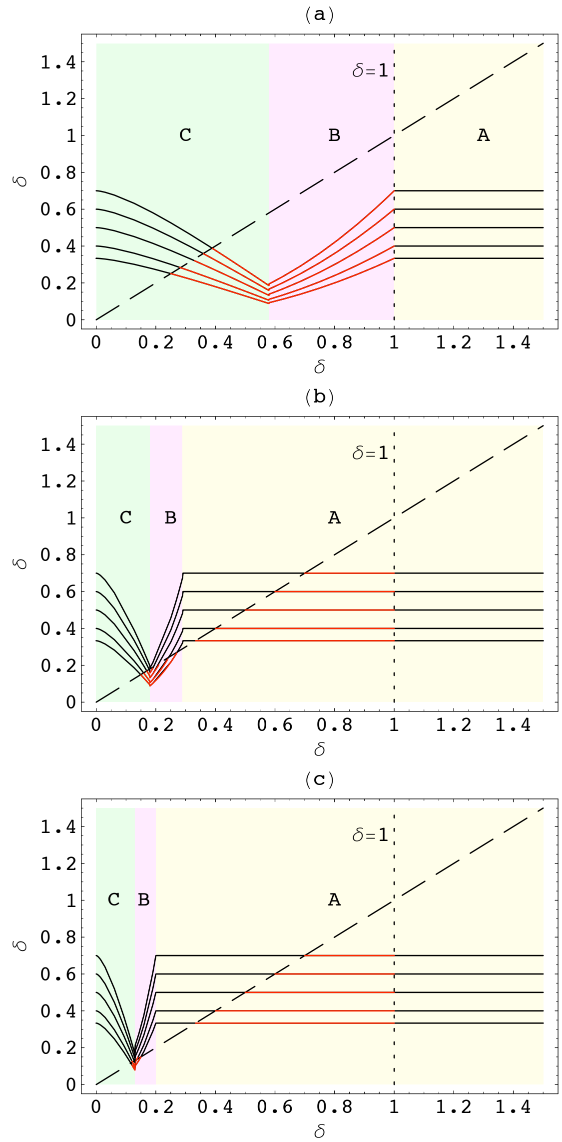

Figure 53: PBH formation during the QCD transition according to the Bag Model for the cases: (a) $x = 2$, (b) $x = 15$, and (c) $x = 30$. The solid curve corresponds to the function $(1 - f)\delta_c$ with, from bottom to top, $\delta_c = 1/3$, $\delta_c = 0.4$, $\delta_c = 0.5$, $\delta_c = 0.6$ and $\delta_c = 0.7$. In red we show the region where PBH formation takes place. The borders between the different classes (which do not depend on the value of δ_c) are given by: (a) $\delta_{AB} = 1$, $\delta_{BC} \approx 0.58$; (b) $\delta_{AB} \approx 0.29$, $\delta_{BC} \approx 0.18$; and (c) $\delta_{AB} \approx 0.20$, $\delta_{BC} \approx 0.13$ (see more details in Figures 50 and 51).

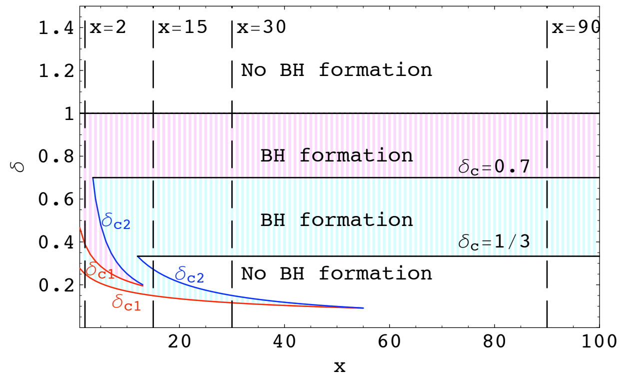

Figure 54: The curve in the (x, δ) plane indicating which parameter values lead to collapse to a BH, within the QCD Bag Model, in the case $x > 1$ with $\delta_c = 1/3$ and $\delta_c = 0.7$. We show the values of x corresponding to the cases presented in Figures 50, 51 and 53. The intersection point $\delta_{c1} = \delta_{c2}$ occurs for $x \approx 54.8$ when $\delta_c = 1/3$ and $x \approx 13.6$ when $\delta_c = 0.7$. The intersection point $\delta_{c2} = \delta_c = 1/3$ occurs for $x \approx 12.0$ when $\delta_c = 1/3$ and $x \approx 3.5$ when $\delta_c = 0.7$.

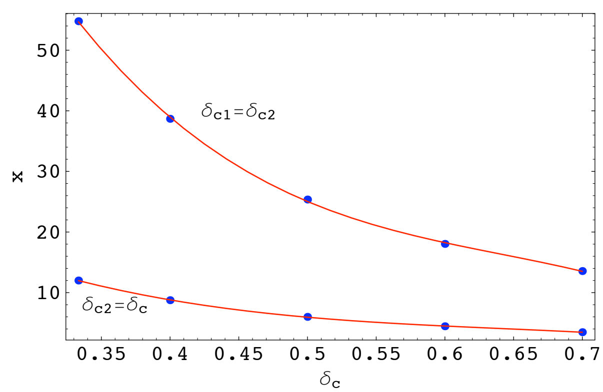

Figure 55: The value of x as a function of δ_c for the special cases $\delta_{c1} = \delta_{c2}$ and $\delta_{c2} = \delta_c$ for the QCD phase transition according to the Bag Model. The dots represent the values obtained numerically (see Table 28) and the solid lines represent the cubic interpolations (equations 259 and 260).

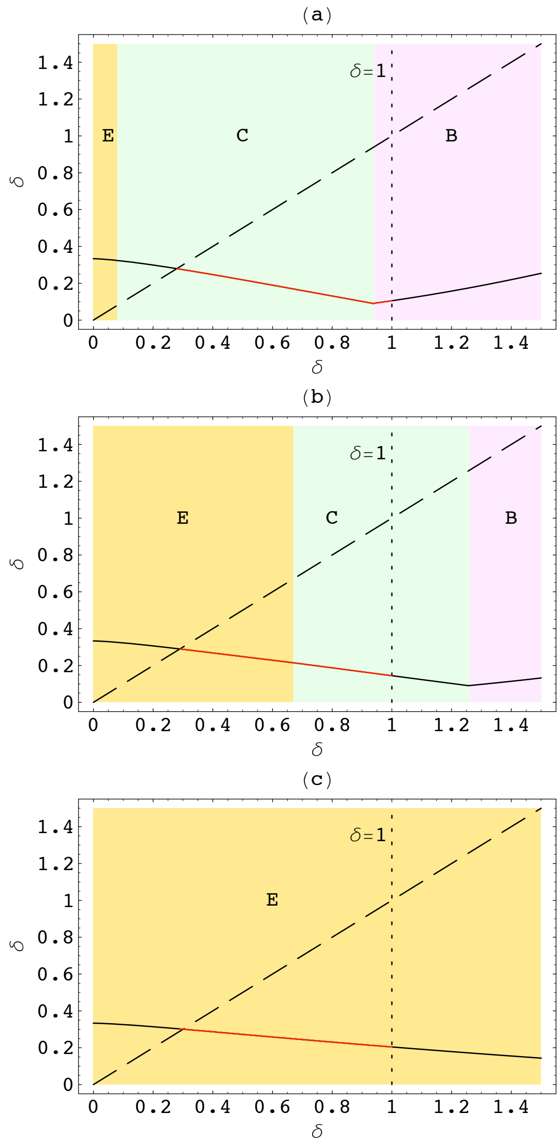

Figure 56: PBH formation during the QCD transition according to the Bag Model for the cases: (a) $x = 0.927$, (b) $x = 0.6$, and (c) $x = 0.308$ with $\delta_c = 1/3$ for all the three cases. The solid curve corresponds to the function $(1 - f)\delta_c$ and the dashed curve corresponds to the identity δ. The borders between the different classes are given by: (a) $\delta_{CE} \approx 0.079$, $\delta_{BC} \approx 0.94$; (b) $\delta_{CE} \approx 0.67$, $\delta_{BC} \approx 1.26$; and (c) $\delta_{CE} \approx 2.24$ (not shown). The new threshold for BH formation is: (a) $\delta_{c1} \approx 0.28$, (b) $\delta_{c1} \approx 0.29$, and (c) $\delta_{c1} \approx 0.30$.

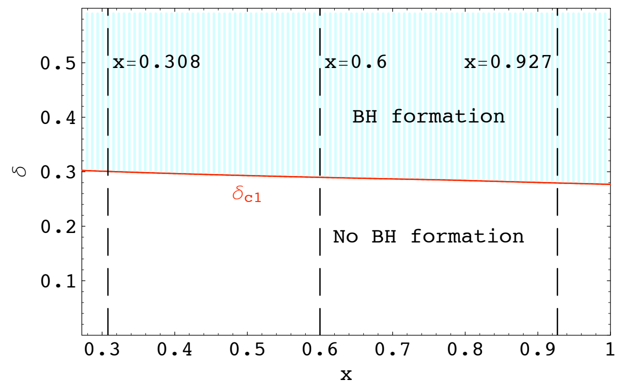

Figure 57: The curve in the (x, δ) plane indicating which parameter values lead to collapse to a BH, within the QCD Bag Model, in the case $y^{-1} < x < 1$ and $\delta_c = 1/3$ (note that the BH formation region extends up to $\delta = 1$). We show the values of x corresponding to the cases presented in Figure 56.

Figure 57 indicates the region in the (x, δ) plane for which collapse to a BH occurs when $y^{-1} < x < 1$ and $\delta_c = 1/3$. Without the phase transition, this would be a straight horizontal line at $\delta = 1/3$.

In Figure 58 we consider, again, the cases $x = 0.927$, $x = 0.6$ and $x = 0.308$ but now with δ_c assuming several values between 1/3 and 0.7. The window for PBH formation is larger for smaller values of δ_c.

Figure 59 indicates the region in the (x, δ) plane for which collapse to a BH occurs with $y^{-1} < x < 1$ for $\delta_c = 1/3$ and for $\delta = 0.7$. Without the phase transition, these would be two straight horizontal lines at $\delta = 1/3$ and $\delta = 0.7$. In Table 30 we show a compilation of the values of δ_{BC}, δ_{CE} and δ_{c1} for different values of x and δ_c.

7.1.3 After the mixed phase

When $x < y^{-1}$ we are dealing with fluctuations of classes E or F (cf. Figure 45). For a given x we can determine, with the help of equation (232) the range of amplitudes which corresponds to each class.

We consider the cases $x = 0.26$, $x = 0.22$, and $x = 0.11$. In Figure 60 we show the plots for $\delta_c = 1/3$, and in Figure 61 the plots for variable δ_c. When $x = 0.26$ or $x = 0.22$ we have BH formation from fluctuations of class E, and when $x = 0.11$, from fluctuations of class F.

In Figure 62 we show the region in the (x, δ) plane for which collapse to a BH occurs when $x < y^{-1}$ and $\delta_c = 1/3$ and, in Figure 63 the same but now with $\delta_c = 1/3$ and $\delta = 0.7$. In Table 31 we have a compilation of the values of δ_{EF} and δ_{c1} for different values of x and δ_c.

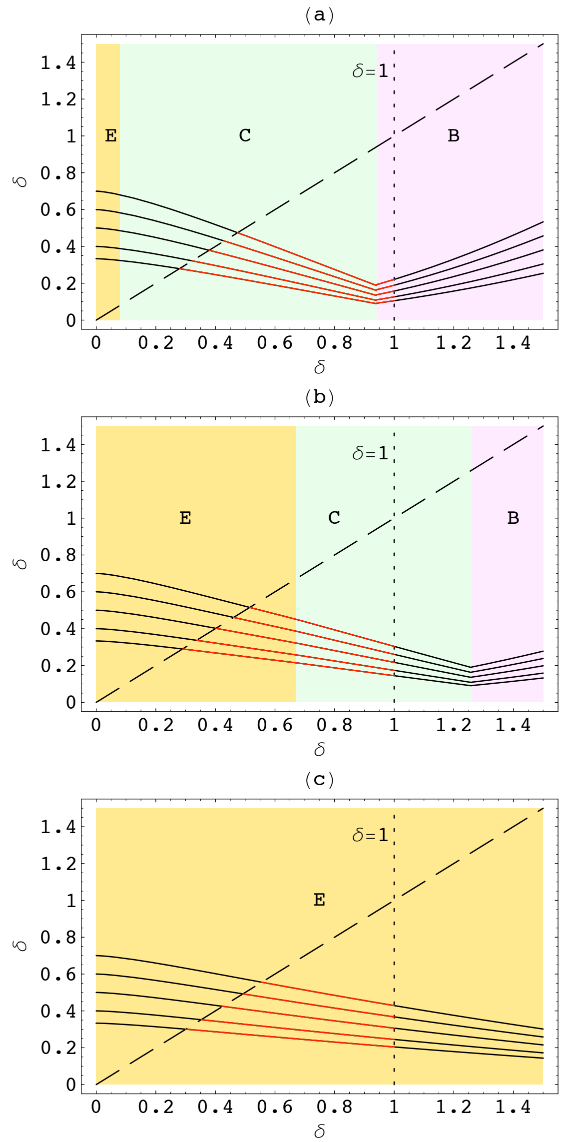

Figure 58: PBH formation during the QCD transition according to the Bag Model for the cases: (a) $x = 0.927$, (b) $x = 0.6$ and (c) $x = 0.308$. The solid curve corresponds to the function $(1-f)\delta_c$ with, from bottom to top, $\delta_c = 1/3$, $\delta_c = 0.4$, $\delta_c = 0.5$, $\delta_c = 0.6$ and $\delta_c = 0.7$. The dashed curve corresponds to the identity δ. The values of the borders between different classes are the same given in Figure 56 (they do not depend on the value of δ_c)

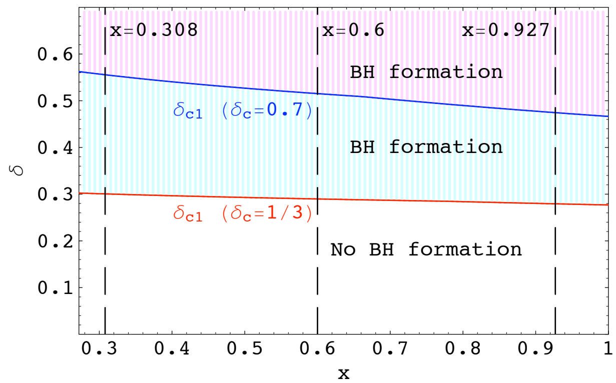

Figure 59: The curve in the (x, δ) plane indicating which parameter values lead to collapse to a BH, within the QCD Bag Model, in the case $y^{-1} < x < 1$ with $\delta_c = 1/3$–blue/pink region, and $\delta_c = 0.7$–pink region (note that, in both cases, the BH formation region extends up to $\delta = 1$). We show the values of x corresponding to the cases presented in Figures 56 and 58.

Table 30: The values of δ_{BC}, δ_{CE} and δ_{c_1} for different values of x ($y^{-1} < x < 1$) and δ_c for the QCD phase transition according to the Bag Model (Figures 56 and 58). Notice that we do not show a value for δ_{BC} when $x = 0.308$, since, in that case, class B has a border with class D rather than with class C (cf. equation (236) and Figure 45).

x	δ_c	δ_{BC}	δ_{CE}	δ_{c_1}
0.308	1/3	–	2.24	0.30
0.6		1.26	0.67	0.29
0.927		0.94	0.079	0.28
0.308	0.4	–	2.24	0.35
0.6		1.26	0.67	0.34
0.927		0.94	0.079	0.32
0.308	0.5	–	2.24	0.43
0.6		1.26	0.67	0.40
0.927		0.94	0.079	0.39
0.308	0.6	–	2.24	0.49
0.6		1.26	0.67	0.46
0.927		0.94	0.079	0.43
0.308	0.7	–	2.24	0.56
0.6		1.26	0.67	0.52
0.927		0.94	0.079	0.47

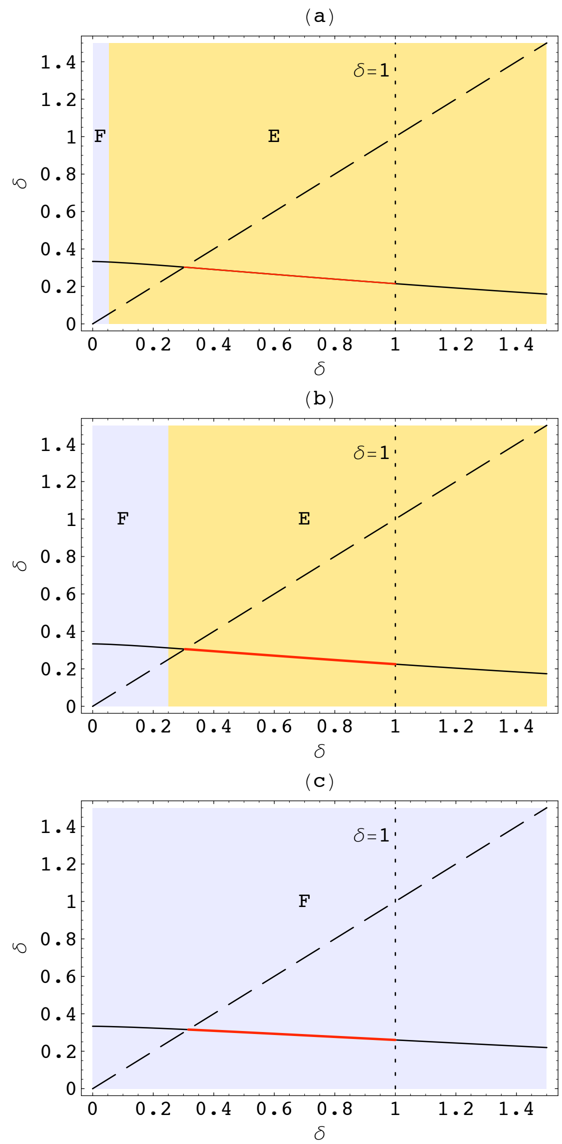

Figure 60: PBH formation during the QCD transition according to the Bag Model for the cases: (a) $x = 0.26$, (b) $x = 0.22$, and (c) $x = 0.11$ with $\delta_c = 1/3$ for all the three cases. The solid curve corresponds to the function $(1-f)\delta_c$ and the dashed curve corresponds to the identity δ. Notice that one should use the function f appropriate to each class (i.e., f_E – equation 257 or f_F – equation 258). The borders between the different classes are given by: (a) $\delta_{EF} \approx 0.053$; (b) $\delta_{EF} \approx 0.25$, and (c) $\delta_{EF} \approx 1.5$ (not shown). The new threshold for BH formation is: (a) $\delta_{c1} \approx 0.30$, (b) $\delta_{c1} \approx 0.31$, and (c) $\delta_{c1} \approx 0.32$. (adapted from Cardall & Fuller, 1998).

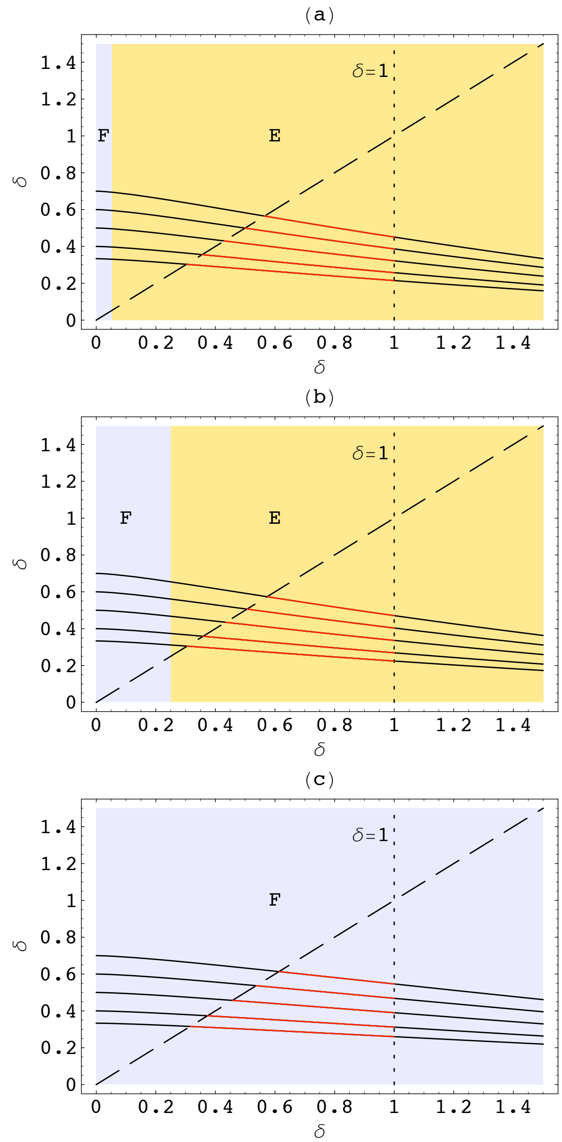

Figure 61: PBH formation during the QCD transition according to the Bag Model for the cases: (a) $x = 0.26$, (b) $x = 0.22$ and (c) $x = 0.11$. The solid curve corresponds to the function $(1-f)\delta_c$ with, from bottom to top, $\delta_c = 1/3$, $\delta_c = 0.4$, $\delta_c = 0.5$, $\delta_c = 0.6$ and $\delta_c = 0.7$. The dashed curve corresponds to the identity δ. The values of the borders between different classes are the same as given in Figure 60 (they do not depend on the value of δ_c).

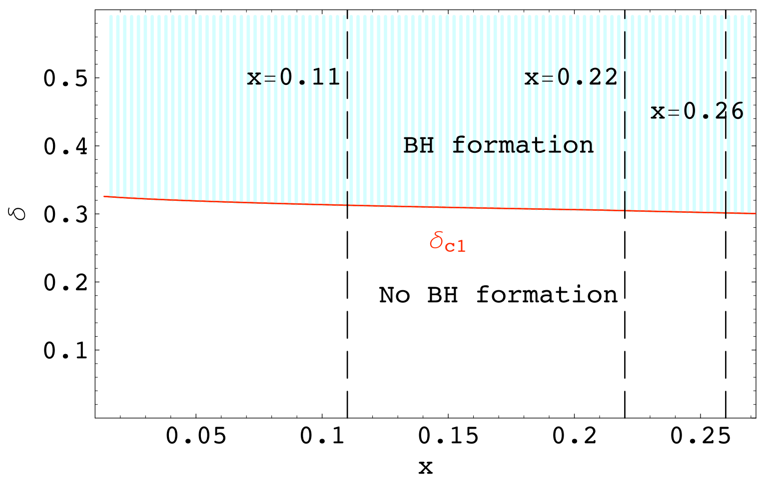

Figure 62: The curve in the (x, δ) plane indicating which parameter values lead to collapse to a BH, within the QCD Bag Model, in the case $x < y^{-1}$ and $\delta_c = 1/3$ (note that the BH formation region extends up to $\delta = 1$). We have indicated the values of x corresponding to the cases presented in Figure 60.

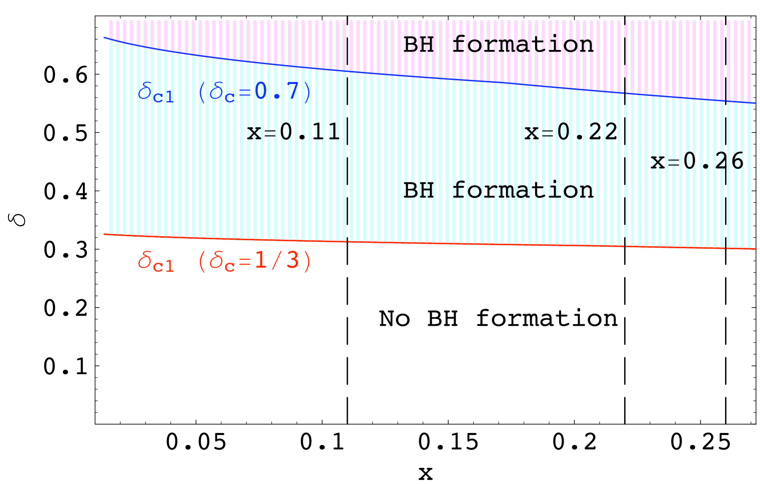

Figure 63: The curve in the (x, δ) plane indicating which parameter values lead to collapse to a BH, within the QCD Bag Model, in the case $y^{-1} < x < 1$ with $\delta_c = 1/3$–blue/pink region, and $\delta_c = 0.7$–pink region (note that the BH formation region extends, in both cases, up to $\delta = 1$). We show the values of x corresponding to the cases presented in Figures 60 and 61.

Table 31: The values of δ_{EF} and δ_{c_1} for different values of x ($x < y^{-1}$) and δ_c for the QCD phase transition according to the Bag Model (Figures 60 and 61).

x	δ_c	δ_{EF}	δ_{c_1}
0.26	1/3	0.053	0.30
0.22		0.25	0.31
0.11		1.5	0.32
0.26	0.4	0.053	0.36
0.22		0.25	0.36
0.11		1.5	0.37
0.26	0.5	0.053	0.43
0.22		0.25	0.43
0.11		1.5	0.46
0.26	0.6	0.053	0.50
0.22		0.25	0.51
0.11		1.5	0.54
0.26	0.7	0.053	0.56
0.22		0.25	0.57
0.11		1.5	0.61

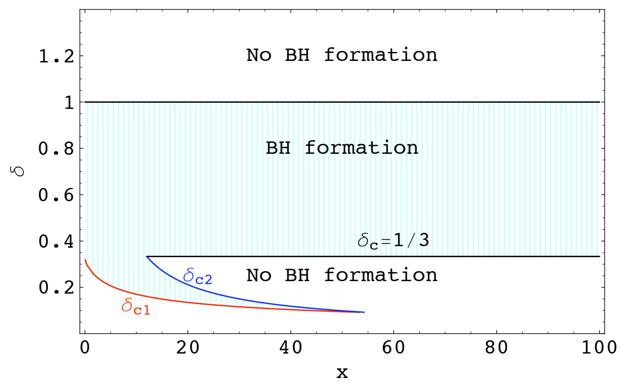

Figure 64: The curve in the $(x,\,\delta)$ plane indicating which parameter values lead to collapse to a BH when $\delta_c = 1/3$ (full QCD Bag Model). This Figure was obtained by joining Figures 52, 57 and 62.

7.1.4 Summary

We now compile the results obtained in Sections 7.1.1 to 7.1.3 (Bag Model). In particular, we have joined Figures 52, 57 and 62 in a single one in order to have a full picture of the QCD phase transition on the $(x,\,\delta)$ plane: Figure 64. Figure 65 represents the same scenario but now in the $(\log_{10} x,\,\delta)$ plane: a better representation if, for example, one wants to find the locus of the transition.

With the help of equation (217) we move from the$(\log_{10} x,\,\delta)$ plane into the $(\log_{10} t,\,\delta)$ plane. As a result, we get Figure 66 where we have also indicated the lines $t = t_-$ and $t = t_+$ (which mark the location of the transition).

During the QCD transition the threshold for PBH formation experiences a reduction. As a result, a new window for PBH formation (between δ_{c1} and δ_c or between δ_{c1} and δ_{c2}) is opened for a brief period. On Table 32 we present some values giving this new threshold for PBH formation during the QCD transition according to the Bag Model when $\delta_c = 1/3$. We have presented the values of δ_{c1} and δ_{c2} (where applicable) as a function of time and as a function of the parameter x.

7.2 Crossover Model

During the QCD Crossover a reduction on the value of the threshold δ_c is expected, due to the reduction on the sound speed. We need to determine the analogous of function f (see condition 253) for the QCD Crossover. This function f should account for the fact that we have a variable sound speed value during the Crossover and that a smaller value of $c_s(t)$ contributes more significantly to the reduction of δ_c than a larger one. We then introduce the function

$$\alpha(t) = 1 - \frac{c_s(t)}{c_{s0}} \tag{261}$$

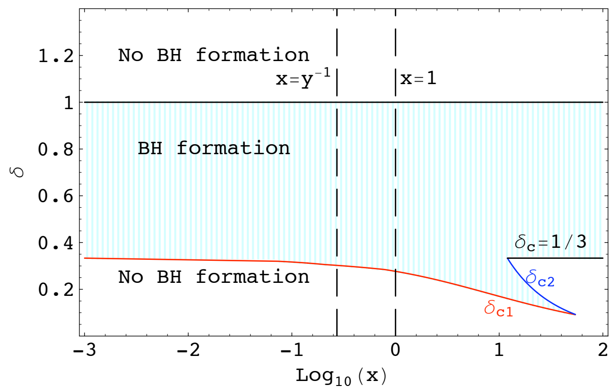

Figure 65: The same as Figure 64 but now with δ as a function of $\log_{10}(x)$. This representation is better if one wants to represent the lines $x = 1$ and $x = y^{-1}$: then give the locus of the QCD phase transition.

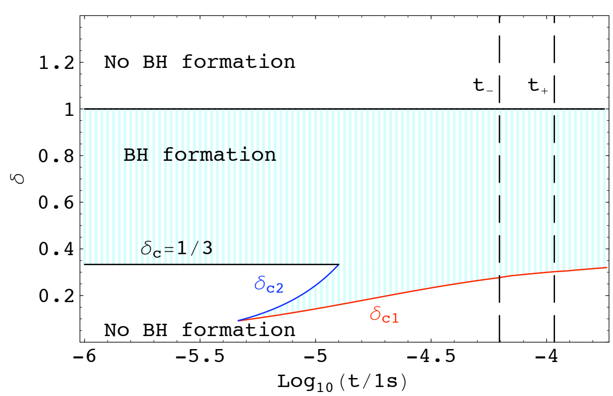

Figure 66: The same as in Figure 65 but now with δ as a function of $\log_{10}(t/1\ \mathrm{s})$. We also represent the lines corresponding to the beginning ($t = t_-$) and end ($t = t_+$) of the QCD phase transition.

Table 32: The evolution of δ_{c1} and δ_{c2} (where applicable) as a function of time and as a function of the parameter x for a QCD phase transition according to the Bag Model when $\delta_c = 1/3$ (see Figures 64 and 66).

$\log_{10}(t_k/1\ \mathrm{s})$	x	δ_{c1}	δ_{c2}
-5.3	48.1	0.0963	0.102
-5.2	34.0	0.111	0.135
-5.1	24.1	0.126	0.181
-5.0	17.0	0.143	0.244
-4.9	12.0	0.161	0.333
-4.8	8.5	0.179	–
-4.7	6.0	0.197	–
-4.6	4.2	0.215	–
-4.5	2.9	0.233	–
-4.4	2.1	0.249	–
-4.3	1.4	0.264	–
-4.2	0.98	0.278	–
-4.1	0.583	0.290	–
-4.0	0.333	0.299	–
-3.9	0.197	0.307	–
-3.8	0.112	0.315	–

where $c_{s0} = 1/\sqrt{3}$. In the case of the Bag Model (Section 2.3.1) we have $\alpha(t) = 1$ during the mixed phase and $\alpha(t) = 0$ otherwise. Now the function f has a more general expression:

$$f = \frac{1}{S_c^3} \int_{S_i}^{S_c} \alpha(t) dS^3, \tag{262}$$

where S_i corresponds to the size of the region when the transition begins. In particular, this expression is valid for the Bag Model. For example, for a fluctuation of class B we recover equation (255)

$$f = \frac{1}{S_{c,B}^3} \int_{S_1}^{S_{c,B}} 1 \times dS^3 = \frac{S_{c,B}^3 - S_1^3}{S_{c,B}^3}. \tag{263}$$

In order to apply equation (262) to the QCD Crossover we start by transforming it into an expression where all the quantities are given as a function of time. Thus, taking into account that $S = S(t)$ represents the evolution of the scale factor during the QCD Crossover (equation 86) and that

$$dS^3 = 3S^2 dS = 3S^2 \frac{dS}{dt} dt, \tag{264}$$

we obtain

$$dS^3 = \frac{3}{2} \left[\exp\left(c\sqrt{\frac{\Lambda}{3}} (t_{SN} - t_0) \right) \left(\frac{t_{eq}}{t_{SN}} \right)^{2/3} \right]^3 \frac{\sqrt{t}}{t_{eq}^{3/2}} dt. \tag{265}$$

Considering equations (86) and (265) and that $S_c = R(t_c)$ (see equation 240) one obtains, from equation (262), the following result:

$$f = \frac{3}{2} \frac{1}{t_c^{3/2}} \int_{t_k}^{t_c} \left(1 - \frac{c_s(t)}{c_{s0}} \right) \sqrt{t} dt \tag{266}$$

where we have taken into account that $S_1 \equiv t_k$ and $S_c \equiv t_c$. Notice that this result is valid also in the case $t_k < t_1$ because f vanishes in the interval $[t_k, t_1]$.

Considering the relation (241), we may write expression (266) in the form

$$f = \frac{3}{2} \left(t_k \frac{1+\delta}{\delta} \right)^{-3/2} \int_{t_1}^{t_k \frac{1+\delta}{\delta}} \left(1 - \frac{c_s(t)}{c_{s0}} \right) \sqrt{t} dt. \tag{267}$$

7.2.1 Examples

In this section we study the changes on the value of the threshold δ_c during a QCD Crossover. We do that by considering examples of fluctuations that cross the horizon before ($t_k \leq t_1$), during ($t_1 < t_k < t_2$) and after ($t_k > t_2$) the transition. The study will be done mainly for $\delta_c = 1/3$ but we also consider the effect of larger values of δ_c (up to 0.7). We consider only the case $\Delta T = 0.1 T_c$ for which (cf. Table 19) $t_1 = 7.1 \times 10^{-5}$ s and $t_2 = 19.6 \times 10^{-5}$ s.

In order to identify the values of δ for which collapse to a BH occurs we plot in Figure 67 both, $(1-f)\delta_c$ and δ itself as functions of δ, (f is given by expression 267) for different values of t_k.

As a first example we consider the case of a fluctuation that crosses the horizon at $t_k = 1.5\times10^{-5}$ s (i.e., before t_1) (Figure 67a). We conclude that the evolution of perturbtions entering the horizon at this epoch are not affected by the presence of a Crossover transition (t_k occurs well before the transition).

As a second example we consider a fluctuation that crosses the horizon at $t_k = 3.5\times10^{-5}$ s. In this case we still have $t_k < t_1$ but now there is a visible effect on the value of δ_c. In fact, we now have a lower threshold for PBH formation $\delta_{c1} \approx 0.28$ (Figure 67b).

In Figure 67c we show the case $t_k \approx t_1 = 7.1\times10^{-5}$ s. The threshold for PBH formation is now $\delta_{c1} \approx 0.31$. Notice that, although we are considering a fluctuation that crosses the horizon at the beginning of the transition, the value of δ_c is less affected than in the previous case.

In Figures 67d to 67h we represent the cases $t_k = 10^{-4}$ s ($t_1 < t_k < t_{min}$ where t_{min} represents the instant for which the sound speed reaches its minimum value during the Crossover, Section 2.4), $t_k = 1.2\times10^{-4}$ s ($t_k \gtrsim t_{min}$), $t_k = 1.5\times10^{-4}$ s ($t_{min} < t_k < t_2$), $t_k = 2.0\times10^{-4}$ s ($t_k \approx t_2$) and, finally, $t_k = 2.3\times10^{-4}$ s ($t_k > t_2$). For all these cases it is clear that the effect of the QCD Crossover, in terms of the reduction of the value of δ_c, is not as significant as it was for fluctuations crossing the horizon a little bit before the beginning of the transition. The value of δ_{c1} smoothly aproaches $\delta_c = 1/3$ as one uses larger values of t_k.

Figure 68 shows the region on the $(\log_{10}(t_k/1\mathrm{s}), \delta)$ plane for which collapse to a BH occurs in the case of a QCD Crossover with $\Delta T = 0.1T_c$ and $\delta_c = 1/3$. Without the phase transition, this would be a straight horizontal line at $\delta = 1/3$.

In Figure 69 we consider, again, the cases $t_k = 1.5\times10^{-5}$ s, $t_k = 3.5\times10^{-5}$ s and $t_k \approx t_1 = 7.1\times10^{-5}$ s but now with δ_c assuming several values between 1/3 and 0.7. The new window for PBH formation, i.e., the region between δ_{c1} and δ_c, is larger for smaller values of δ_c.

Figure 70 shows the region on the $(\log_{10}(t_k/1\mathrm{s}), \delta)$ plane for which collapse to a BH occurs for $\delta_c = 1/3$ and for $\delta_c = 0.7$. Without the phase transition, these would be two straight horizontal lines at $\delta = 1/3$ and $\delta = 0.7$.

7.2.2 Summary

Due to the QCD Crossover, the PBH formation threshold δ_c experiences a reduction on its value. On Table 33 we present a few examples of these new values, δ_{c1}, as a function of time, for the case $\delta_c = 1/3$.

7.3 Lattice Fit

In the case of the Lattice Fit we have a dust–like period ($t_- < t < t_+$) during which the sound speed vanishes. However, this does not occur instantaneously

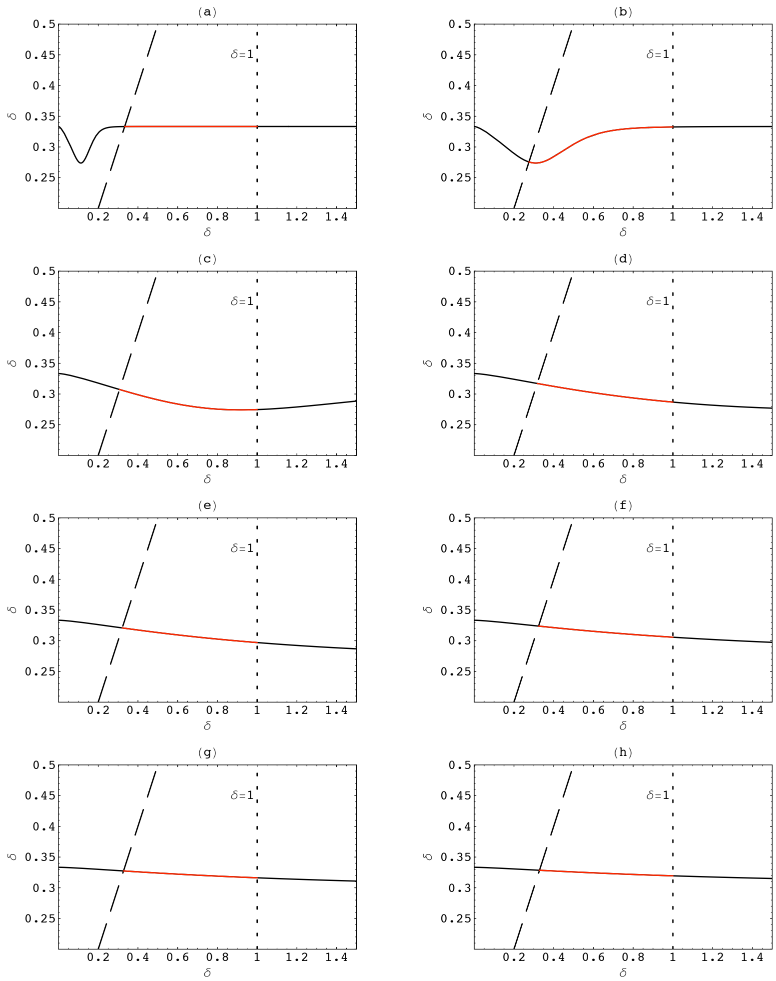

Figure 67: PBH formation during the QCD transition according to the Crossover model for the case $\delta_c = 1/3$ and: (a) $t_k = 1.5 \times 10^{-5}$ s; (b) $t_k = 3.5 \times 10^{-5}$ s; (c) $t_k = 7.1 \times 10^{-5}$ s; (d) $t_k = 10^{-4}$ s; (e) $t_k = 1.2 \times 10^{-4}$ s; (f) $t_k = 1.5 \times 10^{-4}$ s; (g) $t_k = 2.0 \times 10^{-4}$ s; (h) $t_k = 2.3 \times 10^{-4}$ s. The solid curve corresponds to the function $(1 - f)\delta_c$ and the dashed curve (on the left) corresponds to the identity δ. The intersection point between the lines $(1 - f)\delta_c$ and δ (giving the new threshold, δ_{c1}, for BH formation) is: (a) $\delta_{c1} \approx 0.333$; (b) $\delta_{c1} \approx 0.275$; (c) $\delta_{c1} \approx 0.307$; (d) $\delta_{c1} \approx 0.317$; (e) $\delta_{c1} \approx 0.321$; (f) $\delta_{c1} \approx 0.324$; (g) $\delta_{c1} \approx 0.327$; (h) $\delta_{c1} \approx 0.328$ (see text for more details).

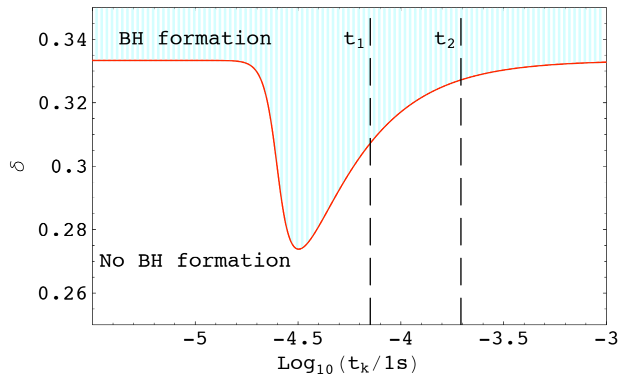

Figure 68: The curve in the $(\log_{10}(t_k/1\text{s}), \delta)$ plane indicating which parameter values lead to collapse to a BH in the case $\delta_c = 1/3$ for a QCD Crossover. We have also represented, for reference, the values of t_1 and t_2 giving the locus of the transition (note that the BH formation region extends up to $\delta = 1$).

Table 33: The evolution of δ_{c1} as a function of time for a QCD Crossover with $\Delta T = 0.1 T_c$ when $\delta_c = 1/3$.

$\log_{10}(t_k/1\text{ s})$	δ_{c1}	$\log_{10}(t_k/1\text{ s})$	δ_{c1}
-5.0	0.333	-4.9	0.333
-4.8	0.333	-4.7	0.330
-4.6	0.299	-4.5	0.274
-4.4	0.281	-4.3	0.293
-4.2	0.303	-4.1	0.311
-4.0	0.317	-3.9	0.322
-3.8	0.325	-3.7	0.327
-3.6	0.329	-3.5	0.330
-3.4	0.331	-3.3	0.332
-3.2	0.332	-3.1	0.333

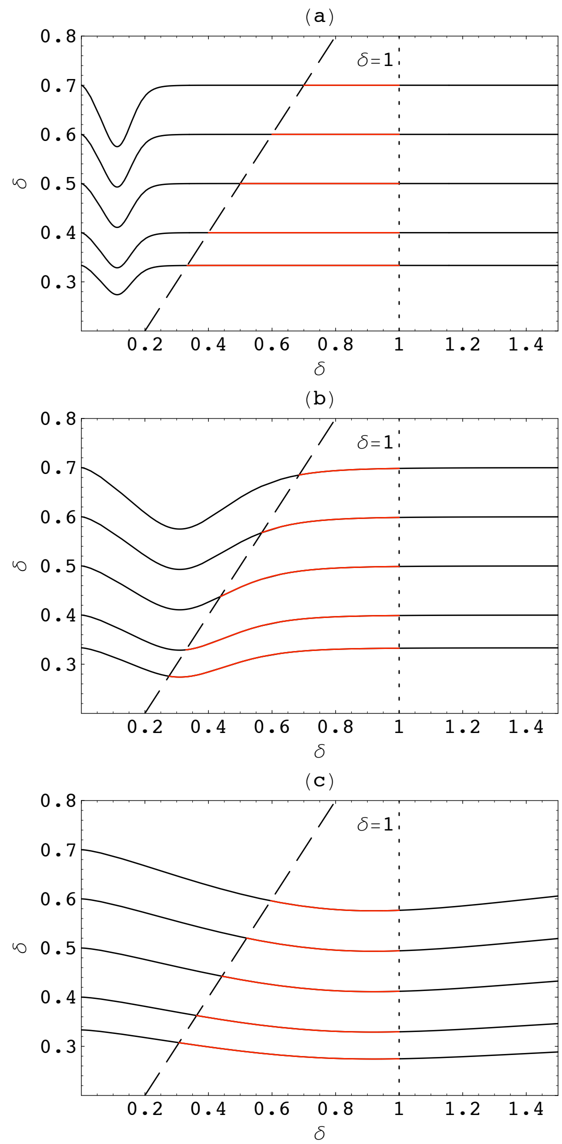

Figure 69: PBH formation during the QCD transition according to the Crossover for the cases: (a) $t_k = 1.5 \times 10^{-5}$ s; (b) $t_k = 3.5 \times 10^{-5}$ s; (c) $t_k = 7.1 \times 10^{-5}$ s. The solid curve corresponds to the function $(1-f)\delta_c$ with, from bottom to top, $\delta_c = 1/3$, $\delta_c = 0.4$, $\delta_c = 0.5$, $\delta_c = 0.6$ and $\delta_c = 0.7$. The dashed curve (on the left) corresponds to the identity δ.

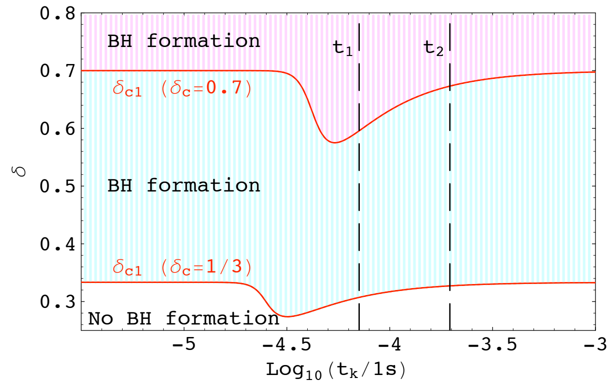

Figure 70: The curve in the $(\log_{10}(t_k/1\mathrm{s}), \delta)$ plane indicating which parameter values lead to collapse to a BH in the case of a QCD Crossover with $\delta_c = 1/3$ and with $\delta_c = 0.7$. We have also represented, for reference, the values of t_1 and t_2 giving the locus of the transition (note that, in both cases, the BH formation region extends up to $\delta = 1$).

as it does for the Bag Model. In fact, there is a period ($t_1 \leq t \leq t_-$) during which the sound speed value drops from $1/\sqrt{3}$ to zero (cf. Figure 30).

We need to write a function f suitable to the Lattice Fit. For the period $t_1 \leq t \leq t_-$ we adopt the ideas from the Crossover case (Section 7.2); for the period $t_- \leq t \leq t_+$ we consider the Bag Model results (Section 7.1).

Let us start with fluctuations of class A. We have $f_A = 0$, as in the Bag Model case, only if $t_c < t_1$. In general, for a fluctuation of class A we write (cf. equation 262)

$$f_{A_{Lat}} = \frac{1}{S_{c,A}^3} \int_{S_k}^{S_{c,A}} \alpha(t) dS^3 \tag{268}$$

where $S_{c,A}$, the size of the overdense region at turnaround (Section 5.2), is given by equation (219), and $S_k \equiv R(t_k)$, the size of the overdense region when the fluctuation crosses the horizon, is given by equation (71) with $n_{qcd} = 2/3$. The function $\alpha(t)$ is given by equation (261), as in the Crossover case, but now with the sound speed $c_s(t)$ given by equation (141). Taking into account that the volume element dS^3 (see equation 264) must be evaluated in the radiation–dominated period ($t_k \leq t \leq t_-$), we have, from equation (71), with $n_{qcd} = 2/3$ that

$$dS^3 = \frac{3}{2} \left[\exp\left(c\sqrt{\frac{\Lambda}{3}} (t_{SN} - t_0) \right) \left(\frac{t_{eq}}{t_{SN}} \right)^{2/3} \left(\frac{t_+}{t_{eq}} \right)^{1/2} \times \right. \\ \left. \times \left(\frac{t_-}{t_+} \right)^{2/3} \right]^3 \frac{\sqrt{t}}{t_-^{3/2}} dt. \tag{269}$$

Inserting expression (269) into equation (268) and replacing $R(t_k)$, as given by equation (71), with $n_{qcd} = 2/3$ in $S_{c,A}$ we obtain

$$f_{A_{Lat}} = \frac{3}{2}\left(t_k \frac{1+\delta}{\delta}\right)^{-3/2} \int_{t_k}^{t_k \frac{1+\delta}{\delta}} \alpha(t)\sqrt{t}dt. \tag{270}$$

In the case of a fluctuation of class B we write

$$f_B = f_{B_{Lat}} + \frac{S_{c,B}^3 - S_1^3}{S_{c,B}^3} \tag{271}$$

with

$$f_{B_{Lat}} = \frac{1}{S_{c,B}^3} \int_{S_k}^{S_1} \alpha(t) dS^3 \tag{272}$$

where S_1 and $S_{c,B}$ are given by expressions (225) and (228) , respectively. Inserting expression (269) into equation (272), replacing $R(t_k)$ in $S_{c,B}$ and considering that $S_1 \equiv R(t_-)$, we obtain

$$f_{B_{Lat}} = \frac{3}{2}\left(t_k^{-1/2} x^{-1/4} \frac{(1+\delta)^{3/4}}{\delta}\right)^{-3} \int_{t_k}^{t_-} \alpha(t)\sqrt{t}dt \tag{273}$$

where $x = x(t_k)$. In the case of a fluctuation of class C we have

$$f_C = f_{C_{Lat}} + \frac{S_2^3 - S_1^3}{S_{c,C}^3} \tag{274}$$

with

$$f_{C_{Lat}} = \frac{1}{S_{c,C}^3} \int_{S_k}^{S_1} \alpha(t) dS^3 \tag{275}$$

where S_{2_C} and $S_{c,C}$ are given by expressions (226) and (229) respectively. Inserting expression (269) into equation (275), replacing $R(t_k)$ in $S_{c,C}$ and considering that $S_1 \equiv R(t_-)$, we obtain

$$f_{C_{Lat}} = \frac{3}{2}\left(t_k \frac{1+\delta}{\delta}\right)^{-3/2} y^{-1/2} \int_{t_k}^{t_-} \alpha(t)\sqrt{t}dt \tag{276}$$

with $y^{-1} \approx 0.729$ (Section 5.3.2). In the case of fluctuations of classes E and F ($t_k > t_-$) we continue to use, respectively, for f_E and f_F, the expressions (257) and (258) of the Bag Model.

In the next section we study PBH formation during the QCD phase transition, from fluctuations of classes A, B, C, E and F, according to the Lattice Fit. We divide the study in Before, During and After, as we did for the Bag Model. At the end of the section we compile the results. The study is mostly done for $\delta_c = 1/3$ but we also consider the effect of larger values of δ_c (up to 0.7).

7.3.1 Before the mixed phase

When $x \geq 1$ ($t_k \leq t_-$) we are dealing with fluctuations of classes A, B or C. For a given x we can determine the range of amplitudes corresponding to each class. More precisely, the solution of the equation $f_B(d) = f_C(d)$ gives the boundary between classes B and C and the solution of the equation $f_A(d) = f_B(d)$ the boundary between classes B and A.

Let us start with the case $x = 15$ ($t_k \approx 1.6 \times 10^{-5}$ s) and $\delta_c = 1/3$. The boundaries between the different classes are $\delta_{AB} \approx 0.25$ and $\delta_{BC} \approx 0.21$. In order to identify the values of δ for which collapse to a BH occurs we plot in Figure 71 both $(1-f)\delta_c$ and δ itself as functions of δ. Notice that one should use the function f appropriate to each class (i.e. f_A – equation 270; f_B – equation 271; f_C – equation 274). As it is clear we could have, in this case, PBHs from fluctuations of classes A (provided that $\delta < 1$), B and C (provided that $\delta > 0.18$ because otherwise the fluctuation will dissipate without forming a PBH). This point $\delta_{c1} \approx 0.18$ marks a new and lower threshold for PBH formation during the QCD phase transition when $x = 15$ and $\delta_c = 1/3$.

We have also represented on Figure 71 the curve $(1 - f_{Bag})\delta_c$ where f_{Bag} regards only to the contribution within the Bag Model (i.e., we are considering $f_{A_{Lat}} = f_{B_{Lat}} = f_{C_{Lat}} = 0$) of the period $t_- < t < t_+$ (i.e., the period during which the sound speed vanishes). We have done this in order to show that the contribution from the period $t_k < t < t_-$ is important. The reduction on the sound speed during this period leads to a shift on the boundaries between different classes of fluctuations towards left (i.e., to lower values of δ). For example δ_{AB} moves from ≈ 0.29 to ≈ 0.25.

In Figure 72 we show the case $x = 2$ ($t_k \approx 6.1 \times 10^{-5}$ s) with $\delta_c = 1/3$. This case illustrates an interesting result. For small values of x ($x < 5$) we only have fluctuations of classes A and C. Fluctuations of class B cannot exist (at least according to the assumptions we made when deducing expressions for f). A fluctuation that crosses the horizon near t_- ($x \approx 1$) evolves as a fluctuation of class A ($t_c < t_-$) if it is strong enough or, otherwise, it will evolve as a fluctuation of class C ($t_c > t_+$).

In Figure 73 we have represented the regions on the (δ_k, $\log_{10} x$) plane corresponding to the classes of perturbations listed in Table 26 (compare this with Figure 46).

In Figure 74a we plot the case $x = 25$ ($t_k \approx 1.2 \times 10^{-5}$ s) with $\delta_c = 1/3$. Now there are two regions for which PBH formation is allowed: i) a region for $\delta \geq 0.25$, which corresponds to PBH formation from fluctuations of class A during the radiation–dominated Universe; ii) a region between $\delta_{c1} \approx 0.15$ and $\delta_{c2} \approx 0.17$, corresponding to the formation of PBHs from fluctuations of classes B and C. The gap between $\delta = 0.17$ and $\delta = 0.25$ corresponds to fluctuations of class A which dissipate because they are not strong enough, and fluctuations of class B which dissipate because they do not spent enough time on the dust–like phase allowing collapse to begin.

In Figure 74b we plot the case $x = 50$ ($t_k \approx 7.3 \times 10^{-6}$ s) with $\delta_c = 1/3$. In this case PBH formation is allowed only from fluctuations of class A. The new

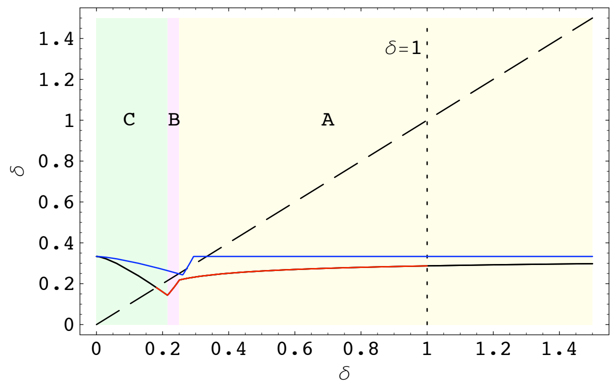

Figure 71: PBH formation during the QCD transition according to the Lattice Fit for the case $x = 15$ ($t_k \approx 1.6 \times 10^{-5}$ s) with $\delta_c = 1/3$. The bottom solid curve (in black and red) corresponds to the function $(1 - f)\delta_c$ and the dashed curve corresponds to the identity δ. The intersection point between these two curves at $\delta_{c1} \approx 0.18$ marks a new threshold for PBH formation. The borders between the different classes of fluctuations are $\delta_{AB} \approx 0.14$ and $\delta_{BC} \approx 0.10$. The top solid curve (in blue) corresponds to the case for which f regards only to the contribution, within the Bag Model, of the period $t_- < t < t_+$ (see text for more details).

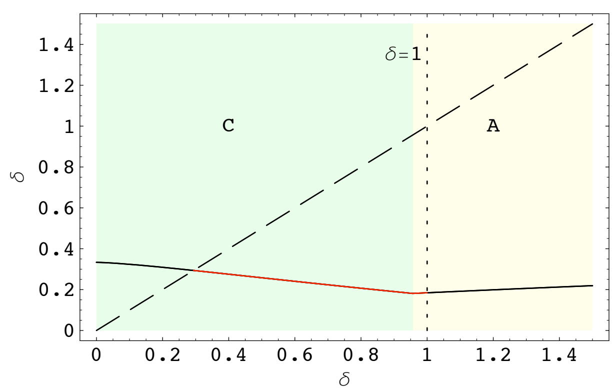

Figure 72: PBH formation during the QCD transition according to the Lattice Fit for the case $x = 2$ ($t_k \approx 6.1 \times 10^{-5}$ s) with $\delta_c = 1/3$. The solid curve corresponds to the function $(1 - f)\delta_c$ and the dashed curve corresponds to the identity δ. The new threshold for PBH formation is now $\delta_{c1} \approx 0.29$ and the border between fluctuations of classes A and C is $\delta_{AC} \approx 0.95$.

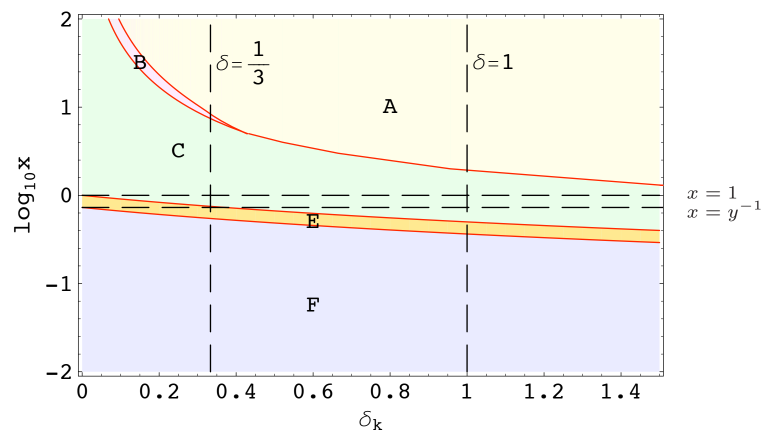

Figure 73: Regions in the $(\delta_k, \log_{10} x)$ plane corresponding to the classes of perturbations listed in Table 26 for the QCD Lattice Fit. The variable x identifies the epoch a perturbation enters the horizon and the quantity δ_k represents the corresponding overdensity at that time (see Section 5.3.2 for more details).

threshold for PBH formation is now $\delta_{c1} \approx 0.27$. As one moves to larger values of x (smaller values of t_k) δ_{c1} will approach 1/3.

In Figure 75 we consider, again, the cases: $x = 2$, $x = 15$, $x = 25$ and $x = 50$ but now with δ_c assuming several values between 1/3 and 0.7. The new window for PBH formation, i.e., the region between δ_{c1} and δ_c or δ_{c2}, if it exists, is larger for smaller values of δ_c.

7.3.2 During the mixed phase

When $y^{-1} < x < 1$ we are dealing with fluctuations of classes C or E (cf. Figure 73). In Figure 76a we plot both $(1 - f)\delta_c$ and δ itself as functions of δ for the case $x = 0.985$ ($t_k \approx 9.5 \times 10^{-5}$ s) when $\delta_c = 1/3$. In this case, PBHs could form only from fluctuations of class C, provided that $0.318 \lesssim \delta_k < 1$. Fluctuations of class C with $\delta < 0.318$ dissipate without forming a PBH. This point $\delta_{c1} \approx 0.318$ marks the new threshold for PBH formation during the QCD phase transition when $x = 0.985$. As a second example we show in Figure 76b the plot for the case $x \approx 0.871$ ($t_k \approx 1.0 \times 10^{-4}$ s) with $\delta_c = 1/3$. In this case the new threshold for PBH formation is $\delta_{c1} \approx 0.319$.

In Figure 77 we consider, once again, the cases $x = 0.985$ and $x = 0.871$ but now with δ_c assuming several values between 1/3 and 0.7. The window for PBH formation is larger for smaller values of δ_c.

7.3.3 After the mixed phase

When $x < y^{-1}$ we are dealing with fluctuations of classes E, F or C (cf. Figure 73). In Figure 78 we plot $(1 - f)\delta_c$ and δ itself as functions of δ for the case

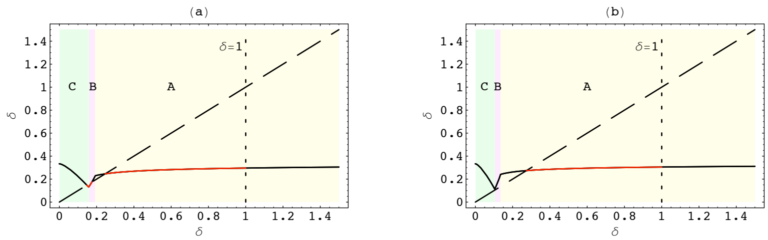

Figure 74: PBH formation during the QCD transition according to the Lattice Fit for the cases: (a) $x = 25$, and (b) $x = 50$; with $\delta_c = 1/3$. The solid curve corresponds to the function $(1 - f)\delta_c$ and the dashed curve corresponds to the identity δ. The borders between the different classes are given by: (a) $\delta_{AB} \approx 0.19$, $\delta_{BC} \approx 0.16$; (b) $\delta_{AB} \approx 0.20$, $\delta_{BC} \approx 0.13$. Collapse to a BH occurs for values of δ for which the dashed line is above the solid curve (while $\delta < 1$). In the case $x = 25$ we have three intersections points: $\delta_{c1} \approx 0.15$, $\delta_{c2} \approx 0.17$ and $\delta_c = 0.25$. This means that, in this case, there are two regions for PBH formation: $0.15 \leq \delta \leq 0.17$ and $0.25 \leq \delta < 1$. In the case $x = 50$ PBHs form if $0.27 \leq \delta < 1$.

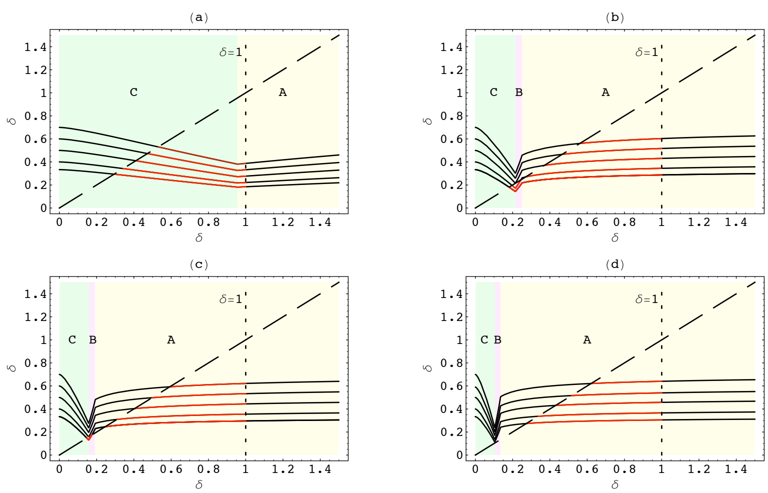

Figure 75: PBH formation during the QCD transition according to the Lattice Fit for the cases: (a) $x = 2$, (b) $x = 15$, (c) $x = 25$, and (d) $x = 50$. The solid curve corresponds to the function $(1 - f)\delta_c$ with, from bottom to top, $\delta_c = 1/3$, $\delta_c = 0.4$, $\delta_c = 0.5$, $\delta_c = 0.6$ and $\delta_c = 0.7$. In red we show the region where PBH formation takes place. The borders between the different classes (which do not depend on the value of δ_c) are given by: (a) $\delta_{AC} = 0.95$; (b) $\delta_{AB} \approx 0.25$, $\delta_{BC} \approx 0.21$; (c) $\delta_{AB} \approx 0.19$, $\delta_{BC} \approx 0.16$; and (d) $\delta_{AB} \approx 0.14$, $\delta_{BC} \approx 0.10$.

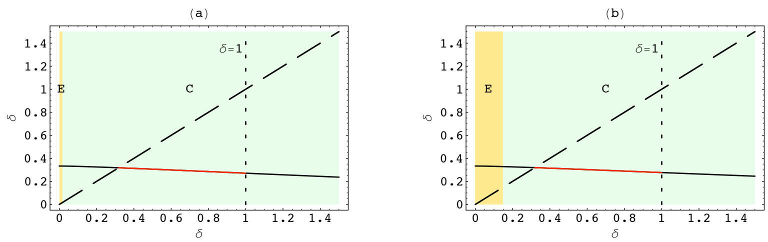

Figure 76: PBH formation during the QCD transition according to the Lattice Fit, when $\delta_c = 1/3$, for the cases: (a) $x = 0.985$ ($t_k \approx 9.5\times10^{-5}$ s); (b) $x = 0.871$ ($t_k \approx 1.0 \times 10^{-4}$ s). The solid curve corresponds to the function $(1 - f)\delta_c$ and the dashed curve corresponds to the identity δ. The new threshold for PBH formation is, in both cases, $\delta_{c1} \approx 0.32$. The borders between classes C and E are: (a) $\delta_{CE} \approx 0.015$; (b) $\delta_{CE} \approx 0.15$.

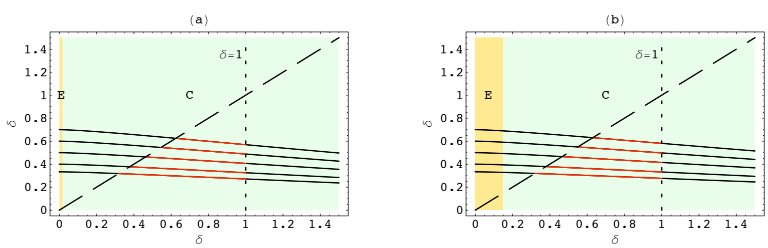

Figure 77: PBH formation during the QCD transition according to the Lattice Fit for the cases: (a) $x = 0.985$ and (b) $x = 0.871$. The solid curve corresponds to the function $(1 - f)\delta_c$ with, from bottom to top, $\delta_c = 1/3$, $\delta_c = 0.4$, $\delta_c = 0.5$, $\delta_c = 0.6$ and $\delta_c = 0.7$. In red we show the region where PBH formation takes place. For the borders between the different classes of fluctuations see Figure 76.

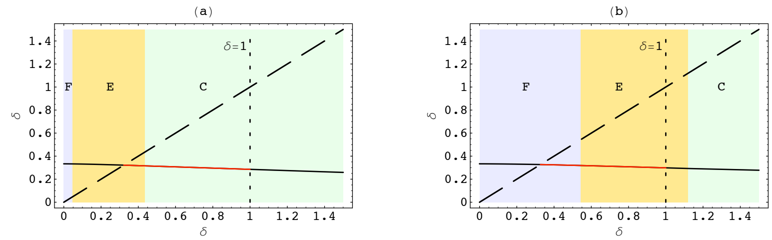

Figure 78: PBH formation during the QCD transition according to the Lattice Fit, when $\delta_c = 1/3$, for the cases: (a) $x = 0.70$ ($t_k \approx 1.2 \times 10^{-4}$ s); (b) $x = 0.47$ ($t_k \approx 1.5 \times 10^{-4}$ s). The solid curve corresponds to the function $(1 - f)\delta_c$ and the dashed curve corresponds to the identity δ. The new threshold for PBH formation is: (a) $\delta_{c1} \approx 0.32$; (b) $\delta_{c1} \approx 0.33$. The borders between classes C, E, and F are given by: (a) $\delta_{CE} \approx 0.44$, $\delta_{EF} \approx 0.045$; (b) $\delta_{CE} \approx 1.12$, $\delta_{EF} \approx 0.54$.

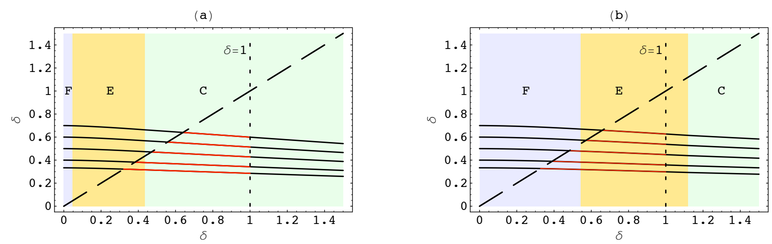

Figure 79: PBH formation during the QCD transition according to the Lattice Fit for the cases: (a) $x = 0.70$ and (b) $x = 0.47$. The solid curve corresponds to the function $(1 - f)\delta_c$ with, from bottom to top, $\delta_c = 1/3$, $\delta_c = 0.4$, $\delta_c = 0.5$, $\delta_c = 0.6$ and $\delta_c = 0.7$. In red we show the region where PBH formation takes place. For the borders between the different classes of fluctuations see Figure 78.

$x = 0.70$ ($t_k \approx 1.2 \times 10^{-4}$ s) when $\delta_c = 1/3$. PBHs could form , in this case, from fluctuations of classes C and E. Fluctuations of class F dissipate without forming a PBH. Fluctuations of class E also dissipate when $\delta < 0.322$. This point $\delta_{c1} \approx 0.322$ marks the new threshold for PBH formation during the QCD phase transition when $x = 0.70$.

As a second example we show in Figure 78b the plot for the case $x \approx\ 0.47$ ($t_k \approx 1.5 \times 10^{-4}$ s), when $\delta_c = 1/3$. In this case PBHs could form from fluctuations of class E and F but no longer from fluctuations of class C. The new threshold for PBH formation is now $\delta_{c1} \approx 0.326$.

In Figure 79 we consider, once again, the cases $x = 0.70$ and $x = 0.47$ but now with δ_c assuming several values between 1/3 and 0.7.

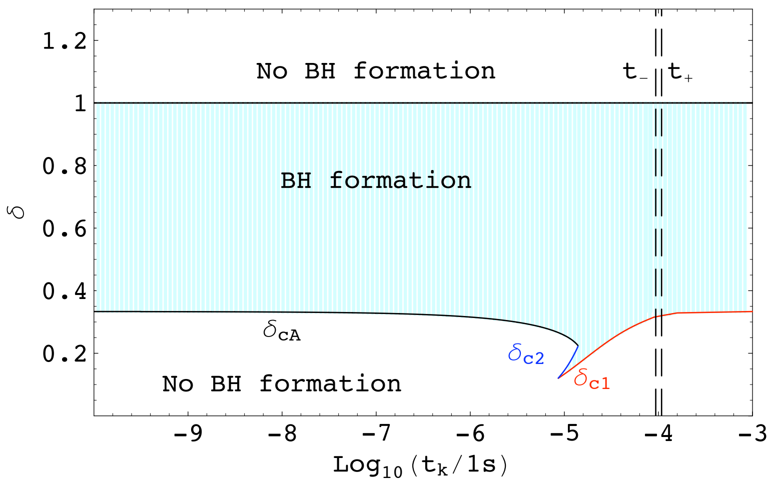

Figure 80: The curve in the $(\log_{10}(t_k/1s),\, \delta)$ plane indicating which parameter values lead to collapse to a BH in the case of the QCD Lattice Fit when $\delta_c = 1/3$. The vertical dashed lines correspond to $t_k = t_-$ and $t_k = t_+$.

7.3.4 Summary

We now compile the results obtained on sections 7.3.1–7.3.3. We have determined the threshold δ_c for the entire QCD phase transition according to the Lattice Fit model. As a result we obtain Figure 80 for the case $\delta_c = 1/3$ and Figure 81 for the case $\delta_c = 0.7$.

During the QCD transition, the threshold for PBH formation (δ_c) experiences a reduction. As a result, a new window for PBH formation (between δ_{c1} and δ_c, between δ_{cA} and δ_c or between δ_{c1} and δ_{c2}) is opened for a brief period. Note that the window between δ_{cA} and δ_c does not exist for the Bag Model case (Section 7.1.4) because, in that case, we have $f_A = 0$. On Table 34 we present some values for this new threshold for PBH formation during the QCD transition according to the Lattice Fit, when $\delta_c = 1/3$.

Table 34: The evolution of δ_{cA}, δ_{c1} and δ_{c2} (where applicable) as a function of time for a QCD phase transition according to the Lattice Fit Model when $\delta_c = 1/3$.

$\log_{10}(t_k/1\text{ s})$	δ_{cA}	δ_{c2}	δ_{c1}
-7.5	0.3304	–	–
-7.4	0.3301	–	–
-7.3	0.3297	–	–
-7.2	0.3292	–	–
-7.1	0.3287	–	–
-7.0	0.3281	–	–
-6.9	0.3274	–	–
-6.8	0.3267	–	–
-6.7	0.3258	–	–
-6.6	0.3249	–	–
-6.5	0.3238	–	–
-6.4	0.3226	–	–
-6.3	0.3212	–	–
-6.2	0.3196	–	–
-6.1	0.3178	–	–
-6.0	0.3157	–	–
-5.9	0.3133	–	–
-5.8	0.3105	–	–
-5.7	0.3073	–	–
-5.6	0.3036	–	–
-5.5	0.2992	–	–
-5.4	0.2940	–	–
-5.3	0.2877	–	–
-5.2	0.2800	–	–
-5.1	0.2702	–	–
-5.0	0.2573	0.1450	0.1334
-4.9	0.2381	0.1941	0.1554
-4.8	–	–	0.1784
-4.7	–	–	0.2016
-4.6	–	–	0.2242
-4.5	–	–	0.2453
-4.4	–	–	0.2644
-4.3	–	–	0.2813
-4.2	–	–	0.2960
-4.1	–	–	0.3090
-4.0	–	–	0.3182
-3.9	–	–	0.3236

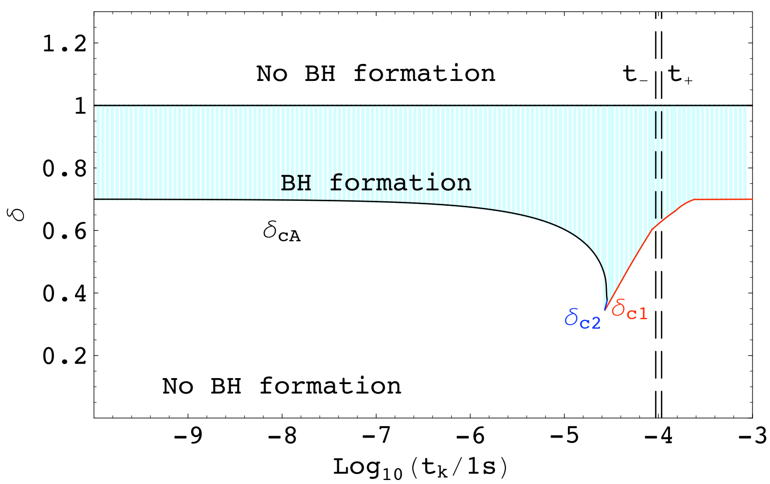

Figure 81: The curve in the $(\log_{10}(t_k/1s),\, \delta)$ plane indicating which parameter values lead to collapse to a BH in the case of the QCD Lattice Fit when $\delta_c = 0.7$. The vertical dashed lines correspond to $t_k = t_-$ and $t_k = t_+$.

8 The threshold δ_c for PBH formation during the EW phase transition

8.1 Crossover Model (SMPP)

During the EW Crossover it is expected a reduction on the value of the PBH formation threshold δ_c due to the decrease on the sound speed. We adopt for f expression (267) derived for the QCD Crossover (Section 7.2) but now with the sound speed, $c_s(t)$, given by equation (180). First, however, we must determine which values of ΔT we will use. We are particularly interested in a value of ΔT for which the threshold δ_c attains a minimum value (because lower values of δ_c favour PBH formation).

For a given ΔT we determine, with the help of funtion $(1-f)\delta_c$, the new threshold δ_{c1} as a function of the horizon crossing time t_k. When $t_k \ll t_{EW-}$ or, when $t_k \gg t_{EW+}$, we get $\delta_{c1} = \delta_c$. Between these two extremes there is a value of t_k for which δ_{c1} attains a minimum value $\delta_{c1,min}$. For example, when $\Delta T = \ 0.001 T_c$ and $\delta_c = 1/3$, we obtain $\delta_{c1,min} \approx 0.33213$ with $t_k \approx 8.32 \times 10^{-11}$ s.

We repeated this procedure for different values of ΔT ($0 < \Delta T \leq T_c$) and concluded that, in the $\delta_c = 1/3$ case, our best value is $\delta_{c1,min} \approx 0.33186$, corresponding to having $\Delta T \approx 0.013 T_c$ and $t_k \approx 8.32 \times 10^{-11}$ s. In Figure 82 we show a selection of the obtained results.

On Table 35 we show the results for different values of δ_c. Note that, although, the value of the parameter ΔT remains almost constant the same does not apply to t_k. For a larger value of δ_c, the instant t_k, for which we get the lowest $\delta_{c1,min}$, is closer to t_{EW-}.

8.1.1 Examples

In this section we study the changes on the value of the threshold δ_c during an EW Crossover, through examples of fluctuations that cross the horizon at different epochs. The study is mainly made for $\delta_c = 1/3$. We are mostly interested in the case $\Delta T = 0.013 T_c$ (because it is the one that leads to the lowest value of δ_c) but we also consider the cases $\Delta T = 0.001 T_c$ and $\Delta T = 0.1 T_c$, with the purpose of comparing the results.

Let us start with $\delta_c = 1/3$ and with a fluctuation that crosses the horizon at $t_k = 5.0 \times 10^{-11}$ s (i.e., before $t_1 = 2.97 \times 10^{-10}$ s, cf. Section 3.2.1). In order to identify the values of δ for which collapse to a BH will occur, in this case, we plot, in Figure 83a, both $(1-f)\delta_c$ and δ itself as functions of δ. We conclude that the evolution of perturbations entering the horizon at this epoch are not affected by the presence of a Crossover transition. That is because t_k occurs sufficiently before the transition.

As a second example, we consider a fluctuation that crosses the horizon at $t_k = 7.0 \times 10^{-11}$ s. In this case, we do have a lower threshold for PBH formation $\delta_{c1} \approx 0.3330$ if $\Delta T = 0.1 T_c$ but not if $\Delta T = 0.001 T_c$ or $\Delta T = 0.013 T_c$ as it is clear from Figure 83b. In Figure 83c we have the case $t_k \approx 8.32 \times 10^{-11}$ s. This

Table 35: The lowest value of $\delta_{c1,min}$ for the EW Crossover for different values of δ_c. It is also shown the corresponding values of $\Delta T/T_c$ and t_k.

δ_c	$\delta_{c1,min}$	$\Delta T/T_c$	$t_k(s)$
1/3	0.33186	0.0131	8.32×10^{-11}
0.4	0.39823	0.0091	9.33×10^{-11}
0.5	0.49778	0.0111	1.10×10^{-10}
0.6	0.59734	0.0101	1.23×10^{-10}
0.7	0.69689	0.0101	1.35×10^{-10}

corresponds to the case for which a minimal value for $\delta_{c1} \approx 0.33186$ is achieved and that occurs for $\Delta T = 0.013T_c$.

We considered also the cases $t_k = 1.5 \times 10^{-10}$ s – Figure 83d ($t_k < t_1$), $t_k = 2.3 \times 10^{-10}$ s – Figure 83e ($t_1 < t_k < t_2$, see Section 3.2.1), and $t_k = 3.5 \times 10^{-10}$ s – Figure 83f ($t_k > t_2$). For all these cases it is clear that the effect of the EW Crossover, in terms of the reduction of the value of δ_c, is not as significant as it was for fluctuations crossing the horizon a little bit before the beginning of the transition (cf. Figures 83a and 83b). The value of δ_{c1} smoothly aproaches $\delta_c = 1/3$ as one moves to larger values of t_k for all the considered values of ΔT.

Figure 84 shows the region on the $(\log_{10}(t_k/1\mathrm{s}), \delta)$ plane for which collapse to a BH occurs in the case of the EW Crossover with $\delta_c = 1/3$ and when ΔT assumes the values $0.001T_c$, $0.013T_c$ and $0.1T_c$. Without the phase transition, these would be three straight horizontal lines at $\delta = 1/3$. We have also represented, for reference, the location of the EW Crossover. It is clear that the case $\Delta T = 0.013T_c$ is the most important in the context of PBH production (with $\delta_c = 1/3$). For that reason we will consider, from now on, for the EW Crossover, only this case.

Figure 85 indicates the region on the $(\log_{10}(t_k/1\mathrm{s}), \delta)$ plane for which collapse to a BH occurs for $\delta_c = 1/3$ and for $\delta = 0.4$. Without the phase transition, these would be two straight horizontal lines at $\delta = 1/3$ and $\delta = 0.4$.

8.1.2 Summary

Due to the EW Crossover the PBH formation threshold δ_c experiences a reduction on its background value. On Table 36 we present some of these new values δ_{c1} as a function of time for the case $\delta_c = 1/3$.

8.2 Bag Model (MSSM)

In the case of an EW first–order phase transition we replace the lower limit in the condition (251) by expression (253). The quantity f, which represents the

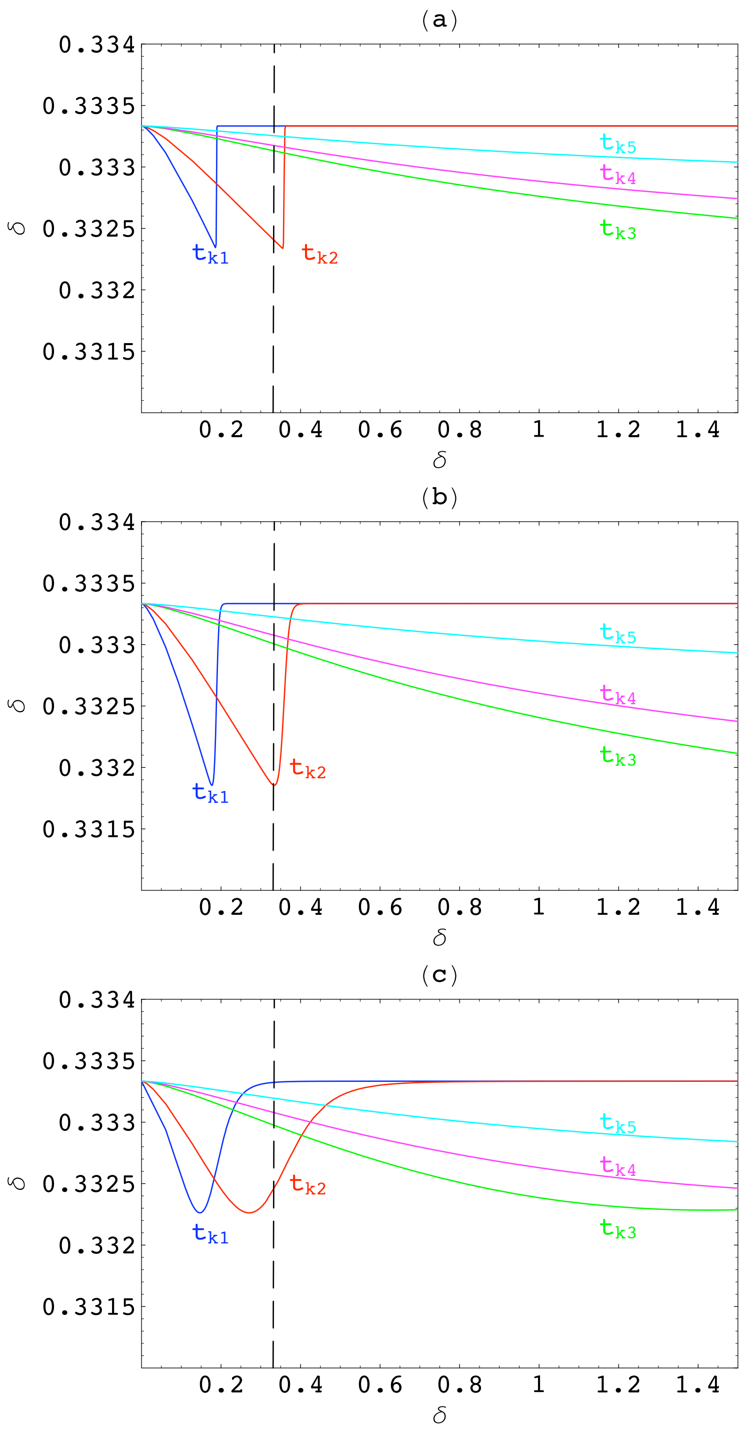

Figure 82: The curve $(1-f)\delta_c$ for the EW Crossover when $\delta_c = 1/3$ and: (a) $\Delta T = 0.001T_c$, (b) $\Delta T = 0.013T_c$ and (c) $\Delta T = 0.1T_c$. Different lines correspond to different values of t_k: $t_{k1} = 5.0 \times 10^{-11}$ s, $t_{k2} = 8.32 \times 10^{-11}$ s, $t_{k3} = t_{EW-} = 2.3 \times 10^{-10}$ s, $t_{k4} = 2.7 \times 10^{-10}$ s, and $t_{k5} = t_{EW+} = 3.15 \times 10^{-10}$ s.

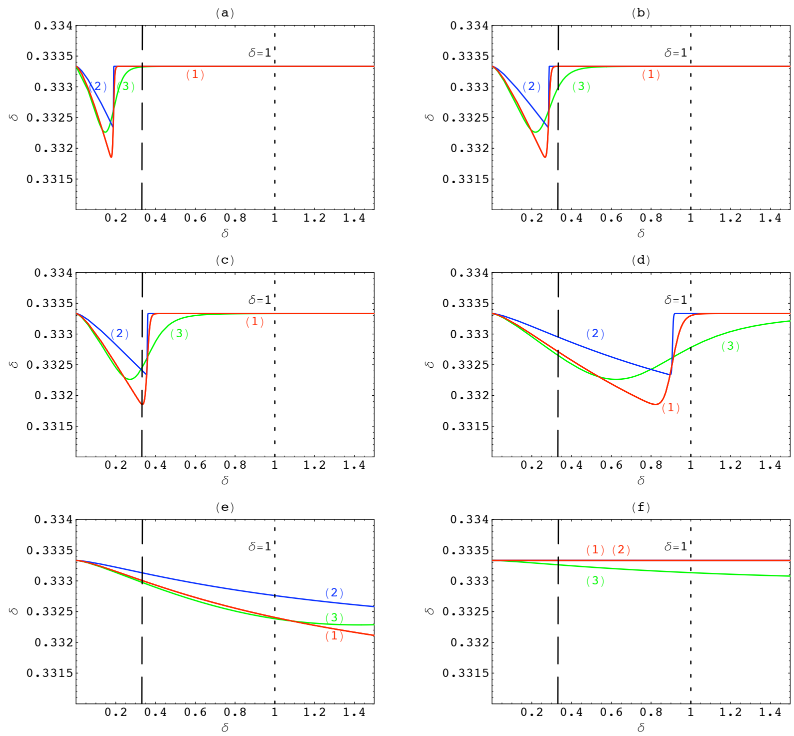

Figure 83: PBH formation during the EW transition according to the Crossover model for the case $\delta_c = 1/3$ and: (a) $t_k = 5.0 \times 10^{-11}$ s, (b) $t_k = 7.0 \times 10^{-11}$ s, (c) $t_k = 8.32 \times 10^{-11}$ s, (d) $t_k = 1.5 \times 10^{-10}$ s, (e) $t_k = 2.3 \times 10^{-10}$ s, and (f) $t_k = 3.5 \times 10^{-10}$ s. The solid curves correspond to the function $(1 - f)\delta_c$ when: (1) $\Delta T = 0.013T_c$, (2) $\Delta T = 0.001T_c$ and (3) $\Delta T = 0.1T_c$. The dashed curve on the left represents the identity δ (which appears to be a vertical line due to the scales chosen for each axis). Collapse to a BH occurs for values of δ between this line and the line $\delta = 1$.

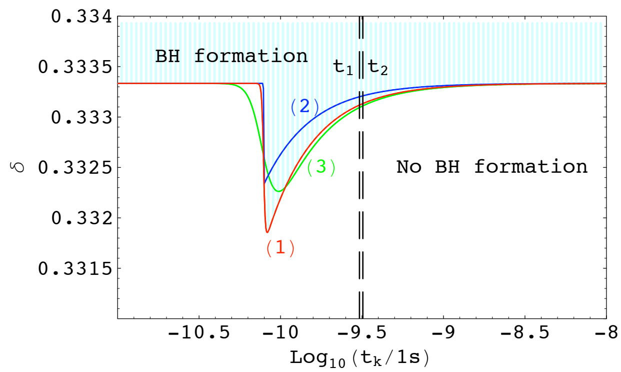

Figure 84: The curve in the $(\log_{10}(t_k/1\mathrm{s}), \delta)$ plane indicating which parameter values lead to collapse to a BH in the case $\delta_c = 1/3$ for the EW Crossover with (1) $\Delta T = 0.013T_c$, (2) $\Delta T = 0.001T_c$ and (3) $\Delta T = 0.1T_c$. Without the transition, these would be three straight horizontal lines at $\delta = 1/3$. We show the BH formation region for the case $\Delta T = 0.013T_c$ (note that this region extends up to $\delta = 1$). We have also represented, for reference, the values of t_1 and t_2 giving the locus of the transition (vertical dashed lines).

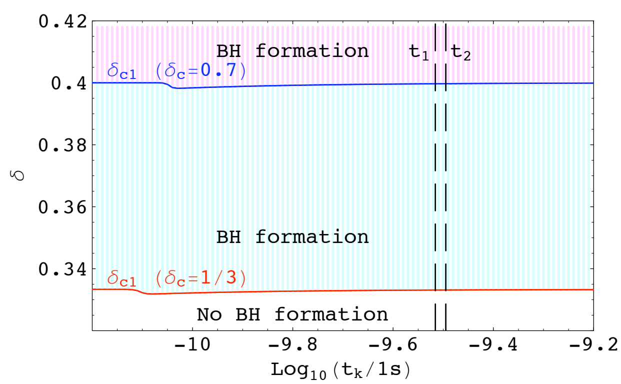

Figure 85: The curve in the $(\log_{10}(t_k/1\mathrm{s}), \delta)$ plane indicating which parameter values lead to collapse to a BH in the case of the EW Crossover ($\Delta T = 0.013T_c$) with $\delta_c = 1/3$–blue region, and $\delta_c = 0.4$–pink region (note that, in both cases, the BH formation region extends up to $\delta = 1$). We have also represented, for reference, the values of t_1 and t_2 giving the locus of the transition (vertical dashed lines).

Table 36: The evolution of δ_{c1} as a function of time for a EW Crossover with $\Delta T = 0.013 T_c$ when $\delta_c = 1/3$.

$\log_{10}(t_k/1\ \mathrm{s})$	δ_{c1}	$\log_{10}(t_k/1\ \mathrm{s})$	δ_{c1}
-10.2	0.33333	-10.1	0.33205
-10.0	0.33221	-9.9	0.33254
-9.8	0.33277	-9.7	0.33293
-9.6	0.33305	-9.5	0.33313
-9.4	0.33319	-9.3	0.33323
-9.2	0.33326	-9.1	0.33328
-9.0	0.33330	-8.9	0.33331
-8.8	0.33332	-8.7	0.33332
-8.6	0.33332	-8.5	0.33333

fraction of the overdense region spent in the dust–like phase, will be given, once again, by expressions (254) to (258), in accordance with the class of fluctuation we are dealing with.

For the QCD Bag Model case we have studied with some detail fluctuations crossing the horizon before the mixed phase (Section 7.1.1), during the mixed phase (Section 7.1.2) and after the mixed phase (Section 7.1.3). Here, in the EW Bag Model case, we just point out that one obtains similar results. For example, one should obtain situations similar to the ones represented on Figure 51 (naturally with different values for x, δ_{c1}, δ_{c2},...).

On Figure 86a we show the region in the (x, δ) plane for which BH formation is allowed in the case $\delta_c = 1/3$. Without the phase transition this would be a straight horizontal line at $\delta = 1/3$. On Figure 86b we show the same situation but now represented on the $(\log_{10}(t), \delta)$. We have represented also, for reference, the values t_{EW-} and t_{EW+}.

On Figure 87 we show the region in the $(\log_{10}(t), \delta)$ plane for which BH formation is allowed in the case $\delta_c = 0.7$. Without the phase transition this would be a straight horizontal line at $\delta = 0.7$.

On Table 37 we present the new values for the threshold of PBH formation during a EW first–order phase transition within the MSSM according to the Bag Model for the case $\delta_c = 1/3$.

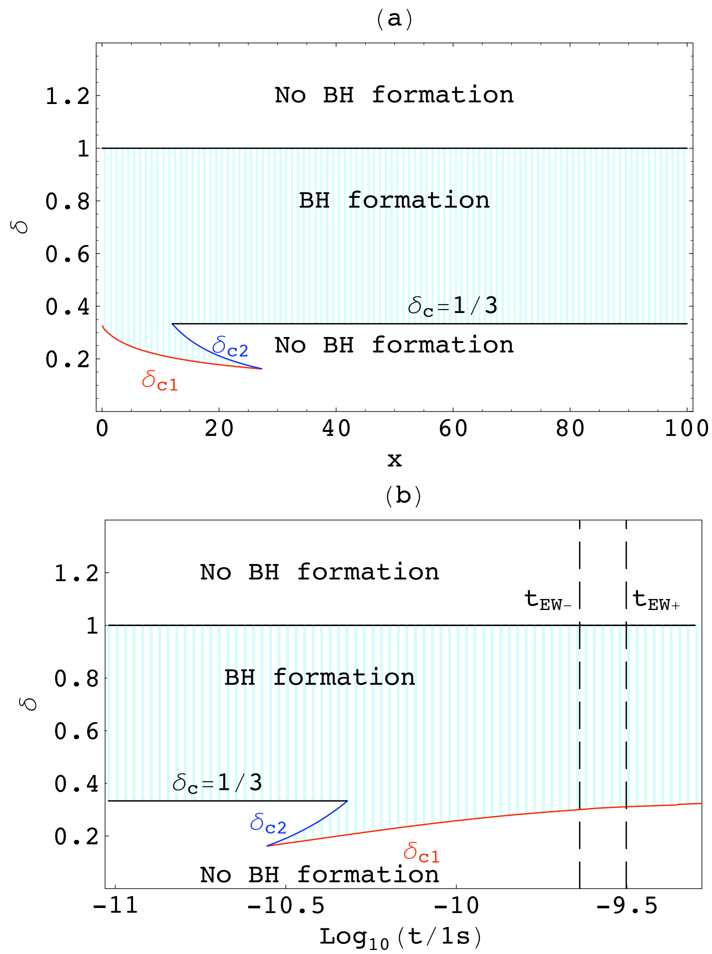

Figure 86: The curve indicating which parameter values lead to collapse to a BH when $\delta_c = 1/3$ during the EW transition within the MSSM: (a) in the (x, δ) plane; (b) in the $(\log_{10}(t/1\text{ s}), \delta)$ plane.

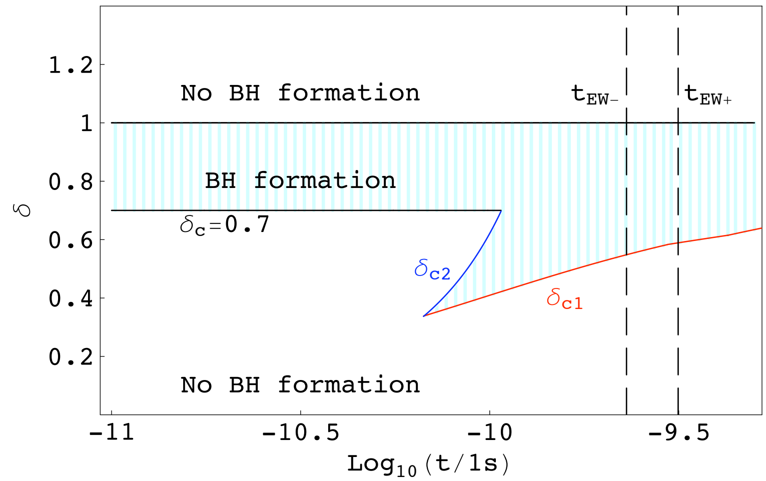

Figure 87: The curve in the $(\log_{10}(t/1\mathrm{s}), \delta)$ plane indicating which parameter values lead to collapse to a BH when $\delta_c = 0.7$ during the EW transition within the MSSM.

Table 37: The evolution of δ_{c1} and δ_{c2} (where applicable) as a function of time and as a function of the parameter x for an EW phase transition according to the Bag Model when $\delta_c = 1/3$ (see Figure 86).

$\log_{10}(t_k/1\ \mathrm{s})$	x	δ_{c1}	δ_{c2}
-10.5	22.5	0.167	0.191
-10.4	15.9	0.185	0.258
-10.3	11.2	0.203	–
-10.2	7.9	0.221	–
-10.1	5.5	0.238	–
-10	3.9	0.254	–
-9.9	2.7	0.268	–
-9.8	1.9	0.281	–
-9.7	1.3	0.292	–
-9.6	0.81	0.302	–
-9.5	0.46	0.310	–
-9.4	0.28	0.316	–
-9.3	0.15	0.322	–

9 The threshold δ_c for PBH formation during the cosmological e^+e^- annihilation

In this section we study the changes on the value of the threshold δ_c during the cosmological electron–positron annihilation. We do that by considering examples of fluctuations that cross the horizon at different epochs. The study is mostly done for $\delta_c = 1/3$. We consider here the cases $\Delta T = 0.115T_c$ (reduction of the sound speed value up to 20%, cf. Table 23) and $\Delta T = 0.276T_c$ (reduction of the sound speed value up to 10%).

Let us start with $\delta_c = 1/3$ and with a fluctuation that crosses the horizon at $t_k = 0.20$ s. In order to identify the values of δ for which collapse to a BH will occur in this case, we plot in Figure 88a both $(1-f)\delta_c$ and δ itself as functions of δ. Now, f is given by expression (267) with the sound speed $c_s(t)$ given by equation (195). We conclude that the evolution of perturbations entering the horizon at this epoch is not affected by the annihilation process. That is because t_k occurs suficiently before t_1 ($t_1 \approx 1.7$ s if $\Delta T = 0.115T_c$ and $t_1 \approx 1.1$ s if $\Delta T = 0.276T_c$ – cf. Table 25).

As a second example we show in Figure 88b the case of a fluctuation that crosses the horizon at $t_k = 0.9$ s. In this case we have a lower threshold for PBH formation $\delta_{c1} \approx 0.3041$ if $\Delta T = 0.115T_c$ and $\delta_{c1} \approx 0.3125$ if $\Delta T = 0.276T_c$.

In Figure 88c we show the case $t_k = 2.3$ s for which $\delta_{c1} \approx 0.3221$ if $\Delta T = 0.115T_c$and $\delta_{c1} \approx 0.3193$ if $\Delta T = 0.276T_c$. As a final example we show in Figure 88d the case $t_k = 8.0$ s for which the effects are much less significative.

Figure 89 shows the region on the $(\log_{10} t_k,\delta)$ plane for which collapse to a BH occurs during the cosmological electron–positron annihilation with $\delta_c = 1/3$ and with ΔT assuming the values $0.115T_c$ and $0.276T_c$. Without the annihilation process these would be straight horizontal lines at $\delta = 1/3$. We have also represented, for reference, the location of the annihilation epoch for the case $\Delta T = 0.276T_c$. It is clear that the case $\Delta T = 0.115T_c$ is the most important in the context of PBH production because it leads to a more significative reduction on the value of δ_c.

Figure 90 indicates the region on the $(\log_{10} t_k,\delta)$ plane for which collapse to a BH occurs for $\Delta T = 0.115T_c$ with $\delta_c = 1/3$ and $\delta_c = 0.7$. Without the annihilation process these would be two straight horizontal lines at $\delta = 1/3$ and $\delta = 0.7$.

9.1 Summary

As a consequence of the cosmological electron–positron annihilation, the PBH formation threshold δ_c experiences a reduction on its background value. On Table 38 we present these new values, δ_{c1}, in function of time for the case $\delta_c = 1/3$ with $\Delta T = 0.115T_c$.

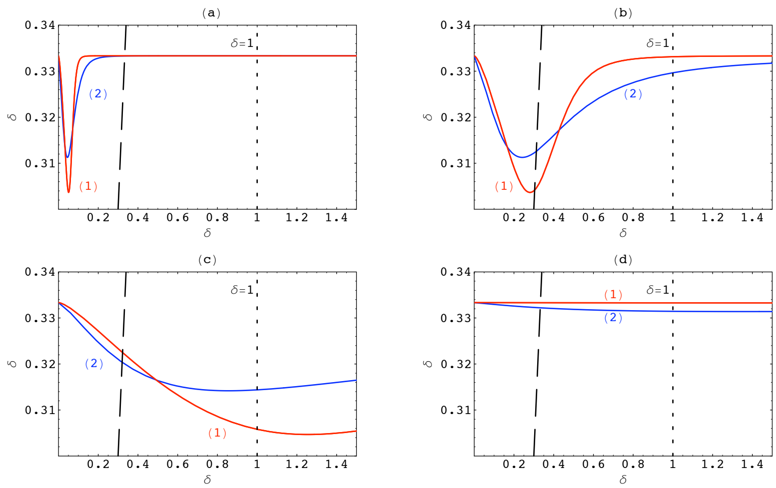

Figure 88: PBH formation during the cosmological electron–positron annihilation when $\delta_c = 1/3$ and: (a) $t_k = 0.2$ s; (b) $t_k = 0.9$ s; (c) $t_k = 2.3$ s; (d) $t_k = 8.0$ s. The solid curve corresponds to the function $(1-f)\delta_c$ when: (1) $\Delta T = 0.115 T_c$ and (2) $\Delta T = 0.276 T_c$. The dashed curve on the left corresponds to the identity δ. Collapse to a BH occurs for values of δ for which the dashed line is above the solid curve (while $\delta < 1$). The new thresholds for PBH formation are: (b)–(1) $\delta_{c1} \approx 0.3041$ and (2) $\delta_{c1} \approx 0.3125$; (c)–(1) $\delta_{c1} \approx 0.3221$ and (2) $\delta_{c1} \approx 0.3193$; (d)–(1) $\delta_{c1} \approx 0.3315$ and (2) $\delta_{c1} \approx 0.3301$. In case (a) the threshold remains $\delta_c = 1/3$ for both curves.

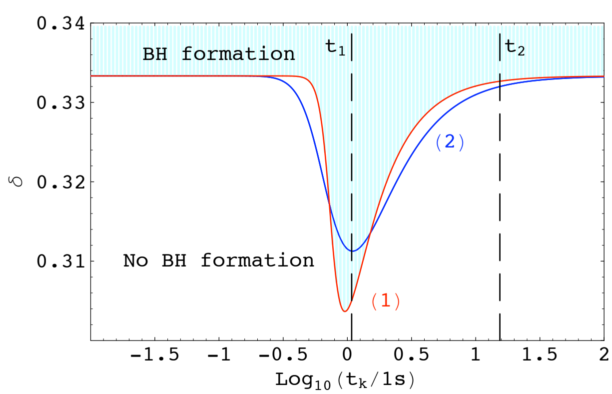

Figure 89: The curve on the $(\log_{10} t_k, \delta)$ plane indicating which parameter values lead to collapse to a BH in the case $\delta_c = 1/3$ for the cosmological electron–positron annihilation with (a) $\Delta T = 0.115 T_c$ and (b) $\Delta T = 0.276 T_c$. Without the annihilation process, these would be straight horizontal lines at $\delta = 1/3$. We have also represented, for reference, the location of the annihilation epoch for the case $\Delta T = 0.276 T_c$ (vertical dashed lines).

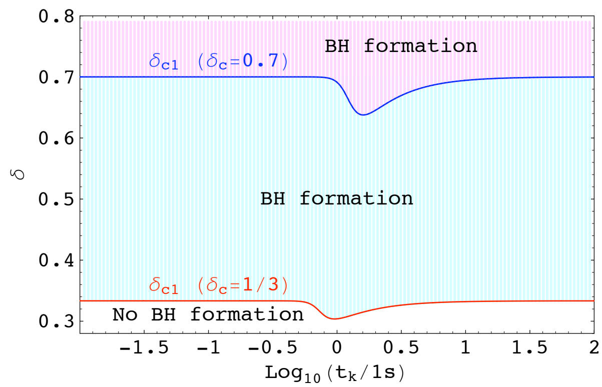

Figure 90: The curve on the $(\log_{10} t_k,\ \delta)$ plane indicating which parameter values lead to collapse to a BH in the case of the cosmological electron–positron annihilation for the cases $\delta_c = 1/3$ and $\delta_c = 0.7$ when $\Delta T = 0.115T_c$. Without the annihilation process these would be two straight horizontal lines at $\delta = 1/3$ and $\delta = 0.7$.

Table 38: The evolution of δ_{c1}, as a function of time, for the cosmological electron–positron annihilation with $\Delta T = 0.115T_c$ when $\delta_c = 1/3$.

$\log_{10}(t_k/1\ \mathrm{s})$	δ_{c1}	$\log_{10}(t_k/1\ \mathrm{s})$	δ_{c1}
-0.5	0.3333	-0.4	0.3333
-0.3	0.3327	-0.2	0.3273
-0.1	0.3096	0	0.3039
0.1	0.3087	0.2	0.3147
0.3	0.3197	0.4	0.3235
0.5	0.3263	0.6	0.3283
0.7	0.3298	0.8	0.3308
0.9	0.3315	1.0	0.3321
1.1	0.3324	1.2	0.3327
1.3	0.3329	1.4	0.3330
1.5	0.3331	1.6	0.3332
1.7	0.3332	1.8	0.3333

10 Running–tilt power–law spectrum

Inflationary models predict that the spectral index of fluctuations n should be a slowly varying function of scale (i.e. $n = n(k)$). Fits of observations of LSS and CMB usually employ a power–law spectrum

$$P(k) = P(k_c)\left(\frac{k}{k_c}\right)^{n(k)} \tag{277}$$

where k_c is some pivot scale and $n(k)$ represents the running of the spectral index. We may write $n(k)$ in the form (e.g. Düchting, 2004)

$$n(k) = n_0 + \sum_{i\geq 1}\frac{n_i}{(i+1)!}\left(\ln\frac{k}{k_c}\right)^i. \tag{278}$$

The value of n_0 depends on the pivot scale used, and represents the *tilt* of the spectrum. It is given by (e.g. Spergel et al., 2003)

$$n_0 = n_s(k) = \frac{d\ln(P(k))}{d\ln(k)}. \tag{279}$$

The value of n_1 represents the *running of tilt* of the spectrum for the chosen pivot scale. It is given by (e.g. Düchting, 2004)

$$n_1 = \alpha_s(k) = \frac{dn_s(k)}{d\ln(k)}. \tag{280}$$

Typical *slow–roll* models predict that the running of the spectal index α_s is unobservably small. However, this issue has generated recent interest after the WMAP team claimed that $\alpha_s < 0$ was favoured over $\alpha_s = 0$ (e.g. Tegmark et al., 2004). The evidence for the running comes, predominantly, from the very largest scales multipoles. Excluding $l < 5$ multipoles from the WMAP temperature we obtain $\alpha_s \approx 0$ (Bridle et al., 2003).

The observational input needed for the running–tilt power spectrum is, besides the value of $\delta_H^2(k_0, t_{k_0})$ (see Sobrinho & Augusto, 2007), the values for the parameters n_i evaluated at some pivot scale k_c. According to the most recent results from the WMAP mission we have (e.g. Spergel et al., 2007)

$$n_0 = n_s(k_c) = 0.951^{+0.015}_{-0.019} \tag{281}$$

$$n_1 = \alpha_s(k_c) = -0.055^{+0.029}_{-0.035} \tag{282}$$

where the pivot scale is $k_c = 0.002\mathrm{Mpc}^{-1} \approx 6.5\times 10^{-26}\mathrm{m}^{-1}$. The values for the other parameters (i.e. the values of n_i, $i \geq 2$) are unknown at the present. A definitive measurement of n_1, and possibly also of n_2 and n_3 is expected from upcoming surveys such as the Planck satellite mission[33] (e.g. Düchting,

[33] Planned to be launched, by the European Space Agency, on October 2008 (http://www.rssd.esa.int/index.php?project=Planck).

2004). Here, we consider a running–tilt power–law spectrum $n(k)$ in the form (see Sobrinho & Augusto, 2007)

$$n(k) = n_0 + \frac{n_1}{2} \ln \frac{k}{k_c} + \frac{n_2}{6} \left(\ln \frac{k}{k_c} \right)^2 + \frac{n_3}{24} \left(\ln \frac{k}{k_c} \right)^3 \tag{283}$$

which is an expansion of equation (278) up to $i = 4$.

The simplest models of inflation suggest that the coefficients n_i scale as powers ϵ^i of some slow–roll parameter $\epsilon \approx 0.1$. This means that the expansion (283) can be expected to be accurate to 10% for about 16 e–foldings around the pivot scale (e.g. Düchting, 2004). This implies sensitivity down to horizon masses of $\sim 10 M_\odot$. For scales probing the QCD epoch, the accuracy of expression (283) is reduced to $20-30\%$ and in the case of the EW epoch the case is by far worse. In that cases we will regard expression (283) as a phenomenological one.

If one wants to have a significant number of PBHs produced at some epoch, then one needs to have a spectrum with more power on that particular epoch. In practice this is done introducing some fine–tunning into the spectrum (e.g. Sobrinho & Augusto, 2007). In our case, this fine–tunning is done by guessing which set of values for n_2 and n_3 would lead to interesting results in terms of PBH production.

Given a location k_+ (or, in terms of time t_+) to the maximum of $n(k)$ it turns out that the corresponding value of n_3 is given by equation (Sobrinho & Augusto, 2007).

$$n_3 = -\frac{4 \left(3n_1 + 2n_2 \ln \frac{k_+}{k_c} \right)}{3 \left(\ln \frac{k_+}{k_c} \right)^2} \tag{284}$$

where k_c is a pivot scale. Inserting this expression of n_3 into the expression of $n(k)$ (Sobrinho & Augusto, 2007, equation 150) with $k = k_+$ and $n(k_+) = n_{max}$ we obtain for n_2 the expression

$$n_2 = -\frac{6 \left(3n_0 - 3n_{max} + n_1 \ln \frac{k_+}{k_c} \right)}{\left(\ln \frac{k_+}{k_c} \right)^2}. \tag{285}$$

On Sobrinho & Augusto (2007, Table 7) we have already presented the values of n_2 and n_3 for different locations of the maximum k_+ and for different values of n_{max}. We have also presented the corresponding graphics with the curves $n(k)$ (Figures 69 to 74 from Sobrinho & Augusto, 2007). However, those values were determined without taking into account the influence of a positive cosmological constant Λ (cf. Section 1.5), which might be used when one converts an instant of time t_k to the corresponding wavenumber k by means of equation (203).

On Table 39 we present, as an example, the values for n_2 and n_3 for the case $n_{max} = 1.4$. Notice that these set of values are model independent in the case of phase transitions. On Figure 91 we show the curves $n_2(t_+)$ and $n_3(t_+)$ for

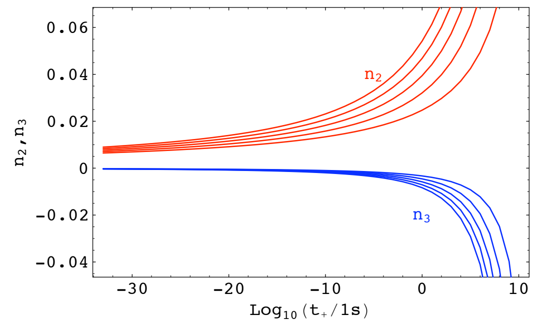

Figure 91: The curves $n_2(t_+)$ and $n_3(t_+)$ for different values of n_{max}. In the case of n_2 we have, from bottom to top $n_{max} = 1$, 1.1, 1.2, 1.3 and 1.4. In the case of n_3 we have, the same sequence of n_{max} from top to bottom.

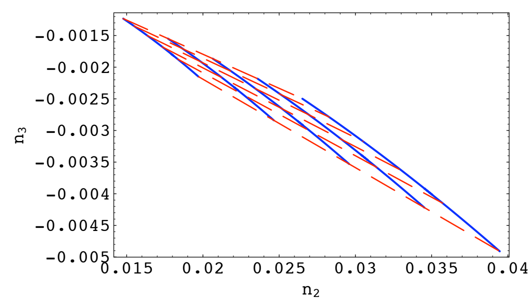

Figure 92: The region on the $(n_2,\, n_3)$ plane that leads to a blue spectrum $(n > 1)$. The solid lines correspond to constant n_{max} starting with $n_{max} = 1$ (left) and ending with $n_{max} = 1.4$ (right), in steps of 0.1. The dashed lines correspond to constant k_+, starting with $\log_{10}(k_+/1\mathrm{m}^{-1}) \approx -14$ (top) and ending with $\log_{10}(k_+/1\mathrm{m}^{-1}) \approx -17$ (bottom), in integer steps.

different values of n_{max}. In Figure 92 we show, in the $(n_2,\, n_3)$ plane, the lines corresponding to constant k_+ and the lines corresponding to constant n_{max} such that $1 < n(k) \leq 1.4$.

Table 39: The values of n_2 and n_3 when $n_{max} = 1.4$.

$\log_{10}(t_+/1\ \mathrm{s})$	$\log_{10}(k_+/1\mathrm{m}^{-1})$	n_2	n_3
-23.0	-6.90	0.0124	-0.000661
-22.0	-7.40	0.0129	-0.000707
-21.0	-7.90	0.0134	-0.000758
-20.0	-8.40	0.0139	-0.000815
-19.0	-8.90	0.0145	-0.000877
-18.0	-9.40	0.0152	-0.000948
-17.0	-9.90	0.0159	-0.00103
-16.0	-10.4	0.0167	-0.00111
-15.0	-10.9	0.0175	-0.00121
-14.0	-11.4	0.0184	-0.00133
-13.0	-11.9	0.0194	-0.00146
-12.0	-12.4	0.0205	-0.00160
-11.0	-12.9	0.0218	-0.00178
-10.0	-13.4	0.0231	-0.00197
-9.00	-13.9	0.0247	-0.00220
-8.00	-14.4	0.0264	-0.00247
-7.00	-14.9	0.0283	-0.00280
-6.00	-15.4	0.0305	-0.00318
-5.00	-15.9	0.0331	-0.00364
-4.00	-16.4	0.0360	-0.00421
-3.00	-16.9	0.0395	-0.00491
-2.00	-17.4	0.0435	-0.00579
-1.00	-17.9	0.0483	-0.00690
0	-18.4	0.0542	-0.00834
1.00	-18.9	0.0613	-0.0102
2.00	-19.4	0.0702	-0.0128
3.00	-19.9	0.0816	-0.0164
4.00	-20.4	0.0963	-0.0215
5.00	-20.9	0.116	-0.0291
6.00	-21.4	0.144	-0.0411
7.00	-21.9	0.184	-0.0611
8.00	-22.4	0.247	-0.0973
9.00	-22.9	0.353	-0.171
10.0	-23.4	0.556	-0.347

11 The fraction of the Universe going into PBHs

The fraction of the Universe going into PBHs at a given epoch t_k is given by (e.g. Sobrinho & Augusto, 2007)

$$\beta(t_k) = \frac{1}{\sqrt{2\pi}\sigma(t_k)} \int_{\delta_c}^{\delta_{max}} \exp\left(-\frac{\delta^2}{2\sigma^2(t_k)}\right) d\delta \tag{286}$$

where $\sigma(t_k)$ represents the mass variance at that epoch, $\delta_{max} = 1$, and δ_c represents the threshold for PBH formation. The value of δ_c is, in the case of a radiation–dominated universe, a constant somewhere between 1/3 and 0.7 (see e.g. Sobrinho & Augusto, 2007). However, if the universe experiences a phase transition, the value of δ_c experiences a reduction which favours PBH formation (Sections 7, 8 and 9). In this section, we consider that, during radiation domination, $\delta_c = 1/3$ and that, during the QCD transition, the EW transition, and the electron–positron annihilation epoch, δ_c assumes the values obtained in Sections 7, 8, and 9, respectively.

In the presence of a Crossover–like transition, such as the QCD Crossover (Section 2.3.3), the EW Crossover (Section 3.2.1) or the electron–positron annihilation (Section 4), equation (286) must be replaced by

$$\begin{aligned}\beta_1(t_k) = &\frac{1}{\sqrt{2\pi}\sigma(t_k)} \int_{\delta_{c1}}^{\delta_c} \exp\left(-\frac{\delta^2}{2\sigma^2(t_k)}\right) d\delta \\ &+\frac{1}{\sqrt{2\pi}\sigma(t_k)} \int_{\delta_c}^{1} \exp\left(-\frac{\delta^2}{2\sigma^2(t_k)}\right) d\delta\end{aligned} \tag{287}$$

where the additional integral accounts for the contribution from the Crossover epoch. We refer to the second integral, which is equal to the integral in expression (286), as the *contribution from radiation*. Denoting this integral by $\beta_{Rad}(t_k)$ equation (287) becomes

$$\beta_1(t_k) = \frac{1}{\sqrt{2\pi}\sigma(t_k)} \int_{\delta_{c1}}^{\delta_c} \exp\left(-\frac{\delta^2}{2\sigma^2(t_k)}\right) d\delta + \beta_{Rad}(t_k) \tag{288}$$

Naturally, if we are dealing with epochs sufficiently apart from the transition such that $\delta_{c1} \approx \delta_c$ then equation (286) remains valid.

On the other hand, in the presence of a Bag Model–like transition, such as the QCD Bag Model transition (Section 2.3.1) or the EW Bag Model transition (Section 3.2.2), equation (286) is valid only up to some instant after which there is an additional window $[\delta_{c1}, \delta_{c2}]$ allowing PBH formation (cf. Figure 66 and Table 32 for the QCD, Figure 86 and Table 37 for the EW). For these cases equation (286) must be replaced by

$$\beta_2(t_k) = \frac{1}{\sqrt{2\pi}\sigma(t_k)} \int_{\delta_{c1}}^{\delta_{c2}} \exp\left(-\frac{\delta^2}{2\sigma^2(t_k)}\right) d\delta + \beta_{Rad}(t_k) \tag{289}$$

Table 40: The different scenarios concerning the calculus of β.

Scenario	EW model	QCD model	e^-e^+ model
1	Crossover	Bag Model	Crossover
2	Crossover	Lattice Fit	Crossover
3	Crossover	Crossover	Crossover
4	Bag Model	Bag Model	Crossover
5	Bag Model	Lattice Fit	Crossover
6	Bag Model	Crossover	Crossover

Eventually, we reach some point where there is no more δ_{c2} (see e.g. Figure 66). In that case there is a single window $[\delta_{c1}, 1]$ for PBH formation and we must use, instead, equation (288).

Finally, in the case of a QCD Lattice Fit (Section 2.3.2) we must consider another extra window $[\delta_{cA}, \delta_c]$ allowing PBH formation (cf. Figure 80, Table 34). In this case we must replace equation (286) by

$$\beta_3(t_k) = \frac{1}{\sqrt{2\pi}\sigma(t_k)} \int_{\delta_{cA}}^{\delta_c} \exp\left(-\frac{\delta^2}{2\sigma^2(t_k)}\right) d\delta + \beta_{Rad}(t_k) \tag{290}$$

Over a brief period we might have to consider the window $[\delta_{c1}, \delta_{c2}]$ (cf. Figure 80). For that period we must use, instead

$$\begin{aligned}\beta_4(t_k) = \frac{1}{\sqrt{2\pi}\sigma(t_k)} \int_{\delta_{c1}}^{\delta_{c2}} \exp\left(-\frac{\delta^2}{2\sigma^2(t_k)}\right) d\delta + \\ + \frac{1}{\sqrt{2\pi}\sigma(t_k)} \int_{\delta_{cA}}^{\delta_c} \exp\left(-\frac{\delta^2}{2\sigma^2(t_k)}\right) d\delta + \beta_{Rad}(t_k)\end{aligned} \tag{291}$$

Moving to later epochs we reach some point after which there is no more δ_{c2} available (see e.g. Figure 80). In that case there is a single window $[\delta_{c1}, 1]$ for PBH formation and we use equation (288).

Taking into account the considered models for the EW phase transition (Section 3.2), for the QCD transition (Section 2.3), and for the electron–positron annihilation (Section 4), there are six different possible scenarios (2 EW models $\times$ 3 QCD models $\times$ 1 e^-e^+ model) concerning the determination of the curve $\beta(t_k)$. We list those scenarios in Table 40.

For a given scenario, and for a given instant t_k, one must choose the appropriate expression to determine the value $\beta(t_k)$. Proceding this way, for different values of t_k, one can determine the curve $\beta(t_k)$ for that particular scenario.

In Sections 11.1 to 11.5 we made use of a few abreviations concerning different contributions to $\beta(t_k)$. We list these abreviations in Table 41. For example, RBE, represents a case for which there are non–negligible contributions from radiation (R), from the QCD Bag Model (B), and from the EW Bag Model (E) but with negligible contributions from the electron–positron annihilation as well as from the QCD Lattice Fit and from the QCD Crossover (if one chooses one of these models instead of the Bag Model).

We might have also situations with one or more contributions exceeding the observational limits (these are labeled with an $*$). For exeample, RB^*LCE^*, represents a case for which we have, besides the contribution from radiation R, contributions from the QCD Lattice Fit (L) or from the QCD Crossover (C). The QCD Bag Model is excluded due to observational constraints (B^*). The same happens for the EW Bag Model (E^*). The contribution from the electron–positron annihilation epoch is negligible in this case.

11.1 Radiation–dominated universe

In this section we determine the fraction of the universe going into PBHs at different epochs for a radiation–dominated universe with a running–tilt power spectrum (Section 10). We consider, for t_+, all orders of magnitude between 10^{-23} s (end of inflation) and 10^8 s. We are interested in a blue spectrum, i.e, a spectrum for which $n > 1$. In fact, if we want to have interesting values for β, then we should have, at least, $n \gtrsim 1.22$. As an upper limit we consider $n \approx 2.0$. This corresponds to a cut–off at $t_k \sim 10^5$ s (see Figure 93) which excludes PBHs with masses larger than $\sim 10^{10} M_\odot$ (which is equivalent to the mass of the present day largest Supermassive Black Hole (SMBH) candidates; e.g. Natarajan & Treister, 2008).

Each pair of the form (t_+, n_{max}) determines a different location and a different value for the maximum value of $\beta(t_k)$. In general one of three things might occur:

(1) $\beta(t_k)$ exceeds the observational constraints $\Rightarrow$ the pair (t_+, n_{max}) must be rejected.

(2) $\beta(t_k)$ is negligible ($< 10^{-100}$) for all values of t_k, in which case we take $\beta(t_k) = 0$.

(3) $\beta(t_k)$ is always bellow the observational constraints and, at least during some epoch, above 10^{-100}; these are the cases of interest to us.

Let us consider, as an example, the case $n = 1.30$. If $t_+ = 10^{-17}$ s, then $\beta(t_k)$ exceeds the observational constraints as it is clear from Figure 94. On the other hand, if $t_+ = 10^{-16}$ s we obtain a valid curve for $\beta(t_k)$ (see Figure 95) with $\beta_{max} \sim 10^{-17}$. As one moves t_+ to later epochs the value of β_{max} becomes smaller (see Figure 95) until, for $t_+ = 10^{-10}$ s, we reach $\beta_{max} \sim 10^{-133}$ (see Figure 96). Thus, we consider that, in the case of $n = 1.30$, there is a window

Table 41: Different contributions to β.

sigla	Meaning
B	QCD Bag Model
BE	QCD Bag Model and EW Bag Model
BL	QCD Bag Model or QCD Lattice Fit
BLE	(QCD Bag Model or QCD Lattice Fit) and EW Bag Model
E	EW Bag Model
ea	e^-e^+ annihilation
L	QCD Lattice Fit
R	Radiation
RB	Radiation and QCD Bag Model
RBE	Radiation and QCD Bag Model and EW Bag Model
RBea	Radiation and QCD Bag Model and e^-e^+ annihilation
RBL	Radiation and (QCD Bag Model or QCD Lattice Fit)
RBLC	Radiation and (QCD Bag Model or QCD Lattice Fit or QCD Crossover)
RBLCE	Radiation and (QCD Bag Model or QCD Lattice Fit or QCD Crossover) and EW Bag Model
RBLCea	Radiation and (QCD Bag Model or QCD Lattice Fit or QCD Crossover) and e^-e^+ annihilation
RBLE	Radiation and (QCD Bag Model or QCD Lattice Fit) and EW Bag Model
RC	Radiation and QCD Crossover
RCea	Radiation and QCD Crossover and e^-e^+ annihilation
RE	Radiation and EW Bag Model
Rea	Radiation and e^-e^+ annihilation
RL	Radiation and QCD Lattice Fit
RLea	Radiation and QCD Lattice Fit and e^-e^+ annihilation

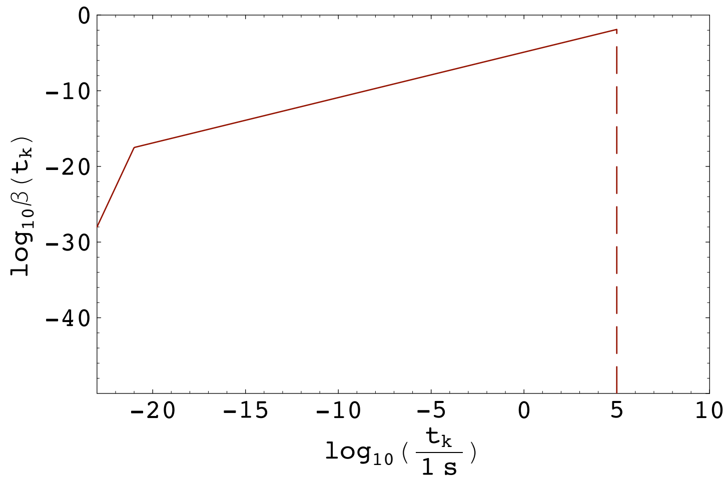

Figure 93: Observational constraints on $\beta(t_k)$. The vertical dashed line ($t_k = 10^5$ s) corresponds to an horizon mass of $\sim 10^{10} M_\odot$ (adapted from Carr, 2005).

10^{-16} s $\leq t_+ \leq 10^{-11}$ s which is suitable for PBH formation. Cases with $t_+ < 10^{-16}$ s are not allowed and cases with $t_+ > 10^{-11}$ s are allowed but with negligible results.

We studied the intervals of this permitted window for different values of n_+ (between 1.20 and 2.00). The window moves to later epochs as one moves to larger values of n_+. As a lower limit, for $n < 1.22$, we get $\beta(t_k) \approx 0$ (no matter t_k or t_+). We selected 165 cases suitable for PBH production, shown in Table 42 (these cases are marked by 'R').

On the lower right corner of Table 42 we show the cases for which $\beta(t_k)$ reaches values to the right of the cut–off line at $t_k = 10^5$ s ('R' with a gray background). We selected three examples, in order to ilustrate this particular situation (see Figures 97, 98, and 99). In the case when $t_+ = 10^7$ s and $n_+ = 2.00$, represented in Figure 99, the maximum of $\beta(t_k)$ is attained when $t_k \approx 10^{-6.5}$ s which corresponds to an horizon mass of $10^{11} M_\odot$ ($> 10^{10} M_\odot$).

11.2 EW Crossover

It was already mentioned that, in the context of the SMPP, the EW transition is a very smooth Crossover (Section 3.2.1). As a consequence of this, the contribution from the EW Crossover to the value of $\beta(t_k)$ is very small. In fact, in this case, the new threshold δ_{c1} stays always very close to δ_c (see Table 36).

We consider, as an example, $t_+ = 10^{-8}$ s and $n_+ = 1.40$. In this case, the contribution from the EW Crossover to the total value of $\beta(t_k)$ is negligible (of order unity – Figure 100)[34]. On the face of this, we neglect all contributions

[34]In order to properly read this graphic start on the left and move across the black line

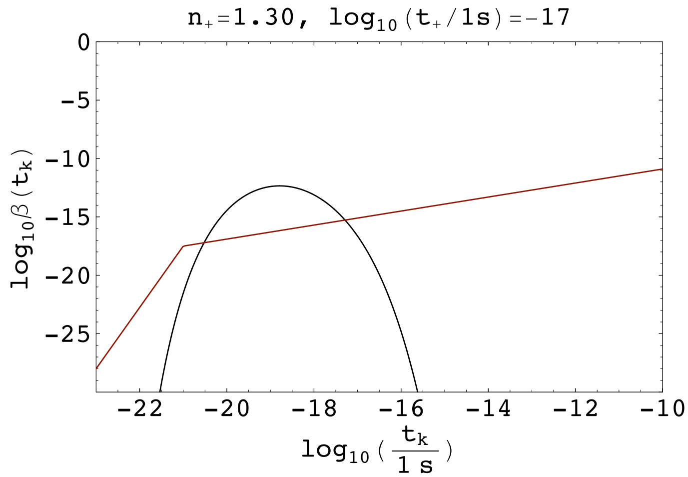

Figure 94: In a radiation–dominated universe with a running–tilt power spectrum, we cannot have $n_+ = 1.30$ together with $t_+ = 10^{-17}$ s since the curve $\beta(t_k)$ – black – does not respect the observational constraints (maroon).

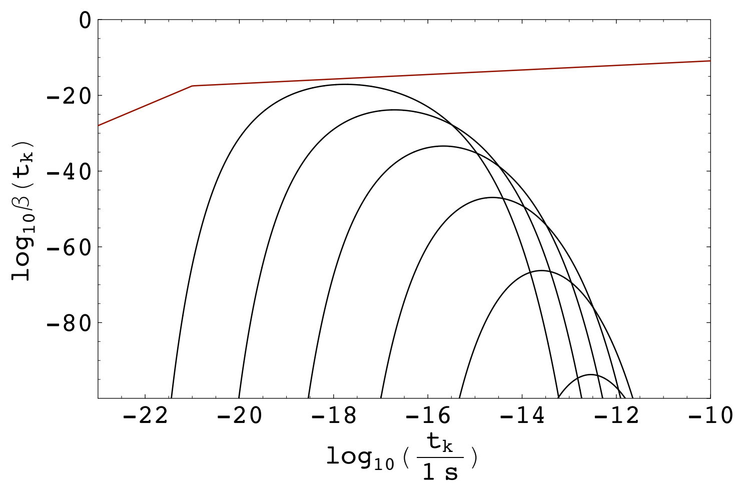

Figure 95: The fraction of the universe going into PBHs for a radiation–dominated universe with a running–tilt power spectrum with $n_+ = 1.30$ and (from left to right): $t_+ = 10^{-16}$ s, $t_+ = 10^{-15}$ s, $t_+ = 10^{-14}$ s, $t_+ = 10^{-13}$ s, $t_+ = 10^{-12}$ s, and $t_+ = 10^{-11}$ s.

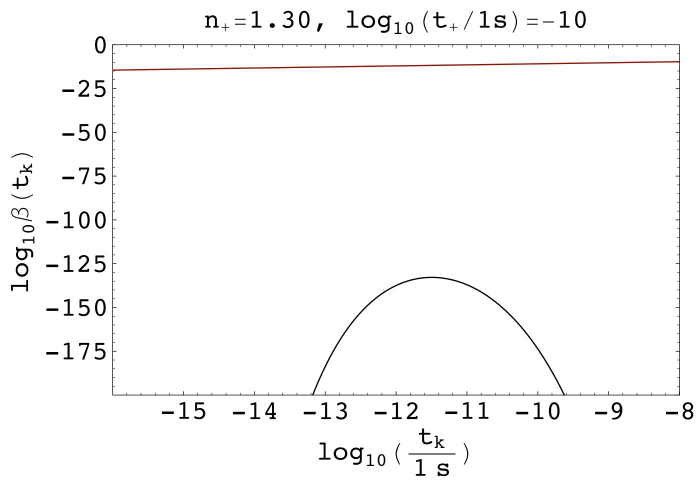

Figure 96: The fraction of the universe going into PBHs for a radiation–dominated universe with a running–tilt power spectrum with $n_+ = 1.30$ and $t_+ = 10^{-10}$ s.

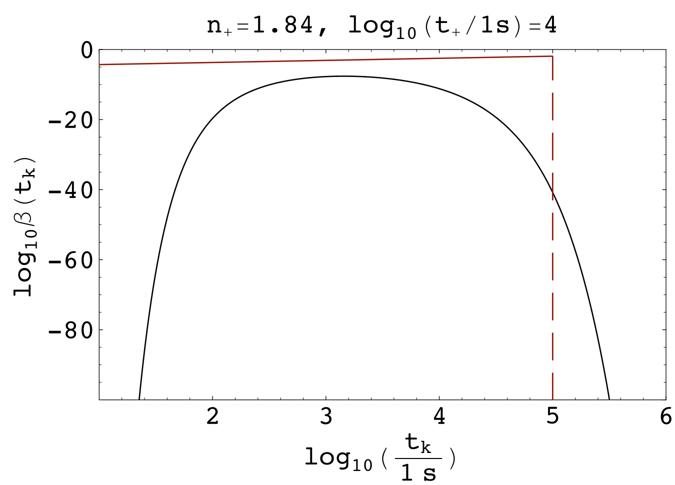

Figure 97: The fraction of the universe going into PBHs in a radiation–dominated universe with a running–tilt power spectrum when $n_+ = 1.84$ and $t_+ = 10^4$ s. Some values go over the $\sim 10^{10} M_\odot$ line (cf. Figure 93).

Table 42: The cases for which $\beta > 10^{-100}$ for a radiation–dominated Universe with a running–tilt power law spectrum. Here n_{max} represents the maximum value of the spectral index $n(k)$, and t_+ gives the location of that maximum (see Section 10). In cyan we show the cases for which $\beta(t_k) \approx 0$ and in red the cases for which $\beta(t_k)$ exceeds the observational constraints (cf. Figure 93). The cases suitable for PBH production are marked by 'R' and in white. In gray we show the cases for which $\beta(t_k)$ crosses the $\approx 10^{10} M_\odot$ line.

	n_{max}																																								
$\log_{10}(t_+/1s)$	1.20	1.22	1.24	1.26	1.28	1.30	1.32	1.34	1.36	1.38	1.40	1.42	1.44	1.46	1.48	1.50	1.52	1.54	1.56	1.58	1.60	1.62	1.64	1.66	1.68	1.70	1.72	1.74	1.76	1.78	1.80	1.82	1.84	1.86	1.88	1.90	1.92	1.94	1.96	1.98	2.00
-23		R	R																																						
-22		R	R																																						
-21		R	R																																						
-20			R																																						
-19			R	R																																					
-18			R	R	R																																				
-17				R	R	Fig. 94																																			
-16				R	R	R Fig. 95																																			
-15					R	R Fig. 95																																			
-14					R	R Fig. 95	R																																		
-13					R	R Fig. 95	R																																		
-12						R Fig. 95	R	R																																	
-11						R Fig. 95	R	R	R																																
-10						Fig. 96	R	R	R																																
-9								R	R	R																															
-8								R	R	R	R																														
-7									R	R	R	R																													
-6										R	R	R	R																												
-5											R	R	R	R																											
-4											R	R	R	R	R	R																									
-3												R	R	R	R	R	R																								
-2														R	R	R	R	R	R																						
-1															R	R	R	R	R	R	R																				
0																R	R	R	R	R	R	R	R																		
1																		R	R	R	R	R	R	R	R	R															
2																				R	R	R	R	R	R	R	R	R	R												
3																						R	R	R	R	R	R	R	R	R	R	R									
4																								R	R	R	R	R	R	R	R	R	R Fig. 97	R	R	R					
5																											R	R	R	R	R	R	R	R	R Fig. 98	R	R	R	R	R	R
6																															R	R	R	R	R	R	R	R	R	R	R
7																																			R	R	R	R	R	R	R Fig. 99
8																																								R	R
9																																									

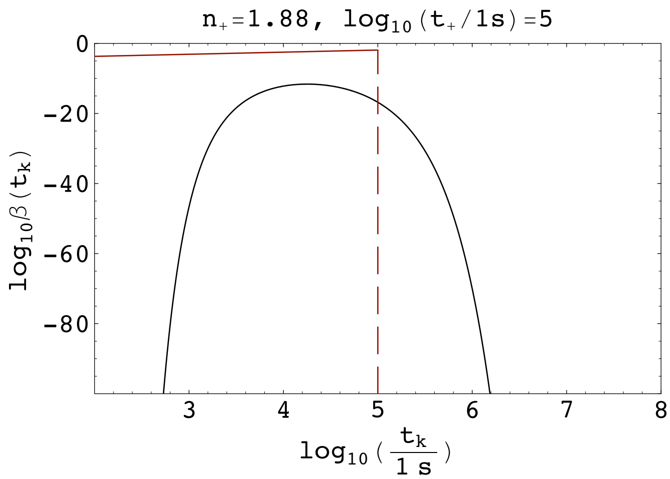

Figure 98: The fraction of the universe going into PBHs in a radiation–dominated universe with a running–tilt power spectrum when $n_+ = 1.88$ and $t_+ = 10^5$ s. Some values go over the $\sim 10^{10} M_\odot$ line (cf. Figure 93).

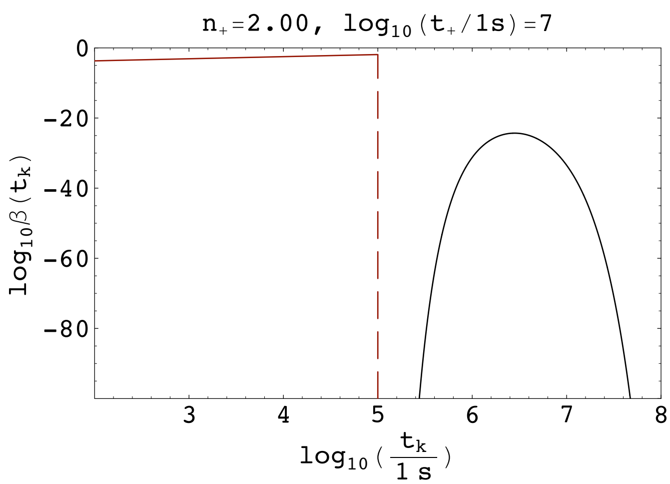

Figure 99: The fraction of the universe going into PBHs in a radiation–dominated universe with a running–tilt power spectrum when $n_+ = 2.00$ and $t_+ = 10^7$ s. In this case the peak, and all non–zero values, fall on the $> 10^{10} M_\odot$ region (cf. Figure 93).

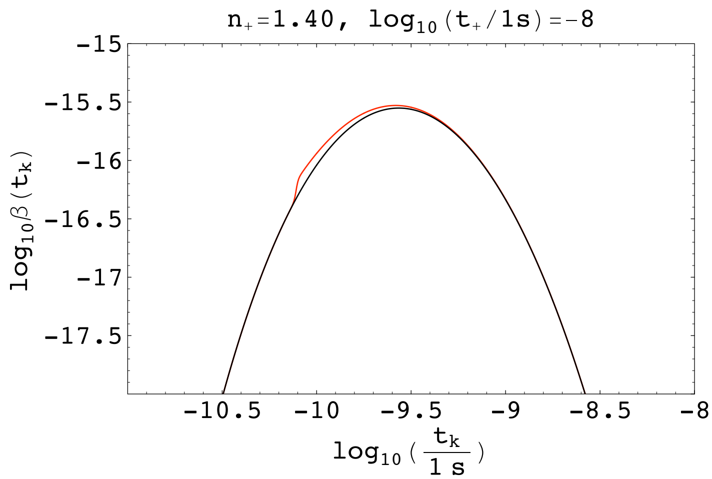

Figure 100: The fraction of the universe going into PBHs for a running–tilt power spectrum with $n_+ = 1.40$ and $t_+ = 10^{-8}$ s. The red line corresponds to the contribution from the EW Crossover while the black line represents the contribution from the radiation domination. The maximum difference between the two in $\beta(t_k)$ is of order unity ($\simeq 10^{0.1}$).

from the EW Crossover.

11.3 Electron–positron annihilation

The cosmological electron–positron annihilation ocurred when the age of the universe was ~ 1 s. Thus, the additional contribution from this epoch to the global value of β is more relevant when $t_+ \sim 1$ s. Integrating equation (288), with the threshold δ_{c1} replaced by the appropriate values (e.g. Table 38), we find that the cases with a non–zero contribution from the electron–positron annihilation are in the range $-2 \leq \log_{10}(t_+/1s) \leq 2$ and $1.52 \leq n_+ \leq 1.76$, as shown on Table 43.

Let us start with $t_+ = 1$ s. In this case the contribution from the electron–positron annihilation epoch is almost equal in magnitude to the contribution from radiation (although with peaks at different epochs). In Figure 101a we show, as a first example, the case $t_+ = 1$ s and $n_+ = 1.56$. From the radiation contribution we have $\beta_{max} \sim 10^{-29}$ located at $t_k \sim 10^{-1.14}$ s and from the electron–positron annihilation contribution we have $\beta_{max} \sim 10^{-34}$ located at $t_k \sim 10^{-0.07}$ s. As a second example we show in Figure 101b the case $t_+ = 1$ s and $n_+ = 1.62$. Now, we have from the radiation contribution $\beta_{max} \sim 10^{-10}$ located at $t_k \approx 10^{-1.2}$ s and from the electron–positron annihilation contribution $\beta_{max} \sim 10^{-12}$ located at $t_k \approx 10^{-0.08}$ s.

(contribution from radiation), then move to the red line (EW Crossover contribution) and, finally, move once again to the black line.

Table 43: The contribution to β from the electron–positron annihilation epoch. In yellow we show the cases for which there is a non–negligible contribution to β from the electron–positron annihilation epoch. For more details see Tables 41 and 42.

	n_{max}														
$\log_{10}(t_+/1s)$	1.50	1.52	1.54	1.56	1.58	1.60	1.62	1.64	1.66	1.68	1.70	1.72	1.74	1.76	1.78
-3	RB*L*C	RB*L*C*													
-2	RBLC	RB*LC	RB*L*Cea Fig. 103	RB*L*Cea											
-1	R	Rea	RBLCea	RBLCea Fig. 102	RBLCea	RBLCea									
0	R	Rea	Rea	Rea Fig. 101a	Rea	Rea	Rea Fig. 101b	Rea							
1		ea	Rea Fig. 101c	Rea	Rea	Rea	Rea	Rea	Rea Fig. 101d	Rea	Rea*				
2					Rea	Rea Fig. 101e	Rea	Rea	Rea	Rea Fig. 101f	Rea	Rea	Rea	Rea*	
3							R	R	R	R	R	R	R	R	R

When $t_+ \approx 10$ s the contribution from the electron–positron annihilation epoch exceeds the contribution from radiation. As a first example let us consider the case $t_+ = 10$ s and $n_+ = 1.54$ (Figure 101c). Now we have a modest contribution from the electron–positron annihilation epoch with $\beta_{max} \sim 10^{-67}$ located at $t_k \sim 10^{-0.02}$ s and an even smaller contribution from radiation with $\beta_{max} \sim 10^{-80}$ located at $t_k \sim 10^{-0.045}$ s. As a second example we consider the case $t_+ = 10$ s and $n_+ = 1.66$ (Figure 101d). We now have more interesting values with $\beta_{max} \sim 10^{-8}$ located at $t_k \sim 10^{-0.025}$ s from the electron–positron annihilation epoch contribution and $\beta_{max} \sim 10^{-10}$ located at $t_k \sim 10^{-0.09}$ s from the radiation contribution (the peaks nearly overlap).

When $t_+ \approx 100$ s the contribution from the electron–positron annihilation epoch appears as an extension to the left on the curve of $\beta(t_k)$ as can be seen in Figures 101e and 101f.

In the case $t_+ = 10^{-1}$ s we might simultaneously have contributions from the electron–positron annihilation epoch and from the QCD phase transition ($RBLCea$ in Table 43). However, in these cases the main contribution always comes from radiation. As an example we have the case $t_+ = 10^{-1}$ s and $n_+ = 1.56$ represented on Figure[35] 102.

When $t_+ = 10^{-2}$ s and $n_+ = 1.54$ or $n_+ = 1.56$ we also simultaneously have contributions from the electron–positron annihilation epoch and from the QCD. However, in these cases the main contribution to $\beta(t_k)$ comes from radiation and from the QCD Crossover (if one adopts for the QCD the Bag Model or the Lattice Fit, then these two cases are excluded due to observational constraints, see Section 11.4). In Figure 103 we show, as an example, the case $t_+ = 10^{-2}$ s and $n_+ = 1.54$, some situations of which are excluded.

11.4 QCD phase transition

The contribution from the QCD phase transition to the global value of β depends on the model one adopts. There are some cases which are allowed when one considers only the contribution from radiation but which must be excluded when one takes into account the QCD phase transition because of the observational limits (cf. Tables 44, 45 and 46).

Consider, for example, the case $t_+ = 10^{-4}$ s and $n_+ = 1.48$, represented in Figure 104. It is clear that if one adopts a Bag Model or a Lattice Fit for the QCD transition, this case must be excluded. However, if one adopts the Crossover model, then it remains valid.

As a peculiar example we show the case $t_+ = 10^{-3}$ s and $n_+ = 1.52$, which is allowed when one takes into account only the contribution from radiation domination but must be excluded whatever the model one adopts for the QCD phase transition (Figure 105).

[35] In order to interpret correctly the curves on Figure 102, assuming a QCD Bag Model, start on the left over the blue line, then move to the black line (contribution from radiation) and, finally, move to the cyan line (contribution from the electron–positron annihilation). In the case of a QCD Lattice Fit start, instead, with the line in magenta and in the case of a QCD Crossover start with the green line.

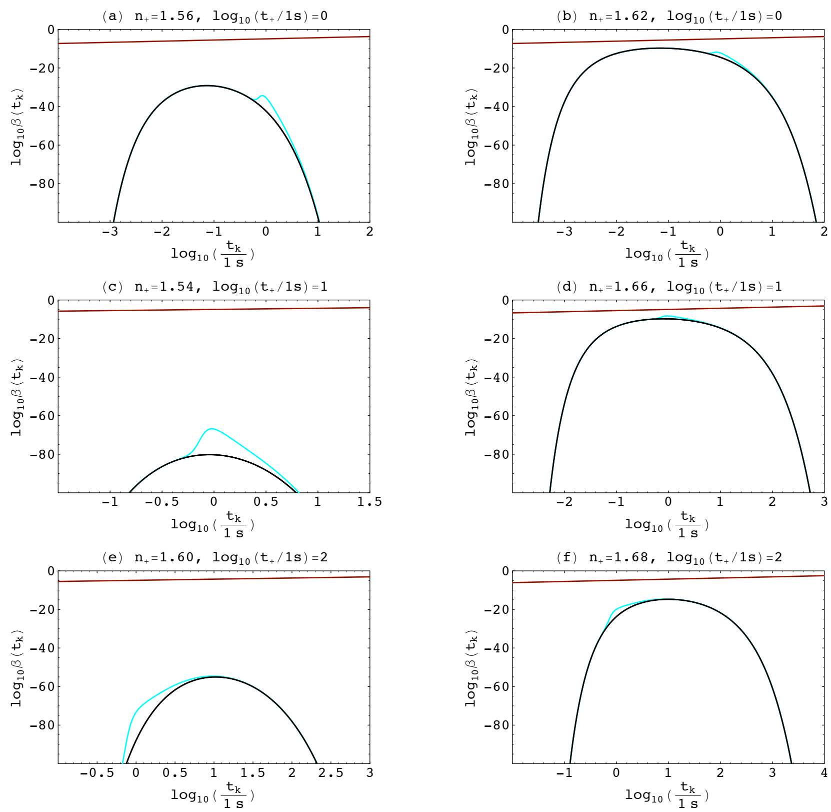

Figure 101: The fraction of the universe going into PBHs in a universe with a running–tilt power spectrum when: (a) $n_+ = 1.52$ and $t_+ = 1$ s; (b) $n_+ = 1.62$ and $t_+ = 1$ s; (c) $n_+ = 1.54$ and $t_+ = 10$ s; (d) $n_+ = 1.66$ and $t_+ = 10$ s; (e) $n_+ = 1.60$ and $t_+ = 100$ s; (f) $n_+ = 1.68$ and $t_+ = 100$ s. The dark curve represents the radiation contribution and the cyan curve represents the contribution from the electron–positron annihilation epoch. Also shown (top of figure, in maroon) is the observational limit.

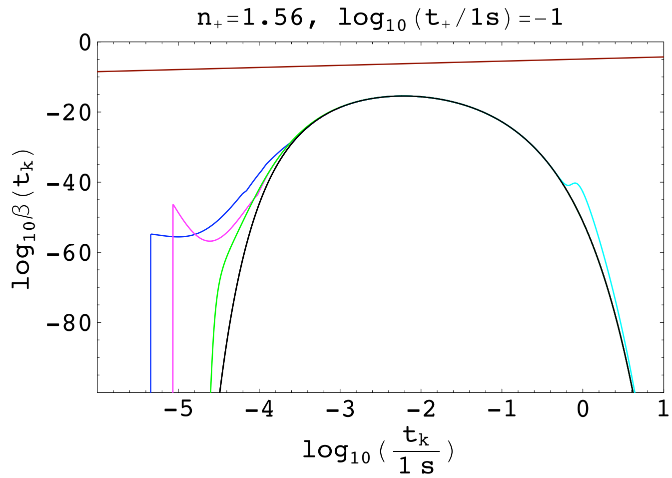

Figure 102: The fraction of the universe going into PBHs in a universe with a running–tilt power spectrum when $n_+ = 1.56$ and $t_+ = 10^{-1}$ s. The dark curve represents the radiation contribution and the cyan curve (on the right) represents the aditional contribution from the electron–positron annihilation epoch. In this case we have also possible contributions from the QCD phase transition: Bag Model (blue curve on the left), Lattice Fit (in magenta), and Crossover (in green). Also shown (top of figure, in maroon) is the observational limit.

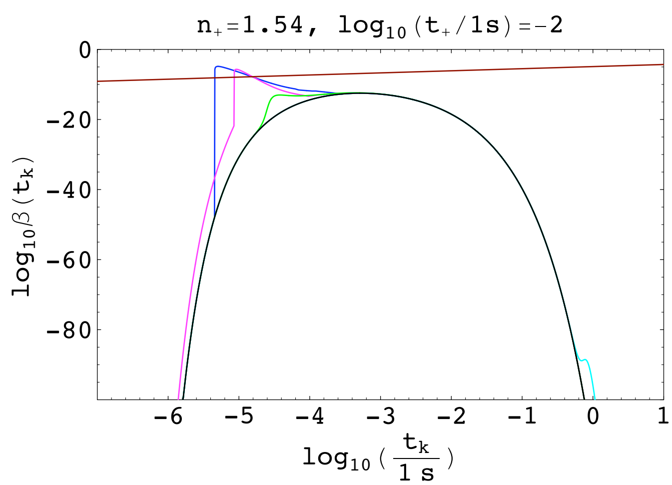

Figure 103: The fraction of the universe going into PBHs in a universe with a running–tilt power spectrum when $n_+ = 1.54$ and $t_+ = 10^{-2}$ s. In this case the QCD Bag Model and the QCD Lattice Fit are excluded due to observational constraints (for more details see Figure 102).

Table 44: The contribution to β from the QCD Bag Model. In yellow we show the cases for which there is a non–negligible contribution to β from the QCD Bag Model. For more details see Tables 41 and 42.

	n_{max}																		
$\log_{10}(t_+/1\mathrm{s})$	1.28	1.30	1.32	1.34	1.36	1.38	1.40	1.42	1.44	1.46	1.48	1.50	1.52	1.54	1.56	1.58	1.60	1.62	1.64
-11		R	R	R	R														
-10			R	R	RB														
-9				RB	RB	RB													
-8			B	RB	RB	RB	RB												
-7		B	B	B	RB	RB	RB	RB*											
-6		B Fig. 106c	B	B	B	RB	RB*	RB*	RB*										
-5		B	B	B	B	B	RB* Fig. 106d	RB*	RB*	RB*									
-4		B	B	B	B	B Fig. 106b	RB Fig. 106a	RB*	RB*	RB*	RB* Fig. 104	RB*							
-3				B	B	B	B	RB*	RB* Fig. 106e	RB*	RB*	RB*	RB* Fig. 105						
-2							B	B	B	RB	RB	RB Fig. 106f	RB*	RB*ea	RB*ea				
-1											R	R	Rea	RBea	RBea	RBea	RBea		
0												R	Rea	Rea	Rea	Rea	Rea	Rea	Rea

Table 45: The contribution to β from the QCD Lattice Fit. In yellow we show the cases for which there is a non–negligible contribution to β from the QCD Lattice Fit. For more details see Tables 41 and 42.

	n_{max}																		
$\log_{10}(t_+/1s)$	1.28	1.30	1.32	1.34	1.36	1.38	1.40	1.42	1.44	1.46	1.48	1.50	1.52	1.54	1.56	1.58	1.60	1.62	1.64
-11		R	R	R	R														
-10			R	R	R														
-9				R	R	RL													
-8				R	RL	RL	RL												
-7				L	RL	RL	RL	RL											
-6			L	L	L	RL	RL	RL	RL*										
-5			L	L	L	L	RL Fig. 106d	RL	RL*	RL*									
-4			L	L	L	L Fig. 106b	RL Fig. 106a	RL	RL*	RL*	RL* Fig. 104	RL*							
-3				L	L	L	L	RL	RL Fig. 106e	RL*	RL*	RL*	RL* Fig. 105						
-2							L	L	L	RL	RL	RL Fig. 106f	RL	RL*ea	RL*ea				
-1											R	R	Rea	RLea	RLea	RLea	RLea		
0												R	Rea	Rea	Rea	Rea	Rea	Rea	Rea

Table 46: The contribution to β from the QCD Crossover. In yellow we show the cases for which there is a non–negligible contribution to β from the QCD Crossover. For more details see Tables 41 and 42.

	n_{max}																		
$\log_{10}(t_+/1s)$	1.28	1.30	1.32	1.34	1.36	1.38	1.40	1.42	1.44	1.46	1.48	1.50	1.52	1.54	1.56	1.58	1.60	1.62	1.64
-11		R	R	R	R														
-10			R	R	R														
-9				R	R	R													
-8				R	R	R	R												
-7					R	R	R	RC											
-6						R	RC	RC	RC										
-5							RC Fig. 106d	RC	RC	RC									
-4							RC Fig. 106a	RC	RC	RC	RC Fig. 104	RC							
-3								RC	RC Fig. 106e	RC	RC	RC	RC* Fig. 105						
-2										RC	RC	RC Fig. 106f	RC	RCea	RCea				
-1											R	R	Rea	RCea	RCea	RCea	RCea		
0												R	Rea	Rea	Rea	Rea	Rea	Rea	Rea

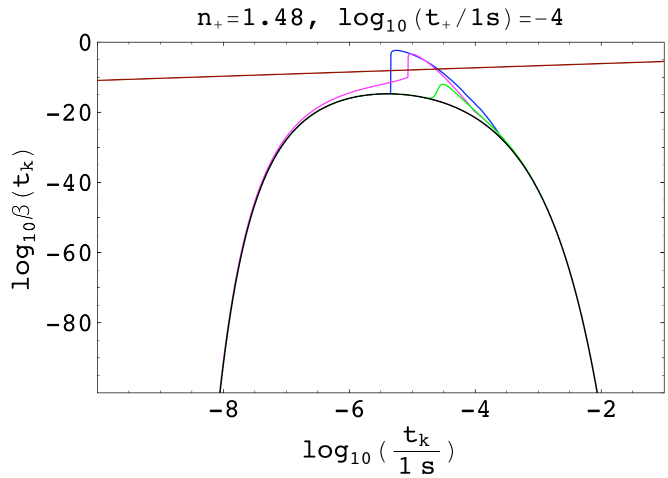

Figure 104: The fraction of the universe going into PBHs in a universe with a running–tilt power spectrum when $n_+ = 1.48$ and $t_+ = 10^{-4}$ s. The dark curve represents the radiation contribution and the maroon line the observational constraints. The other curves represent the contribution from the QCD phase transition: Crossover (green), Lattice Fit (magenta) and Bag Model (blue). The latter two models for the QCD transition are excluded, due to observational constraints.

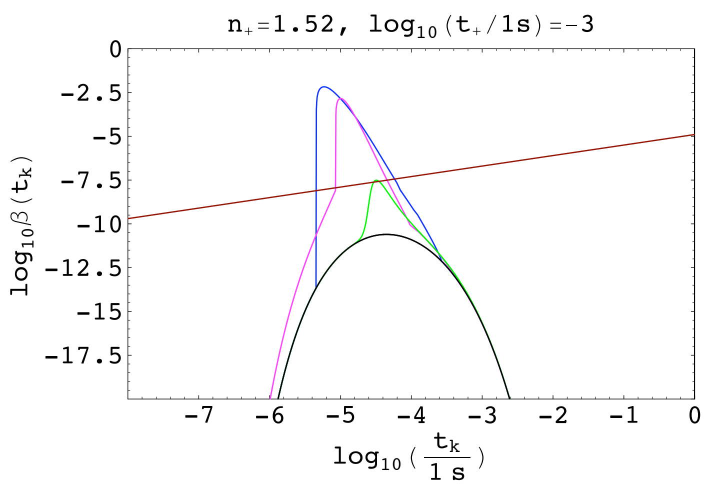

Figure 105: The fraction of the universe going into PBHs in a universe with a running–tilt power spectrum when $n_+ = 1.52$ and $t_+ = 10^{-3}$ s (see Figure 104 for more details). Whatever the model adopted for the QCD transition this case must be excluded, due to observational constraints.

In Figure 106a we show the case $t_+ = 10^{-4}$ s and $n_+ = 1.40$. In this case we have important contributions from the QCD transition ($\beta_{max} \sim 10^{-9}$ in the case of a Bag Model, $\beta_{max} \sim 10^{-14}$ in the case of a Lattice Fit and $\beta_{max} \sim 10^{-75}$ in the case of a Crossover) and an almost negligible contribution from radiation ($\beta_{max} \sim 10^{-97}$).

We have also to consider new cases for which the contribution from radiation is negligible ($\beta < 10^{-100}$ for all t_k, cases represented on Table 42 in cyan) but with some contribution from the QCD phase transition (cf. Table 44 – cases marked with 'B', and Table 45 – cases marked with 'L').

In Figure 106b we show the case $t_+ = 10^{-4}$ s and $n_+ = 1.38$, for which we have only meaningful contributions from the QCD Bag Model ($\beta_{max} \sim 10^{-13}$) or from the QCD Lattice Fit ($\beta_{max} \sim 10^{-22}$). In Figure 106c we show the case $t_+ = 10^{-6}$ s and $n_+ = 1.30$, for which the only relevant contribution comes from the QCD Bag Model, with $\beta_{max} \sim 10^{-69}$.

In the example of Figure 106d we show the case $t_+ = 10^{-6}$ s and $n_+ = 1.40$. Notice that we now have a visible contribution from radiation ($\beta_{max} \sim 10^{-61}$) as well as an important contribution from the QCD Lattice Fit ($\beta_{max} \sim 10^{-12}$). The contribution from the QCD Crossover ($\beta_{max} \sim 10^{-74}$) is very small, compared with the others. In this case the QCD Bag Model is excluded, due to observational constraints.

In Figure 106e we show, as a similar example, the case $t_+ = 10^{-3}$ s and $n_+ = 1.44$, now with a more important contribution from the QCD Crossover ($\beta_{max} \sim 10^{-43}$). The contribution from the Lattice Fit remains important ($\beta_{max} \sim 10^{-11}$) and the QCD Bag Model remains excluded. Finally, in Figure 106f we show the case $t_+ = 10^{-2}$ s and $n_+ = 1.50$. In this case we might have contributions from the QCD Bag Model ($\beta_{max} \sim 10^{-9}$), from the QCD Lattice Fit ($\beta_{max} \sim 10^{-11}$) or from the QCD Crossover ($\beta_{max} \sim 10^{-28}$).

We might have cases with simultaneous contributions from both QCD and EW transitions. Those are considered in Section 11.5. We might also have cases with simultaneous contributions from the QCD phase transition and from the electron–positron annihilation epoch. We have already presented two examples of these in Figures 102 and 103.

11.5 EW phase transition (MSSM)

In this section we consider the contribution from the EW phase transition to the global value of β (in the context of the MSSM and taking into account the assumptions made at the end of Section 3.2.2). In Table 47 we point out the cases for which there is a non–negligible contribution from the EW phase transition.

There are some cases allowed when one considers only the contribution from radiation but which must be excluded when one takes into account the EW phase transition. For example, the case $t_+ = 10^{-9}$ s and $n_+ = 1.36$, represented in Figure 107. This case is not allowed in the context of a first order EW phase transition. However, if there is no such transition, or if this is not strong enough,

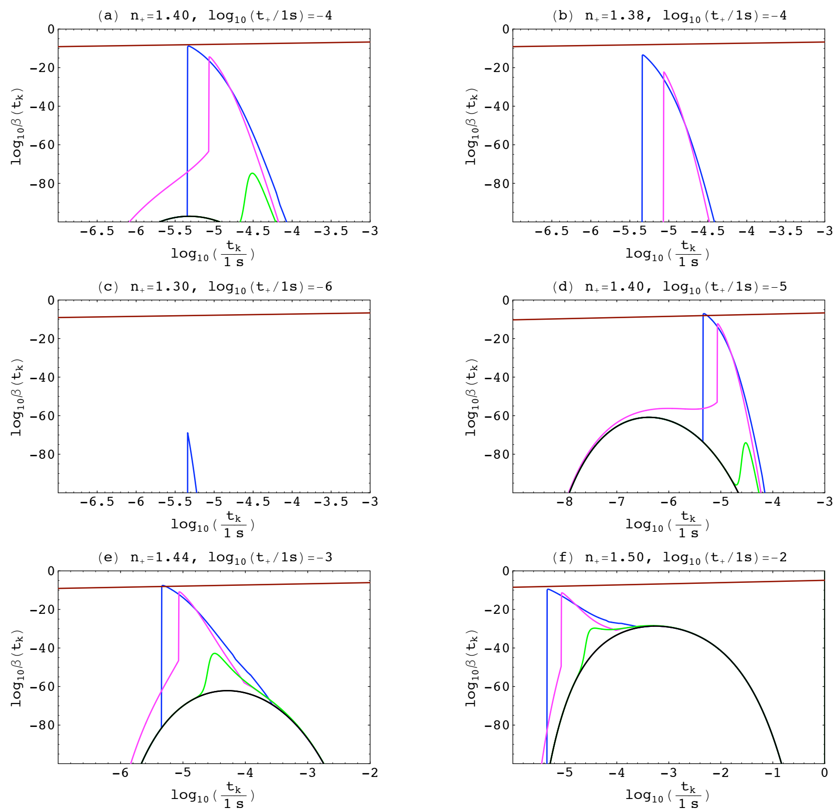

Figure 106: The fraction of the universe going into PBHs, during the QCD phase transition, in a universe with a running–tilt power spectrum when: (a) $n_+ = 1.40$ and $t_+ = 10^{-4}$ s; (b) $n_+ = 1.38$ and $t_+ = 10^{-4}$ s; (c) $n_+ = 1.30$ and $t_+ = 10^{-6}$ s; (d) $n_+ = 1.40$ and $t_+ = 10^{-5}$ s; (e) $n_+ = 1.44$ and $t_+ = 10^{-3}$ s; (f) $n_+ = 1.50$ and $t_+ = 10^{-2}$ s (see Figure 104 for more details).

Table 47: The contribution to β from the EW Bag Model (MSSM). In yellow we show the cases for which there is a non–negligible contribution to β from the EW Bag Model. For more details see Tables 41 and 42.

	1.26	1.28	1.30	1.32	1.34	1.36	1.38	1.40	1.42	1.44	1.46	1.48
-15		R	R									
-14		R	RE	RE								
-13		RE	RE	RE Fig. 108c								
-12		E	RE Fig. 108e	RE	RE Fig. 108d							
-11		E	RE	RE	RE*	RE*						
-10		E Fig. 108a	E	RE Fig. 108f	RE*	RBE*						
-9		E	E	E Fig. 108b	RBE	RBE* Fig. 107	RBLE*					
-8			E	BE	RBE	RBLE	RBLE*	RBLE*				
-7			B	B	BLE Fig. 109a	RBLE Fig. 109b	RBLE	RBLE Fig. 109c	RB*LCE*			
-6			B	BL	BL	BL	RBL	RB*LCE	RB*LCE	RB*L*CE Fig. 109d		
-5			B	BL	BL	BL	BL	RB*LC	RB*LC	RB*L*C	RB*L*C	

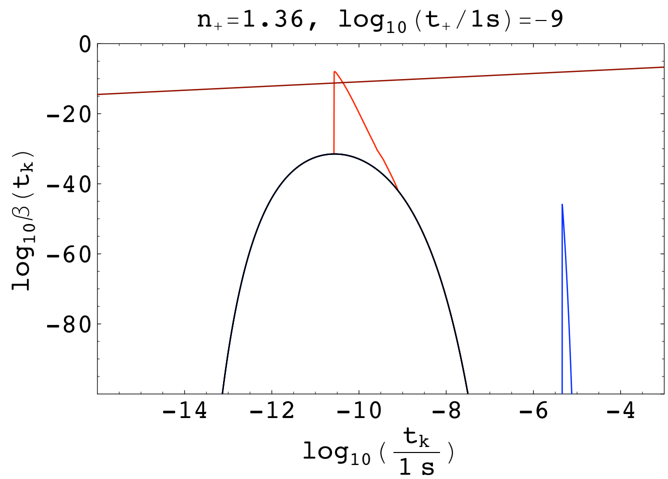

Figure 107: The fraction of the universe going into PBHs in a universe with a running–tilt power spectrum when $n_+ = 1.36$ and $t_+ = 10^{-9}$ s. The curves represent the contribution from the EW phase transition (red), from the QCD phase transition (blue, Bag Model) and from radiation (black). The maroon line represents the observational constraints, which are violated here by the EW phase transition contribution.

then this case becomes valid, with a possible contribution also from the QCD transition (Bag Model).

There are a few cases for which the contribution from radiation is negligible (i.e., cases shown in cyan on Table 42) but with an appreciable contribution from the EW phase transition. These cases are labeled on Table 47 with 'E', 'BE' and 'BLE'. In Figures 108a and 108b we present, as examples, the cases $t_+ = 10^{-10}$ s and $n_+ = 1.28$, and $t_+ = 10^{-9}$ s and $n_+ = 1.32$, with, respectively, $\beta_{max} \sim 10^{-60}$ and $\beta_{max} \sim 10^{-23}$.

There are also a lot of cases for which we have a contribution from the EW phase transition as well as from radiation (cf. Table 47, labeled 'RE'). In Figures 108c and 108d, we show as examples of this, the cases $t_+ = 10^{-13}$ s and $n_+ = 1.32$, and $t_+ = 10^{-12}$ s and $n_+ = 1.34$. Notice that in both cases the two contributions are quite comparable (in terms of β_{max}). In the first case we have $\beta_{max} \sim 10^{-24}$ from radiation and $\beta_{max} \sim 10^{-28}$ from the EW transition, and in the second case we have $\beta_{max} \sim 10^{-18}$ from radiation and $\beta_{max} \sim 10^{-12}$ from the EW transition.

In Figures 108e and 108f we present two mores cases with contributions from radiation and from the EW phase transition. Notice that in these cases the contribution from the EW phase transition is a lot more relevant than the contribution from radiation. For example, in the case $t_+ = 10^{-10}$ s and $n_+ = 1.32$, represented in Figure 108f, we have that the contribution from radiation gives $\beta_{max} \sim 10^{-71}$ and the contribution from the EW transition

$\beta_{max} \sim 10^{-19}$.

Finally, we consider a few examples of a set of cases that have possible contributions from both the EW and QCD phase transitions (cf. Table 47, labeled BE, RBE, BLE, $RBLE$, RB^*LCE, and RB^*L^*CE). We start with the case $t_+ = 10^{-7}$ s and $n_+ = 1.34$, represented in Figure 109a. In this case we have contributions from the EW phase transition ($\beta_{max} \sim 10^{-61}$) and from the QCD phase transition (Bag Model – $\beta_{max} \sim 10^{-33}$, Lattice Fit – $\beta_{max} \sim 10^{-68}$).

In figures 109b and 109c we show the cases $t_+ = 10^{-7}$ s and $n_+ = 1.36$ (see also Table 48 and Figure 110), and $t_+ = 10^{-7}$ s and $n_+ = 1.40$, respectively. These are examples of cases characterized by contributions from the EW phase transition, QCD phase transition (Bag Model and Lattice Fit only) as well as from radiation. In particular, the second one (Figure 109c) shows very interesting values for β with two noticeable peaks ($\beta_{max} \sim 10^{-13}$ from the EW and $\beta_{max} \sim 10^{-9}$ from the QCD Bag Model or $\beta_{max} \sim 10^{-17}$ from the QCD Lattice Fit).

In Figure 109d we present the case $t_+ = 10^{-6}$ s and $n_+ = 1.44$. In this case, the main contribution to β comes from radiation ($\beta_{max} \sim 10^{-14}$), because the QCD Bag Model and Lattice Fit are excluded. We also have contributions from the EW phase transition and from the QCD phase transition (Crossover only).

11.6 Results

In Table 49 we list the peaks of the curve $\beta(t_k)$, as well as their locations, for the various cases (and different scenarios) studied in Sections 11.1 to 11.5. The contribution from radiation assumes a radiation–dominated universe ($\delta_c = 1/3$ at all epochs) with the curve $\beta(t_k)$ showing a single peak. In addition we might also have contributions from the QCD phase transition, from the EW phase transition, or from the electron–positron annihilation epoch, each showing its own peak.

If the peak from the radiation contribution is located near the epoch of a particular phase transition then it might be hidden by the corresponding peak. Consider, for example, the case $n_+ = 1.44$ and $t_+ = 10^{-3}$ s (Figure 106e). In this case, we have non–negligible contributions from radiation and from the QCD Lattice Fit or from the QCD Crossover (the QCD Bag Model is excluded due to the observational constraints). Whatever the model one chooses to the QCD, the peak of the radiation contribution (black curve) remains hidden. Thus, in this case, the curve $\beta(t_k)$ exhibits only one peak. On table 49 there are other cases for which the peak from the radiation contribution is also hidden. For these cases we show the corresponding value of $\log_{10} \beta_{max}$ inside brackets and labeled with 'A' (meaning *Always* hidden).

As another example, consider the case $n_+ = 1.36$ and $t_+ = 10^{-7}$ s (Figure 109b). In this case we might have one, two or three peaks, depending on the choosen scenario (see Table 48). This and other similar cases, are shown in Table 49, with the $\log_{10} \beta_{max}$ value inside brackets and labeled 'S' (meaning *Sometimes* hidden).

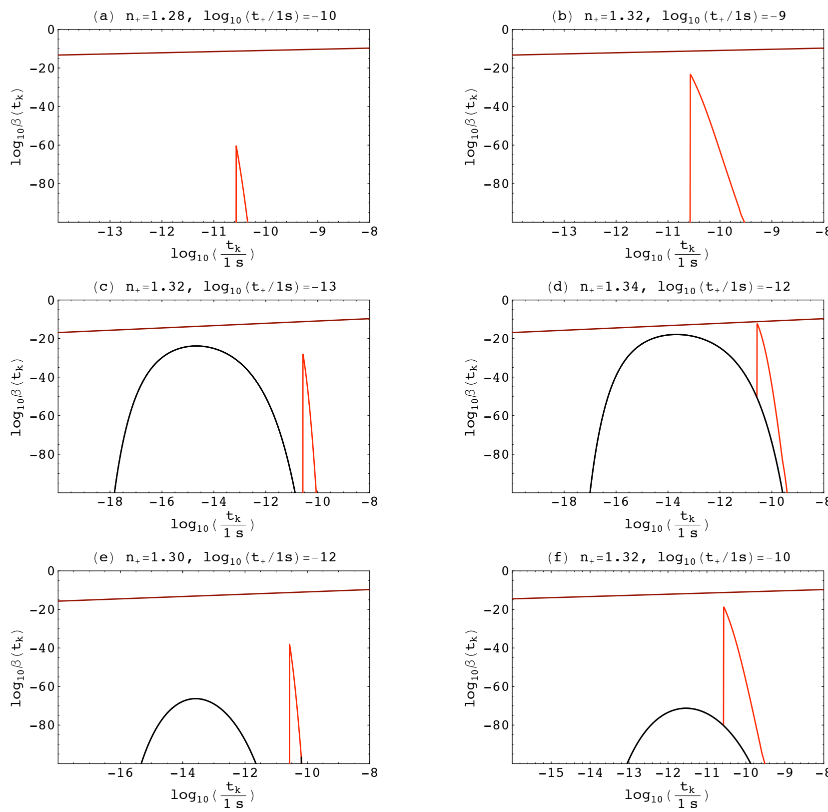

Figure 108: The fraction of the universe going into PBHs in a universe with a running–tilt power spectrum when: (a) $n_+ = 1.28$ and $t_+ = 10^{-10}$ s; (b) $n_+ = 1.32$ and $t_+ = 10^{-9}$ s; (c) $n_+ = 1.32$ and $t_+ = 10^{-13}$ s; (d) $n_+ = 1.34$ and $t_+ = 10^{-12}$ s; (e) $n_+ = 1.30$ and $t_+ = 10^{-12}$ s; (f) $n_+ = 1.32$ and $t_+ = 10^{-10}$ s. The curves represent the contribution from the EW phase transition (red) and the contribution from radiation (black). Also shown (top of figures, in maroon) are the observational constraints.

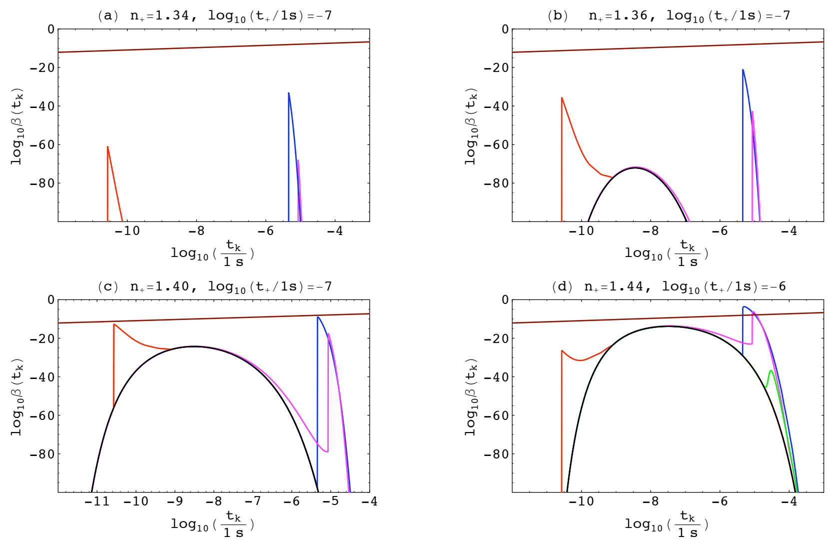

Figure 109: The fraction of the universe going into PBHs in a universe with a running–tilt power spectrum when: (a) $n_+ = 1.34$ and $t_+ = 10^{-7}$ s; (b) $n_+ = 1.36$ and $t_+ = 10^{-7}$ s (see also Table 48 and Figure 110); (c) $n_+ = 1.40$ and $t_+ = 10^{-7}$ s; (d) $n_+ = 1.44$ and $t_+ = 10^{-6}$ s. The curves represent the contribution from the QCD phase transition (blue – Bag Model; magenta – Lattice Fit; green – Crossover), from the EW phase transition (red), and from radiation (black). Also shown (top of figures, in maroon) are the observational constraints.

Table 48: Peaks of the curve $\beta(t_k)$ in the case $n_+ = 1.36$ and $t_+ = 10^{-7}$ s. See Table 40 for the description of different scenarios.

Scenario	Number of peaks	Description	Figure
1	2	Radiation + QCD Bag Model	110a
2	2	Radiation + QCD Lattice Fit	110b
3	1	Radiation	110c
4	3	Radiation + EW Bag Model + QCD Bag Model	110d
5	3	Radiation + EW Bag Model + QCD Lattice Fit	110e
6	2	Radiation + EW Bag Model	110f

When $n_+ = 1.22$ and $n_+ = 1.24$ there are a few cases for which the peak from the radiation contribution occurs for $t_k < 10^{-23}$ s. Taking into account that our expression for $\beta(t_k)$ is classic (Section 5.1), not valid for epochs earlier than $\sim\ 10^{-23}$ s where the maximum is attained, we consider, for these particular cases, the values correspondent to $t_k = 10^{-23}$ s (which correspond to PBHs exploding right now), and we show those values in Table 49 inside square brackets.

For the QCD Crossover and for the electron–positron annihilation there are a lot of cases for which there is an important contribution to β, similar to the radiation contribution, but without any peak. As an example of this, we mention the case $n_+ = 1.68$ and $t_+ = 100$ s (Figure 101f) for which we have a single peak from the radiation contribution. These cases are labeled, in Table 49, with 'NA' (meaning *Not Applicable*).

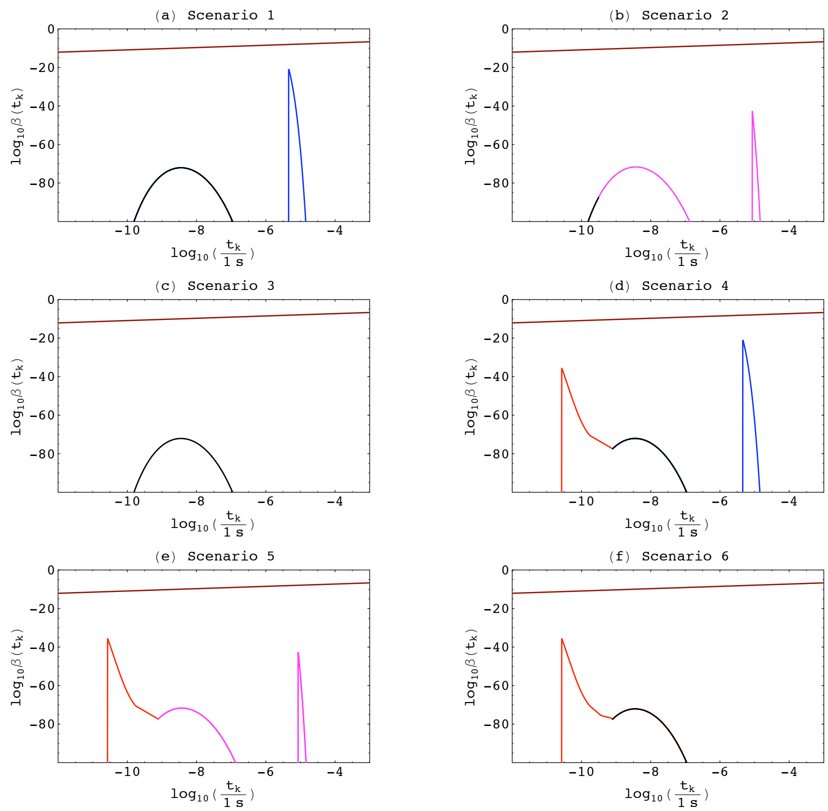

Figure 110: The fraction of the universe going into PBHs in a universe with a running–tilt power spectrum when $n_+ = 1.36$ and $t_+ = 10^{-7}$ s (see also Figure 109b and Table 48). The curves represent the contribution from the QCD phase transition (blue – Bag Model; magenta – Lattice Fit), from the EW phase transition (red – Bag Model), and from radiation (black). Also shown (top of figures, in maroon) are the observational constraints. Each Figure represents a different scenario (see Table 40 for the description of different scenarios): (a) Scenario 1; (b) Scenario 2; (c) Scenario 3; (d) Scenario 4; (e) Scenario 5; (f) Scenario 6. The contribution from the QCD Crossover (scenarios 3 and 6) is not shown because it is negligible. The contribution from the electron–positron annihilation is also negligible. Assembling these six Figures in a single one we recover Figure 109b.

Table 49: The fraction of the universe going into PBHs during radiation domination and during cosmological phase transitions. The value t_+ corresponds to the instant for which the value of the spectral index attains its maximum n_+. The value $t_{k,max}$ corresponds to the instant for which β attains its maximum value (β_{max}). A gray background means that the value of β_{max} exceeds the observational constraints. A coloured background means that the value of β_{max} belongs to the top ten highest contributions for a particular transition model: EW Bag Model (red, Table 53), QCD Bag Model (blue, Table 51), QCD Lattice Fit (magenta, Table 52), QCD Crossover (green, Table 50), and electron–positron annihilation (cyan, Table 54). We have labeled with 'NA' (not applicable) situations for which the curve of $\beta(t_k)$ exists but does not show any maximum, with 'A' the cases for which the radiation peak is always hidden (column 4), and with 'S' the cases for which the radiation peak is only sometimes hidden (column 4). Values inside square brackets correspond to situations for which the peak from radiation occurs for $t_k < 10^{-23}$ s (see text for more details).

		Radiation		EW Bag Model		QCD Bag Model		QCD Lattice Fit		QCD Crossover		e^-e^+ Crossover	
n_+	$\log_{10}(\frac{t_+}{1s})$	$\log_{10}(\frac{t_{k,max}}{1s})$	$\log_{10}\beta_{max}$	$\log_{10}(\frac{t_{k,max}}{1s})$	$\log_{10}\beta_{max}$	$\log_{10}(\frac{t_{k,max}}{1s})$	$\log_{10}\beta_{max}$	$\log_{10}(\frac{t_{k,max}}{1s})$	$\log_{10}\beta_{max}$	$\log_{10}(\frac{t_{k,max}}{1s})$	$\log_{10}\beta_{max}$	$\log_{10}(\frac{t_{k,max}}{1s})$	$\log_{10}\beta_{max}$
1.22	-23	[-23]	[-74]	–	–	–	–	–	–	–	–	–	–
	-22	[-23]	[-79]	–	–	–	–	–	–	–	–	–	–
	-21	-22.6	-98	–	–	–	–	–	–	–	–	–	–
1.24	-23	[-23]	[-31]	–	–	–	–	–	–	–	–	–	–
	-22	[-23]	[-33]	–	–	–	–	–	–	–	–	–	–
	-21	-22.7	-41	–	–	–	–	–	–	–	–	–	–
	-20	-21.7	-54	–	–	–	–	–	–	–	–	–	–
	-19	-20.7	-71	–	–	–	–	–	–	–	–	–	–
	-18	-19.6	-94	–	–	–	–	–	–	–	–	–	–
1.26	-19	-20.7	-31	–	–	–	–	–	–	–	–	–	–
	-18	-19.7	-42	–	–	–	–	–	–	–	–	–	–
	-17	-18.7	-56	–	–	–	–	–	–	–	–	–	–
	-16	-17.6	-76	–	–	–	–	–	–	–	–	–	–
1.28	-18	-19.8	-19	–	–	–	–	–	–	–	–	–	–
	-17	-18.7	-26	–	–	–	–	–	–	–	–	–	–
	-16	-17.7	-36	–	–	–	–	–	–	–	–	–	–
	-15	-16.7	-49	–	–	–	–	–	–	–	–	–	–
	-14	-15.6	-68	–	–	–	–	–	–	–	–	–	–
	-13	-14.6	-94	-10.6	-90	–	–	–	–	–	–	–	–
	-12	–	–	-10.6	-69	–	–	–	–	–	–	–	–
	-11	–	–	-10.6	-60	–	–	–	–	–	–	–	–
	-10	–	–	-10.6	-60	–	–	–	–	–	–	–	–
	-9	–	–	-10.6	-75	–	–	–	–	–	–	–	–

(continues on next page)

Table 49 (continued).

		Radiation		EW Bag Model		QCD Bag Model		QCD Lattice Fit		QCD Crossover		e^-e^+ Crossover	
n_+	$\log_{10}(\frac{t_+}{1s})$	$\log_{10}(\frac{t_{k,max}}{1s})$	$\log_{10}\beta_{max}$	$\log_{10}(\frac{t_{k,max}}{1s})$	$\log_{10}\beta_{max}$	$\log_{10}(\frac{t_{k,max}}{1s})$	$\log_{10}\beta_{max}$	$\log_{10}(\frac{t_{k,max}}{1s})$	$\log_{10}\beta_{max}$	$\log_{10}(\frac{t_{k,max}}{1s})$	$\log_{10}\beta_{max}$	$\log_{10}(\frac{t_{k,max}}{1s})$	$\log_{10}\beta_{max}$
1.30	-16	-17.8	-17	–	–	–	–	–	–	–	–	–	–
	-15	-16.7	-24	–	–	–	–	–	–	–	–	–	–
	-14	-15.7	-33	-10.6	-72	–	–	–	–	–	–	–	–
	-13	-14.6	-47	-10.6	-50	–	–	–	–	–	–	–	–
	-12	-13.6	-66	-10.6	-38	–	–	–	–	–	–	–	–
	-11	-12.5	-94	-10.6	-33	–	–	–	–	–	–	–	–
	-10	–	–	-10.6	-33	–	–	–	–	–	–	–	–
	-9	–	–	-10.6	-42	–	–	–	–	–	–	–	–
	-8	–	–	-10.6	-71	–	–	–	–	–	–	–	–
	-7	–	–	–	–	-5.3	-85	–	–	–	–	–	–
	-6	–	–	–	–	-5.3	-69	–	–	–	–	–	–
	-5	–	–	–	–	-5.3	-67	–	–	–	–	–	–
	-4	–	–	–	–	-5.3	-84	–	–	–	–	–	–
1.32	-14	-15.7	-17	-10.6	-41	–	–	–	–	–	–	–	–
	-13	-14.7	-24	-10.6	-28	–	–	–	–	–	–	–	–
	-12	-13.6	-36	-10.6	-21	–	–	–	–	–	–	–	–
	-11	-12.6	-49	-10.6	-18	–	–	–	–	–	–	–	–
	-10	-11.5	-71	-10.6	-19	–	–	–	–	–	–	–	–
	-9	–	–	-10.6	-23	–	–	–	–	–	–	–	–
	-8	–	–	-10.6	-40	-5.3	-74	–	–	–	–	–	–
	-7	–	–	–	–	-5.3	-53	–	–	–	–	–	–
	-6	–	–	–	–	-5.3	-43	-5.1	-84	–	–	–	–
	-5	–	–	–	–	-5.3	-41	-5.1	-77	–	–	–	–
	-4	–	–	–	–	-5.3	-52	-5.1	-90	–	–	–	–
1.34	-12	-13.7	-18	-10.6	-12	–	–	–	–	–	–	–	–
	-11	-12.6	-26	-10.6	-11	–	–	–	–	–	–	–	–
	-10	-11.6	-38	-10.6	-11	–	–	–	–	–	–	–	–
	-9	-10.5	$(-57)_S$	-10.6	-13	-5.3	-72	–	–	–	–	–	–
	-8	-9.5	$(-84)_S$	-10.6	-23	-5.3	-47	–	–	–	–	–	–
	-7	–	–	-10.6	-61	-5.3	-33	-5.1	-68	–	–	–	–
	-6	–	–	–	–	-5.3	-27	-5.1	-52	–	–	–	–
	-5	–	–	–	–	-5.3	-26	-5.1	-48	–	–	–	–
	-4	–	–	–	–	-5.3	-33	-5.1	-56	–	–	–	–
	-3	–	–	–	–	-5.3	-63	-5.1	-96	–	–	–	–
1.36	-11	-12.7	-14	-10.6	-6	–	–	–	–	–	–	–	–
	-10	-11.6	-21	-10.6	-7	-5.3	-76	–	–	–	–	–	–
	-9	-10.6	-31	-10.6	-8	-5.3	-46	–	–	–	–	–	–
	-8	-9.5	$(-46)_S$	-10.6	-13	-5.3	-30	-5.1	-63	–	–	–	–
	-7	-8.5	-72	-10.6	-36	-5.3	-21	-5.1	-43	–	–	–	–
	-6	–	–	–	–	-5.3	-17	-5.1	-33	–	–	–	–
	-5	–	–	–	–	-5.3	-16	-5.1	-30	–	–	–	–
	-4	–	–	–	–	-5.3	-21	-5.1	-35	–	–	–	–
	-3	–	–	–	–	-5.3	-40	-5.1	-61	–	–	–	–

(continues on next page)

Table 49 (continued).

		Radiation		EW Bag Model		QCD Bag Model		QCD Lattice Fit		QCD Crossover		e^-e^+ Crossover	
n_+	$\log_{10}(\frac{t_+}{1s})$	$\log_{10}(\frac{t_{k,max}}{1s})$	$\log_{10}\beta_{max}$	$\log_{10}(\frac{t_{k,max}}{1s})$	$\log_{10}\beta_{max}$	$\log_{10}(\frac{t_{k,max}}{1s})$	$\log_{10}\beta_{max}$	$\log_{10}(\frac{t_{k,max}}{1s})$	$\log_{10}\beta_{max}$	$\log_{10}(\frac{t_{k,max}}{1s})$	$\log_{10}\beta_{max}$	$\log_{10}(\frac{t_{k,max}}{1s})$	$\log_{10}\beta_{max}$
1.38	-9	-10.6	-18	-10.6	-5	-5.3	-30	-5.1	-65	–	–	–	–
	-8	-9.5	-27	-10.6	-8	-5.3	-19	-5.1	-40	–	–	–	–
	-7	-8.5	-42	-10.6	-21	-5.3	-14	-5.1	-27	–	–	–	–
	-6	-7.4	-65	–	–	-5.3	-11	-5.1	-21	–	–	–	–
	-5	–	–	–	–	-5.3	-11	-5.1	-19	–	–	–	–
	-4	–	–	–	–	-5.3	-13	-5.1	-22	–	–	–	–
	-3	–	–	–	–	-5.3	-26	-5.1	-39	–	–	–	–
1.40	-8	-9.6	-16	-10.5	-5	-5.3	-13	-5.1	-26	–	–	–	–
	-7	-8.5	-24	-10.6	-13	-5.3	-9	-5.1	-18	–	–	–	–
	-6	-7.4	-38	-10.6	-69	-5.3	-7	-5.1	-13	-4.5	-92	–	–
	-5	-6.4	$(-61)_S$	–	–	-5.3	-7	-5.1	-12	-4.5	-74	–	–
	-4	-5.3	$(-97)_S$	–	–	-5.3	-9	-5.1	-14	-4.5	-75	–	–
	-3	–	–	–	–	-5.3	-17	-5.1	-25	–	–	–	–
	-2	–	–	–	–	-5.3	-66	-5.1	-83	–	–	–	–
1.42	-7	-8.5	-14	-10.6	-8	-5.3	-6	-5.1	-12	-4.5	-85	–	–
	-6	-7.5	-23	-10.6	-43	-5.3	-5	-5.1	-9	-4.5	-58	–	–
	-5	-6.4	$(-37)_S$	–	–	-5.3	-5	-5.1	-8	-4.5	-46	–	–
	-4	-5.3	$(-60)_S$	–	–	-5.3	-6	-5.1	-10	-4.5	-47	–	–
	-3	-4.3	$(-98)_A$	–	–	-5.3	-11	-5.1	-16	-4.5	-67	–	–
	-2	–	–	–	–	-5.3	-44	-5.1	-55	–	–	–	–
1.44	-6	-7.5	-14	-10.6	-24	-5.3	-4	-5.1	-6	-4.5	-37	–	–
	-5	-6.4	-23	–	–	-5.3	-4	-5.0	-6	-4.5	-29	–	–
	-4	-5.4	-37	–	–	-5.3	-4	-5.1	-6	-4.5	-30	–	–
	-3	-4.3	$(-62)_A$	–	–	-5.3	-8	-5.1	-11	-4.5	-43	–	–
	-2	–	–	–	–	-5.3	-30	-5.1	-36	–	–	–	–
1.46	-5	-6.4	-14	–	–	-5.3	-3	-5.0	-4	-4.5	-19	–	–
	-4	-5.4	-23	–	–	-5.3	-3	-5.0	-5	-4.5	-19	–	–
	-3	-4.3	$(-40)_A$	–	–	-5.3	-5	-5.1	-7	-4.5	-27	–	–
	-2	-3.2	-67	–	–	-5.3	-20	-5.1	-24	-4.4	-70	–	–
1.48	-4	-5.4	-15	–	–	-5.3	-2	-5.0	-3	-4.5	-12	–	–
	-3	-4.3	$(-25)_A$	–	–	-5.3	-4	-5.0	-5	-4.5	-18	–	–
	-2	-3.2	-44	–	–	-5.3	-14	-5.1	-17	-4.4	-45	–	–
	-1	-2.2	-77	–	–	–	–	–	–	–	–	–	–

(continues on next page)

Table 49 (continued).

		Radiation		EW Bag Model		QCD Bag Model		QCD Lattice Fit		QCD Crossover		e^-e^+ Crossover	
n_+	$\log_{10}(\frac{t_+}{1s})$	$\log_{10}(\frac{t_{k,max}}{1s})$	$\log_{10}\beta_{max}$	$\log_{10}(\frac{t_{k,max}}{1s})$	$\log_{10}\beta_{max}$	$\log_{10}(\frac{t_{k,max}}{1s})$	$\log_{10}\beta_{max}$	$\log_{10}(\frac{t_{k,max}}{1s})$	$\log_{10}\beta_{max}$	$\log_{10}(\frac{t_{k,max}}{1s})$	$\log_{10}\beta_{max}$	$\log_{10}(\frac{t_{k,max}}{1s})$	$\log_{10}\beta_{max}$
1.50	-4	-5.4	-9	–	–	-5.2	-2	-5.0	-3	-4.5	-8	–	–
	-3	-4.3	$(-16)_A$	–	–	-5.3	-3	-5.0	-4	-4.5	-11	–	–
	-2	-3.3	-29	–	–	-5.3	-10	-5.1	-11	-4.4	-30	–	–
	-1	-2.2	-51	–	–	–	–	–	–	–	–	–	–
1.52	-3	-4.4	-11	–	–	-5.2	-2	-5.0	-3	-4.5	-8	–	–
	-2	-3.3	-19	–	–	-5.3	-7	-5.0	-8	-4.4	-20	–	–
	-1	-2.2	-34	–	–	–	–	–	–	–	–	-0.1	-84
	0	-1.1	-62	–	–	–	–	–	–	–	–	-0.1	-72
	1	–	–	–	–	–	–	–	–	–	–	0.0	-96
1.54	-2	-3.3	-13	–	–	-5.3	-5	-5.0	-6	-4.4	-13	-0.1	-89
	-1	-2.2	-23	–	–	-5.3	-76	-5.1	-65	NA	NA	-0.1	-58
	0	-1.1	-43	–	–	–	–	–	–	–	–	-0.1	-50
	1	-0.1	$(-80)_A$	–	–	–	–	–	–	–	–	0.0	-67
1.56	-2	-3.3	-8	–	–	-5.3	-4	-5.0	-4.4	-4.4	-9	-0.1	-62
	-1	-2.2	-15	–	–	-5.3	-55	-5.1	-47	NA	NA	-0.1	-40
	0	-1.1	-29	–	–	–	–	–	–	–	–	-0.1	-34
	1	-0.1	$(-56)_A$	–	–	–	–	–	–	–	–	0.0	-47
1.58	-1	-2.2	-11	–	–	NA	NA	-5.1	-33	NA	NA	-0.1	-28
	0	-1.1	-20	–	–	–	–	–	–	–	–	-0.1	-24
	1	-0.1	$(-39)_A$	–	–	–	–	–	–	–	–	0.0	-33
	2	1.0	-77	–	–	–	–	–	–	–	–	NA	NA
1.60	-1	-2.2	-7	–	–	NA	NA	-5.1	-24	NA	NA	-0.1	-20
	0	-1.2	-14	–	–	–	–	–	–	–	–	-0.1	-17
	1	-0.1	$(-27)_A$	–	–	–	–	–	–	–	–	0.0	-23
	2	1.0	-55	–	–	–	–	–	–	–	–	NA	NA
1.62	0	-1.2	-10	–	–	–	–	–	–	–	–	-0.1	-12
	1	-0.1	$(-19)_A$	–	–	–	–	–	–	–	–	0.0	-16
	2	1.0	-39	–	–	–	–	–	–	–	–	NA	NA
	3	2.1	-82	–	–	–	–	–	–	–	–	–	–
1.64	0	-1.2	-7	–	–	–	–	–	–	–	–	-0.1	-8
	1	-0.1	$(-14)_A$	–	–	–	–	–	–	–	–	0.0	-12
	2	1.0	-28	–	–	–	–	–	–	–	–	NA	NA
	3	2.1	-60	–	–	–	–	–	–	–	–	–	–

(continues on next page)

Table 49 (continued).

		Radiation		EW Bag Model		QCD Bag Model		QCD Lattice Fit		QCD Crossover		e^-e^+ Crossover	
n_+	$\log_{10}(\frac{t_+}{1s})$	$\log_{10}(\frac{t_{k,max}}{1s})$	$\log_{10}\beta_{max}$	$\log_{10}(\frac{t_{k,max}}{1s})$	$\log_{10}\beta_{max}$	$\log_{10}(\frac{t_{k,max}}{1s})$	$\log_{10}\beta_{max}$	$\log_{10}(\frac{t_{k,max}}{1s})$	$\log_{10}\beta_{max}$	$\log_{10}(\frac{t_{k,max}}{1s})$	$\log_{10}\beta_{max}$	$\log_{10}(\frac{t_{k,max}}{1s})$	$\log_{10}\beta_{max}$
1.66	1	-0.1	$(-10)_A$	–	–	–	–	–	–	–	–	0.0	-8
	2	1.0	-20	–	–	–	–	–	–	–	–	NA	NA
	3	2.1	-44	–	–	–	–	–	–	–	–	–	–
1.68	1	-0.1	$(-7)_A$	–	–	–	–	–	–	–	–	0.0	-6
	2	1.0	-15	–	–	–	–	–	–	–	–	NA	NA
	3	2.1	-32	–	–	–	–	–	–	–	–	–	–
	4	3.2	-71	–	–	–	–	–	–	–	–	–	–
1.70	1	-0.1	-5	–	–	–	–	–	–	–	–	0.0	-4
	2	1.0	-11	–	–	–	–	–	–	–	–	NA	NA
	3	2.1	-24	–	–	–	–	–	–	–	–	–	–
	4	3.2	-53	–	–	–	–	–	–	–	–	–	–
1.72	2	1.0	-8	–	–	–	–	–	–	–	–	1.0	-8
	3	2.1	-17	–	–	–	–	–	–	–	–	–	–
	4	3.2	-40	–	–	–	–	–	–	–	–	–	–
	5	4.3	-93	–	–	–	–	–	–	–	–	–	–
1.74	2	1.0	-6	–	–	–	–	–	–	–	–	1.0	-6
	3	2.1	-13	–	–	–	–	–	–	–	–	–	–
	4	3.2	-30	–	–	–	–	–	–	–	–	–	–
	5	4.3	-72	–	–	–	–	–	–	–	–	–	–
1.76	2	0.98	-4.4	–	–	–	–	–	–	–	–	0.95	-4.4
	3	2.1	-10	–	–	–	–	–	–	–	–	–	–
	4	3.2	-23	–	–	–	–	–	–	–	–	–	–
	5	4.3	-55	–	–	–	–	–	–	–	–	–	–
1.78	3	2.1	-7	–	–	–	–	–	–	–	–	–	–
	4	3.2	-17	–	–	–	–	–	–	–	–	–	–
	5	4.3	-42	–	–	–	–	–	–	–	–	–	–
1.80	3	2.1	-6	–	–	–	–	–	–	–	–	–	–
	4	3.2	-13	–	–	–	–	–	–	–	–	–	–
	5	4.3	-32	–	–	–	–	–	–	–	–	–	–
	6	5.4	-83	–	–	–	–	–	–	–	–	–	–
1.82	3	2.1	-4	–	–	–	–	–	–	–	–	–	–
	4	3.2	-10	–	–	–	–	–	–	–	–	–	–
	5	4.3	-25	–	–	–	–	–	–	–	–	–	–
	6	5.4	-65	–	–	–	–	–	–	–	–	–	–
1.84	4	3.2	-8	–	–	–	–	–	–	–	–	–	–
	5	4.3	-19	–	–	–	–	–	–	–	–	–	–
	6	5.4	-51	–	–	–	–	–	–	–	–	–	–

(continues on next page)

Table 49 (continued).

		Radiation		EW Bag Model		QCD Bag Model		QCD Lattice Fit		QCD Crossover		e^-e^+ Crossover	
n_+	$\log_{10}(\frac{t_+}{1\mathrm{s}})$	$\log_{10}(\frac{t_{k,max}}{1\mathrm{s}})$	$\log_{10}\beta_{max}$	$\log_{10}(\frac{t_{k,max}}{1\mathrm{s}})$	$\log_{10}\beta_{max}$	$\log_{10}(\frac{t_{k,max}}{1\mathrm{s}})$	$\log_{10}\beta_{max}$	$\log_{10}(\frac{t_{k,max}}{1\mathrm{s}})$	$\log_{10}\beta_{max}$	$\log_{10}(\frac{t_{k,max}}{1\mathrm{s}})$	$\log_{10}\beta_{max}$	$\log_{10}(\frac{t_{k,max}}{1\mathrm{s}})$	$\log_{10}\beta_{max}$
1.86	4	3.2	-6	–	–	–	–	–	–	–	–	–	–
	5	4.3	-15	–	–	–	–	–	–	–	–	–	–
	6	5.4	-40	–	–	–	–	–	–	–	–	–	–
1.88	4	3.2	-5	–	–	–	–	–	–	–	–	–	–
	5	4.3	-12	–	–	–	–	–	–	–	–	–	–
	6	5.4	-32	–	–	–	–	–	–	–	–	–	–
	7	6.5	-89	–	–	–	–	–	–	–	–	–	–
1.90	4	3.2	-4	–	–	–	–	–	–	–	–	–	–
	5	4.3	-9	–	–	–	–	–	–	–	–	–	–
	6	5.4	-25	–	–	–	–	–	–	–	–	–	–
	7	6.5	-72	–	–	–	–	–	–	–	–	–	–
1.92	5	4.3	-7	–	–	–	–	–	–	–	–	–	–
	6	5.4	-20	–	–	–	–	–	–	–	–	–	–
	7	6.5	-58	–	–	–	–	–	–	–	–	–	–
1.94	5	4.3	-6	–	–	–	–	–	–	–	–	–	–
	6	5.4	-16	–	–	–	–	–	–	–	–	–	–
	7	6.5	-46	–	–	–	–	–	–	–	–	–	–
1.96	5	4.2	-5	–	–	–	–	–	–	–	–	–	–
	6	5.4	-12	–	–	–	–	–	–	–	–	–	–
	7	6.5	-37	–	–	–	–	–	–	–	–	–	–
1.98	5	4.2	-4	–	–	–	–	–	–	–	–	–	–
	6	5.3	-10	–	–	–	–	–	–	–	–	–	–
	7	6.5	-30	–	–	–	–	–	–	–	–	–	–
	8	7.6	-96	–	–	–	–	–	–	–	–	–	–
2.00	5	4.2	-3	–	–	–	–	–	–	–	–	–	–
	6	5.3	-8	–	–	–	–	–	–	–	–	–	–
	7	6.5	-24	–	–	–	–	–	–	–	–	–	–
	8	7.6	-79	–	–	–	–	–	–	–	–	–	–

12 Conclusions and Future work

12.1 Results achieved and conclusions

The Universe is a well developed structure on the scale of galaxies and smaller formations. This requires that at the beginning of the expansion of the Universe (Section 1) there should have existed fluctuations (Section 5) which lead to the formation of such structures. We now have a successful cosmological paradigm based on the existence of an inflationary stage (Section 1.3) which allows us to consider the quantum origin of the fluctuations. These quantum fluctuations, produced during inflation, are stretched to scales much larger than the Hubble radius (at the time when they were produced) and, as the expansion of the universe goes on, each fluctuation will reenter inside the Hubble radius at some later epoch, depending on its wavelength. With this mechanism we can explain not only all the inhomogeneities we see today, even on the largest cosmological scales, but also the production of PBHs.

If a perturbation crossing the horizon at time t_k is large enough, then it will begin to collapse at some later instant t_c called the *turnaround point*. The location of t_k and t_c with respect to the transition epoch allows us to identify, in the case of a first–order phase transition, six different classes of fluctuations (cf. Tables 26 and 27) – A, B, C, D, E, and F. In the presence of a first–order phase transition, the PBH formation threshold δ_c is affected by some factor $(1-f)$ where f is a function which gives the fraction of the overdense region spent in the dust–like phase of the transition. In the approach considered, f relates the sizes of the overdense region at t_k and t_c (Section 7.1).

The inflationary stage is followed by a radiation–dominated era during which the Universe successively visits the different scales at which particle physics predicts symmetry–breaking phase transitions. The SMPP (Section 1.8) predicts two phase transitions: the EW phase transition (Section 3), at an energy ~ 100 GeV, and the QCD phase transition (Section 2), at an energy ~ 170 MeV.

The occurence of a phase transition turns out to be very important in the context of PBH formation. In fact, during such epochs, the sound speed vanishes for some instants (first–order phase transition) or, at least, it suffers, depending on the strength of the transition, a more or less relevant reduction (Crossover) and, as a consequence, the effect of pressure in stopping gravitational collapse becomes less important, favouring PBH formation (Section 6.2).

Only the fluctuations with amplitude δ above some threshold δ_c can lead to the formation of PBHs. If $\delta < \delta_c$ the fluctuation dissipates and there is no PBH formation at all. In the case of a radiation–dominated universe we have, from analytical considerations, that $\delta_c = 1/3$ (although recent numerical simulations revealed different values for δ_c, all in the range $1/3 - 0.7$ (e.g. Sobrinho & Augusto, 2007). During a phase transition, this constant background value δ_c, valid for radiation domination, becomes smaller and, as a consequence, the value of $\beta(t_k)$ (equation 286), which is very sensitive to the threshold δ_c, could show a peak located near the phase transition epoch.

In order to determine the probability of PBH formation at a given epoch or, equivalently, the fraction of the universe going into PBHs at that epoch $\beta(t_k)$, we must know the value of the mass variance $\sigma(t_k)$ at that epoch. In order to determine $\sigma(t_k)$ it is also crucial to know the shape of the primordial spectrum of the fluctuations. In Sobrinho & Augusto (2007) we considered different kinds of spectra: i) scale–free power–law spectrum; ii) scale–free power–law spectrum with a pure step; iii) broken scale invariance spectrum; iv) running–tilt power–law spectrum. In the present work we concentrated on the running–tilt power–law spectrum because it is highly supported by recent WMAP observations (Section 10) and, besides that, it possesses a variable index $n(k)$ that might give more power during some epochs relevant to PBH formation.

However, the running–tilt power–law spectrum introduces a pair of additional parameters to the equations: a parameter n_+ giving the maximum value attained by $n(k)$ and a parameter t_+ giving the location of that maximum. At present, the best we can do is to constrain these parameters in accordance with the observational results (Section 10). We have considered, $1.2 < n_+ < 2.0$ and 10^{-23} s $< t_+ < 10^8$ s. As a result, we selected 165 cases of interest for PBH formation in the context of a radiation–dominated universe (see Table 42 – cases marked 'R'). Other cases were rejected because either they exceed the observational constraints or gave negligible values for all epochs ($\beta < 10^{-100}$). Considering only a radiation–dominated universe, we already have some interesting results (see e.g. Figure 97). These can be improved if we consider the effects of phase transitions (in particular, the QCD phase transition).

12.1.1 QCD phase transition

The QCD phase transition is related to the spontaneous breaking of the chiral symmetry of QCD when quarks and gluons become confined into hadrons. The QCD phase transition was suggested, for a long time, as a prime candidate for a first–order phase transition. Recent results provided strong evidence that the QCD transition is only a simple Crossover. Here we have considered the two possibilities. In the case of a first–order phase transition we have considered the Bag Model (Section 2.3.1) and the Lattice Fit model (Section 2.3.2) which is based on LGT results. In Section 2.3.3 we considered the Crossover model.

We are particularly interested on the determination of the epoch and on the duration of the phase transition as well as on the expression for the sound speed during this transition (Sections 2.3 and 2.4) since that is all we need to determine the behaviour of the threshold δ_c during the transition. A crucial parameter needed to determine the mentioned quantities is the number of degrees of freedom Δg (Section 1.10) elapsed during the transition. A larger Δg means a stronger and longer phase transition (in the case of the QCD we have $\Delta g \sim 40$ – Section 2.4).

In Section 7 we determined the values for δ_c during the QCD epoch. In the case of the Bag Model (Section 7.1) we divided the study in *before*, *during* and *after*, since a key–point on the evolution of a fluctuation is, besides the amplitude, the moment t_k when it crosses the horizon (before, during or after the QCD epoch). As a result, we found a new window for PBH formation with

δ_c reaching values as low as ≈ 0.091 for a background value $\delta_c = 1/3$ (Figure 66).

In Section 7.2 we considered the variation of δ_c during the QCD Crossover. We introduced a new function f (see equation 262) which takes into account the fact that, during the Crossover, the sound speed decreases but does not vanish. We have done this through an adimensional function $\alpha(t)$ (equation 261) which gives the fraction of the sound speed with respect to the background value $(1/\sqrt{3})$ at a given moment. We found that, in the case of a Crossover, the reduction on the value of δ_c is much less pronunced than in the Bag Model case with $\delta_{c,min} \approx 0.274$ for a background value $\delta_c = 1/3$ (Figure 70).

In Section 7.3 we considered the variation of δ_c during the QCD Lattice Fit. In this case we have a period with a vanishing sound speed which is similar to the Bag Model case and also a period during which the sound speed decreases down to zero, resembling the Crossover situation (cf. Figure 30). Thus, we interpret the Lattice Fit as a mixture of both situations and derive an appropriate expression for the function f (see equations 268 to 276). The study was divided, as in the Bag Model case, in *before*, *during* and *after*. As a result, we obtained a reduction of δ_c from $1/3$ to ≈ 0.12 (Figure 80).

Tipically, we have curves for β with two peaks: one from the radiation contribution and another from the QCD contribution (e.g. Figures 106f and 109c). Contributions from the QCD Bag Model or from the QCD Lattice Fit are, naturally, more visible than those from the QCD Crossover, since, in the latter, the sound speed never reaches zero. However, in the case of the QCD Crossover we might also reach high values for β (e.g. Figure 104).

There are many cases for which the contribution from the QCD (in particular in the case of a Bag Model or a Lattice Fit) exceeds the observational constraints (cf. Tables 44, 45 and 46).

Cut from Table 49, in Table 50 we present a list with the ten largest contributions from the QCD Crossover. In each case we have also indicated the contribution from radiation. For the cases shown, the contribution from the EW phase transition is negligible and the contribution from the electron–positron annihilation appears only in two cases (labeled 'ea'). If one considers, for the QCD phase transition, the Bag Model instead of a Crossover, then the ten cases are excluded due to observational constraints. On the other hand, if one considers the Lattice Fit model, then only the case $n_+ = 1.52$ and $t_+ = 10^{-2}$ s is allowed (labeled 'L').

Cut from Table 49, in Table 51 we present a list with the ten largest contributions from the QCD Bag Model. In each case we have also indicated the contribution from radiation. Notice that for all ten cases the contribution from the QCD is, by far, much greater than the contribution from radiation. A choice of a Lattice Fit model for the QCD gives similar results for all cases. On the contrary, the Crossover model gives, for these cases, very modest results (see also Table 49).

As an interesting situation we mention the case $n_+ = 1.40$ and $t_+ = 10^{-7}$ s, for which we have, besides the contribution from the QCD, an important contribution from the EW phase transition as well as from radiation (Figure 109c). The curve $\beta(t_k)$ spans from $\sim 10^{-11}$ s to $\sim 10^{-5}$ s, showing three noticeable

Table 50: Extended from Table 49 (cases in green), the ten cases with the largest contribution from the QCD Crossover to $\beta(t_k)$. We have also indicated, in each case, the peak from the radiation contribution. In the case $n_+ = 1.54$ and $t_+ = 10^{-2}$ we also have a non–negligible contribution from the QCD Lattice Fit. A label 'ea' indicates a non–negligible contribution from the electron–positron annihilation epoch (see text for more details).

		QCD Crossover		Radiation		
n_+	$\log_{10}(\frac{t_+}{1\ \mathrm{s}})$	$\log_{10}(\frac{t_{k,max}}{1\mathrm{s}})$	β_{max}	$\log_{10}(\frac{t_{k,max}}{1\mathrm{s}})$	β_{max}	Obs.
1.46	-5	-4.5	-19	-6.4	-14	
	-4	-4.5	-19	-5.4	-23	
	-3	-4.5	-27	–	–	
1.48	-4	-4.5	-12	-5.4	-15	
	-3	-4.5	-18	–	–	
1.50	-4	-4.5	-8	-5.4	-9	
	-3	-4.5	-11	–	–	
1.52	-2	-4.4	-20	-3.3	-19	L
1.54	-2	-4.4	-13	-3.3	-13	ea
1.56	-2	-4.4	-9	-3.3	-8	ea

Table 51: Extended from Table 49 (cases in blue), the ten cases with the largest contribution from the QCD Bag Model to $\beta(t_k)$. We have also indicated, in each case, the peak from the radiation contribution. In cases labeled with 'E' we might have contributions from the EW phase transition (Bag Model). In all cases a QCD Lattice Fit is also allowed (labeled 'L') as well as the QCD Crossover (labeled 'C' for cases with non–negligible results). For all cases the contribution from the electron–positron annihilation epoch is negligible.

		QCD Bag Model		Radiation		
n_+	$\log_{10}(\frac{t_+}{1\text{ s}})$	$\log_{10}(\frac{t_{k,max}}{1\text{s}})$	β_{max}	$\log_{10}(\frac{t_{k,max}}{1\text{s}})$	β_{max}	Obs.
1.38	-7	-5.3	-14	-8.5	-42	L,E
	-6	-5.3	-11	-7.4	-65	L
	-5	-5.3	-11	–	–	L
	-4	-5.3	-13	–	–	L
1.40	-8	-5.3	-13	-9.6	-16	L
	-7	-5.3	-9	-8.5	-24	L,E
	-4	-5.3	-9	–	–	L,C
1.42	-3	-5.3	-11	–	–	L,C
1.48	-2	-5.3	-14	-3.2	-44	L,C
1.50	-2	-5.3	-10	-3.3	-29	L,C

peaks: i) $\beta_{max} \sim 10^{-13}$ located at $t_k \sim 10^{-10.6}$ s – the contribution from the EW phase transition; ii) $\beta_{max} \sim 10^{-24}$ located at $t_k \sim 10^{-8.5}$ s – the contribution from radiation; iii) $\beta_{max} \sim 10^{-9}$ located at $t_k \sim 10^{-5.3}$ s – the contribution from the QCD Bag Model (or $\beta_{max} \sim 10^{-18}$ located at $t_k \sim 10^{-5.1}$ s, in the case of a Lattice Fit).

Cut from Table 49, in Table 52 we present a list with the ten largest contributions from the QCD Lattice Fit. In each case we have also indicated the contribution from radiation. For most of the ten cases the contribution from the QCD is by far much greater than the contribution from the radiation (the exception is the case $t_+ = 10^{-7}$ s and $n_+ = 1.42$, for which we have similar contributions from both components). Values inside brackets correspond to situations for which the contribution from the QCD Lattice Fit hides the peak from the radiation contribution. A choice of a Bag Model, instead of a Lattice Fit, leads to results exceeding the observational constraints for most of the ten cases of Table 52. Only in cases labeled with 'B' the QCD Bag Model is also allowed. For all cases the QCD Crossover is allowed, giving non–negligible results.

Table 52: Extended from Table 49 (cases in magenta), the ten cases with the largest contribution from the QCD Lattice Fit to $\beta(t_k)$. We have also indicated, in each case, the peak from the radiation contribution. In cases labeled with 'E' we might have contributions from the EW phase transition (Bag Model). In all cases a QCD Crossover is also allowed (labeled 'C'). The QCD Bag Model is allowed for the cases labeled 'B' and must be excluded, due to observational constraints, in the other cases. For all cases the contribution from the electron–positron annihilation epoch is negligible.

		QCD Lattice Fit		Radiation		
n_+	$\log_{10}(\frac{t_+}{1\ \mathrm{s}})$	$\log_{10}(\frac{t_{k,max}}{1\mathrm{s}})$	β_{max}	$\log_{10}(\frac{t_{k,max}}{1\mathrm{s}})$	β_{max}	Obs.
1.40	-6	-5.1	-13	-7.4	-38	E,C
	-5	-5.1	-12	–	–	C
	-4	-5.1	-14	–	–	B,C
1.42	-7	-5.1	-12	-8.5	-14	C
	-6	-5.1	-9	-7.5	-23	E,C
	-5	-5.1	-8	–	–	C
	-4	-5.1	-10	–	–	C
1.44	-3	-5.1	-11	–	–	C
1.50	-2	-5.1	-11	-3.3	-29	B,C
1.52	-2	-5.0	-8	-3.3	-19	C

12.1.2 EW phase transition

The EW phase transition (Section 3) was responsible for the spontaneous EW symmetry breaking which gave mass to all *massive particles*. Within the context of the SMPP, the EW phase transition is a very smooth Crossover (Section 3.2.1) with $\Delta g \sim 1$.

Taking this into account, we tried to determine which value of the parameter ΔT (see equation 180) would give rise to the strongest effect in terms of the reduction of δ_c (Section 8.1). We found out that, in the case $\delta_c = 1/3$, we should have $\Delta T \approx 0.013 T_c$ in order to get $\delta_{c,min} \approx 0.332$ which reflects, in practical terms, an almost negligible variation (Figure 85).

As a result we found out that the EW Crossover has no visible effects in terms of PBH production (Section 11.2). This means that when working in the context of the SMPP, one can safely neglect the EW transition as a potential source of PBH production.

A first–order phase transition might be allowed for the EW but only in the context of some extensions of the SMPP, such as the speculative framework of the MSSM (Section 1.9). We have considered that possibility and modelled it by a Bag Model (Section 3.2.2) with $\Delta g \approx 80$ (which appears to be a reasonable value in the context of the MSSM). In this case the results are, by far, more interesting (Section 8.2) than in the Crossover case. We obtained a reduction from $\delta_c = 1/3$ to $\delta_{c,min} \approx 0.17$ (Figure 86).

In Section 11.5 we determined the contribution from the EW Bag Model to the curve $\beta(t_k)$. Some of the results are encouraging, with the curve showing two peaks. For example, in the case shown in Figure 108c we have a large peak representing the radiation contribution and a sharp peak representing the contribution from the EW phase transition.

There are a few cases for which the contribution from the EW exceeds the observational constraints (cf. Table 47). These must be excluded. On the other hand, there are also a few extra cases (i.e. cases not shown on Table 42) for which, although the contribution from radiation is negligible, there is a non–negligible contribution from the EW transition (e.g. Figure 108a).

We also have cases for which there is a significant contribution from both the QCD and the EW transitions. An example of this is the case shown in Figure 109a for which we have two sharp peaks. Notice, however, that the peak on the right, which relates to the QCD, exists only in the case of the Bag Model or the Lattice Fit model. In the example of Figure 109b we have, besides the contribution from the EW phase transition, a (modest) contribution from radiation and a possible contribution from the QCD phase transition (valid only if one adopts the Bag Model or the Lattice Fit).

Cut from Table 49, in Table 53 we present a list with the ten largest contributions from the EW Bag Model. In each case we have also indicated the contribution from radiation.

Table 53: Extended from Table 49 (cases in red), the ten cases for which there is a larger contribution from the EW Bag Model to $\beta(t_k)$. We have also indicated, in each case, the peak from the radiation contribution. For some cases we might have also a contribution from the QCD Bag Model (labeled 'B') or from the QCD Lattice Fit (labeled 'L'). The QCD Crossover as well as the electron–positron annihilation lead to negligible results for all cases.

		EW Bag Model		Radiation		
n_+	$\log_{10}(\frac{t_+}{1\ \mathrm{s}})$	$\log_{10}(\frac{t_{k,max}}{1\mathrm{s}})$	β_{max}	$\log_{10}(\frac{t_{k,max}}{1\mathrm{s}})$	β_{max}	Obs.
1.32	-12	-10.6	-21	-13.6	-36	
	-11	-10.6	-18	-12.6	-49	
	-10	-10.6	-19	-11.5	-71	
	-9	-10.6	-23	–	–	
1.34	-12	-10.6	-12	-13.7	-18	
	-9	-10.6	-13	–	–	B
	-8	-10.6	-23	–	–	B
1.36	-8	-10.6	-13	–	–	B,L
1.38	-7	-10.6	-21	-8.5	-42	B,L
1.40	-7	-10.6	-13	-8.5	-24	B,L

Table 54: Extended from Table 49 (cases in cyan), the ten cases with the largerst contribution to $\beta(t_k)$ from the electron–positron annihilation epoch. We have also indicated, in each case, the peak from the radiation contribution. In the case $t_+ = 10^{-1}$ s and $n_+ = 1.60$ we have a contribution from the QCD (Bag Model, Lattice Fit or Crossover – B,L,C).

		electron–positron		Radiation		
n_+	$\log_{10}(\frac{t_+}{1\text{ s}})$	$\log_{10}(\frac{t_{k,max}}{1\text{s}})$	β_{max}	$\log_{10}(\frac{t_{k,max}}{1\text{s}})$	β_{max}	Obs.
1.60	-1	-0.1	-20	-2.2	-7	B,L,C
	0	-0.1	-17	-1.2	-14	
1.62	0	-0.1	-12	-1.2	-10	
	1	0.0	-16	–	–	
1.64	0	-0.1	-8	-1.2	-7	
	1	0.0	-12	–	–	
1.66	1	0.0	-8	–	–	
1.68	1	0.0	-6	–	–	
1.72	2	1.0	-8	–	–	
1.74	2	1.0	-6	–	–	

12.1.3 Electron–positron annihilation

Other possible scenarios during which the sound speed might experience a reduction (besides cosmological phase transitions), are the cosmological particle annihilation periods. As an example, we considered the electron–positron annihilation epoch during which the sound speed might have decreased by about 20% (Section 4). This is a very interesting case because it corresponds to an epoch for which the horizon mass was $\sim 10^5 M_\odot$. We considered that, during this period, the sound speed has a 'Crossover'–like profile.

We have determined that a reduction of 20% on the value of the sound speed requires $\Delta T \approx 0.115 T_c$ (Section 4) and that this value leads to a reduction on the value of δ_c from 1/3 to ≈ 0.30 (Section 9, Figure 89).

The electron–positron annihilation epoch is a smooth event with $\Delta g = 3.5$ (cf. Section 4), but not as smooth as the EW Crossover with $\Delta g = 1$ (Section 3.2.1). So, we have non–negligible contributions to β (cf. Figure 101). Cut from Table 49, in Table 54 we present a list containing the ten highest contributions from the electron–positron annihilation epoch. In each case we have also show the contribution from radiation because it reaches important values for all ten cases.

12.2 Future work

So far, we have determined the fraction of the universe going into PBHs, $\beta(t_k)$, during radiation domination and during cosmological phase transitions. Here we present some objectives and ideas for future work; in approximately chronological order:

- We plan to determine the PBH distribution in the Universe based on the results obtained so far. There are two main possibilities: (a) the distribution of PBHs is homegeneous throught the entire universe and (b) PBHs are clustered around galactic halos. We want to explore both.

- The existence of critical phenomena suggests that PBHs may be much smaller tant the particle horizon at formation with masses that might be as small as $10^{-4}M_H$. We want to explore this subject and how it affects the PBH mass spectrum.

- At this stage, the results should show some dependence on the model one uses for the spectrum of primordial density fluctuations. So far, we have concentrated mainly on a running–tilt power–law spectrum because it is highly supported by recent WMAP observations. However, even in this case, there is a strong lack of observational data. It is expected that upcoming missions, such as the Planck Satellite (planned to launch in April 2009), could provide some of these data.

- We plan to work aslo with other types of spectra (e.g. broken scale invariance spectrum) and compare the results with the ones achieved so far.

- When a PBH forms at a given epoch it could swallow smaller mass PBHs existing in the neighboord. We plan to study the importance of this process and evaluate how it affects the values of $\beta(k)$.

- If PBHs are created highly clustered, then this could lead to a huge number of PBH binaries and also to a huge number of PBH mergers (which would lead to the formation of bigger BHs). We plan to determine how this could affect the density distribution function of PBHs on the universe, possibly through simulations.

- In the not so near future we want to improve our results considering a single model accounting for all these ideas. We also want to extend our study to the period between the end of inflation $\sim 10^{-33}$ s and 10^{-23} s.

References

Adelman–McCarthy J. K., et al. 2008, *The Sixth Data Release of the Sloan Digital Sky Survey*, ApJSS, 175, 297, [arXiv:0707.3413].

Aguilar–Saavedra J. A., et al. 2006, *Supersymmetry Parameter Analysis: SPA Convention and Project*, Eur. Phys. Jour. C, 46, 43 [hep-ph/0511344].

Aitchison I. J. R., 2005, *Supersymmetry and the MSSM: An Elementary Introduction*, hep-ph/0505105v1.

Allanach B. C., et al. 2002, *The Snowmass Points and Slopes: Benchmarks for SUSY Searches*, Eur. Phys. Jour. C, 25, 113 [hep-ph/0202233].

Anderson G. W. & Hall, L. J., 1992, *The electroweak phase transition and baryogenesis*, PhRvD, 45, 2685.

Aoki Y. et al., 2006a, *The QCD transition temperature: Results with physical masses in the continuum limit*, Phys. Let. B, 643, 46 [hep-lat/0609068].

Aoki Y. et al., 2006b, *The order of the quantum chromodynamics transition predicted by the standard model of particle physics*, Nature, 443, 675 [hep-lat/0611014].

Arnold P. & Espinosa O., 1993, *The Effective Potential and First–Order Phase Transitions: Beyond Leading–Order*, PhRvD, 47, 3546 (Erratum: 1994, PhRvD, 50 6662) [hep-ph/9212235].

Baierlein R., 2001, *The elusive chemical potential*, Am. J. Phys., 69, 423.

Barbier B. et al. 2005, *R–parity violating supersymmetry*, Phys. Rept., 420, 1 [hep–ph/0406039].

Bennett C. L. et al. 2003, *First year Wilkinson Microwave Anisotropy Probe (WMAP) observations: Preliminary Maps and Basic Results*, ApJSS, 148, 1 [astro-ph/0302207].

Bernard C. et al., 1997, *Kaon interferometry as signal for the QCD phase transition at RHIC*, Nuc. Phys. A, 625, 473 [nucl-th/9703017].

Bernard C. et al. (the MILC collaboration), 2004, *QCD thermodynamics with three flavours of improved staggered quarks*, PhRvD, 71, 034504 [hep-lat/0405029].

Bertone G., Hooper, D. & Silk, J., 2005, *Particle dark matter: evidence, candidates and constraints*, Phys. Rep., 405, 279 [hep-ph/0404175].

Blais D., Bringmann T., Kiefer C. & Polarski D., 2003, *Accurate results for primordial black holes from spectra with a distinguished scale*, PhRvD, 67, 024024 [astro-ph/0206262].

Bodmer A. R., 1971, *Collapsed Nuclei*, PhRvD, 4, 1601.

Boggess N. W., 1992, *The COBE mission: its design and performance two years after launch*, ApJ, 397,420.

Boyanovsky D., Vega H. J. & Schwarz D. J., 2006, *Phase transitions in the early and present Universe* , Ann. Rev. Nucl. Part. Sci., 56, 441 [hep-ph/0602002].

Brandenberger R. et al., 1998, *Baryogenesis with QCD domain walls*, Abstracts of the 19th Texas Symposium on Relativistic Astrophysics and Cosmology, held in Paris, France, Dec. 14-18, 1998. Eds.: J. Paul, T. Montmerle, and E. Aubourg (CEA Saclay) [hep-ph/9808471].

Brandenberger R. et al., 1999, *Baryogenesis at the QCD scale*, Strong and Electroweak Matter '98, Proceedings of a conference held in Copenhagen, Denmark, 2-5 December, 1998. Edited by Jan Ambjrn, Poul Henrik Damgaard, Kimmo Kainulainen, and Kari Rummukainen, Published by World Scientific Publishers, 1999, p.141 [hep-ph/9903318].

Bridle S.L., Lewis A.M., Weller J. & Efstahiou G., 2003, *Reconstructing the primordial power spectrum*, MNRAS, 342, L72 [astro–ph/0302306].

Bringmann T., Kiefer C. & Polarski D., 2002, *PBHs from inflationary models and without broken scale invariance*, PhRvD, 65, 024008 [astro–ph/0109404].

Burles S. et al. 1999, *Big–Bang Nucleosynthesis: Linking Inner Space and outer Space*, astro–ph/9903300.

Cardall C. Y. & Fuller G. M., 1998, *Semianalytic Analysis of Primordial Black Hole Formation During a First–order QCD Phase Transition*, astro–ph/9801103.

Carr B. J., 1975, *The PBH mass spectrum*, ApJ, 201, 1.

Carr B. J., 2003, *Primordial Black Holes as a Probe of Cosmology and High Energy Physics*, Lect. Notes Phys. 631, 301 [astro–ph/0310838].

Carr B. J., 2005, *Primordial black holes: recent developments*, 22nd Texas Symposiun at Stanford, Dec. 2004 [astro–ph/0504034].

Carr B. J. & Hawking S. W., 1974, *BHs in the early Universe*, MNRAS, 168, 399.

Carr B.J., Gilbert J. H. & Lidsey J. E., 1994, *Black hole relics and Inflation: limits on blue perturbation spectra*, PhRvD, 50, 4853 [astro-ph/9405027].

Christiansen M. B. & Madsen J., 1996, *Large nucleation distances from impurities in the cosmological quark-hadron transition*, PhRvD, 53, 5446 [astro-ph/9602071].

Cole S. et al., 2005, *The 2dF Galaxy Redshift Survey: power–spectrum analysis of the final data set and cosmological implications*, MNRAS, 362, 505 [astro-ph/0501174].

Coleman T. S. & Roos M., 2003, *Effective degrees of freedom during the radiation era*, PhRvD, 68, 27702 [astro-ph/0304281].

Colless M. et al., 2003, *The 2dF Galaxy Redshift Survey: Final Data Release*, astro–ph/0306581.

Covi L., 2003, *Status of Observational Cosmology and Inflation*, Physics in Collision, Proceedings of the XXIII International Conference, Edited by S. Riemann and W. Lohmann. SLAC, p. 67 (http://www.slac.stanford.edu/econf/C030626) [hep-ph/0309238].

Csikor F. et al., 1998, *Endpoint of the hot electroweak phase transition*, PhRvL, 82 ,21 [hep-ph/9809291].

Csikor F., 1999, *Electoweak phase transition: recent results*, Talk presented at the International Europhysics Conference on High Energy Physics, Tampere, Finland, July 15-21, 1999 [hep-ph/9910354].

d'Inverno R., 1993, *Introducing Einstein's relativity*, Oxford, Claredon Press.

Düchting N., 2004, *Supermassive black holes from primordial black hole seeds*, PhRvD, 70, 064015 [astro–ph/0406260].

Ejiri S., 2000, *Lattice QCD at finite temperature*, Nuc. Phys. B procedings supplements, 94, 19 [hep-lat/0011006].

Ejiri S., 2007, *Lattice QCD thermodynamics with Wilson quarks*, Talk at Yukawa International Seminar 2006 (Kyoto) [astro-ph/0704.3747].

Ellis J. et al., 2007, *Higgs Boson Properties in the Standard Model and its Supersymmetric Extensions*, hep-ph/0702114.

Enqvist K. et al., 1992, *Nucleation and bubble growth in a first order cosmological electroweak phase transition*, PhRvD, 45, 3415.

Espinosa J. R., 1996, *Dominant two–loop corrections to the MSSM finite temperature Effective Potential*, Nucl. Phys. B, 475, 273 [hep-ph/9604320].

Espinosa J. R. et al., 1993, *On the electroweak phase transition in the Minimal Supersymmetric Standard Model*, Phys. Lett. B, 307, 106 [hep-ph/9303317].

Fabiano N., 1997, *Top mesons*, EPJC, 2, 345 [hep–ph/9704261].

Fodor Z. & Hebecker A., 1994, *Finite Temperature Effective Potential to Order g^4, λ^2 and the Electroweak Phase Transition*, Nucl. Phys. B, 432, 127 [hep-ph/9403219].

Forcrand P. & Philipsen O., 2006, *Towards the QCD diagram*, Proceedings of the XXIVth International Symposium on Lattice Field Theory, July 23-28, 2006, Tucson, Arizona, p.130 [hep-lat/0611027].

Gamow G., Alpher R. A. & Bethe H., 1948, *The Origin of Chemical Elements*, Phys. Rev., 73, 803.

Green A. M., Liddle A. R., Malik K. A. & Sasaki M., 2004, *A new calculation of the mass fraction of PBHs*, PhRvD, 70, 041502 [astro–ph/0403181].

Gupta S., 2003, *The quark gluon plasma: lattice computations put to experiment test*, Pramana, 61, 877 [hep-ph/0303072].

Guth A. H., 2000, *Inflation and eternal inflation*, Phys. Rep., 333, 555 [astro-ph/0002156].

Gynther A., 2006, *Thermodynamics of electroweak matter*, PhD Thesis, University of Helsinki, HU-P-D130.

Hands S., 2001, *The phase diagram of QCD*, Comtemp. Phys., 42, 209 [physics/0105022].

Harada T. & Carr B. J., 2005, *Growth of primordial black holes in a universe containing a massless scalar field*, PhRvD, 71, 104010 [astro–ph/0412135].

Hinshaw G. et al. 2008, *Five–Year Wilkinson Microwave Anisotropy Probe (WMAP) Observations: Data Processing, Sky Maps, & Basic Results*, arxiv: 0803.0732.

Hirata C. M. & Sigurdson K., 2007, *The spin–resolved atomic velocity distribution and 21–cm line profile of dark–age gas*, MNRAS, 375, 1241 [astro-ph/0600507].

Hu W. & Dodelson S., 2002, *Cosmic Microwave Background Anisotropies*, ARA&A, 40, 171 [astro-ph/0110414].

Huang, Q.-G., 2007, *Simplified chain inflation*, JCAP, 05, 9 [hep-th/0704.2835v2].

Hubble E., 1929, *A Relation between Distance and Radial Velocity among Extra–Galactic Nebulae*, Proceedings of the National Academy of Sciences of the United States of America, 15, 168.

Hwang W-Y. P., 2007, *What happened to the cosmological QCD phase transition?*, astro-ph/0705.4149.

Ignatius J., 1993, *Cosmological phase transitions*, Academic Dissertation, University of Helsinky, HU-TFT-IR-3-1.

Ignatius, J. & Schwarz, D. J. 2001, *The QCD phase transition in the inhomogeneous Universe*, PhRvL, 86, 2216 [hep–ph/0004259v2].

Jedamzik K., 1997, *Primordial black hole formation during the QCD epoch*, PhRvD, 55, 5871 [astro-ph/9605152].

Jedamzik K., 1998, *Could MACHOs be primordial black holes formed during the QCD epoch?*, Phys. Rep., 307, 155 [astro-ph/9805147].

Jedamzik K. & Niemeyer J. C., 1999, *PBH formation during first–order phase transitions*, PhRvD, 59, 124014 [astro–ph/9901293].

Jones M. H., & Lambourne R. J. A., 2004, *An introduction to galaxies and cosmology*, by Mark H. Jones and Robert J.A. Lambourne. Co-published with The Open University, Milton Keynes. Cambridge, UK: Cambridge University Press.

Kajantie K., et al., 1998, *The universal properties of the electroweak phase transition*, Talk presented by K.R. at the 5th International Workshop on Thermal Field Theory and their applications, Regensburg, Germany, August 1998 [hep-ph/9809435].

Kämpfer B., 2000, *Cosmic phase transitions*, Ann. Phys., 9, 605 [astro-ph/0004403].

Karsch F. et al., 1996, *Critical Higgs Mass and Temperature Dependence of Gauge Boson Masses in the SU(2) Gauge-Higgs Model*, Nuc. Phys. B - Proc. Supp., 53, 623 [hep-lat/9608087].

Karsch F. et al., 2000, *The pressure in 2,* $2+1$ *and 3 flavour QCD*, Phys. Let. B, 478, 447 [hep-lat/0002003].

Kiefer C., 2003, *Quantum aspects of black holes*, In *The Galactic black hole*– Lectures on general relativity and astrophysics; Edited by Heino Falcke & Friedrich W. Hehl; Series in high energy physics, cosmology and gravitation; Bristol: IoP; Institute of Physics Publishing [astro–ph/0202032].

Koch V., 1997, *Aspects of Chiral Symmetry*, IJMP–E, 6, 203 [nucl–th/9706075].

Laermann E. & Philipsen O., 2003, *Status of lattice QCD at finite temperature*, Ann. Rev. Nucl. Part. Sci., 53, 163 [hep-ph/030304].

Liddle A. R., 1999, *An Introduction to Cosmological Inflation*, High Energy Physics and Cosmology, 1998 Summer School, ICTP, Trieste, Italy, 29 June – 17 July 1998, Edited by A. Masiero, G. Senjanovic, and A. Smirnov, World Scientific Publishers, 1999, pag. 260 [astro-ph/9901124].

Liddle A. R. & Lyth D. H., 1993, *The cold dark matter density perturbation*, Phys. Rep., 231, 1 [astro–ph/9303019].

Linde A. D., 2005, *Particle Physics and Inflationary Cosmology*, hep–th/0503203.

Longair M. S., 1998, *Galaxy formation*, Astronomy & Astrophysics Library, Springer–Verlag, Berlin.

Lyth D. H., 1993, *Introduction to Cosmology*, Lectures given at the *Summer School in High Energy Physics and Cosmology*, ICTP (Trieste) 1993 [astro-ph/9312022].

Martin S. P., 1997 (version 4, June 2006), *A Supersymmetry Primer*, hep-ph/9709356.

Mégevand A., 2000, *Development of the electroweak phase transition and baryogenesis*, Int. Jour. Mod. Phys. D, 9, 733 [hep-ph/0006177].

Moreno J. M., et al., 1997, *Sphalerons in the MSSM*, Nucl. Phys. B, 483, 267 [hep-ph/9605387].

Musco I., Miller J. C. & Rezzolla L., 2005, *Computations of PBH formation*, CQG, 22, 1405 [gr–qc/0412063].

Narlikar J. V. & Padmanabhan T., 1991, *Inflation for Astronomers*, ARA&A, 29, 325.

Natarajan, P., & Treister, E. 2008, *Is there an upper limit to black hole masses?*, ArXiv e–prints, 808, arXiv:0808.2813.

Novikov I. D., Polnarev A. G., Starobinsky A. A. & Zeldovich Ya. B., 1979, *Primordial Black Holes*, A&A, 80, 104.

Padmanabhan T., 2001, *Theoretical astrophysics* (Vol. 3), Cambridge University Press, Cambridge.

Penzias A. A. & Wilson R. W., 1965, *A measurement of excess antenna temperature at 4080 Mc/s* , ApJL, 1, 419.

Polarski D., 2001, *Classicality of primordial fluctuations and primordial black holes*, Int. Jour. Mod. Phys. D, 10, 927 [astro-ph/0109388].

Polarski D. & Starobinsky A. A., 1996, *Semiclassicality and decoherence of cosmological perturbations*, CQG, 13, 377.

Rangarajan R. et al., 2002, *Electroweak Baryogenesis in a Cold Universe*, Astroparticle Physics, 17, 167 [hep-ph/9911488].

Riotto A. & Trodden M., 1999, *Recent progress in Baryogenesis*, Ann. Rev. Nucl. Part. Sci., 49, 35 [hep-ph/9901362].

Ryden B., 2003, *Introduction to Cosmology*, Pearson Eduction, Inc., publishing as Addison Wesley, San Francisco.

Schmid C., Schwarz D. J. & Widerin P., 1997, *Peaks above the Harrison-Zel'dovich spectrum due to the Quark-Gluon to Hadron Transition*, PhRvL, 78, 791 [astro-ph/9606125].

Schmid C., Schwarz D. J. & Widerin P., 1999, *Amplification of cosmological inhomogeneities by the QCD transition*, PhRvD, 59, 43517 [astro-ph/9807257].

Schwarz D. J., 1998, *Evolution of gravitational waves through the cosmological QCD transition*, Mod. Phys. Lett. A, 13, 2771 [gr-qc/9709027].

Schwarz D. J., 2003, *The first second of the Universe*, Annalen der Physik, 12, 220 [astro-ph/0303574].

Schutz B. F., 1985, *A first course in General Relativity*, Cambridge University Press, Cambridge.

Scott D., 2006, *The standard cosmological model*, Canadian Journal of Physics, 84, 419 [astro-ph/0510731].

Slipher V. M., 1917, *Nebulae*, Proceedings of the American Philosophical Society, 56, 403.

Sobrinho J. L. G., 2003, *Possibilidade de detecção directa de Buracos Negros por radiação electromagnética*, Tese submetida nas Provas de Aptidão Pedagógica e Capacidade Científica para habilitação à categoria de Assistente, Universidade da Madeira.

Sobrinho J. L. G. & Augusto P., 2007, *The fraction of the Universe going into Primordial Black Holes*, Internal Report, CCM, 126/07.

Spergel D. N., et al. 2003, *First-Year Wilkinson Microwave Anisotropy Probe (WMAP) Observations: Determination of Cosmological Parameters*, ApJS, 148, 175 [astro–ph/0302209].

Spergel D. N., et al. 2007, *Three-Year Wilkinson Microwave Anisotropy Probe (WMAP) Observations: Implications for Cosmology*, ApJS, 170, 337 [astro-ph/0603449].

Stern D. et al., 2000, *Discovery of a color–selected Quasar at* $z = 5.50$, ApJ, 533, L75.

Stuart R. G., 1999, *An Improved Determination of the Fermi Coupling Constant, GF* (talk presented at DPF 99, UCLA, Los Angeles, USA, 5-9 January, 1999), hep-ph/9902257.

Tegmark M. et al., 2004, *Cosmological parameters from SDSS and WMAP*, PhRvD, 69, 103501 [astro–ph/0310723].

Trodden M., 1999, *Electroweak baryogenesis*, Reviews of Modern Physics, 71, 1463 [hep-ph/9803479].

Tsujikawa S., 2003, *Introductory review of cosmic inflation*, lecture notes given at The Second Tah Poe School on Cosmology "Modern Cosmology", Naresuan University, Phitsanulok, Thailand, April 17 -25, 2003 [hep-ph/0304257].

Unsöld A. & Bascheck B., 2002, *The new Cosmos*, Springer Verlag, Berlin.

Weinberg S., 2000, *The Cosmological Constant Problems* (Talk given at Dark Matter 2000, February, 2000), astro-ph/0005265.

Witten E., 1984, *Cosmic separation of phases*, PhRvD, 30, 272.

Yao W.-M., et al., 2006, *Review of Particle Physics*, Journal of Physics G, 33, 1 [also available on the *Particle Data Group* pages: http://pdg.lbl.gov/].

Zimdahl W. & Pavón D., 2001, *Cosmological two–fluid thermodynamics*, GR&G, 33, 791 [astro-ph/0005352].